Recent progress on 2D magnets: Fundamental mechanism, structural design and modification

Cite as: Appl. Phys. Rev. **8**, 031305 (2021); https://doi.org/10.1063/5.0039979
Submitted: 08 December 2020 • Accepted: 21 May 2021 • Published Online: 23 July 2021

Xue Jiang, Qinxi Liu, Jianpei Xing, et al.

Applied Physics Reviews REVIEW scitation.org/journal/are

Recent progress on 2D magnets: Fundamental mechanism, structural design and modification

Cite as: Appl. Phys. Rev. 8, 031305 (2021); doi: 10.1063/5.0039979
Submitted: 8 December 2020 · Accepted: 21 May 2021 ·
Published Online: 23 July 2021

Xue Jiang,[1] Qinxi Liu,[1] Jianpei Xing,[1] Nanshu Liu,[1] Yu Guo,[1] Zhifeng Liu,[2] and Jijun Zhao[1,a)]

AFFILIATIONS

[1]Key Laboratory of Material Modification by Laser, Ion and Electron Beams, Dalian University of Technology, Ministry of Education, Dalian 116024, China

[2]School of Physical Science and Technology, Inner Mongolia University, Hohhot 010021, China

[a)]Author to whom all correspondence should be addressed: zhaojj@dlut.edu.cn

ABSTRACT

The two-dimensional (2D) magnet, a long-standing missing member in the family of 2D functional materials, is promising for next-generation information technology. The recent experimental discovery of 2D magnetic ordering in CrI_3, $Cr_2Ge_2Te_6$, VSe_2, and Fe_3GeTe_2 has stimulated intense research activities to expand the scope of 2D magnets. This review covers the essential progress on 2D magnets, with an emphasis on the current understanding of the magnetic exchange interaction, the databases of 2D magnets, and the modification strategies for modulation of magnetism. We will address a large number of 2D intrinsic magnetic materials, including binary transition metal halogenides; chalogenides; carbides; nitrides; oxides; borides; silicides; MXene; ternary transition metal compounds $CrXTe_3$, MPX_3, Fe-Ge-Te, MBi_2Te_4, and MXY (M = transition metal; X = O, S, Se, Te, N; Y = Cl, Br, I); *f*-state magnets; *p*-state magnets; and organic magnets. Their electronic structure, magnetic moment, Curie temperature, and magnetic anisotropy energy will be presented. According to the specific 2D magnets, the underlying direct, superexchange, double exchange, super-superexchange, extended superexchange, and multi-intermediate double exchange interactions will be described. In addition, we will also highlight the effective strategies to manipulate the interatomic exchange mechanism to improve the Curie temperature of 2D magnets, such as chemical functionalization, isoelectronic substitution, alloying, strain engineering, defect engineering, applying electronic/magnetic field, interlayer coupling, carrier doping, optical controlling, and intercalation. We hope this review will contribute to understanding the magnetic exchange interaction of existing 2D magnets, developing unprecedented 2D magnets with desired properties, and offering new perspectives in this rapidly expanding field.

TABLE OF CONTENTS

I. INTRODUCTION

Since the discovery of magnetic phenomena in ancient times, magnetism has attracted vast research interest due to its technological importance and theoretical complexity. From the technique point of view, permanent magnets, which are required for high coercivity and large energy product, are widely used in loudspeakers, earphones, electric meters, small motors, and wind power generation. The more esoteric applications of magnetism are in magnetic recording and storage devices of computers, as well as in audio and video systems. Only ten years after the discovery of interlayer exchange coupling and related giant magnetoresistance (GMR) effect in the magnetic multilayers, GMR devices were routinely used in the hard disk drives of computers.[1] They are also crucial for the emerging field of spintronics, which is regarded as the core of the next-generation information technology. By using electron spin rather than charge as the information carrier, spintronics possesses prominent advantages of speeding up data processing, high circuit integration density, and low energy consumption.[2,3]

From the theoretical point of view, two fundamental concepts have been proposed to explain the fascinating magnetic phenomenon, namely, exchange interaction and spin-orbit coupling (SOC). The interplay between exchange interaction, spin-orbit coupling, and Zeeman effect is the essence of magnetism research. Together, they explain the origin of spin arrangement, orbital moment, and magnetocrystalline anisotropy, and the effect of external field on these quantities.[4] Among them, the interatomic/interelectronic exchange interactions are at the heart of the phenomenon of long-range magnetic ordering. Parallel and antiparallel arrangements of spins constitute long-range ferromagnetic (FM) and antiferromagnetic (AFM) orderings. As the dimensionality decreases, the net magnetic moment per atom generally increases. This might be ascribed to lower coordination number, quantum confinement effect, less quenching of orbital magnetic moment, and so on. Meanwhile, in two-dimensional (2D) lattices, exchange interactions would be stronger along one or two spatial directions than others, showing large anisotropy. Depending on the type of magnetic ions and the electronic band structures, the traditional exchange mechanisms, including direct exchange interaction,[5–7] superexchange interaction,[8–14] double exchange interaction,[15] itinerant electrons,[16–21] and Ruderman-Kittel-Kasuya-Yosida (RKKY) mechanisms,[22] are all found in various 2D systems, as well as three new interesting exchange interaction mechanisms, known as super-superexchange,[23,24] extended superexchange,[25,26] and multi-intermediate double exchange interactions.[27] These magnetic spin coupling mechanisms will be discussed in Sec. II.

The magnetism in 2D materials has been an emerging and rapidly growing research field. Much on-going progress on 2D magnets has been made mainly in the following three aspects. First, the experimentally unprecedented realizations of high quality 2D magnetic monolayer/multilayer materials using micromechanical cleavage, chemical vapor deposition (CVD), and molecular beam epitaxy (MBE) methods, including CrI_3,[28] VI_3,[29] $CrCl_3$,[30] $CrBr_3$,[31] α-$RuCl_3$,[32,33] VSe_2,[34] VTe_2,[35] $NbTe_2$,[35] $MnSe_x$,[36] $CrGeTe_3$,[37] MPS_3 (M = Fe, Mn, Ni),[38–40] $Fe_{3,5}GeTe_2$,[41,42] and $MnBi_2Te_4$.[43] These exciting experiments not only bring about the missing magnetic member in the family of 2D materials but also solve a long-standing controversy about the existence of magnetism in low-dimensional systems. Based on Mermin-Wagner theorem,[44] 2D magnetic systems cannot have any long-range FM or AFM ordering at $T > 0$ for isotropic Heisenberg model. The main reason for the existence of magnetism is the magnetocrystalline anisotropy and the dipolar interaction. Although the strength of these interactions is of order of magnitude of $\sim$1 meV, they will have a crucial impact on the 2D materials by breaking the conditions of Mermin-Wagner theorem.

Second, optical and electronic means have also been widely developed to characterize the 2D magnets.[45] Spin-polarized scanning tunneling microscope (SP-STM), and x-ray magnetic circular dichroism (XMCD) are the standard experimental techniques. They are highlighted in the recently developed 2D van der Waals magnets. SP-STM can provide valuable and precise information about the magnetic ordering and differentiate magnetic structures as well as exchange interactions. Based on excitation of spin polarized carriers from core levels to Fermi levels via circularly polarized x rays, XMCD is an efficient photocurrent technique used to obtain the local electronic configuration of the valence states. Moreover, due to the theoretical development of the sum rules, the element-specific spin and orbital moments can be obtained separately.[46] XMCD can also yield the orbital moment anisotropy, which is related to the magnetocrystalline anisotropy energy (MAE) via perturbation model. X-ray magnetic linear dichroism (XMLD) has been proposed as a mean of measuring the anisotropy in the spin orbit interaction, which can be related to the MAE using a straight forward sum rule.[47] Inelastic light scattering provides access to the energy, symmetry, and statistics of lattice, electronic, and magnetic excitations in nanomaterials. In addition, Raman spectroscopy can also provide indirect evidence of magnetism, based on either spin-phonon coupling or magnons. Raman scattering from

spin-phonon excitations yields incisive information on magnetic materials, which can be used to reveal magnetic ordering and phase transitions. For example, the studies of Kerr rotation versus the applied magnetic field (MOKE) produced the first indirect evidence of magnetic ordering in ultrathin films of $Cr_2Ge_2Te_6$[37] and CrI_3.[28] Specifically, single-layer $FePS_3$[48] and $Cr_2Ge_2Te_6$[49] at high temperatures showed a broad feature above the Curie temperature (T_C), which resulted from thermal magnetic fluctuations. In addition to the optical probes, the magnetic state of 2D itinerant magnets with conduction electrons can be detected by the anomalous Hall effect (AHE). So far, AHE has been applied to explore the magnetic ordering of layered Fe_3GeTe_2 down to the monolayer limit[50] and few-layer antiferromagnetic $MnBi_2Te_4$.[43]

Third, due to the benefit of a continuous increase in computing power, it is possible to predict the magnetic ground state and corresponding magnetic parameters of a given 2D material from first-principles calculations. The most important quantities of 2D magnets include the magnetic moment, exchange integral, MAE, and T_C. The former three terms can be accurately determined by density functional theory (DFT) calculations of total energy and electronic structure with or without considering SOC.[51] Commonly, combining DFT with Monte Carlo simulations implemented with Heisenberg model,[52] one can trace the variation of magnetization with temperature and determine the magnetic transition temperature (T_C/T_N) of the 2D systems. For example, 2D CrI_3 has been predicted as a FM material by three theoretical groups during 2015 and 2016,[8,53,54] individually. The reported magnetic moment and Curie temperature were 3∼3.44 μ_B per formula unit and 61∼107 K, respectively, in good agreement with the successive experimental results reported in 2017.[28] To our knowledge, the magnetic behavior of α-$RuCl_3$, VSe_2, VTe_2, $NbTe_2$, $MnSe_x$, CrGe(Si)Te_3 single- or few-layer sheets have also been discussed by DFT calculations.[18,55–64]

The powerful DFT tool and high-throughput computations would efficiently accelerate the screening of 2D magnetic candidate materials without having to synthesize them first.[65–68] Starting from the existing database of inorganic compounds, Mounet *et al.*[67] performed comprehensive DFT calculations to explore these 3D parent materials for possible exfoliation and finally identified 2662 prospective layered structures with weak interlayer binding energy. Among them, 36 ferromagnetic systems with relatively simple unit cells (less than six atoms) were identified with long-range magnetic order. After a further screening, monolayer materials of LaCl, YCl, ScCl, $LaBr_2$, and CrSBr have been identified as robust ferromagnets with $T_C > 200$ K.[65] Very recently, the ferromagnetic ordering of 2D CrSBr has been confirmed by experimental evidence, and the predicted T_C is very likely beyond 132 K.[69] In another study, a larger set of a 2D materials database (∼65 000) has been screened by high-throughput DFT calculations, yielding a total of 89 magnetic monolayer systems.[66] Among them, 56 showed FM ordering, while 33 prefer antiferromagnetic behavior. Furthermore, 24 FM monolayers were promising candidates possessing T_C higher than that of CrI_3.

To broaden the scope of intrinsic 2D magnets, atomic substitutions[65,70] and alloying[71,72] have been introduced in 2D materials and led to complex variations to the magnetic properties. In addition, many advanced techniques for exploring the potential energy landscapes can also be employed to theoretically design 2D magnets. For instance, the evolutionary algorithm and particle swarm optimization (PSO) approach have already demonstrated their validity in discovering potential 2D magnets,[73] including V_3X_8 (X = F, Cl, Br),[74] MnAs,[75] Co_2P,[5] Fe_3P,[76] PtN_2,[77] CoB_6.[78] For 2D organic frameworks, bottom-up design is also a common strategy to achieve promising 2D magnets by properly selecting the building units and linkers.[79–82]

Driven by all these three aspects, the research of 2D magnets has boomed in the last few years. In recent years, a great deal of new 2D magnetic materials have been experimentally discovered and theoretically predicted. In this review, however, we restricted the term to the 2D intrinsic magnets. The 2D intrinsic nonmagnetic materials, which have already been concluded in the previous review,[83] will not be covered here. In this review, we classified these emerging 2D intrinsic magnets into binary transition metal halogenides; chalogenides; carbides; nitrides; oxides; borides; silicides; ternary transition metal compounds $CrXTe_3$, MPX_3, Fe-Ge-Te, MBi_2Te_4, and MXY (M = transition metal; X = O, S, Se, Te, N; Y = Cl, Br, I); *f*-state magnets; *p*-state magnets; and organic magnets such as metal organic framework (MOF) and covalent organic framework (COF). The most common prototypes of 2D inorganic magnetic materials are shown in Fig. 1. Their key magnetic properties, especially the magnetic ground state, magnetic moment, T_C, and MAE will be comprehensively described in Sec. III.

For 2D layered materials, their magnetic properties can be readily modulated by chemical compositions, functional groups, intercalation, and substrates. Moreover, the spin coupling to external perturbations like strain, electronic/magnetic fields, and carrier doping could be the other critical factors for tailoring the strength of exchange interactions or magnetic anisotropy. These modulation methods could be utilized on 2D intrinsic magnets to further enhance Curie temperature. The corresponding mechanisms for modulating the charge distributions, energy level, orbital occupation, symmetry, and hopping paths will be discussed in Sec. IV.

In the final Sec. V, we will conclude with a discussion about future challenges and opportunities of 2D magnets. Four potential future directions regarding the practical applications have been proposed. In addition, this review article mainly focuses on the underlying mechanisms of exchange interaction, which not only determine the Curie temperature of 2D intrinsic magnets but also shed light on the strategies to manipulate the magnetic coupling. Therefore, this discussion is complementary to the other recent review articles on 2D magnets, which have discussed the history,[84] representative 2D magnets,[45,85,86] experimental synthesis,[87] probing techniques,[88] magnetic anisotropy,[89] device applications,[84,90–92] and their emergent phenomena.[93]

II. THE ORIGIN OF MAGNETISM IN 2D MATERIALS

A. The magnetic moment of free atoms

To start discussing the magnetic properties of 2D materials, we should first know the magnetic ground state of a multi-electron atom, which is mainly determined by Hund's rules. Generally speaking, Hund's rules refer to a set of rules that describe spin-spin coupling, orbital-orbital coupling, and spin-orbit coupling, respectively. The first rule about the spin-spin coupling in a multi-electron atom, whose strength is at the order of c.a. 2 eV is especially important. Hence, the magnetic moment is mainly determined by the intra-atomic exchange interaction. The spin-orbit interaction describing the coupling between spin and orbital angular momentum further produces the energy level

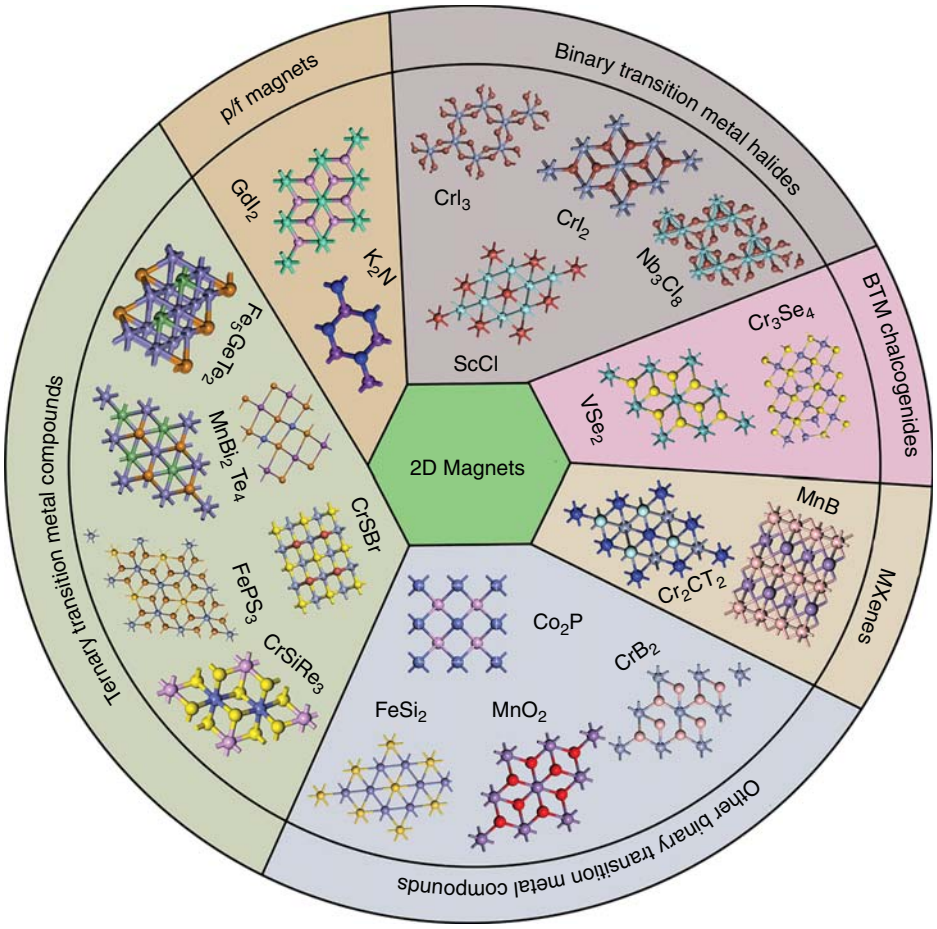

FIG. 1. The most common 2D inorganic magnetic materials. The representative crystal lattices are included, such as Binary transition metal halides (CrI_3, CrI_2, Nb_3Cl_8, and ScCl), binary transition metal (BTM) chalcogenides (Cr_3Se_4 and VSe_2), MXenes (MnB and Cr_2CT_2), other binary transition metal compounds (Co_2P, CrB_2, MnO_2, and $FeSi_2$), Ternary transition metal compounds ($CrSiTe_3$, CrSBr, $FePS_3$, $MnBi_2Te_4$, Fe_3GeTe_2, and Fe_5GeTe_2), and p/f magnets (GdI_2 and K_2N). They have been either experimentally realized or theoretically proposed for each type of magnetic lattice.

splitting with the order of several to hundreds mega-electron volts. We can estimate the moment per atom from this rule by maximizing spin (S), orbital momentum (L), and angular moment (J).

In a solid, exchange interaction and SOC are two most important concepts for magnetism. First of all, without interatomic exchange, there would be no spontaneous magnetization. Interatomic exchange interaction determines the long-range spin ordering, i.e., parallel or antiparallel spin alignment in a magnetic material. Meanwhile, spin-orbit interaction creates orbital magnetism and couples the spin to the lattice. Through the SOC interaction, spin and charge can talk to each other via exchanging energy and angular momentum, thereby establishing magnetic anisotropy. In addition, the other competition interactions have also been investigated to determine the size of the moment, including crystal fields, Hund's rule coupling, and onsite Coulomb repulsion.[94] These factors will be discussed in a following paper.

B. Ligand field theory

When a free ion is placed in a lattice and subjected to the interaction with its surrounding atoms, another key interaction arises, termed a ligand (crystal) field. The ligand effect on the central atom is entirely determined by symmetry and strength of field produced by these surrounding atoms. The symmetry and degenerate states of typical 2D magnets with 3d transition metals are summarized in Table I. It should be noted that the amplitude of splitting energy due to ligand field is comparable to the intra-atomic Coulomb and exchange interactions. Thus, the final ground state depends on the relative amplitude of them. For example, the d^4-d^7 configurations would show either low-spin or high-spin states in an octahedral ligand field.

In fact, ligand field theory provides a simple model to predict the magnetic behavior of 2D transition metal compounds, which is strongly influenced by the coordination environment and the number of d electrons. For example, the configurations of M_2NT_2 MXene are shown in Figs. 2(a) and 2(b).[12] For a transition metal ion located in an octahedral crystal field, its d orbitals split into the lower-energy t_{2g} states and higher-energy e_g orbitals. Similar to the transition metal dichalcogenides (TMDs), these nonbonding t_{2g} and e_g states of the MXenes are positioned between the bonding and antibonding states (σ and σ^*) of M–X and M–T bonds [Fig. 2(c)]. We assume a perfect bonding case as follows: (1) the nonmetal elements are in their nominal oxidation state, i.e., C^{4-}, N^{3-}, O^{2-}, F^-, and OH^-; (2) the M–X and M–T bonding states are filled; (3) the M–X and M–T antibonding states are empty. Therefore, only the electrons occupying the nonbonding d orbitals will contribute to the magnetism. For example, the nominal oxidation state of Cr ion in Cr_2CF_2 is +3. Based on Hund's

TABLE I. The types of crystal field point group symmetry, and orbital splitting of central transition metals ions in some typical 2D magnets.

Crystal field	Point group	Orbitals	2D magnets
Octahedral	O_h	t_{2g} (d_{xy}, d_{xz}, d_{yz}), e_g (d_{x2-y2}, d_{z2})	MX_3 (X = F, Cl, Br, I);[53,104] MX_2 (X= Cl, Br, I);[100] 1T-MX_2 (X = S, Se, Te);[105] MPS_4;[95] $CoGaX_4$ (X = S, Se, Te)[96] MGe(Si)X_3 (X = Se, Te)[99,291]
Distorted octahedral	D_{4h}	a_1 (d_{z2}), b_1 (d_{x2-y2}), b_2 (d_{xy}), e (d_{xz}, d_{yz})	Mn-Pc,[101] Mn-TCNB[102]
Trigonal prismatic	D_{3h}	e_1 (d_{xz}, d_{yz}); e_2 (d_{x2-y2}, d_{xy}); a_1 (d_{z2})	2H-MX_2 (X = S, Se, Te, F, Cl, Br, I, H)[10,27,103,283]
Triangular prism	C_{3v}	a_1 (d_{z2}); e′ (d_{xz}, d_{yz}) e (d_{x2-y2}, d_{xy})	Fe_2C;[97] M_2XT_x MXene[12]
Hexagonal	C_{6V}	e_1 (d_{xz}, d_{yz}); e_2 (d_{x2-y2}, d_{xy}); a_1 (d_{z2})	MN (M = Cr, V, Mn)[264–266]

rules, the remaining 3 electrons on Cr ion will occupy the t_{2g} band half filled, thereby giving a local magnetic moment of 3 μ_B. Similarly, the local magnetic moments of Mn_2CO_2, Mn_2CF_2, and $Mn_2C(OH)_2$ are 3 μ_B, 4 μ_B, and 4 μ_B, respectively. The electron spin arrangements on the transition metals in the nitride MXene are shown in the Fig. 2(d).[12] Similar analyses based on symmetry have also been used to identify the magnetic properties of binary transition metal halides, carbides, nitrides, oxides, borides, phosphides, silicides, arsenides, hydrides, and ternary transition metal compounds. The representative examples are shown in Table I. All these results are consistent with the results from DFT calculations.[10,12,45,65,93,95–105]

C. The importance of exchange interaction

Heisenberg model is a simple theoretical model to describe the physical effects of magnetic systems. Due to the strong local magnetic moment, the leading term is symmetric exchange interaction in Heisenberg model, which has the form

$$\hat{H}_{ex} = -\sum_{i \neq j} J_{ij} \hat{S}_i \cdot \hat{S}_j, \tag{1}$$

where i and j denote the lattice sites bearing a localized magnetic moment, and $\hat{S}_i$ or $\hat{S}_j$ is a quantum mechanical spin operator. J_{ij} is the exchange constant, which is the basis of most studies of magnetism. Evidently, J_{ij} will decrease rapidly with the distance between lattice i and j. The positive J_{ij} favors parallel spin alignment (i.e., FM), while the negative J_{ij} favors antiparallel spin alignment (i.e., AFM). Theoretically, the values of J_{ij} can be obtained from first-principles calculations. The simplest way is to calculate from the total energy difference between different spin orderings. In experiment, J_{ij} can be determined by fitting the inelastic neutron scattering data to the Heisenberg Hamiltonian.

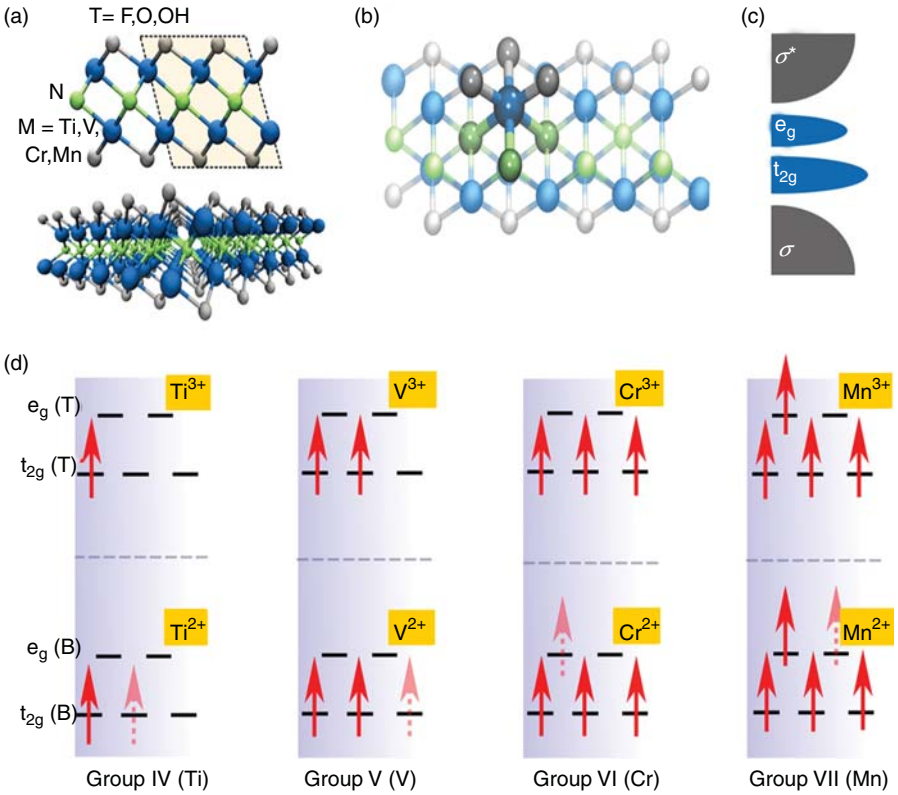

FIG. 2. Schematic diagram to explain the local magnetic moment of M_2NT_2 MXene (M = Ti, V, Cr, Mn; T = F, OH, O) with different transition metal groups. (a–b) The local coordination of transition metals, each transition-metal ion is subjected to an octahedral crystal field. (c) The simplified density of states, the nonbonding d-orbitals of the MXenes are positioned between bonding (σ) and antibonding (σ^*) states of M−X and M−T bonds. (d) Occupation of the electrons on the transition metal centers. Dotted spin indicates electron occupation is equally probable in the states corresponding to either the top (T) or the bottom (B) layer. Each N atom gains three electrons either by accepting two electrons from M atom in the top layer and one electron from the bottom layer M atom or vice versa, which leads to the coexistence of two different oxidation states for the two M atoms. Reproduced with permission from Kumar *et al.*, ACS Nano **11**, 7648 (2017). Copyright 2017 American Chemical Society.[12]

Generally speaking, these microscopic parameters of J_{ij} define most of macroscopic magnetic properties, especially the Curie temperature and the magnetic response function to an external field. For example, one can estimate magnetic transition temperatures via mean field theory (MFT)[106] as follows:

$$T_C = \frac{J_0 S(S+1)}{3k_B}, \tag{2}$$

where S is the atomic spin, J_0 is the sum of exchange interactions, and k_B is the Boltzmann constant. For 2D magnets, MFT usually overestimates the transition temperature by around 20% or even more, which is dependent on the coordination number.[106] Monte Carlo (MC) method gives a numerical solution to the Heisenberg model with reasonable accuracy. Therefore, it becomes the most commonly used method to predict the critical temperature in 2D magnets. However, MFT is still meaningful in establishing an upper limit of T_C at much less computational cost, which can be compared to MC results.

To explain the origin of spontaneous magnetization in metallic magnets with itinerant/localized electrons, such as single layer of Fe_3GeTe_2, T phase of TMDs, Cr_2C, and Fe_2C MXenes, another two models—Stoner model and RKKY model—have also been proposed, which will be discussed in Secs. II F and II G, respectively.

D. Spin orbital coupling in 2D magnets

The exchange term is isotropic in the sense that the scalar product $\hat{S}_i \cdot \hat{S}_j$ in Eq. (1) does not change under any rotation applied to every spin in the system. Based on Mermin-Wagner theorem,[44] 2D materials can be neither FM nor AFM at nonzero temperature due to thermal fluctuations under isotropic Heisenberg model. However, considering the spin-orbit interaction, this symmetry is broken. Besides the symmetric exchange term H_{ex} discussed in Sec. II C, the spin orbital coupling gives rise to the antisymmetric anisotropic exchange terms. Generally, the strength of antisymmetric anisotropic exchange terms are far less than H_{ex}. However, they become crucial for the magnetic ground state of 2D systems.

So far, many simple anisotropic spin models have been proposed to interpret the emerging magnetism in 2D materials. A typical 2D magnet possesses easy-plane magnetic anisotropy, uniaxial anisotropy, and isotropic anisotropy, which can be described in 2D XY, Ising, and Heisenberg models (XXZ), respectively. Specifically, 2D XY-like behavior has been observed in $Cr_2Ge_2Te_6$,[37] $MnPS_3$,[107] $CoGa_2X_4$,[96] CaI_2,[108] and so on; 2D Ising FM behavior was also demonstrated in plenty of 2D magnets, such as $Cr_2Si_2Te_6$,[109] CrI_3,[8] VI_3,[29] $NiCl_3$,[110] $NiCl_2$,[111] H-VTe_2,[57] T-VTe_2,[57] T-$MnTe_2$,[57] H-$FeTe_2$,[57] and $NiPS_3$.[112]

The antisymmetric anisotropic exchange terms contain various generic forms, for example, Dzyaloshinski-Moriya (DM) interaction term and single ion magnetocrystalline anisotropy term.[113,114] As stated above, both of them were determined by spin-orbit interaction. They have the following forms:

$$\hat{H}_{DM} = \sum_{i \neq j} \vec{D}_{ij} \cdot (\hat{S}_i \times \hat{S}_j), \tag{3}$$

$$\hat{H}_{an} = \sum_i A_i (\hat{S}_i)^2. \tag{4}$$

In 2D materials, the spin orbital interaction plays a similar role with non-metal atoms in superexchange interaction. As shown in Eq. (3), the DM interaction is characterized by the vector $\vec{D}_{ij}$, which is proportional to spin orbit coupling constant. It is also dependent on the position of the non-metal atom between the two magnetic atoms. Clearly, DM interaction favors an orthogonal alignment between spins.

In Eq. (4), A_i is the easy-axis single ion anisotropy factor. The magnetic anisotropy energy (MAE) is defined as the largest possible energy difference between two different magnetization directions. Within DFT framework, it can be easily obtained by performing total energy calculations including SOC.[51] To clarify the origin of MAEs, the torque method[115] was implemented in either all-electron full potential linearized augmented plane wave (FPLAPW) or Vienna Ab-initio Simulation Package (VASP) with plane wave basis sets.[116,117] To evaluate the contribution of SOC to the magnetic anisotropy, second-order perturbation theory has also been introduced.[116]

The DM interaction and single ion magnetocrystalline anisotropy term are typically a few percent of the isotropic term, producing a modest canting to symmetric exchange interactions. Nevertheless, the DM and single ion magnetocrystalline anisotropy terms are the good supplement to the 2D materials. A spontaneous rearrangement of atoms to favor the DM interaction can produce a large electric polarization in magnetoelectric materials. Meanwhile, the competition of spin-spin directions would be helpful to understand complicated magnetic behavior, such as magnetic skyrmions, and quantum spin liquid. The magnetic anisotropy is a prerequisite to realize FM or AFM states at the 2D limit.

A much-studied spin model (Kitaev model) is developed to describe the anisotropic spin exchange coupling for honeycomb spin lattice.[118] It has the form

$$H_K = \sum_{\langle i,j \rangle_\gamma} K_\gamma S_{i\gamma} S_{j\gamma}. \tag{5}$$

Neighboring spins couple depending on the direction of their bond γ with S_xS_x, S_yS_y, or S_zS_z. This exchange term and the symmetric Heisenberg term (Kitaev-Heisenberg model) together serve as a putative minima model for several materials, including α-$RuCl_3$[119] and $Li(Na)_2IrO_3$.[120]

Beyond these terms, one should also note that the real materials may have additional exchange couplings other than these couplings, including dipolar term, biquadratic interaction, and Zeeman coupling to the external magnetic field.[121] The strength of these exchange interactions is also much lower than that of symmetric exchange interaction. Therefore, to simplify, only the dominated spin models are investigated and discussed in this review, which are roughly enough to describe the critical parameters of 2D magnets.

E. The known exchange interaction

In this section, we discuss the identified exchange mechanisms in the real 2D magnets based on the abovementioned three models, including direct exchange, superexchange, double exchange, super-superexchange, extended superexchange, multi-intermediate double exchange interaction, itinerant electrons, and RKKY (Fig. 3). Their regimes of applicability depend on the electronic band structures and the types of magnetic ions, i.e., metal or insulator, and localized or delocalized. However, it is really difficult to distinguish them completely. For example, 3*d* electrons are partially localized on the

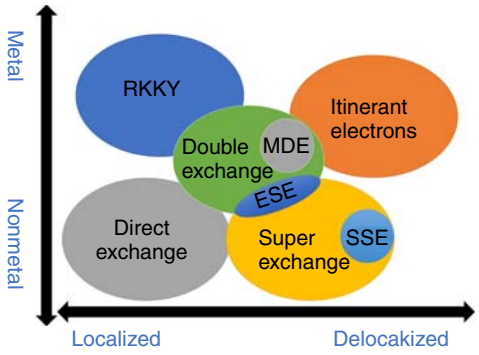

FIG. 3. Schematic diagram of the representative exchange interaction mechanisms. Several kinds of magnetic interaction between localized moments have been included, such as the conventional direct exchange, superexchange, double exchange, indirect exchange, and RKKY. The exchange interaction between itinerant electrons have also been covered. In addition, the small blue circle in superexchange region is super-superexchange interaction (SSE). The small grey circle in double exchange region is multi-intermediate double exchange interaction (MDE). The overlap region of double exchange and superexchange—the blue part—is the extended superexchange (ESE) interaction.

atomic sites and also partially delocalized in the crystal. In each exchange interaction, the magnetic ground state and Curie temperature will be further discussed, which are determined from the competition between the kinetic exchange energy and the Coulomb repulsion. It is worth noting that magnetic exchange interactions in the 2D magnets are rather complicated; thus, they are unable to be generalized under a one-theory umbrella. Although these types of exchange mechanism have been utilized to explain different materials appropriately, there are no clear borderlines between them. Moreover, several exchange interactions may possibly coexist in one real material. To understand the magnetic ordering and magnetic coupling strength, we always need to ask which one is dominant.

1. Direct exchange interaction

Direct exchange interaction is based on the overlap of electronic wavefunctions and is therefore very short ranged.[122] It is always confined to electrons in the orbitals from the nearest neighboring atoms. Considering the distance of the magnetic atoms, the strength of direct exchange interaction is always very weak. As a consequence, the direct exchange interaction is neither the main source of magnetism nor can it appropriately describe the magnetic behavior in most of the reported 2D magnets. Even so, direct exchange interaction between the neighboring sites is still dominant in the magnetic materials with peculiar *d-d*, *d-p*, and *p-p* hybridizations. With sufficiently large overlap, the exchange integral J_{ij} tends to be antiferromagnetic, ferromagnetic, or ferrimagnetic, depending on symmetry relationship and occupation number of the orbitals.

As a specific example, Liu *et al.*[5] proposed a novel class of 2D magnetic metal-shrouded materials, namely tetragonal transition metal phosphides (TM_2P), which showed peculiar coexistence of in-plane TM–P covalent bonds and interlayer TM–TM metallic bonds. For Co_2P, the spin-up d_{z2} orbital contributes to the total on-site moment of ∼1 μ_B. The electrons can hop from the occupied d_{z2} orbital to the empty d_{z2} orbital via Co–Co metallic bonds; thus, the *d-d* exchange between the neighboring sites is ferromagnetic. However, the more active *dxz*/*dyz* orbitals dominate the AFM ground states in Fe_2P. There is overlap between *dxz*/*dyz* orbitals at two neighboring metal sites, and electrons would hop between these two active orbitals of Fe atoms. The resulting exchange interaction is antiferromagnetic and strong. Consequently, Fe_2P behaves as an antiferromagnetic material with $T_N = 23$ K, while Co_2P is a ferromagnetic material with $T_C = 580$ K. The corresponding AFM and FM direct interaction mechanisms are shown in Fig. 4(a).

To clarify the novel AFM ground state of ternary MPS_3 monolayer, the dominant electron hopping paths were analyzed. As a representative case, the first neighboring-to-neighboring interaction for $MnPSe_3$ monolayer is shown in Fig. 4(b).[123] Electrons hopping from two paths has been discussed—one is short-range direct interaction between the two neighboring Mn ions, and the other one is long-range Mn–Se–Mn superexchange with an angle of 84.1°. Owing to the strong interaction between neighboring Mn^{2+} cations and the large electron excitation energy from Se *p* orbital to Mn *d* orbital, direct AFM exchange interaction prevails over FM superexchange interaction.

Moreover, robust FM coupling with high Curie temperature was also observed in 1T-TaN_2[124] and 1T-YN_2 monolayers.[6] In these systems, the N–N distances (∼1.74 Å) are short enough to generate the strong direct exchange interaction. In TaN_2, the magnetic moment arises mainly from the fully filled spin-up p_z orbitals and nearly unfilled spin-down p_z orbitals. Benefiting from the delocalized feature of *p* orbitals of N atoms, *p-p* direct exchange interaction [see Fig.4(c)] leads to strong long-range FM coupling. In 1T-YN_2, the J_1 parameter is 11.3 meV, confirming again that the direct interaction is FM coupling.

Robust ferrimagnetic ordering was proposed in 2D metal organic frameworks with conjugated electron acceptors diketopyrrolopyrrole (DPP) as organic linkers and transition metal Cr as nodes, namely, Cr-DPP [Fig. 4(d)].[7] In 2D Cr-DPP, each Cr atom possesses a spin magnetic moment of around 4 μ_B, and each DPP unit has a spin magnetic moment of about 1 μ_B. Considering the symmetry matching rule, the majority of magnetic coupling between Cr and DPP can be ascribed to direct exchange interaction between $d_{xy}\uparrow$ orbital of Cr and $p\downarrow$ orbital (p_x or p_y) of the adjacent N atoms. Meanwhile, direct exchange between $d_{xz}/d_{yz}\uparrow$ orbital of Cr and $p_z\downarrow$ orbital of N contributes to the minority part due to the comparatively big energy gap between the two orbitals. The strong *d-p* direct exchange coupling of 2D Cr-DPP yields a Curie temperature of 316 K. Robust *d-p* direct exchange coupling was also found in 2D ferrimagnetic V-DPP[7] and Cr-pentalene MOF,[125] and the corresponding T_C was 406 and 560 K, respectively.

2. Superexchange interaction

Among the reported 2D magnets, there is a large number of transition metal compounds, such as binary/ternary transition metal halides, chalcogenides, borides, carbides, nitrides, oxides, hydrides, and silicides. Their detailed magnetic properties will be discussed in Sec. III. As we stated above, the direct overlap between *d* orbitals in these transition metal compounds is generally too small due to the large distance. Thus, *d* electrons can only move through hybridization with the ligand atoms between them, like 2*p* orbitals of B, C, N, O, H, and F.

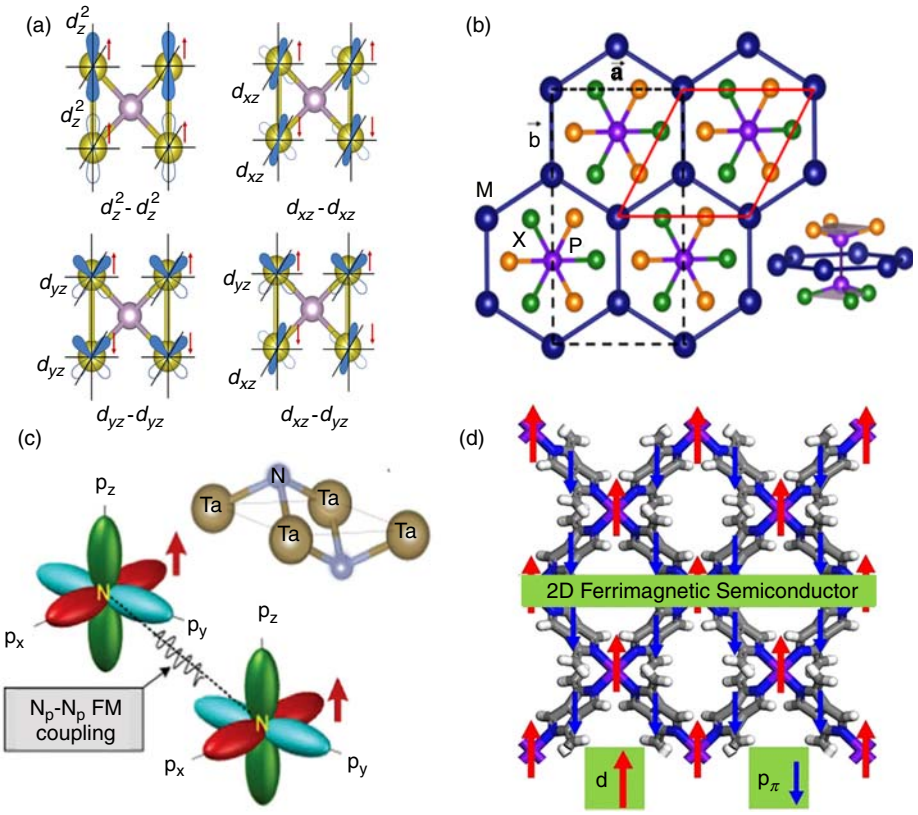

FIG. 4. (a) Direct FM (AFM) exchange interactions between d_{z2}-d_{z2} (d_{yz}/d_{xz}-d_{yz}/d_{xz}) orbitals. (b) Schematic diagram of the possible paths for magnetic exchange interaction in MPS_3 (M = Ni, Mn, Fe) monolayer. (c) Schematic diagram of the FM coupling mechanism: *p-p* direct exchange interaction in TaN_2 monolayer. (d) Schematic diagram of the FM coupling mechanism: *d-p* direct exchange interaction in 2D organometallic lattices. Panel (a) reproduced with permission from Liu *et al.*, Nanoscale **12**, 6776 (2020). Copyright 2020, Royal Society of Chemistry.[5] Panel (b) reproduced with permission from Lançon *et al.*, Phys. Rev. B **98**, 134414 (2018). Copyright 2018 American Physical Society.[112] Panel (c) reproduced with permission from Liu *et al.*, J. Mater. Chem. C **5**, 727 (2017). Copyright 2017 Royal Society of Chemistry.[124] Panel (d) reproduced with permission from Li *et al.*, J. Phys. Chem. Lett. **10**, 2439 (2019). Copyright 2019 American Chemical Society.[7]

Such *p-d* hybridization provides a common type of exchange mechanism, known as superexchange interaction. That is to say, superexchange interaction arises from the non-neighboring magnetic ions mediated by the neighboring non-magnetic ions. Empirically, the magnetic ground state is determined by Goodenough-Kanamori-Anderson (GKA) rules,[126–128] which are based on the symmetry relationships and electron occupancy of the overlapping atomic orbitals. According to these rules: (1) A 180° superexchange interaction of two magnetic ions with partially filled *d* shells is AFM if virtual electron transfer occurs between the overlapping orbitals that are each half filled. (2) A 180° superexchange interaction of two magnetic ions with partially filled *d* shells is FM if virtual electron transfer occurs from a half-filled to an empty orbital or from a filled to a half-filled orbital. (3) A 90° superexchange interaction where the occupied *d* orbitals of metal atom overlap with different orthogonal *p* orbitals of the ligands results in weak ferromagnetism. In addition, the strength of superexchange coupling is also sensitive to two factors, i.e., (1) the degree of *p-d* hopping process and (2) the strength of SOC.

Based on the superexchange mechanism and GKA rules, the magnetic behavior of a variety of 2D magnets has been successfully explained, including the recently highlighted CrI_3,[8] VI_3,[9] VS_2,[10] $Cr_2Ge_2Te_3$,[11] MXenes,[12,13] $MnBi_2Te_4$,[14] GdI_2,[129] and so on. For instance, 2D CrI_3 is an insulator [Fig. 5(a)] with local spin of $S = 3/2$.[8] Considering the local octahedral coordination field [Fig. 5(b)], the valence bands and the conduction bands consist of t_{2g} states and e_g states, respectively. The closed t_{2g}^3 configuration indicates the formal Cr^{3+} charge state. The exchange splitting in 2D CrI_3 is about 3 eV, which is larger than the t_{2g}-e_g crystal field splitting. For the corner sharing I atoms, their in-plane p_x/p_y orbitals couple to the Cr d_{x2-y2} orbital, and the out-of-plane I p_z to Cr $d_{xz/yz}$ [Fig. 5(c)]. Owing to the closed t_{2g}^3 subshell, the direct exchange interaction between two neighboring Cr^{3+} ions is AFM, which is associated with Pauli exclusion principle in the virtually excited t_{2g}^2-t_{2g}^4 state. However, the Cr–Cr distance is as large as 3.95 Å; thus the AFM exchange should be weak. As a consequence, the two nearly 90° Cr–I–Cr superexchange mechanisms dominate in 2D CrI_3. One originates from the stronger *p-d* hybridization via the orthogonal orbitals [Figs. 5(d) and 5(f)], and the other involves the relatively weak *p-d* hybridization via the same p_x orbital [Figs. 5(d) and 5(e)]. Both of them give an effective Cr–Cr FM coupling. According to the weak 90° *d-p-d* superexchange interaction, the Curie temperature of CrI_3 monolayer is 45 K.[28] In fact, the weak superexchange interaction also results in low Curie temperatures for the experimentally reported 2D magnets, such as 30 K for $Cr_2Ge_2Te_6$[37] and 34 K for $CrBr_3$.[31]

3. Double exchange interaction

Besides direct exchange and superexchange, double exchange interaction always exists in the 2D magnets with high-spin states. It arises between the ions in different oxidation states. In double exchange pictures, the interaction occurs when one atom has an extra electron compared to the other one. The electron transfer from the neighboring sites should have the same direction of spin. Therefore, the magnetic coupling is ferromagnetic.[130] For example, Zhang *et al.*[15]

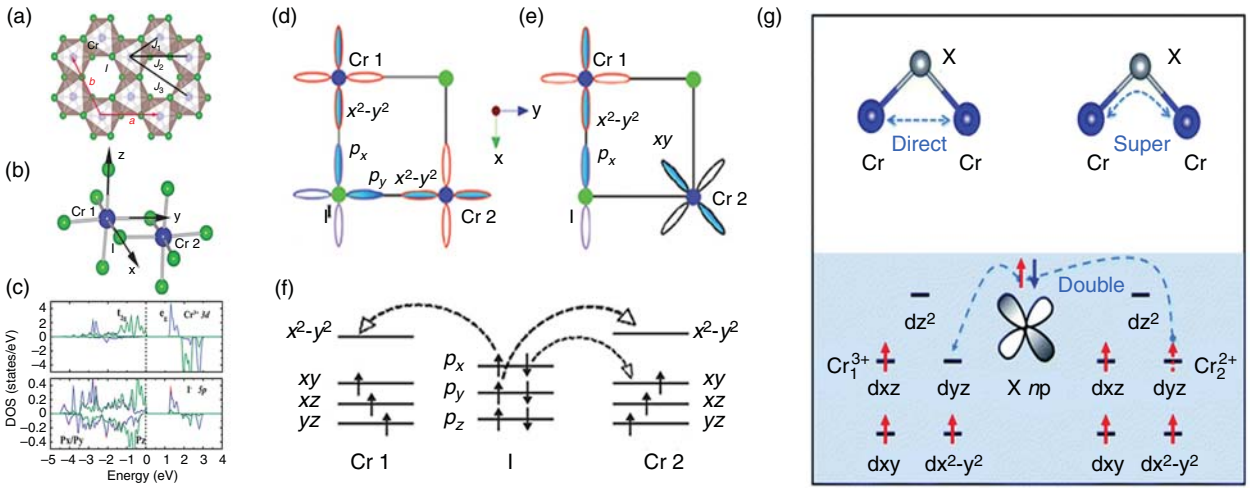

FIG. 5. (a) Honeycomb lattice of CrI_3 monolayer. Three magnetic pair interactions are marked with J_1, J_2, and J_3. (b) Edge-sharing CrI_6 octahedra. (c) Partial density of states (DOS) for Cr 3*d* and I 5*p* orbitals, and the Fermi level is set to zero. (d)–(f) Schematic structures of FM superexchange interactions in CrI_3 monolayer. (g) Illustrations of the Cr–Cr direct exchange, Cr–X–Cr superexchange, and Cr–X–Cr double exchange interactions in Cr_3X_4 (X = S, Se, Te) monolayers. Panels (a)–(f) reproduced with permission from Wang *et al.*, Europhys. Lett. **114**, 47001 (2016). Copyright 2016 IOP.[8] Panel (g) reproduced with permission from Zhang *et al.*, Nanoscale Horiz. **4**, 859 (2019). Copyright 2019 Royal Society of Chemistry.[15]

provided a double exchange model [Fig. 5(g)] in Cr_3X_4 monolayers (X = S, Se, Te), where seven hexagonal atomic layers are stacked in the sequence of X_1–Cr_1–X_2–Cr_2–X_2–Cr_1–X_1 along the *z* direction. The Cr_1 and Cr_2 atoms have different local coordination environments and show different valence states as Cr_1^{3+} and Cr_2^{2+}, respectively. The X atom connects the nearest-neighboring Cr_1^{3+} and Cr_2^{2+} ions and gives up its spin-up or spin-down electron to Cr_1^{3+}. Then its vacant orbital could be filled by an electron from Cr_2^{2+}. Mediated by the X atom, double exchange process is revealed by the electron hopping from one Cr ion to the other neighboring Cr ion of different oxidation state. Such mechanism dominates in Cr_3Se_4 and Cr_3Te_4 monolayers, and strengthens the FM coupling. Consequently, high Curie temperatures of 370 and 460 K were reported for Cr_3Se_4 and Cr_3Te_4 monolayers, respectively.

4. Extended superexchange theory

The above three fundamental magnetic interactions have already explained the origin of most 2D magnetic insulators. However, the magnetic ground state of some complicated 2D materials are still too difficult to be determined from these theories. In such situations, a few new theories, i.e., extended superexchange interaction, super-superexchange interaction, and multi-intermediate double exchange interactions, have been proposed recently.

For the 2D materials containing anions with different valence states, an extended superexchange theory was further proposed.[25] It has been validated in the representative CrOCl and FeOCl monolayers. Four possible superexchange paths (P1–P4) in CrOCl are displayed in Fig. 6(a). Similar to 2D CrI_3, the Cr atoms in 2D CrOCl are still located in a distorted octahedral crystal field. The d^3 state (Cr^{3+}) in CrI_3 can be written as $t_{2g}^3 e_g^0$ while the d^3 state (Cr^{3+}) and d^4 state (Cr^{2+}) in CrOCl is $t_{2g}^3 e_g^0$ and $t_{2g}^3 e_g^1$, respectively. The extended superexchange theory indicates that (1) a 180° bond angle in the interaction path Cr–O–Cr (P4) favors strongly FM configuration through the dominated p_σ-p_σ bond; (2) a 180° bond angle in the P3 path corresponds to strong AFM, where the interaction is conducted through p_σ-p_σ bond; (3) For Cr–O–Cr path (P2) with 90° bond angle, the d^3 state has a crucial unfilled e_g orbital; thus, the interaction is FM with weak coupling strength, owing to the competition of the two p_σ-p_π bonds; (4) For a 90° bond angle in the interaction path of Cr-Cl-Cr (P1), the d^4 states interact through two p_σ-p_π bonds with moderate strength of AFM coupling. Based on first-principles calculations, they further clarified that monolayer CrOCl exhibited antiferromagnetic ordering.[25] On all accounts, this extended superexchange theory supports the strongly FM/AFM configurations, which are highly anticipated to design robust 2D magnetic materials with polyvalent anions. Based on this theory, the high Curie/Néel temperatures in 2D MXY (M = metal; X = S, Se, Te; Y = F, Cl, Br, I) compounds could be explained.[26,65,70,131–133] According to above discussions, the extended superexchange theory may be regarded as a combination of superexchange and double exchange. Similar mechanism has also been proposed by Wang *et al.*[26]

5. Super-superexchange interaction

The super-superexchange interaction is different from the typical superexchange interactions by the mediated ligands.[23,24] As we stated above, single anion serves as an intermediate to bridge two magnetic cations in the superexchange interaction (M–X–M). In contrast, the super-superexchange interaction involves longer M–X···X–M hopping paths. According to the distance between magnetic ions, the strength of super-superexchange interaction is generally much weaker than those of direct interaction and superexchange interaction. Taking single layer $CrAsS_4$ as a representative, the exchange interaction parameter contributed by both short-range Cr–Cr direct exchange interaction and Cr–S–Cr superexchange interaction is 3.03 meV, while

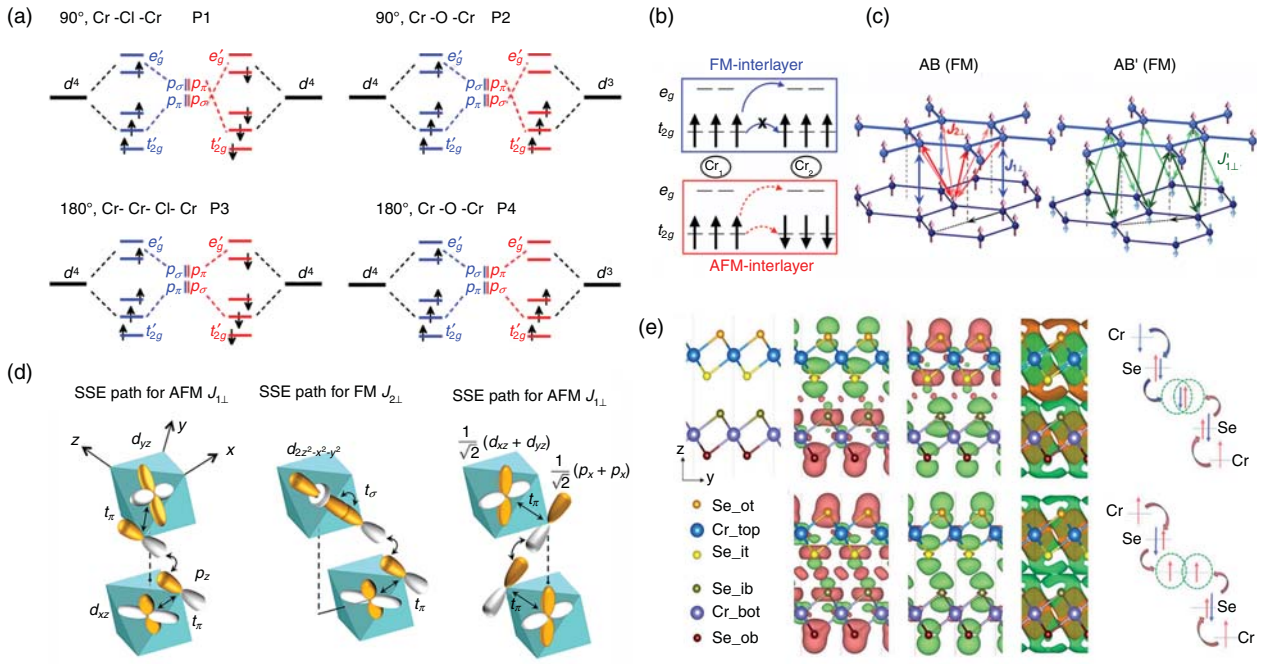

FIG. 6. (a) Four possible superexchange paths in CrOCl monolayer. Electrons can only hop between orbitals that are connected by dashed blue and red lines. (b) Hopping of t_{2g}−t_{2g} and t_{2g}-e_g orbitals in the FM/AFM alignment. (c) Interlayer Cr nearest-neighboring J_1, the second-nearest-neighboring J_2 in AB-stacking, and the nearest-neighboring J_1' in AB′-stacking CrI_3. (d) Schematic diagrams for the AFM/FM super-superexchange interaction involving different orbital hybridizations. (e) Electronic structure, FM-AFM, and FM-FM interlayer double superexchange mechanism of bilayer $CrSe_2$. The up and down solid arrows represent the electron with different spin components and the hollow arrows display different magnetic moments of the Cr atoms. The interlayer sharing electrons are surrounded by dashed green circles. The length of the arrow qualitatively shows the amounts of electrons with given spin component. Panel (a) reproduced with permission from Zhang *et al.*, New J. Phys. **21**, 053033 (2019). Licensed under a Creative Commons Attribution (CC-BY-3.0).[25] Panels (b)–(d) reproduced with permission from Sivadas *et al.*, Nano Lett. **18**, 7658 (2018). Copyright 2018 American Chemical Society.[23] Panel (e) reproduced with permission from Wang *et al.*, Phys. Rev. B **102**, 020402 (2020). Copyright 2020 American Physical Society.[27]

the value for long-range Cr–S–As–S–Cr super-superexchange interaction is –0.49 meV. Therefore, the super-superexchange interaction is usually neglected in most investigations. However, it could become stronger than superexchange interaction in some few-layer magnetic systems with non-covalent van der Waals (vdW) gaps. The importance of super-superexchange interaction is highlighted in the well-known bilayer CrI_3.[23,28,134] For bilayer CrI_3, the local magnetic moments form intralayer FM ordering below 45 K.[28] However, its interlayer magnetic coupling varies between FM and AFM, depending on local stacking geometry.[23] These significant results reveal that even weak overlap has a large impact on the interlayer magnetic coupling through exchange between two adjacent interlayer I atoms, which signifies a new exchange interaction mechanism, i.e., super-superexchange. It also means that the super-superexchange is basically the coupling between next-next nearest neighbor.

Sivadas *et al.*[23] carefully investigated the details of stacking-dependent interlayer exchange interaction for bilayer CrI_3 systems. The AB stacking (S_6 point group) from the low-temperature bulk structure and the AB′ stacking (C_{2h} point group) from the high-temperature bulk structure were considered. Figure 6(b) schematically shows different exchange interactions between Cr atoms in different layers. One can see that hopping from a t_{2g} to t_{2g} orbital is prohibited for FM alignment, while this is allowed for AFM alignment. Therefore, t_{2g} to t_{2g} hybridization leads to AFM ordering. On the other hand, hopping from t_{2g}-e_g leads to an exchange coupling that is predominantly FM because of the local Hund coupling. All these interlayer Cr−Cr exchange interactions are mediated by the hybridization between I p_z orbitals in different layers, which is the nature of super-superexchange interaction.

The stacking-dependent magnetism originates from a competition between different interlayer orbital hybridizations. Interlayer Cr−Cr nearest neighboring interaction J_1 and the second neighboring one J_2 in AB-stacking are shown in Fig. 6(c). One can see that J_1 is dominated by the virtual excitations between the half-filled t_{2g} orbitals of Cr and induces an AFM coupling, while J_2 is dominated by a virtual excitation from the half-filled t_{2g} orbitals of Cr to the empty e_g orbitals, resulting in a FM coupling [Fig. 6(c)]. Clearly, the second neighboring FM interlayer super-superexchange prevails as the AFM nearest neighboring interlayer exchange, making AB-stacking system ferromagnetic. A lateral shift of one layer to AB′-stacking of the bilayer system breaks the interlayer hybridization between I p states and generates a new type of hybridization, which in turn would reduce the strength of FM exchange interactions and result in an AFM ground state for AB′-stacking [Fig. 6(d)].

6. Multi-intermediate double exchange interaction

Compared to bilayer CrI_3 with the same Cr^{3+} ions, a mixture of Cr^{4+} and Cr^{3+} was found in bilayer CrS_2 due to the charge transfer

from e_g to t_{2g} orbitals. This mixed valance state, together with delocalized S p orbitals and their resulting strongly interlayered S-S hopping, favor the double exchange interaction mechanism.[135] With further increase of the strength of interlayer coupling, a novel multi-intermediate double exchange interaction has been revealed by extensively investigating nine TMD bilayers MX_2 (M = V, Cr, Mn; X = S, Se, Te).[27] Taking 2D $CrSe_2$ as a prototype, one can see a distinct overlapped region (OR) at the interlayer area, as displayed in Fig. 6(e). In other words, OR could be effectively considered as an area accumulating an appreciable shared charge from the two adjacent interfacial Se sublayers. The OR can be regarded as a real atomic site and plays an important role in determining the interlayer magnetic coupling. In the interlayer FM configuration, the transferred spin-up charge of Se p_z to Cr leaves the spin-down component predominated at the OR [Fig. 6(e)]. Hence, the spin-up electrons of the bottom Cr atom could hop into the top Cr atom through $4p_z$ orbital of Se_ib atom [defined in Fig. 6(e)], and then through OR upon excitation, and further through Se_it $4p_z$, as denoted by the wave-like red-dotted arrow [Fig. 6(e)]. Such electron hopping process largely reduces the kinetic energy of spin-up electron across the bilayer. The process in $CrSe_2$ is similar to double exchange interaction of CrS_2[135] but is mediated by multiple sites, which is termed as a new multi-intermediate double exchange interaction. Similarly, the interlayer AFM bilayer also has stacking-induced charge transfer and the interfacial Se p_z overlapping area. As displayed in Fig. 6(e), the spin-up electron of bottom Cr could still hop into the Se_ib $4p_z$ orbital and reach the OR. However, the next hopping step from OR to the Se_it $4p_z$ orbital is forbidden since the spin-up component is fully occupied. This appreciably lifts up the kinetic energy. Based on the modified interlayer Hubbard model, the competition between the interlayer hopping across the bilayer and the Pauli and Coulomb repulsions at OR will determine the MX_2 bilayers to have FM or AFM magnetic ground state.

F. Stoner model

In the above discussions, we mainly focus on 2D FM/AFM insulators. Their magnetism originates from local magnetic moments with exchange interactions that can be interpreted by the Heisenberg exchange mode. For 2D magnetic metals, a simplified model called Stoner model,[16] can be formulated in terms of dispersion relations for the spin-up and spin-down electrons. In the Stoner model, there is a competition between kinetic energy and exchange energy due to Coulomb repulsion. In ferromagnetic metals, the exchange interaction will split the energy of states with different spins. This restructuring of the spins leads to a change in the energy of the system. The up spins occupying higher energy states would cost the kinetic energy. At the same time, the potential energy would decrease due to spin-spin exchange interaction. These changes in total energy provide the Stoner criterion for itinerant ferromagnetism. The Stoner criterion for itinerant ferromagnetic ordering is $D(E_F)\times I > 1$, where $D(E_F)$ is the total density of states at the Fermi level (E_F), and the Stoner parameter I can be estimated from dividing the exchange splitting of spin-up and spin-down bands by the corresponding magnetic moments. These two parameters reflect the competition between the exchange energy and kinetic energy. The former parameter $D(E_F)$ is inversely proportional to the kinetic energy of electrons, whereas the latter one, I, describes the strength of electron exchange. Owing to the nature of itinerant electrons, Stoner model is applicable to illustrate the origin of the spontaneous magnetization in plenty of 2D metallic magnets, such as Fe_3GeTe_2,[16] TMDs,[17,18,20,21] MXene,[19,97,136] as well as a variety of charge doped 2D materials.[137–142] Most of these reported 2D magnetic metals have excitingly high Curie temperatures.

The electronic and magnetic properties of 2D Fe_3GeTe_2 have been investigated by Zhuang *et al.*[16] The spin orbital projected band structures [Fig. 7(a)] show its metallic behavior. Several partially occupied d bands crossing the Fermi level contribute to the noninteger magnetic moment of Fe (1.484 μ_B). Both characters indicate the itinerant ferromagnetism in Fe_3GeTe_2. The two important parameters of Stoner model, i.e., $D(E_F)$ and I, were determined from DOS as 1.56 states/eV per Fe atom and 0.71 eV, respectively. Therefore, Stoner's criterion of $I\times D(E_F) > 1$ is satisfied, giving rise to the itinerant ferromagnetic ordering in monolayer Fe_3GeTe_2. The validity of Stoner model was also extended to the successively reported 2D Fe_5GeTe_2,[143] which has a Curie temperature of 270 K.[42]

Intrinsic vdW ferromagnets with T_C above 300 K have been experimentally reported in some binary transitional metal dichalcogenides (MX_2) with structural phases containing the octahedral units [Fig. 7(b)], including 1T-$MnSe_x$,[144] 1T-VSe_2,[34,145] 1T-VTe_2,[146] and 1T-$CrTe_2$.[147] Both theoretical and experimental results suggested that exchange coupling due to the enhancement of itinerant type is responsible for their room-temperature ferromagnetism. The above four 2D room-temperature ferromagnets are compared to the corresponding elemental metals and some ferromagnetic elemental metals like Fe, Co, and Ni. As expected, only Fe, Co, and Ni among all the considered elemental metals meet the Stoner criterion to exhibit band ferromagnetism. In contrast, 2D VSe_2, $CrTe_2$, $MnTe_2$, and $MnSe_2$ sheets have much higher $I\times D(E_F)$ values than those of the corresponding elementary metals; thus the Stoner criterion is met for a band ferromagnetism in these 2D materials.[147]

G. RKKY mechanism

RKKY is a particular form of magnetic interaction that occurs in metals with localized magnetic moments. In the RKKY picture, the magnetic moments interact effectively through an indirect exchange process mediated by the conduction electrons. A localized magnetic moment induces spin polarization to the surrounding conduction electrons, and such polarization in turn couples to another neighboring localized moment. The coupling strength takes the form of distance-dependent exchange interaction given by

$$J_{ij}(r) \propto \sin\left[\frac{(\vec{k}_F^{\uparrow} + \vec{k}_F^{\downarrow})\cdot \vec{R}_{ij}}{R_{ij}^3}\right], \tag{6}$$

where k_F is the Fermi wave vector for two spin channels, and R_{ij} is the distance between the two magnetic atoms i and j. First, this interaction is of the long-range type. Second, FM or AFM ground states depend on the interatomic distance. Third, its strength oscillates with the distance. Similar to the Heisenberg model, the strength of exchange coupling is related to the magnetic transition temperature, but is not rooted in the symmetry. RKKY interaction is well understood in conventional 3D intermetallic compounds, which is the dominant coupling mechanism between rare earth ions. In 2D materials, however, only a few theoretical studies have directly discussed the existence of RKKY-type interaction.[22] In this regard, Zhang *et al.*[22] inferred that ferromagnetic interaction between Mn ions in $MnSiTe_3$ monolayer

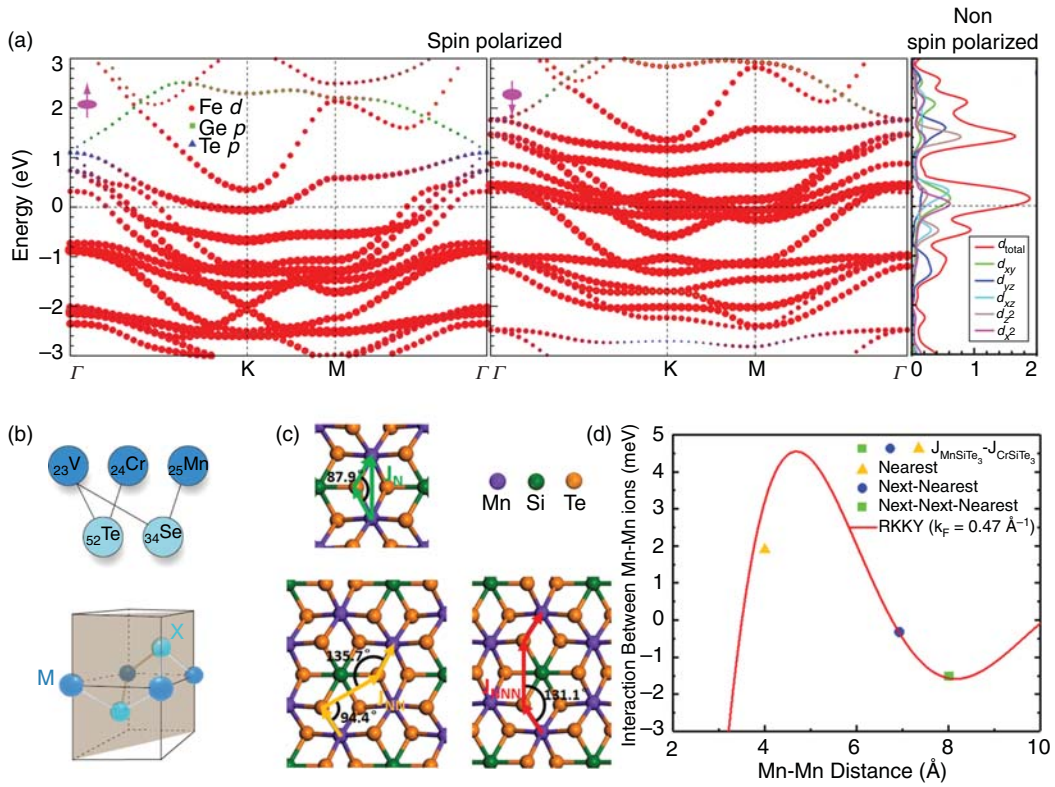

FIG. 7. (a) Orbital-resolved spin-up and spin-down band structures of single-layer Fe_3GeTe_2. (b) A summary of four types of known room-temperature vdW ferromagnets and their unit cell. (c) Hopping paths of the nearest, next-nearest, and next-next-nearest interactions in a $MnSiTe_3$ monolayer. (d) RKKY interaction strength as a function of Mn–Mn distance and first-principles results for ($J_{MnSiTe3}$–$J_{CrSiTe3}$). The yellow triangle, blue circle, and green square denote the first-principles results for the difference between $J_{MnSiTe3}$ and $J_{CrSiTe3}$ for the N, NN, and NNN neighbors, respectively. The red solid line denotes the interaction strength calculated within RKKY model with $k_F = 0.47$ Å^{-1}. Panel (a) reproduced with permission from Zhuang *et al.*, Phys. Rev. B **93**, 134407 (2016). Copyright 2016 American Physical Society.[16] Panel (b) reproduced with permission from Sun *et al.*, Nano Res. **13**, 3358 (2020). Copyright 2020 Springer Nature.[147] Panels (c) and (d) reproduced with permission from Zhang *et al.*, Phys. Rev. B **101**, 205119 (2020). Copyright 2020 American Physical Society.[22]

possibly originated from the RKKY coupling. Figure 7(c) displays the possible electron hopping paths between Mn ions of the nearest (N), next-nearest (NN), and next-next-nearest (NNN) interactions (J_N, J_{NN}, J_{NNN}). Unlike $CrSiTe_3$ and $CrGeTe_3$, the theoretical results showed that $MnSiTe_3$ monolayer is a half metal with the largest positive J_{NNN}, which is inconsistent with superexchange model. Benefiting from the half metallic nature, the mediation carriers between Mn ions are 100% spin-polarized free carriers. Figure 7(d) presents the RKKY interaction as a function of Mn–Mn distance. The RKKY contributions to the interaction for the N, NN, NNN neighbors in the model show good agreement with the results from first-principles calculations.[22] Nevertheless, further theoretical and experimental efforts are still needed to exploit the RKKY mechanism in other 2D magnets.

III. THE 2D VDW MAGNETS DATABASE

Two-dimensional vdW magnets are defined as the layered materials that adopt ferromagnetic/antiferromagnetic ground states at finite temperature. The theoretical concept was first established 150 years ago.[148] Since 2004, many efforts have been devoted to searching for new 2D magnetic materials with spontaneous magnetization.[84] In 2017, for the first time, the intrinsic 2D ferromagnetism in atomically thin CrI_3 and $Cr_2Ge_2Te_6$ was demonstrated in an experiment.[28,37] Nowadays, finding 2D ferromagnets with high Curie temperatures remains an important issue for spintronics, and many promising 2D materials have been attained theoretically and experimentally over the past five years.

A. Binary transition metal halides

1. MX_3

The first class of widely investigated 2D vdW magnets is binary transition metal halides. During the past 150 years, many bulk crystals of transition metal halides have been synthesized in the laboratory.[149] These bulk materials adopted simple AA or ABC layered stacking geometry with weak interlayer vdW interaction; thus, they can be mechanically exfoliated to fabricate 2D monolayer or few-layered sheets.[54,149] The compounds composed of transition metals with partially filled *d* shell are commonly observed, since they are easy to host local magnetic moments and produce ordered magnetism. Most of transition metal trihalides (MX_3), transition metal dihalides (MX_2), transition metal monohalides (MX), and other stoichiometric M-X monolayers reported to date are listed in Table II and categorized by their compositions as well as magnetic properties for discussion.

TABLE II. A list of 2D magnets in binary transition metal halides family with their compositions and key electronic and magnetic properties, including magnetic ground state (GS), values of Hubbard U term, energy gap (E_g), magnetic moment on per transition metal atom (Ms), Curie temperature (T_C), and magnetic anisotropy energy per unit cell (MAE). The experimental result is indicated by the superscript i. Positive/negative MAE value corresponds to the out-of-plane/in-plane easy magnetization direction.

	Compositions	GS	U (eV)	E_g (eV)	Ms (μ_B)	T_C (K)	MAE (meV)	Ref.
MX_3	CrI_3	FM[i]	–	–	–	45[i]	–	28
	CrI_3	FM	2.65	1.09	3.44	107	–	54
	CrI_3	FM	–	1.53	3	95	0.686	53
	CrI_3	FM	2.7	∼1.0	3	33	0.65	151
	CrI_3	FM	–	1.1	–	75	–	8
	CrI_3	FM	–	0.89	–	46	0.804	104
	CrI_3	FM	2.65	1.1	3.44	45	1.674	155
	CrI_3	FM	–	1.85	3.15	60	–	164
	$CrBr_3$	FM	2.68	1.76	3.25	86	–	54
	$CrBr_3$	FM	–	2.54	3	73	0.186	53
	$CrBr_3$	FM[i]	–	–	∼3	34	–	31
	$CrBr_3$	FM	–	1.38	–	41	0.16	104
	$CrBr_3$	FM	2.68	1.82	3.25	33	0.327	155
	$CrBr_3$	FM	–	2.87	3.03	105	–	164
	$CrCl_3$	FM	2.63	2.28	3.12	66	–	54
	$CrCl_3$	FM	–	3.44	3	49	0.031	53
	$CrCl_3$	FM	–	1.58	–	30	0.025	104
	$CrCl_3$	FM	2.63	2.3	2.12	23	0.038	155
	$CrCl_3$	FM	–	2.93	3.84	35	–	164
	CrF_3	FM	–	4.68	3	41	0.119	53
	CrF_3	FM	–	5.09	2.86	40	–	164
	VF_3	FM	–	3.23	1.89	760	–	164
	VCl_3	FM	3.35	DHM	4	80	–	161
	VCl_3	FM	–	2.51	1.96	500	–	164
	VI_3	FM	3.68	DHM	4	98	–	161
	VI_3	FM	3	0.89	2.01	27	–	160
	VI_3	FM	–	1.26	2.17	410	–	164
	VBr_3	FM	–	HM	1.97	190	−0.15	162
	VBr_3	FM	–	2.12	2.03	430	–	164
	NiF_3	FM	–	0	0.86	720	–	164
	$NiCl_3$	FM	–	DHM	2	400	–	110
	$NiCl_3$	FM	–	0	0.94	400	–	164
	$NiBr_3$	FM	–	HM	–	100	−0.05	162
	$NiBr_3$	FM	–	0	1.02	460	2	164
	NiI_3	FM	–	0	1.09	440	–	164
	$PdBr_3$	FM	–	HM	–	110	−0.196	162
	FeF_3	AFM	–	5.10	4.15	180	–	164
	$FeCl_3$	AFM	–	3.03	4.02	100	–	164
	$FeBr_3$	AFM	–	HM	–	70	–	162
	$FeBr_3$	AFM	–	2.57	3.94	160	–	164
	FeI_3	AFM	–	1.83	3.82	70	–	164
	ReI_3	FM	1	HM	2	165	–	170
	$ReBr_3$	FM	1	HM	2	390	–	170
	α-$RuCl_3$	FM	–	0.003	1	14	–	55
	α-$RuCl_3$	AFM	2	0.69	0.9	–	0.95	156
	$RuBr_3$	FM	1.5	0.70	1	13	5.26	171
	RuI_3	FM	0∼1.5	0.011	1	360	–	169

TABLE II. (*Continued.*)

	Compositions	GS	U (eV)	E_g (eV)	Ms (μ_B)	T_C (K)	MAE (meV)	Ref.
	RuI_3	FM	1.5	0.32	1	2	12.88	171
	α-$MoCl_3$	AFM[i]	–	–	3	780	–	167
	MnF_3	FM	3.9	DHM	3.92	450	−0.013	163
	MnF_3	FM	–	0	3.87	600	–	164
	$MnCl_3$	FM	3.9	DHM	4.08	750	−0.46	163
	$MnCl_3$	FM	–	0	3.95	100	–	164
	$MnBr_3$	FM	3.9	DHM	4.18	810	−8.71	163
	$MnBr_3$	FM	–	0	3.03	120	–	164
	MnI_3	FM	3.9	DHM	4.27	820	−11.86	163
	MnI_3	FM	–	0	3.15	140	–	164
	UI_3	FM	–	HM	1.4	110	−28.5	336
	$PtCl_3$	FM	2	WHS	0.95	200	−5.29	172
	$OsCl_3$	FM	0.6	0.067	0.87	∼350	–	173
	H-$CoBr_3$	FM	1.2	0.0087	–	264	7.7	166
	$TiCl_3$	FM	–	HM	–	376	–	165
MX_2	VCl_2	AFM	3.1	–	3	–	–	100
	VCl_2	AFM	2	∼0.5	3	–	<0.01	103
	VCl_2	AFM	4	I	2.67	–	0.53	174
	VBr_2	AFM	3.1	–	3	–	–	100
	VBr_2	AFM	2	∼2.0	3	–	<0.01	103
	VBr_2	AFM	4	I	2.67	–	0.33	174
	VI_2	AFM	3.1	–	3	–	–	100
	VI_2	AFM	2	∼1.8	3	–	<0.01	103
	VI_2	AFM	4	I	2.67	–	0.25	174
	$CrCl_2$	AFM	3.5	–	4	–	–	100
	$CrBr_2$	AFM	3.5	–	4	–	–	100
	CrI_2	AFM	3.5	–	4	–	–	100
	$MnCl_2$	AFM	4	–	5	–	–	100
	$MnCl_2$	AFM	2	∼2.5	4	–	<0.01	103
	$MnCl_2$	AFM	4	I	4.54		0.2	174
	$MnBr_2$	AFM	4	–	5	–	–	100
	$MnBr_2$	AFM	4	I	4.52		0.25	174
	MnI_2	AFM	4	–	5	–	–	100
	MnI_2	AFM	4	∼1.5	4	–	<0.01	103
	MnI_2	AFM	4	I	4.46		0.18	174
	$FeCl_2$	FM	4	–	4	109	–	100
	$FeCl_2$	FM	4	HM	3.57	160	0.89	174
	$FeCl_2$	FM	4	HM	4	–	0.07	177
	$FeCl_2$	FM	4	HM	–	165	∼0.06	178
	$FeBr_2$	FM	4	–	4	81	–	100
	$FeBr_2$	FM	4	HM	–	210	∼0.06	178
	$FeBr_2$	FM	4	HM	3.53	89	0.33	174
	FeI_2	FM	4	–	4	42	–	100
	FeI_2	FM	4	HM	–	122	∼0.06	178
	FeI_2	FM	4	HM	3.45	47	0.59	174
	$CoCl_2$	FM	3.3	–	3	85	–	100
	$CoCl_2$	FM	4	I	2.54	135	0.69	174
	$CoBr_2$	FM	3.3	–	3	23	–	100

TABLE II. (*Continued.*)

	Compositions	GS	U (eV)	E_g (eV)	Ms (μ_B)	T_C (K)	MAE (meV)	Ref.
	$CoBr_2$	FM	4	I	2.49	24	0.68	174
	$CoBr_2$	FM	3.67	2.35	2.67	2	0.52	142
	CoI_2	AFM	3.3	–	3	–	–	100
	CoI_2	AFM	2	∼0.2	3	–	<0.01	103
	CoI_2	AFM	4	I	2.23	–	0.50	174
	$NiCl_2$	FM	6.4	–	2	138	–	100
	$NiCl_2$	FM	2	∼1.8	2	57	<0.01	103
	$NiCl_2$	FM	4	I	1.68	205	0.12	174
	$NiBr_2$	FM	6.4	–	2	132	–	100
	$NiBr_2$	FM	4	I	1.63	173	0.02	174
	NiI_2	FM	6.4	–	2	129	–	100
	NiI_2	FM	4	I	1.53	178	0.18	174
	$PtCl_2$	FM	2	∼0.8	1	–	<0.01	103
	$AgCl_2$	FM	2	HM	1	–	–	103
	$AgBr_2$	FM	2	HM	1	–	–	103
	AgI_2	FM	2	HM	1	–	–	103
	$LaBr_2$	FM	–	–	1	235	–	179
	GdI_2	FM	8	0.62	8	241	0.553	129
MX	ScCl	FM	–	Metal	1.56	185	–	180
	ScCl	FM	4	Metal	0.364	355	–	65
	LaCl	FM	4	Metal	0.333	460	–	65
	YCl	FM	5	Metal	0.317	260	–	65
M_3X_8	Nb_3Cl_8	FM	2	1.164	–	31	–	181
	Nb_3Br_8	FM	2	1.125	–	56	–	181
	Nb_3I_8	FM	2	0.758	–	87	–	181
	Nb_3F_8	FM	–	HM	1.167	77	–	74
	Nb_3Cl_8	AFM	–	0.086	1.167	–	–	74
	Nb_3Br_8	FM	–	HM	1.167	–	–	74
	Nb_3I_8	FM	–	HM	1.167	103	–	74

The successful exfoliation of bulk CrI_3 crystal into atomic monolayers opened a new era of 2D magnetism.[28] Using scanning magneto-optic Kerr microscopy, neutron scattering, and NMR spectroscopy, pristine monolayer CrI_3 has been proven to be an Ising ferromagnetic semiconductor with a bandgap of 1.2 eV,[150] a Curie temperature of 45 K,[28] and an out-plane MAE of 0.69 meV [Figs. 8(a)–(e)].[53] In fact, the study of magnetism of layered CrI_3 began even before that. In prior experiments, several theoretical groups already predicted robust long-range ferromagnetic ordering in the monolayer limit of CrI_3.[8,53,54] The reported magnetic moment, magnetic anisotropy energy, and Curie temperature of 2D CrI_3 were 3∼3.44 μ_B per formula unit, 0.65∼0.686 meV, and 61∼107 K, respectively.[8,53,54] The magnetic moment in monolayer CrI_3 with honeycomb lattice is contributed by the Cr^{3+} ions with electronic configuration of $3s^0 3d^3$ under edge sharing octahedral crystal field coordinated by six nonmagnetic $I^{\bar{}}$ ions. In the octahedral crystal field, Cr^{3+} ions prefer $S = 3/2$ with three d electrons occupying the lower-energy t_{2g} triplet state via splitting. The long-range FM ordering is driven by the competition between direct antiferromagnetic exchange interaction of Cr–Cr sites and the super-exchange interaction in the near 90° Cr–I–Cr bonds.[8] The large magnetic anisotropy is attributed to the spin-orbit coupling of the intermediate I atom along the superexchange path.[151] Using magneto-Raman spectroscopy, Xu *et al.*[152] directly observed 2D magnons with acoustic magnon mode of 0.3 meV in monolayer CrI_3. Moreover, the magnetism in CrI_3 is layer dependent, that is, monolayer, trilayer, bulk CrI_3 systems are ferromagnetic, whereas the weak magnetic coupling between the individual FM monolayer leads to the AFM ground state in bilayer CrI_3 [Figs. 8(f)–8(h)].[28] An exfoliated thin film of CrI_3 sandwiched between graphene contacts acts as a spin-filter tunnel barrier, showing a record high tunneling magnetoresistance of 190 000%.[153,154]

Motivated by the discovery of CrI_3, its sister transition metal compounds, i.e., chromium trihalides CrX_3 (X= F, Cl, Br) monolayers have been explored as potential 2D intrinsic magnetic semiconductors by many groups.[30,53,54,104,155,156] Owing to the structural similarity with CrI_3, FM is also the ground state for monolayer CrX_3 (X= F, Cl, and Br), and the magnetic moment of each Cr^{3+} ion in these systems is about 3 μ_B. However, with the increase in the atomic radius of halogen, the theoretical bandgap reduces from 4.68 eV for CrF_3, to 3.44 eV for $CrCl_3$, to 2.54 eV for $CrBr_3$, and finally to 1.53 eV for CrI_3 at

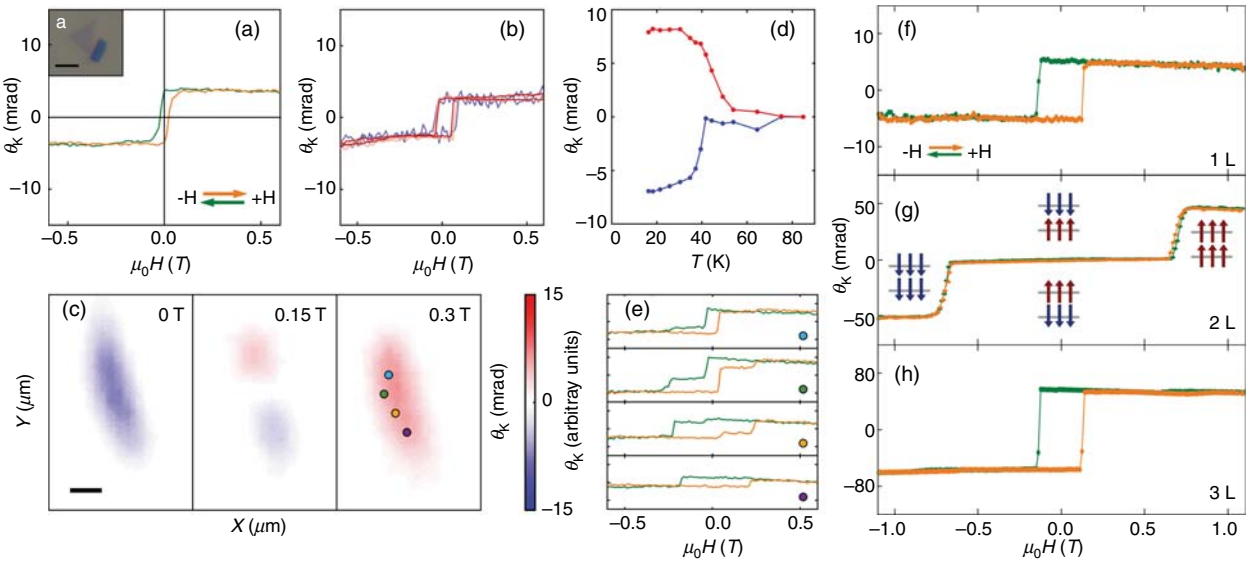

FIG. 8. Magneto-optical Kerr effect (MOKE) measurements of monolayer CrI_3. (a) Polar MOKE signal for a CrI_3 monolayer. (b) Power dependence of the MOKE signal taken at three different incident powers (3, 10, and 30 μW). (c) MOKE maps at $\mu_0 H = 0$ T, 0.15 T, and 0.3 T. (d) Temperature dependence of MOKE signal. (e) The relationship between θ_K abd $\mu_0 H$ marked by dots in (c). (f)–(h) Layer-dependent magnetic ordering in atomically thin CrI_3. MOKE signal on a monolayer, bilayer, and trilayer flakes. They show ferromagnetic, antiferromagnetic, and ferromagnetic behavior, respectively. Reproduced with permission from Huang *et al.*, Nature **546**, 270 (2017). Copyright 2017 Springer Nature.[28]

HSE06 level of theory.[53] Considering the microscopic origin of long-range FM ordering, a strongly increased hybridization between X-*p* and Cr-3*d* states will strengthen the Cr–X–Cr FM exchange interactions as X goes from F to I. However, direct AFM exchange interaction is expected to be weakened with increasing Cr–Cr distance along this series. Indeed, MC simulations based on classical Heisenberg model predicted Curie temperatures of CrF_3, $CrCl_3$, $CrBr_3$, and CrI_3 monolayers to be 41, 49, 73, and 95 K, respectively. Moving from Cl to I would increase the strength of spin-orbit coupling of halogen, which accounts for the enhancement of MAE from 0.031 meV for $CrCl_3$, to 0.186 meV for $CrBr_3$, and then to 0.686 meV for CrI_3.[53] Similar theoretical results were also reported in the other four papers.[54,104,155,156] Experimentally, Gao *et al.*[31] demonstrated ferromagnetism in 2D vdW $CrBr_3$ using direct *d*-*d* transition induced photoluminescence probing. They argued that spontaneous magnetization persists in monolayer $CrBr_3$ with Curie temperature of 34 K. The magnetic moment of each Cr^{3+} ion in monolayer $CrBr_3$ aligns in the out-of-plane direction, and the corresponding magnetic moment is about 3 μ_B. Although the Curie temperature and MAE are slightly smaller than those of monolayer CrI_3, monolayers of other chromium trihalides CrX_3 (X= F, Cl, Br) could be more stable in air.[28,157]

Beyond chromium halides, the magnetic properties of vanadium trihalides (e.g., VI_3) monolayer were also intensively investigated as potential 2D magnetic materials. In the periodic table, vanadium locates as the left neighbor of chromium. Thus, V atom in VI_3 tends to adopt high-spin state of V^{3+} with $3d^2$ electronic configuration, that is, two valence electrons occupy the triply degenerate t_{2g} state. Such partial occupancy could raise the possibility for weak Jahn-Teller distortion of the octahedra and the orbital ordering in vanadium trihalides, which would modify the superexchange interactions in its planar honeycomb lattice. Recently, two experimental groups confirmed that bulk VI_3 is a correlated Mott insulator with a bandgap of ~1 eV.[29,158] In addition, the exfoliation energy from first-principles calculation revealed that VI_3 is more easily decoupled than CrI_3.[159] Hence, vanadium trihalides provide a new platform to investigate 2D magnets with $S = 1$. Using CVD method, Tian *et al.*[29] firstly confirmed layered VI_3 is a FM semiconductor with a Curie temperature of 50 K. It was further demonstrated to be a 2D Ising ferromagnet by DFT calculations, crystal field level diagrams, superexchange model analyses, and MC simulations.[9] The monolayer limit of VI_3 has also been explored by first-principles calculations. The intrinsic ferromagnetism can persist and the Curie temperature is reduced to 17 K from the bulk value of 60 K.[160] Based on DFT calculations combined with self consistently determined Hubbard U approach, He *et al.*[161] reported that monolayer VI_3 possesses not only intrinsic ferromagnetism but also exciting Dirac half-metallicity, and VCl_3 shows similar magnetic behavior. Their corresponding Curie temperatures were 80 and 98 K, respectively. For monolayer VBr_3, first-principles calculations predicted that it has intrinsic half-metallicity and high Curie temperature of 190 K. Moreover, topological nontrivial states, which were identified by calculations of Berry curvature and the corresponding edge states, surprisingly emerge at the Fermi level.[162]

Manganese atom is the right neighbor of chromium in periodic table. In the manganese trihalides MnX_3 (X = F, Cl, Br, I), low crystal field splitting is caused by the octahedral coordination of Mn ions. Thus, Mn ion has +3 oxide state with spin configuration of $S = 2t_{2g}^3 e_g^1$, exhibiting a magnetic moment of c.a. 4 μ_B. Sun and Kioussis predicted that 2D MnX_3 sheets are intrinsic Dirac half metals (DHMs).[163] The bandgaps of the minority spin channel from PBE+U calculations were 6.3, 4.33, 3.85, and 3.10 eV for MnF_3, $MnCl_3$, $MnBr_3$, and MnI_3, respectively. In-plane magnetization orientation was found in all MnX_3 systems and the magnetocrystalline anisotropy

increases with increasing atomic size of halogen. Based on DFT derived exchange interaction parameters, the estimated Curie temperatures were greater than 450 K. Spin-polarized Dirac half metallic states in MnF_3, $MnCl_3$, and $MnBr_3$ were also confirmed by Tomar *et al.*[164] using DFT calculations with both PBE and HSE06 functionals. Based on Curie-Weiss mean field theory, MnF_3 was demonstrated as a room-temperature ferromagnet.

Two-dimensional intrinsic magnets are also predicted for many other trihalides of open-shell 3*d* transition metals (M = Ti, Fe, Co, Ni). For instance, $TiCl_3$ monolayer possesses weak interlayer interaction of 0.33 J/m^2, half metallicity with a bandgap of 0.6 eV in the majority spin channel, long-range FM ordering contributed by 3*d* valence states, and a high Curie temperature of 376 K.[165] FeX_3 monolayers were found to have antiferromagnetic ground state with Néel temperature of 70∼180 K.[162,164] Using DFT and DFT+U calculations, Sun *et al.*[162] found Dirac spin-gapless half-metallic features in $NiBr_3$ monolayer, and the corresponding Curie temperature was 100 K. The $NiCl_3$ monolayer was also shown to have Dirac spin-gapless semiconducting characteristics and high-temperature ferromagnetism.[110] The MC simulations based on Ising model demonstrated that the Curie temperature of $NiCl_3$ monolayer is as high as ∼400 K. The calculated Fermi velocity of Dirac fermions was about 4×10^5 ms^{-1}. Among them, Ti, Fe, and Ni ions are still octahedrally coordinated to the halogen atoms, thus they can exist in either high-spin or low-spin state due to crystal field splitting. According to the calculated magnetic moment listed in Table II, low-spin state is observed in the cases of Ti^{3+} and Ni^{3+} with magnetic moment of about 1 μ_B. The magnetic moment of iron ion is found to be close to 4 μ_B, which corresponds to neither high-spin (5 μ_B) nor low-spin (1 μ_B) state of Fe^{3+}. It could explain why AFM coupling is only found in FeX_3 series among the transition metal trihalides with CrI_3 type structure. For Co ion located in the octahedral coordination environments of bromides, non-magnetic behavior was observed in $CoBr_3$ with P-31*m* phase.[162] However, DFT calculations[166] demonstrated that the P6/*mmm* phase of $CoBr_3$ monolayer hosts 2D intrinsic ferromagnetism with metallic behavior, Dirac cone, and quantum anomalous Hall effect simultaneously. Its Curie temperature was 264 K and Chern number was $C = 2$.

Another important group of transition metal trihalides contains the heavier 4*d* and 5*d* open-shell transition metal elements like Mo, Ru, Rh, Tc, Pd, Ir, Pt, and Os. Moving from 3*d* to 4*d* and 5*d* series increases the spin-orbit coupling effect, which is beneficial for designing 2D spintronic devices with large MAE, topological phenomena, and spin controlling. Antiferromagnetic coupling between Mo atoms was confirmed in the high-temperature phase of α-$MoCl_3$ by an combined experimental and theoretical study.[167] Unlike $CrCl_3$, α-$MoCl_3$ adopts the monoclinic $AlCl_3$ structure with space group of C2/*m* at room temperature. Originated from the magneto-structural phase transition, magnetic interactions in the high-temperature phase of α-$MoCl_3$ are stronger by at least one order of magnitude than those in the analogous $CrCl_3$ and $CrBr_3$. Similar coupled structural and magnetic transition is also expected in $TcCl_3$ and $TiCl_3$. Experimentally, the fractional Majorana fermion excitations of a Kitaev quantum spin liquid have been observed in α-$RuCl_3$,[32] which leads to enormous amounts of research on the magnetic properties of layered α-$RuCl_3$. Motivated by the exfoliation of α-$RuCl_3$ monolayer from its 3D crystal,[168] the magnetic property has been further analyzed by DFT calculations and MC simulations.[55,156] It was demonstrated to be a stable 2D intrinsic ferromagnetic semiconductor. The obtained Curie temperature and MAE were 14.21 K and 0.95 meV, respectively. Using first-principles calculations, Kan *et al.*[169] predicted RuI_3 monolayer to be an intrinsic ferromagnetic quantum anomalous Hall (QAH) insulator with topologically nontrivial global bandgap of 11 meV. The Curie temperature and nearest-neighboring exchange coupling parameter were estimated to be 360 K and 82 meV, respectively. It was also found that FM $RuCl_3$ and $RuBr_3$ monolayers show similar electronic behavior as RuI_3 monolayer. However, their exchange energies are very small and sensitive to the choice of effective U value. For $RuBr_3$ and RuI_3 monolayers,[170] the bandgap, possible magnetic ground state, Curie temperature, and magnetic anisotropy energy have been reexamined by DFT calculations with PBE+U and inclusion of SOC. It was shown that they are FM semiconductors with indirect bandgaps of 0.7 and 0.32 eV, respectively. According to MC simulations, their magnetic transition temperatures from FM to PM were 13.0 and 2.1 K, respectively. The magnetic anisotropy energies obtained for $RuBr_3$ and RuI_3 were 5.26 and 12.88 meV, respectively. Robust intrinsic ferromagnetism has also been realized in 2D rhenium trihalides.[171] The dynamic and thermodynamic stabilities were found in the heavier halides (Br and I), in contrast to the lighter halides (F and Cl). $ReBr_3$ and ReI_3 are half metals with large bandgap in the spin-up channel. Moreover, high Curie temperatures (390 and 165 K) and Chern number ($C = -4$) were obtained from DFT calculations with PBE functional. Both Weyl half semimetal and tunable QAH effects were simultaneously realized in monolayer $PtCl_3$,[172] as signified by the in-plane magnetization, high Curie temperature, and mirror symmetry protected two 2D Weyl points. A room-temperature intrinsic QAH insulator was predicted in the ferromagnetic insulating $OsCl_3$ monolayer, which is characterized by an energy gap of 67 meV, a Chern number of $C = 1$, and a Curie temperature of 350 K.[173]

2. MX_2

Similar to transition metal trihalides, layered transition metal dihalides have also drawn significant attentions for exhibiting ferromagnetic, antiferromagnetic, and half-metallic characteristics. The structure of monolayer MX_2 is analogous to transition metal dichalcogenides, which contains a triangular lattice of transition metal cations. In these compounds, the metal ions are in the formal oxidation state of +2. Divalence and octahedral coordination renders V, Cr, Mn, Fe, Co, and Ni cations partially filled $3d^3$, $3d^4$, $3d^5$, $3d^6$, $3d^7$, and $3d^8$ electronic configurations, with $S = 3/2$, 2, 5/2, 2, 3/2, and 1, respectively. Considering their structural similarity, the sign of superexchange interaction is mainly determined by the orbital occupations, and thus a variety of magnetic ground states are anticipated.

The evolution of electronic and magnetic properties of these first-row transition metal dihalides MX_2 (M = V, Cr, Mn, Fe, Co, Ni; X = Cl, Br, I) has been systemically examined by first-principles calculations.[100,111,142,174] Using PBE functional, T configuration (P-3*m*1) is energetically favorable for the monolayers of all considered cases, while correction by a Hubbard U term leads to inversion of the favorable monolayer configuration to H phase (P-6*m*2), as demonstrated for $FeBr_2$ and FeI_2.[111] Among them, $FeCl_2$, $FeBr_2$, and FeI_2 monolayers are ferromagnetic half metals, while $CoCl_2$, $CoBr_2$, $NiCl_2$, $NiBr_2$, and NiI_2 monolayers are ferromagnetic insulators. For VCl_2, VBr_2, VI_2, $MnCl_2$, $MnBr_2$, MnI_2, CrI_2, and CoI_2 monolayers, they were found to

be antiferromagnetic semiconductors with bandgap in range of 0.2∼2.5 eV. Introducing U correction will largely enlarge their bandgap.[111] For example, the theoretical bandgaps of VBr_2 monolayer are 1.1 and 3.1 eV at PBE and PBE+U level, respectively. The easy axis of all eight abovementioned MX_2 monolayers in FM state is perpendicular to the basal plane with MAE in range of 0.02 to 0.89 meV. The highest T_C is observed in $NiCl_2$, which is 205 K predicted by Ising model.

Among the first-row transition metal dihalides, FeX_2 series have attracted more attentions, mainly due to the following two reasons: (1) largest out-of-plane MAE is found in $FeCl_2$, which is beneficial for the presence of 2D long-range magnetic ordering; (2) monolayer 1T-$FeCl_2$ films on Au(111) and graphite have been successfully synthesized using MBE technique.[175] Torun *et al.*[176] investigated the structural and magnetic properties of $FeCl_2$ monolayer using first-principles calculations. They found that 1T-$FeCl_2$ is more favorable than the 1H phase. Both PBE and HSE06 calculations demonstrated that 1T-$FeCl_2$ is an intrinsic half-metallic ferromagnet with Curie temperature of 17 K.[177] Hennig *et al.* have found that the Fe^{2+} ions in $FeCl_2$, $FeBr_2$, and FeI_2 are in a high-spin octahedral d^6 configuration, resulting in a large magnetic moment of 4 μ_B.[178] A classical XY model with nearest neighboring coupling was used to estimate their critical temperatures, which range from 122 K for FeI_2 to 210 K for $FeBr_2$. Moreover, all three 2D FeX_2 materials as half metals were predicted to have appreciable electron densities of state at the Fermi level comparable to those of typical metals, suggesting good on/off ratios in spintronic devices.[178]

In addition to first-row transition metals, the magnetic ground state of 4*d*/5*d* MX_2 monolayers in both 1T and 2H phases have been investigated by high-throughput first-principles calculations.[103] Among them, 23 out of 90 MX_2 monolayers exhibit robust magnetic ground states that are retained even after introducing the U terms. Besides the previously reported $NiCl_2$, VCl_2, $MnCl_2$, VBr_2, VI_2, MnI_2, and CoI_2, $PtCl_2$ is predicted to be a new noncollinear antiferromagnetic insulator. Meanwhile, $AgCl_2$, $AgBr_2$, and AuI_2 are found to be half metallic ferromagnets with spin splitting of 0.2∼0.5 eV. To find more 2D intrinsic magnets in MH_2 family, Shen *et al.*[179] also focused on 5*d* transition metal based MX_2 monolayers. They screened more than 6000 kinds of 2D electrenes (i.e., materials with excess electrons acting as anions) and found that $LaBr_2$ is one of most intriguing FM semiconductors with unusual long-range ferromagnetism induced by anions. From DFT calculations, its on-site moment, Curie temperature, and coercive field are 1 μ_B, 235 K, and 0.53 T, respectively.[179] For $LaBr_2$ monolayer, delocalized spin density in the intermediate region between La atoms was also unveiled in another theoretical paper by Jiang *et al.*[65]

3. MX

Among transition metal halides, MX compounds have the simplest stoichiometric ratio of 1:1. Without octahedral type crystal field, MX monolayer structures mainly consist of double hexagonal layers of metal atoms sandwiched by two hexagonal layers of halogen atoms. It is interesting to ask whether such MX monolayers still possess long-range magnetic ordering. By comprehensive first-principles calculations and MC simulations, Jiang *et al.*[65] have identified ScCl, YCl, and LaCl monolayers as ferromagnetic metals with appreciable Curie temperatures of 280, 240, and 260 K, respectively, while PBE+U calculations revised those values to 355, 460, and 260 K, respectively. Band structure analysis has shown that the spin density is relatively delocalized in the intermediate region between metal atoms, resulting in a small magnetic moment of 0.364, 0.333, and 0.317 μ_B per Sc, Y, and La atom, respectively. Wang *et al.*[180] also found that 2D ScCl monolayer is an intrinsic ferromagnet with large spin polarization. Their predicted Curie temperature was 185 K. Even so, both studies indicated that introduction of more transition metal in M-X systems would strongly quench its magnetic moment, while retaining Curie temperature at rather high value.

4. M_3X_8

Niobium halides form another kind of potential 2D vdW magnets with an unusual composition—Nb_3X_8. In Nb_3X_8 monolayer,[181] triangular Nb clusters are formed by Nb atoms; and consequently, every Nb atom is still arranged in a distorted octahedral environment. Therefore, both ferromagnetic ground state and semiconducting behavior were found in 2D Nb_3X_8 (X = Cl, Br, I) monolayers from GGA+U calculations. The Curie temperatures estimated by mean field approximation based on Heisenberg model were 31, 56, and 87 K for Nb_3Cl_8, Nb_3Br_8, and Nb_3I_8, respectively. Among them, the Nb_3I_8 monolayer has been successfully cleaved from its bulk phase.[182] Without considering U term, Xiao *et al.*[74] investigated the magnetic properties of the family 2D V_3X_8 (X = F, Cl, Br, I) in the framework of DFT. They found that V_3Cl_8 monolayer is an intrinsic AFM semiconductor, while the other three systems are FM half metals. The estimated Curie temperatures from MC simulations were 77 and 103 K for 2D V_3F_8 and V_3I_8, respectively.

B. Binary transition metal chalcogenides

Two-dimensional binary transition metal chalcogenides, including transition metal dichalcogenides, transition metal monochalcogenides, and other stoichiometries in a general form of M_mX_n (M refers to transition metal, and X represents S, Se, and Te), have provided a gorgeous platform for exploring interesting electronic and magnetic properties, such as valley polarization and 2D magnetism.

1. Transition metal dichalcogenides

Among 2D binary transition metal chalcogenides, the most widely studied ones are TMDs. Generally speaking, 2D TMDs form sandwich type structures in the X-M-X sequence, where transition metal atoms are sandwiched in between two layers of chalcogen atoms. There are four reported structural phases for TMDs, i.e., trigonal prismatic H-phase, octahedral T-phase, distorted octahedral 1T'-type, and T_d-type lattices.[183] In all these phases, each transition metal atom is surrounded by six chalcogen atoms. The five formerly degenerate *d* orbitals of 3*d* transition metal ion would split in energy as it is bonded to the chalcogen ligands. Under the crystal field with D_{3h} symmetry in H phase, the five degenerate 3*d* orbitals split into a single state a_1 (d_{z2}) and two twofold degenerate states e_1 (d_{x2-y2}/d_{xy}) and e_2 (d_{xz}/d_{yz}). While in T phase, the triangle sublattice of transition metal atoms gives rise to first-neighboring coordination number of 6, forming octahedral crystal field; thus, the *d* states split into t_{2g} and e_g manifolds. Due to the trigonal distortion, t_{2g} degeneracy is further lifted to form

higher-lying a_{1g} level and twofold degenerate e_g states in T′ and T_d phases. Intuitively, the magnetic properties of 2D TMDs should be determined by splitting and filling behavior of *d* orbitals of the transition metal ions under various crystal fields. For the same transition metal ion, the electronegativity of a chalcogen atom also plays some role, such that the lighter chalcogen atom draws more electrons from the metal ions and affects their on-site magnetic moments.

It was computationally confirmed that intrinsic long-range magnetic ordering can be realized on the transition metal sites with respect to delocalized *p* states of S/Se/Te atoms in a variety of transition metal dichalcogenides. Early in 2002, extensive analyses of the stability of TMD monolayers based on DFT calculations predicted that, out of 88 combinations of TMDs compounds, 52 H or T structures can occur as the freestanding phase. Among them, H-phase TMDs with M = Cr, Mo, V, Mn, Co, and W, and X = S, Se, and Te were predicted to be ferromagnetic metals with net magnetic moment ranging from 0.2 to 3.0 μ_B per formula.[56] Similarly, Chen *et al.*[57] also systematically explored the magnetic properties of MTe_2 (M = Ti, V, Cr, Mn, Fe, Co, Ni) monolayers in both H and T phases. Their results indicated that H-VTe_2, T-$MnTe_2$ and H-$FeTe_2$ are ferromagnetic metals with magnetic moments of 0.78, 2.80, and 1.48 μ_B per formula unit (f.u.), respectively, while T-VTe_2 is an indirect bandgap semiconductor with a magnetic moment of 1.0 μ_B per formula. Using 2D Ising model and MFT, the estimated Curie temperatures were 301, 33, 88, and 229 K for H-VTe_2, T-VTe_2, T-$MnTe_2$, and H-$FeTe_2$ monolayers, respectively. Moreover, non-collinear DFT calculations revealed that H-VTe_2, T-VTe_2, and H-$FeTe_2$ monolayers have in-plane easy magnetization direction with MAE values of 0.51, 1.74, and 2.57 meV/f.u., respectively, while T-$MnTe_2$ has a perpendicular easy magnetization axis with MAE of 0.54 meV/f.u. DFT calculations within LDA+U approximation demonstrated that single-layer VS_2 of 1T phase is a strongly correlated material, where 2H structure of monolayer VS_2 is a ferromagnetic semiconductor.[10] The magnetic moments are localized on the V atoms and couple ferromagnetically via superexchange interactions mediated by the S atoms. Calculations of magnetic anisotropy showed an easy plane for the magnetic moment in 2H VS_2. The magnetic properties of 2D NbS_2 and ReS_2 nanosheets have been investigated using the HSE06 hybrid functional.[184,185] Both of them are bipolar magnetic semiconductors with spin gaps of 0.27 and 1.63 eV. Furthermore, MC simulations predicted the Curie temperatures to be 141 and 157 K for 2D NbS_2 and ReS_2 systems, respectively.

Among the large family of potential 2D magnetic TMDs, VSe_2, VTe_2, $MnSe_x$, $NbTe_2$, $NbSe_2$, and $CrTe_2$ have attracted more and more attentions from both experimental and theoretical aspects, mainly because of the reported room-temperature T_C. In the following content, we will discuss the major developments that have paved the way to this point. First, all these six materials belong to the family of T phase [Fig. 9(a)] and exhibit metallic nature. The magnetic coupling mechanism stems from the competition between indirect superexchange and itinerant exchange interactions. Second, 2D metallic TMDs are well-known charge density wave (CDW) systems and the CDW phase transition steers the change of electronic structures in them. Therefore, the correlation effect and the possible competition between CDW ordering and magnetic ordering also needs to be clarified.

Monolayer VSe_2 material has been reported as one of the first room-temperature 2D ferromagnets.[34] From the electronic structure point of view, VSe_2 exhibits a $3d^1$ configuration, which invokes both metallic and magnetic properties. Bonilla *et al.*[34] synthesized single- and few-layer VSe_2 sheets on HOPG and MoS_2 substrates using MBE and performed magnetic characterization by protecting the films with a Se capping layer. Their studies revealed a significant enhancement of magnetic moment in single-layer samples compared with multi-layer ones. Surprisingly, the ferromagnetic ordering is very robust and persists above room temperature. The room-temperature ferromagnetism was also observed on the exfoliated 2D VSe_2 flakes using superconducting quantum interference device (SQUID), XMCD [Figs. 9(b) and 9(c)], and magnetic force microscopy (MFM), where the monolayer flake displayed the strongest ferromagnetic properties.[186] First-principles calculations using both GGA and high-level LDA+DMFT (dynamical mean-field theory) approaches explained that it might be a ferromagnet with both itinerant and localized characters.[17,18,20] For example, LDA+DMFT calculations predicted ferromagnetic ordering in VSe_2 monolayer without CDW below 250 K. However, the origin of ferromagnetism in VSe_2 has spurred great controversies. First, the reported experimental magnetic moments (5∼15 μ_B)[34,187] are too large in comparison with the calculated values (0.365∼0.6 μ_B).[17,18,20] Second, no magnetic signal was detected in another XMCD experiment and the angle resolved photoemission spectrum showed no exchange splitting.[188,189] Third, several studies[145,187,189–191] suggested CDW transition distortion can suppress the intrinsic ferromagnetic ground states in VSe_2. Wong *et al.*[145] observed traits of spin frustration in monolayer VSe_2 with long-range intrinsic ferromagnetism from complementary temperature- and field-dependent susceptibility measurements. They have also reported that the frustrated intrinsic magnetism in 2D VSe_2 can be lifted by the introduction of the Se-deficient defects.[192] Yu *et al.* inferred that a defect-free sample is the key to verify the intrinsic ferromagnetism of VSe_2.[186] Nakano *et al.*[193] demonstrated the emergence of intrinsic ferromagnetism in V_5Se_8 ($V_{0.25}VSe_2$) epitaxial thin films grown by MBE, which can be classified as itinerant 2D Heisenberg ferromagnets with weak magnetic anisotropy.

Due to strong $3d^1$ electron coupling in the neighboring M^{4+}–M^{4+} pairs (M = V, Nb, Ta) of 2D TMDs, metallic VTe_2, $NbTe_2$, $NbSe_2$, and $TaTe_2$ systems composed of group VB elements have been regarded as the potential intrinsic magnets. In some theoretical investigations, 2D VTe_2, $NbTe_2$, and $TaTe_2$ have been predicted to exhibit intrinsic magnetic ordering.[58,59,194,195] In particular, VTe_2 monolayer was found to be a room-temperature ferromagnet with highest T_C value of 553∼618 K. Meanwhile, MC simulation of the hysteresis features of VTe_2 monolayer illustrated that it is possible to observe finite remanence and coercivity treatments nearly or well beyond room temperature.[146] Similar to the discussions on VSe_2, Wong *et al.*[196] also found that CDW order would rule out the ferromagnetic behavior in VTe_2 monolayer. Experimentally, the single crystalline ultrathin VTe_2, $NbTe_2$, and $TaTe_2$ sheets were synthesized using atmospheric pressure CVD approach.[35] The magnetic hysteresis (M-H) measurements demonstrated that VTe_2 and $NbTe_2$ exhibit room-temperature ferromagnetism [Figs. 9(d) and 9(e)]. The reported saturation magnetization, coercivity, and remnant magnetization values of VTe_2 were 0.3 emu g^{-1}, 1173.0 Oe, 0.16 emu g^{-1} at 10 K, and 0.21 emu g^{-1}, 592 Oe, 0.10 emu g^{-1} at 300 K, respectively. However, the competition between CDW and magnetic instability in VTe_2 is still under debate. On the one hand, formation of the CDW phase in 2D VSe_2 was observed in experiment, and

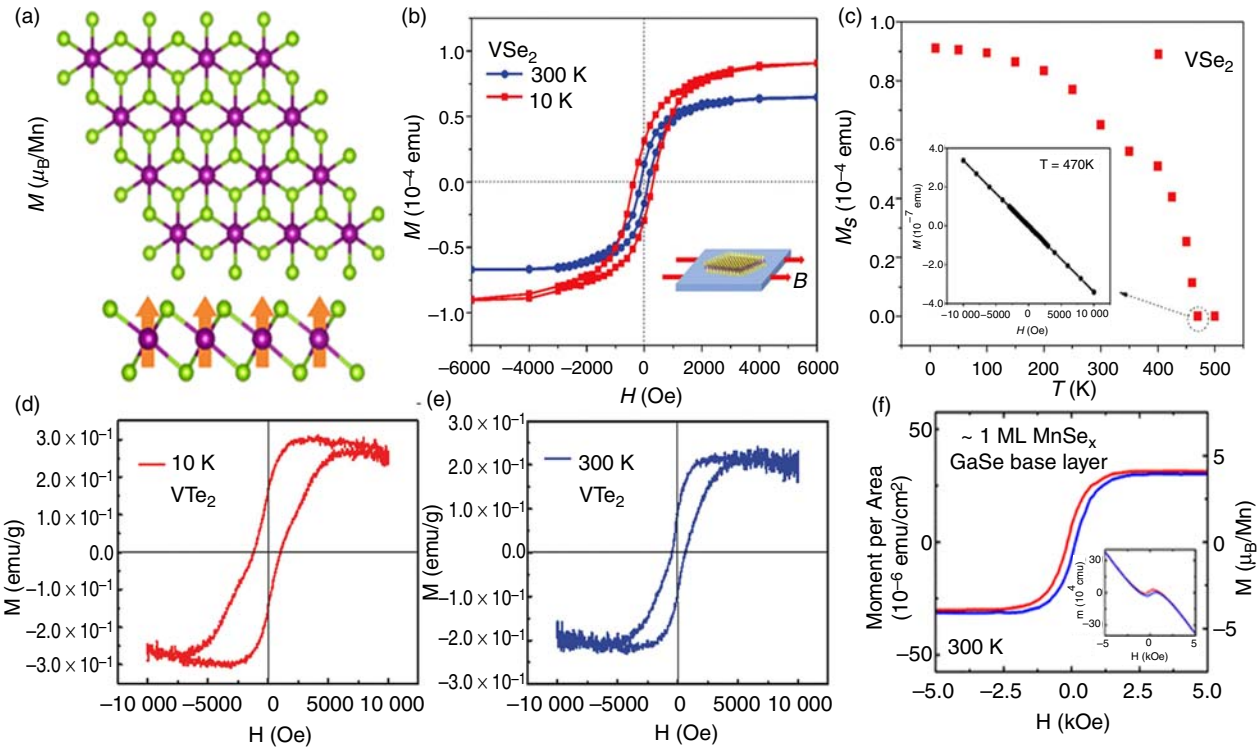

FIG. 9. (a) Top and side views of 1T TMD lattice. (b) M–H hysteresis loop of bare VSe_2 flakes on SiO_2 substrate under an in-plane magnetic field at 300 and 10 K. (c) Temperature-dependent saturated magnetization (M_s) of bare VSe_2 from 10 to 500 K. Inset: M–H curve for the sample at 470 K indicating the loose of magnetization. (d), (e) Magnetic hysteresis loops for VTe_2 at 10 and 300 K, respectively. (f) Magnetic hysteresis loop of ~1 ML $MnSe_x$ on the GaSe base layer showing ferromagnetic ordering. Inset: the unprocessed SQUID data prior to background subtraction. Panels (a)–(c) reproduced with permission from Yu *et al.*, Adv. Mater. **31**, 1903779 (2019). Copyright 2019 John Wiley and Sons.[186] Panels (d) and (e) reproduced with permission from Li *et al.*, Adv. Mater. **30**, 1801043 (2018). Copyright 2018 John Wiley and Sons.[35] Panel (f) reproduced with permission from O'Hara *et al.*, Nano Lett. **18**, 3125 (2018). Copyright 2018 American Chemical Society.[36]

three possible CDW transitions at 135, 240, and 186 K have been reported.[35,197,198] The CDW effect would suppress the magnetic instability and further lead to the absence of magnetic ordering. Through a combination of *in situ* microscopic and spectroscopic techniques, Wong *et al.*[196] observed a 4×4 CDW order and further excluded the intrinsic ferromagnetic ordering in VTe_2 by XMCD data. One the other hand, Sugawara and coworkers[199] recently found a large triangular Fermi surface at the K point that satisfies a nearly perfect nesting condition, whereas CDW is suppressed as highlighted by the observation of band crossing of the Fermi level at low temperature, in contrast to monolayer VSe_2. Combining DFT calculations with scanning tunneling microscopy and spectroscopy (STM/STS) measurements, ferrimagnetic ground state of 2D $NbSe_2$ was demonstrated with a magnetic moment of 1.09 μ_B.[200] More importantly, their results also inferred that substrate is the key to verifying the intrinsic ferromagnetism of TMD materials.[196,200] It was shown that single-layer $NbSe_2$ does not display CDW instability unless a graphene layer is utilized as substrate.

Motivated by DFT calculations,[56,60] O'Hara *et al.*[36] also observed room-temperature ferromagnetism in manganese selenide ($MnSe_x$) films grown by MBE. Magnetic and structural characterizations provided strong evidence that, at the monolayer limit, ferromagnetism originates from the vdW $MnSe_2$ monolayer. Using DFT calculations combined with MC simulations, Kan *et al.*[60] have shown that 2D $MnSe_2$ sheets are ideal magnetic semiconductors with long-range magnetic ordering, where all Mn atoms are ferromagnetically coupled and the estimated T_C is 250 K [Fig. 9(f)]. Interestingly, first-principles calculations further revealed the great defect tolerance in $MnSe_2$. Despite the presence of high-density Se vacancies, the defective $MnSe_2$ monolayer can retain its stable ferromagnetic behavior.[144] Magnetic tunneling junctions based on monolayer $MnSe_2$ with room-temperature ferromagnetism were also observed with a large tunneling magnetoresistance of 725%.[201] Moreover, by optical and electronic measurements, Sun *et al.*[147] disclosed that the intrinsic ferromagnetically aligned spin polarization can hold up to 316 K in a metallic phase of 1T-$CrTe_2$. Detailed spin transport measurements suggested half-metallicity in its spin polarized band structure as well as in-plane room-temperature negative anisotropic magnetoresistance. Importantly, their study found that exchange coupling due to an enhancement of itinerant type was the source of room-temperature ferromagnetism in both bulk and few-layered Cr_2Te_3.[21]

2. Other transition metal chalcogenides

Owing to the variable valence of transition metal elements, transition metal chalcogenides have diverse stoichiometric compositions. In addition to TMDs with M:X = 1:2, the 2D transition metal

chalcogenide compounds with higher stoichiometries (M:X = 5:8, 2:3, 3:4, and 1:1) also exhibit interesting magnetic properties. In V_5S_8 nanosheets, an AFM to FM phase transition was observed when the thickness is down to 3.2 nm. Using DFT calculations, Zhang *et al.*[202] further investigated the thickness-dependent magnetic ordering in V_5S_8 thin films, and confirmed an antiferromagnetic to ferromagnetic phase transition when V_5S_8 is thinned down to 2.2 nm. The magnetic moments of the thin films in both antiferromagnetic and ferromagnetic states are mainly located on V atoms in the intermediate layer. Utilizing vdW epitaxy techniques, Cr_2S_3 sheets with one-unit cell thickness down to 1.78 nm have been successfully synthesized, which exhibited ferrimagnetic behavior with a Néel temperature of 120 K and the maximum saturation magnetic momentum of up to 65 emu.[203] In addition, Lv *et al.*[204] identified Co_2Se_3 as a 2D half-metal among a series of M_2Se_3 candidate materials, and the calculated T_C from the mean field theory was about 600 K. Using first-principles calculations, Ouyang and coworkers predicted a family of stable 2D honeycomb lattices of Cr_2X_3 (X = O, S, Se). Cr_2S_3 and Cr_2Se_3 are ferromagnetic half-metals with mirror symmetry protected nodal lines for the spin-down channels, while Cr_2O_3 layers are ferromagnetic semiconductors with large out-of-plane MAE.[205] A hexagonal Ta_2S_3 sheet has also been predicted as 2D magnet from the spin-wave theory, which possesses sizeable out-of-plane MAE of 4.6 meV and high Curie temperature of 445 K.[206]

Based on first-principles calculations, a new composition of stable 2D transition metal chalcogenides, i.e., Cr_3X_4 (X = S, Se, Te) monolayers, has been predicted to possess fascinating magnetic properties.[15] Among them, Cr_3S_4 monolayer is a ferrimagnetic semiconductor, while Cr_3Se_4 and Cr_3Te_4 monolayers are ferromagnetic half-metals with T_C of 370 and 460 K, respectively. Unlike the *d–p–d* superexchange interaction found in the other transition metal compounds, double exchange magnetic coupling mechanism is dominated in these 2D Cr_3X_4 sheets, finally leading to enhanced FM ordering and room temperature T_C. That is to say, a delocalized unpaired electron could hop between the two neighboring Cr ions with different oxidation states in 2D Cr_3X_4.

Using PSO technique combined with first-principles calculations, Zhang *et al.*[207] predicted a new transition metal chalcogenide monolayer composed of cobalt and sulfur atoms—Co_2S_2. Their results revealed that a single-layer Co_2S_2 sheet is a ferromagnetic metal with a Curie temperature of 404 K. Two-dimensional ultrathin CrSe crystals were successfully synthesized on mica substrate via ambient pressure CVD method.[208] Such CVD-grown 2D CrSe crystals exhibit evident ferromagnetic behavior at temperatures below 280 K. Kang *et al.*[209] reported the synthesis of ultrathin FeTe film by CVD approach and discussed their structural and magnetic transition. Transport measurements revealed that tetragonal FeTe is an antiferromagnetic metal with T_N of about 71.8 K, while hexagonal FeTe is a ferromagnetic metal with T_C of around 220 K. Very recently, Yuan *et al.*[210] have grown FM MnSe monolayer on silicon substrate using MBE method. The thickness dependence of Curie temperature was found in the MnSe ultrathin films. The measured T_C was 54 K for monolayer, while it sharply increased to 225 K for three-layer MnSe, and 235 K for four-layer MnSe.

C. MXene and MXene analogues

MXene, a category of 2D transition metal carbides, nitrides, and carbonitrides, possibly terminated by functional group (T) on the surface, with a general formula of $M_{n+1}X_nT_x$ (M = transition metal; X = C and/or N; T = O, OH, F) are attractive additions to the family of 2D materials. Since the discovery of Ti_3C_2 in 2011, MXenes of Ti_2C, V_2C, Nb_2C, Mo_2C, Zr_3C_2, Nb_4C_3, Ta_4C_3, and Ti_4N_3, as well as of TiNbC, $(Ti_{0.5}Nb_{0.5})_2C$, $(V_{0.5}Cr_{0.5})_3C_2$, Ti_3CN, Mo_2TiC_2, Mo_2ScC_2, Cr_2TiC_2, $Mo_2Ti_2C_3$, $(Nb_{0.8}Ti_{0.2})_4C_3$, and $(Nb_{0.8}Zr_{0.2})_4C_3$ have already been fabricated in a laboratory. According to the large number of M-X compositions, more than a hundred MXenes have been theoretically predicted.[211]

The diverse compositions and controllable thickness of $M_{n+1}X_nT_x$ systems provide an ideal playground to achieve 2D intrinsic magnetism (Table III).[92,211,212] As mentioned above, transition metal M atom usually has a partially filled *d* shell with unpaired electrons. First of all, the magnetic properties of MXene are influenced by the total number of *d* electrons. The M site can be also occupied by the ordered double transition metal species, i.e., M′M″. Generally, M′ atoms locate in the outer layers and M″ atoms occupy the middle layer, yielding $[M'X]_nM''$ arrangement. However, some in-plane ordered double transition metal MXenes have also been reported. The competition of electron hopping and electronic coupling between M′ and M″ ions will further modify the magnetic ground state of MXene. Each X (C or N) anion bounds with six transition metal M cations, forming XM_6 octahedral configuration. The transition metal atoms on the surface of M_2X are subjected to a C_{3v} ligand field contributed by the neighboring X atoms. Hence, the five 3*d* orbitals of transition metal atom would split into a single state a_1 (d_{z2}), two twofold degenerate states e_1 (d_{x2-y2}/d_{xy}) and e_2 (d_{xz}/d_{yz}). The splitting between a_1 and e_1/e_2 is determined by the strengths of M–X interactions. In addition, long-range spin interaction between the metal atoms always occurs through X atoms in MXene, which plays an important role in mediating the magnetic coupling.

In experiments, MXene materials have been achieved by selective etching of the A-layers (mostly Al) using acid solution in the bulk MAX phases [Fig. 10(a)].[213,214] Therefore, the majority of MXenes are synthesized with mixed surface functional groups. In the functional group terminated M_2X MXene, each transition metal ion is subjected to a new octahedral or distorted octahedral crystal field, which in turn splits the *d* orbitals into the lower-energy t_{2g} states (d_{xy}, d_{yz}, and d_{xz}) and higher-energy e_g states (d_{x2-y2} and d_{z2}).[215,216] Moreover, the functional groups have strong affinity with MXene surface and may serve as chemical dopants. The electron transfer from transition metal ions to functional groups would directly affect the magnetic configuration of transition metal ions, which can be interpreted as a competition between localized and itinerant *d* states. Generally speaking, the itinerant *d* electrons in MXene favor superexchange mechanism, while the localized *d* orbitals tend to have direct exchange interaction. In addition to MXenes in M_2XT_x stoichiometry, thicker MXene systems of $M_{n+1}X_nT_x$ are also available in experiments, where the dimensionality, n, describes the number of XM_6 octahedral layers in $M_{n+1}X_nT_x$. The stacking of octahedra and the number of occupied *d* orbitals would depend on the ratio of M and X atoms. The sensitive correlation between the magnetic ordering and dimensionality has also been observed.[217,218]

1. Pristine MXene ($M_{n+1}X_n$)

We start from discussing the simplest case—the magnetic properties of pristine MXenes. Although most MXenes have been synthesized with surface functional groups, few pristine MXene materials $M_{n+1}X_n$ are also evidenced by experimental observations and

TABLE III. A list of 2D magnets in MXene family with their compositions and key electronic and magnetic properties, including the magnetic ground state (GS), the values of Hubbard U, energy gap (E_g), magnetic moment on per transition metal (Ms), Curie temperature (T_C), and magnetic anisotropy energy per unit cell (MAE).

	Compositions	GS	U (eV)	E_g (eV)	Ms (μ_B)	T_C (K)	MAE (meV)	Ref.
$M_{n+1}X_n$	Cr_2C	FM	–	HM	3	–	–	136
	Ti_2C	FM	–	M	0.96	–	–	222
	Ti_2C	FM	–	HM	0.96	–	–	223
	Ti_2C	AFM	2∼5	0.42	0.95	–	–	224
	Ti_2C	FM	–	M	0.97	146	–	243
	2H-Ti_2C	FM	2∼5	HM	1.0	290	–	224
	Cr_2N	AFM	3	M	4.45	–	–	226
	Ti_2N	FM	–	HM	0.5	–	–	223
	V_2N	AFM	–	M	0.07	–	–	223
	V_2C	AFM	4	M	–	–	–	240
	Zr_2C	FM	–	M	0.63	–	–	222
	Fe_2C	FM	–	M	1.96	861 (MFT)	−0.114	97
	Mn_2C	AFM	–	M	3	720	−0.025	220
	Cr_3C_2	FM	–	M	1.3	886 (MFT)	–	229
	Ti_3C_2	PM [i]	–	–	–	10 [i]	–	233
	Ti_3C_2	FM	–	M				228
	Ti_3CN	FM	–	M				228
	Ti_4C_3	FM	–	M	0.875	–	–	236
	$Ti_{n+1}C_n$ (n=1∼9)	FM			0.98∼0.15			217
	$Ti_{n+1}N_n$ (n=1∼9)	FM			0.62∼0.06			217
	Ta_2C	NM	–	–	–	–	–	218
	Ta_2C	AFM	–	–	–	–	–	218
	Ta_3C_2	AFM	–	–	–	–	–	218
	Ta_3C_2	FiM	–	–	–	–	–	218
	Ta_4C_3	AFM	–	–	–	–	–	218
	Ta_4C_3	AFM	–	–	–	–	–	218
	2H-Ru_2C	FM	–	M	0.86	–	–	225
	Fe_2N	AFM	4.0					227
	Co_2N	AFM	3.3					227
	Ni_2N	AFM	6.4					227
$M_{n+1}X_nT_x$	$Sc_2C(OH)_xO_{2-x}$	FM	–	0.506	0.5	–	–	234
	$Mo_3N_2F_2$	FM	3	HM	2.1	237	0.1736	235
	Mn_2NF_2	FM	4	HM	4.5	1877	–	12
	Mn_2NO_2	FM	4	HM	3.8	1379	–	12
	$Mn_2N(OH)_2$	FM	4	HM	4.4	1745	–	12
	Cr_2NF_2	AFM	4	–	3.7/3.0	–	–	12
	Cr_2NO_2	FM	4	HM	2.8	566	–	12
	$Cr_2N(OH)_2$	AFM	4	–	3.0	–	–	12
	V_2NF_2	AFM	3	–	2.5/2.0	–	–	12
	V_2NO_2	AFM	3	–	1.8/1.0	–	–	12
	$V_2N(OH)_2$	AFM	3	–	2.2	–	–	12
	Ti_2NF_2	AFM	4	–	1.3/1.0	–	–	12
	Ti_2NO_2	FM	4	HM	0.5	–	–	12
	$Ti_2N(OH)_2$	AFM	4	–	0.9	–	–	12
	Mn_2CH_2	FM	4	M	3.22	293	–	237
	Mn_2CO_2	FM	4	M	3.1	323	–	237
	$Mn_2CO_{1.5}$	FM	4	M	3.06	–	–	237

TABLE III. (*Continued.*)

Compositions	GS	U (eV)	E_g (eV)	Ms (μ_B)	T_C (K)	MAE (meV)	Ref.
Cr_2CF_2	FM	–	M	2.71	–	–	525
$Cr_2C(OH)_2$	FM	–	M	2.24	–	–	525
Cr_2NF_2	FM	–	M	3.23	–	–	525
Cr_2NOH_2	FM	–	M	3.01	–	–	525
Cr_2NO_2	FM	–	M	2.50	–	–	525
Mn_2NOF	FM	4	SC	3.94	173	0.0241	252
Mn_2NOF	FM	4	SC	3.94	163	0.0488	252
Mn_2NOF	FM	4	HM	3.95	310	0.0202	252
$Mn_2NO_{0.5}F_{1.5}$	FM	4	HM	4.17	187	0.0148	252
$Mn_2NO_{1.5}F_{0.5}$	FM	4	M	3.72	180	0.0326	252
Cr_2NOF	AFM	4	HM	3.21	65	–	252
Cr_2NOF	AFM	4	HM	2.90	4	–	252
Cr_2NOF	AFM	4	HM	3.10	23	–	252
$Cr_2NO_{0.5}F_{1.5}$	AFM	4	HM	3.29	86	–	252
$Cr_2NO_{1.5}F_{0.5}$	AFM	4	M	3.03	335	–	252
V_2NOF	AFM	4	SC	1.64	347	–	252
V_2NOF	AFM	4	SC	1.64	62	–	252
V_2NOF	AFM	4	SC	1.63	128	–	252
$V_2NO_{0.5}F_{1.5}$	AFM	4	HM	1.88	83	–	252
$V_2NO_{1.5}F_{0.5}$	AFM	4	SC	1.53	281	–	252
Cr_2CF_2	AFM	–	3.15	2.53	–	–	244
$Cr_2C(OH)_2$	AFM	–	1.39	2.39	–	–	244
Ni_2NF_2	FM	6.4	HM	1.60	1800	–	227
$Ni_2N(OH)_2$	FM	6.4	HM	1.60	2400	–	227
Ni_2NO_2	FM	6.4	HM	0.97	3300	–	227
Fe_2NF_2	AFM	4.0	–	–	–	–	227
$Fe_2N(OH)_2$	FM	4.0	HM	–	–	–	227
Fe_2NO_2	FM	4.0	HM	–	–	–	227
Co_2NF_2	AFM	3.3	–	–	–	–	227
$Co_2N(OH)_2$	AFM	3.3	–	–	–	–	227
Co_2NO_2	FM	3.3	–	–	–	–	227
Mn_2NO_2	FM	4	HM	3.8	67	63	238
$Mn_2N(OH)_2$	FM	4	HM	4.5	–	1.3	238
Mn_2NF_2	FM	4	HM	4.5	1148	2.0	238
Cr_2NO_2	FM	4	HM	2.9	53	22	238
Ti_2NO_2	FM	4	HM	0.51	–	0.78	238
Cr_2CFCl	AFM	3	SM	3	395	–	239
Cr_2CHBr	AFM	3	SM	3	320	–	239
Cr_2CClBr	AFM	3	SM	3	385	–	239
Cr_2CFBr	AFM	3	SM	3	310	–	239
Cr_2CBrOH	AFM	3	SM	3	300	–	239
Cr_2CHCl	AFM	3	SM	3	430	–	239
Cr_2CHF	AFM	3	SM	3	380	–	239
Cr_2CClOH	AFM	3	SM	3	375	–	239
Cr_2CFOH	AFM	3	SM	3	390	–	239
Cr_2CHOH	AFM	3	SM	3	270	–	239
Mn_2CF_2	FM	3	HM	4	520	0.024	13
Mn_2CO_2	AFM	3	SM	3	110	0.090	13

TABLE III. (*Continued.*)

	Compositions	GS	U (eV)	E_g (eV)	Ms (μ_B)	T_C (K)	MAE (meV)	Ref.
	$Mn_2C(OH)_2$	FM	3	HM	4	460	0.019	13
	Mn_2CCl_2	FM	3	HM	4	380	0.037	13
	Mn_2CH_2	AFM	3	M	3.03	120	0.233	13
	Cr_2CH	FM	4	HSC	3.83/2.36	–	–	241
	Cr_2CF	FM	4	HSC	3.83/3.15	–	–	241
	Cr_2CF_2	FM	4	HSC	3.11	–	–	241
	Cr_2CO	FM	4	HM	2.88	–	–	241
	Cr_2CO_2	FM	4	BHM	3.72/3.01	–	–	241
	Cr_2CH_2	FM	4	BMS	3.19	–	–	241
M′M″XT	TiZrC	FM	–	M	0.57	418	–	243
	TiHfC	FM	–	M	0.52	329	–	243
	TiCrC	AFM	–	M	0.2	–	–	243
	$Cr_2TiC_2F_2$	AFM	–	1.35	Cr: 2.59	–	–	244
	$Cr_2TiC_2(OH)_2$	AFM	–	0.84	Cr: 2.54	–	–	244
	$Cr_2VC_2F_2$	FM	–	M	Cr: 2.49	696	–	244
	$Cr_2VC_2O_2$	FM	–	M	Cr: 1.95	77	–	244
	$Cr_2TiC_2(OH)_2$	FM	–	M	Cr: 2.41	618	–	244
	$Ti_2MnC_2O_2$	FM	4/4	SM	0.99	495	–	245
	$Ti_2MnC_2(OH)_2$	FM	4/4	M	1.3	1103	–	245
	$Ti_2MnC_2F_2$	FM	4/4	M	1.413	109	–	245
	$Hf_2MnC_2O_2$	FM	2/4	0.238	1	829	–	245
	$Hf_2MnC_2(OH)_2$	AFM	2/4	M	1.613	–	–	245
	$Hf_2MnC_2F_2$	AFM	2/4	1.027	1.67	–	–	245
	$Hf_2VC_2O_2$	FM	2/3	0.055	0.33	1133	–	245
	$Hf_2VC_2(OH)_2$	AFM	2/3	M	0.443	–	–	245
	$Hf_2VC_2F_2$	AFM	2/3	M	0.423	–	–	245
	Mo_2TiC_2Tx	AFM	4/4	S	–	–	–	246
	$Cr_2Ti_2C_3O_2$	FM	–	–	1.983/0.011	721	–	247
	$Cr_2Ti_2C_3(OH)_2$	AFM	–	–	2.543/0.043	–	–	247
	$Cr_2Ti_2C_3F_2$	AFM	–	–	2.602/0.036	–	–	247
	$Cr_2V_2C_3O_2$	FM	–	–	2.015/0.049	247	–	247
	$Cr_2V_2C_3(OH)_2$	AFM	–	–	2.399/0.271	–	–	247
	$Cr_2V_2C_3F_2$	AFM	–	–	2.498/0.289	–	–	247
	$Cr_2Nb_2C_3O_2$	AFM	–	–	2.259/0.040	–	–	247
	$Cr_2Nb_2C_3(OH)_2$	AFM	–	–	2.448/0.159	–	–	247
	$Cr_2Nb_2C_3F_2$	AFM	–	–	2.539/0.172	–	–	247
	$Cr_2Ta_2C_3O_2$	AFM	–	–	2.285/0.041	–	–	247
	$Cr_2Ta_2C_3(OH)_2$	AFM	–	–	2.359/0.161	–	–	247
	$Cr_2Ta_2C_3F_2$	AFM	–	–	2.457/0.182	–	–	247
	TiV_2C_2O	AFM	0/4	–	∼1.0	–	–	249
	$TiCr_2C_2$	AFM	0/4	∼0.45	∼3.4	–	–	249
	$TiCr_2C_2H$	AFM	0/4	∼0.8	∼3	–	–	249
	$TiCr_2C_2O$	AFM	0/4	∼0.9	∼1.8	–	–	249
	$TiCr_2C_2F$	AFM	0/4	∼1.4	∼3.3	–	–	249
	$TiCr_2C_2OH$	AFM	0/4	∼0.6	∼3	–	–	249
	$TiMn_2C_2$	AFM	0/4	–	∼3.75	–	–	249
	$TiMn_2C_2F$	FM	0/4	–	∼4	–	–	249
	TiV_2C_2H	AFM	0/4	–	∼2.1	–	–	249

TABLE III. (*Continued.*)

	Compositions	GS	U (eV)	E_g (eV)	Ms (μ_B)	T_C (K)	MAE (meV)	Ref.
	TiV_2C_2OH	AFM	0/4	–	∼2.4	–	–	249
	$TiCr_2N_2$	AFM	0/4	–	∼3.6	–	–	249
	$TiCr_2N_2O$	AFM	0/4	–	∼2.1	–	–	249
	$TiCr_2N_2OH$	AFM	0/4	–	∼3.5	–	–	249
	$TiMn_2N_2$	AFM	0/4	–	∼4.3	–	–	249
	$TiMn_2N_2H$	AFM	0/4	∼0.2	∼4.4	–	–	249
	$TiMn_2N_2F$	AFM	0/4	∼1.9	∼4.5	–	–	249
	Cr_2TiC_2FCl	BAFS	3	1.26	–	–	–	248
	$Cr_2TiC_2F_2$	AFM	3	1.06	–	–	–	248
	$Cr_2TiC_2Cl_2$	AFM	3	0.91	–	–	–	248
	$Cr_2TiC_2FxCl_{2-x}$ (x=0.25∼1.75)	BAFS	3	–	–	–	–	248
	$(Ta_{2/3}Fe_{1/3})_2C$	AFM	–	SC	1.82	–	0.86	251
	$(Zr_{2/3}Fe_{1/3})_2C$	FM	–	SC	1.71	268	0.74	251
	$(Hf_{2/3}Fe_{1/3})_2C$	FM	–	SC	1.79	894	1.39	251
	$(Hf_{2/3}Cr_{1/3})_2C$	FM	–	SC	1.01	344	0.76	251
	$(Ti_{2/3}Hf_{1/3})_2C$	FM	–	SC	0.3	190	0.71	251
MBene	MnB	FM	–	M	3.2	345	0.025	215
	MnBF	FM	–	M	3.24	405	–	215
	MnBOH	FM	–	M	3.15	600	–	215
	Ti_2B	FM	–	M	0.75	39	0.032	262

theoretical calculations. For instance, a recent experiment confirmed that the surface functional groups F and OH on Ti_2C monolayer can be eliminated by heat treatment at different temperatures.[219] The Mn_2C MXene as the global minimum structure in two dimensions was confirmed by PSO structure search combined with first-principles calculations.[220] Mo_2C MXene was successfully prepared with the traditional CVD method.[221]

Table III summarizes the unterminated MXenes that have been theoretically predicted to be stable 2D intrinsic magnets, such as Fe_2C, Cr_2C, Cr_2N, Mn_2N, Ru_2C, Fe_2N, Co_2N, Ni_2N, Ti_2C, Zr_2C, Ti_2N, Ti_3C_2, Ti_3CN, Cr_3C_2, $Ta_{n+1}C_n$, $Ti_{n+1}C_n$, and $Ti_{n+1}N_n$. Si *et al.*[136] firstly pointed out that Cr_2C is a half-metallic ferromagnet with a bandgap of 2.85 eV. The ferromagnetism arises from the itinerant Cr 3*d* electrons fractionally occupied in the majority spin channel [Fig. 10(b)]. Similar to Cr_2C, Fe_2C is also an itinerant ferromagnet, and Stoner model is able to explain the mechanism to induce magnetic orderings.[97] The corresponding exchange interaction parameters are J_1= 6.17 meV and J_2 = 5.70 meV, which provide further evidences for the robust ferromagnetic coupling of Fe atoms. Moreover, the calculated MAE of Fe_2C in reciprocal space is −22.8 μeV per unit cell, which has an easy plane for the magnetization. From the distribution of MAEs, the negative contributions around the sides of hexagonal Brillouin zone are responsible for the in-plane magnetization. The Curie temperature within mean-field approximation was 861 K. First-principles calculations were carried out to investigate the electronic and magnetic properties of a series of M_2C (M = Hf, Nb, Sc, Ta, Ti, V, Zr) monolayers.[222] Among them, Ti_2C and Zr_2C possesses magnetic moments of 1.92 and 1.25 μ_B/unit, respectively. Gao *et al.* further confirmed that Ti_2C exhibits nearly half-metallicity with a magnetic moment of 0.96 μ_B/Ti.[223] Based on the spin-resolved partial density of states, it is not surprising that the large exchange splitting of Ti 3*d* electrons and the strong hybridization of Ti 3*d* electrons with C 2*p* electrons are responsible for the formation of half-metallic magnetism. By considering all possible spin configurations, Akgenc *et al.*[224] indicated that Ti_2C MXene is antiferromagnetic metal that is 36 meV/cell lower in energy than FM state. However, room-temperature half-metallic ferromagnetism was observed in 2H-Ti_2C. The room-temperature half-metallic ferromagnetism was also found in Ti_2N MXene, and the magnetic moments were mainly located at Ti ions with 1.00 μ_B per formula unit. Although the individual atom of W, Mo, Ru, Os, Tc, and Re has a magnetic moment of 4, 6, 2, 4, 5, and 3 μ_B, respectively, most MXenes with 4*d*/5*d* transition metals are non-magnetic, except that 2H-Ru_2C is a FM metal with magnetic moment of 0.86 μ_B per Ru.[225]

Besides the above discussed ferromagnetic MXenes, Mn_2C is an antiferromagnetic metal with magnetic moment of 3 μ_B per Mn atom.[220] Both high Néel temperature (720 K) and appreciable in-plane MAE (25 μeV) are simultaneously observed in this system. Strong Mn–Mn coupling within the basal plane is responsible for both AFM ordering and magnetic anisotropy. Cr_2N is also an AFM metal. Each Cr atom has a magnetic moment of 4.45 μ_B, while each N atom possesses a magnetic moment of −0.30 μ_B. These values are quite different from those of FM Cr_2C system.[226] Ni_2N MXene also prefers AFM ground state.[227] In bare Ni_2N MXene, the direct Ni–Ni exchange interaction within short distance is strong, which results in antiferromagnetic coupling between Ni atoms. Similar results have also been found in Fe_2N and Co_2N.[227]

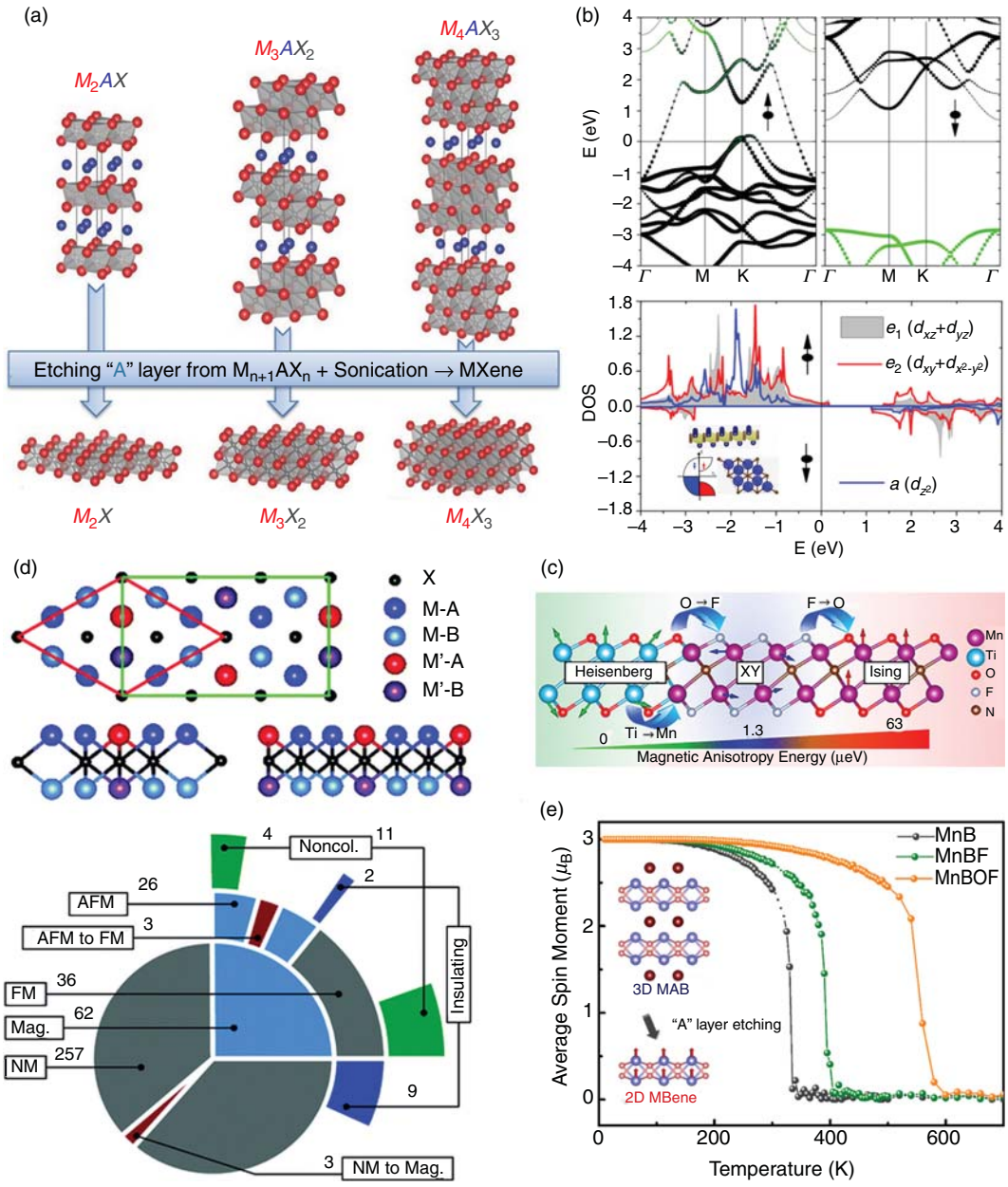

FIG. 10. (a) Structures of the MAX and MXene phases. (b) Band structure and partial density of states of Cr *d* orbitals for Cr_2C MXene, and the Fermi level is set to zero. (c) Tunable magnetic anisotropy and noncollinear magnetism in MXenes. (d) Structure of i-MXene $(M_{2/3}M'_{1/3})_2X$ and classification of the magnetic ground states for 319 kinds of i-MXene systems. (e) On-site magnetic moments of Mn atom as function of temperature in bare and functionalized MnB MBene. Panel (a) reproduced with permission from Naguib *et al.*, Adv. Mater. **26**, 992 (2014). Copyright 2014 John Wiley and Sons.[214] Panel (b) reproduced with permission from Si *et al.*, ACS Appl. Mater. Inter. **7**, 17510 (2015). Copyright 2015 American Chemical Society.[136] Panel (c) reproduced with permission from Frey *et al.*, ACS Nano **12**, 6319 (2018). Copyright 2018 American Chemical Society.[238] Panel (d) reproduced with permission from Gao *et al.*, Nanoscale **12**, 5995 (2020). Copyright 2020 Royal Society of Chemistry.[251] Panel (e) reproduced with permission from Jiang *et al.*, Nanoscale Horiz. **3**, 335 (2018). Licensed under a Creative Commons Attribution (CC-BY-3.0).[215]

To reveal the effect of dimensionality, we have compared the magnetic behavior of different $M_{n+1}X_n$ ($n > 1$) systems. In MXene with the formula of M_3X_2, there are three metal atoms per unit cell, i.e., one in the middle (M_m) and two on the surface (M_s). The distance between M_m and M_s is short, which enhances the direct interaction between *d* orbitals and thus induces AFM coupling between them. Since both M_s atoms couple antiferromagnetically with the M_m atom, these two M_s atoms must couple ferromagnetically with each other. Additionally, after insertion of X atoms, the M_m–M_s antiferromagnetic coupling is weakened. Therefore, Ti_3C_2,

Ti_3CN, and Cr_3C_2 sheets are indeed ferromagnetic metals, and their magnetism originates from Ti and Cr ions on the surface.[228,229] The possible magnetic ground states of $Ti_{n+1}C_n$ and $Ti_{n+1}N_n$ (n = 1∼9) were examined by DFT calculations with PBE functional.[217] The results suggested that these unterminated carbide and nitride MXenes with different thicknesses are all magnetic. The magnetism still originates from the 3*d* electrons of Ti atoms on the surface. However, $Ti_{n+1}C_n$ and $Ti_{n+1}N_n$ MXene show different magnetic characteristics. The total magnetic moment of carbides increases from 2 to 3 μ_B per f.u. with increasing n, while the total magnetic moment fluctuates with n around 1.2 μ_B per f.u. for nitrides. Using first-principles calculations, Lane *et al.*[218] have also investigated the effect of dimensionality and electron correlations on the magnetic ordering in Ta-C ($Ta_{n+1}C_n$, n = 1∼3). With LDA+U formulism, AFM configurations were predicted for Ta_2C and Ta_4C_3, whereas ferrimagnetism was predicted for Ta_3C_2. Without U term, however, their magnetic ground states are non-magnetic for Ta_2C and antiferromagnetic for Ta_3C_2 and Ta_4C_3, respectively. Using the salt-templating method, Xiao *et al.* recently synthesized ultrathin Mn_3N_2 flakes on KCl substrate, which represent the first solution-processed 2D transition metal nitride with intrinsic antiferromagnetism at room temperature.[230]

2. Functional terminated MXenes ($M_{n+1}X_nT_x$)

As stated above, surface functional group is a key degree of freedom in MXene, which are originally introduced during MXene synthesis. Experimentally, when MXenes are chemically exfoliated by HF acid solutions, the outer layers are often saturated with F, O, and/or OH groups. According to the distributions of these functional groups, MXenes can be categorized as symmetrically functionalized MXenes, asymmetrically functionalized MXene (namely, Janus MXene), and mixed functionalized MXenes. The symmetrically functionalized MXenes are terminated by identical groups on both sides of transition metal surfaces, while the top and bottom transition metals surfaces are terminated by two alternative functional groups in the asymmetrically functionalized MXenes. In the mixed functionalized MXenes, the distribution of functional groups is random and nonuniform. The positions and proportions of functional groups in MXene are highly dependent on the synthesis route and post-synthesis treatments. It is necessary to point out that the MXenes produced to date may prefer to have mixed functional groups of F, OH, and O.[231] From a theoretical point of view, Singh *et al.*[232] also found that the mixed functionalized $Ti_3C_2F_x(OH)_{1-x}$ (x = 0∼1) MXenes are very close in Gibbs free energy.

Remarkably, magnetism has already been realized in the functional group terminated MXene. Yoon *et al.*[233] developed a low-temperature solution based synthetic method to reduce 2D $Ti_3C_2T_x$ multilayers. The X-ray photoelectron spectroscopy, electron spin resonance, and magnetization measurements implied that the reduced $Ti_3C_2T_x$ is Pauli paramagnetic, which is important experimental evidence for magnetism in MXene. The presence of Ti^{3+} ions is the origin of the electron spin resonance signal. At temperature less than 10 K, a Curie-like concentration was observed, as indicative of singly occupied states at the Fermi level.

The correlation between the magnetic properties of MXene and the functional groups is a subject of increasing concern in the research of 2D MXenes. The effects of different functional groups on the magnetic ground state of MXenes have been widely investigated by theoretical simulations, which will be described in detail below. Similar to the discussions about transition metal trihalides in Sec. III A 1, the relative strengths of direct, superexchange, and double exchange interactions can explain the diverse magnetic ground states of the functionalized MXenes.[12,13]

First, it is believed that magnetism can been introduced in the originally non-magnetic MXene after the presence of functional groups. Zha *et al.*[234] have investigated the mechanism for structural conversion from $Sc_2C(OH)_2$ to Sc_2CO_2 MXene. The atomic configurations and magnetic properties for all the intermediate states were determined. Bipolar magnetic semiconductors were identified from these rearranged configurations with inhomogeneous distribution of hydrogen atoms on different sides with x approximately in the range of $0.188 \leq x \leq 0.812$. First-principles calculations predicted a novel ferrimagnetic half-metallic state in 2D F-terminated Mo_3N_2 with a Curie temperature of 237 K.[235] Such ferrimagnetic coupling comes mainly from the interactions of itinerant *d* electrons between different Mo layers, and thus endows 100% spin polarization at the Fermi level with a sizable half-metallic gap of 0.47 eV. Kumar *et al.*[12] carried out a comprehensive theoretical study on the magnetic properties of twelve nitride MXenes of M_2NT_2 (M = Ti, V, Cr, Mn; T = F, OH, O). They identified a new series of Mn_2NF_2, Mn_2NO_2, and $Mn_2N(OH)_2$ that exhibit FM half metallic behavior. The total magnetic moments are 9.0, 8.8, and 7.0 μ_B per f.u. for Mn_2NF_2, Mn_2NO_2, and $Mn_2N(OH)_2$, respectively. Both the exchange parameters between intralayer nearest neighbors and interlayer nearest neighbors are positive, indicating FM coupling. Impressively, the Curie temperatures from MC simulations for Mn_2NF_2, Mn_2NO_2, and $Mn_2N(OH)_2$ are as high as 1877, 1379, and 1745 K, respectively.

Second, theoretical calculations predicted that magnetism would disappear in certain kinds of MXenes due to the presence of surface termination. In the bare $Ti_{n+1}C_n$ and $Ti_{n+1}N_n$, the magnetism originates mainly from the unpaired electrons in Ti atoms. Upon functionalization of F, O, OH, and H, the unpaired electron on each Ti atom would be completely donated to the functional group by forming ionic bonds. Thus, the magnetically ordered ground states would be destroyed in the functionalized $Ti_{n+1}C_n$ and $Ti_{n+1}N_n$.[217] Once two sides of Ti_3C_2 surfaces are saturated by external groups, a large number of electronic states distributed around the Fermi level would be removed and the whole system would become non-magnetic.[228] Urbankowski *et al.*[236] also reported that the magnetic moment of FM bare Ti_4N_3 with 7.0 μ_B per unit cell is reduced to almost zero by OH termination. One can therefore conclude that the magnetism of Ti atoms in MXene would be destroyed by −1 valence functional group such as F, Cl, and OH.

Third, an interesting magnetic phase transition could be induced by functionalization. Compared to pristine FM Cr_2C, Cr_2C terminated by F, H, OH, or Cl groups are AFM. The underlying mechanism for such FM-AFM transition is that the functional groups induce stronger localization behavior on the *d* electrons of Cr atoms.[136] $Fe_2N(OH)_2$, Fe_2NO_2, Co_2NO_2, Ni_2NF_2, $Ni_2N(OH)_2$, and Ni_2NO_2 have FM ground state, which are different from the AFM ground state in bare phase of Fe_2N, Co_2N, and Ni_2N. In those functionalized MXenes, the nearest interlayer distance of metal atoms increases after O, OH, and F terminations.[226] The ferromagnetic coupling between metal atoms is stronger than AFM coupling, which is explained by a superexchange interaction mechanism mediated by the spin polarized N atoms.[227]

Although bare Cr_2N MXene is an AFM metal, Cr_2NO_2 has a ferromagnetic ground state that acts as a half-metal.[226] The electrons with minority spin at the Fermi level are suppressed by O groups. Similar to Cr_2N, Mn_2C monolayer also transforms from AFM to FM state under hydrogenation and oxygenation.[237] The magnetic moments are 3.22 μ_B per Mn atom under 100% degree of hydrogenation, and 3.10 and 3.06 μ_B per Mn atom under 75% and 100% oxygenation degrees, respectively, which are slightly higher than that of bare Mn_2C.[220] The Stoner criterion can explain the AFM to FM transition in Mn_2C well. From MC simulations, the Curie temperatures are 293 and 323 K for fully hydrogenated and oxygenated Mn_2C, respectively.[237] By modifying the surface termination, the spin-orbit interaction and bond directionality of M_2NT_x nitride can be also manipulated.[238] These two important factors give rise to a rich diversity of noncollinear spin structures and finely tunable magnetocrystalline anisotropy [Fig. 10(c)]. Specifically, Ti_2NO_2 and Mn_2NF_2 have continuous O(3) and O(2) spin symmetries, respectively, while Cr_2NO_2 and Mn_2NO_2 are intrinsic Ising ferromagnets with out-of-plane easy axes and magnetic anisotropy energies up to 63 μeV/atom. The magnetic properties of Mn_2CT_2 (T = F, Cl, OH, O, H) have been computationally investigated.[13] Depending on the electronegativity of functional groups, the AFM Mn_2C change to FM ground state upon functionalization of F, Cl, or OH groups. They are intrinsic half metals with high Curie temperature (280∼520 K) and sizable magnetic anisotropy (MAE = 24∼38 μeV). Theoretical studies of the asymmetrically functionalized MXenes have predicted that Janus Cr_2C behaves as a bipolar antiferromagnetic semiconductor with zero magnetization and high Néel temperatures (270∼430 K).[239] With appropriate choice of surface functional group pairs (H, F, Cl, Br, and OH), one can tailor the bandgap of Cr_2C from 0.15 to 1.51 eV. The itinerant *d* electrons in Cr_2C are favorable to $Cr_1\uparrow$-$C\downarrow$-$Cr_2\uparrow$ superexchange mechanism, while the localized $Cr_{T'}\uparrow$ *d* orbitals can directly interact with the $Cr_{T''}\downarrow$ one in $Cr_2CT'T''$. In other words, the distinct characteristics of *d* electrons in Cr_2C and $Cr_2CT'T''$ induce FM and AFM ordering, respectively.[239]

In addition, magnetism can be retained by precisely controlling the surface functional groups on MXenes. For example, the fully covered functional groups of O^{2-} and H^+ keep the magnetic properties of bare Mn_2C, showing AFM semiconductor and AFM metal, respectively.[13] The stable magnetic configurations of both V_2C and V_2C derivatives, i.e., V_2CF_2 and $V_2C(OH)_2$, are antiferromagnetic coupling.[240] Moreover, metal-semiconductor transition behavior upon functionalization was also observed. Two-dimensional Fe_2N, Co_2N, and Ni_2N as well as their surface passivated structures were investigated using DFT calculations. All the bare MXenes and functionalized systems, including Fe_2NF_2, Co_2NF_2, and Co_2NF_2, prefer AFM state. For Cr_2N, the bare system is an antiferromagnetic metal, and passivation of F atoms or OH groups would not change the antiferromagnetic characteristics.[226] If only one side is saturated, long-range FM ordering can be retained in F and H modified Ti_3C_2 monolayers. However, the strength of spin-spin coupling is weakened after chemical modification, in comparison with that of pristine Ti_3C_2 monolayer. The simulated Curie temperatures of Ti_3C_2, Ti_3CN, and HTi_3C_2 were about 300, 350, and 1000 K, respectively.[228] CrC_2 with single-side and two-side functionalization (H, O, F) have also been investigated by first-principles calculations. The CrC_2 monolayer functionalized with O atoms on both sides shows bipolar half-metallic characteristics, while it becomes a half-metal with O atoms terminated on one side only. CrC_2 monolayer with H/F at one side and F at two sides are half semiconductors, while it is a bipolar magnetic semiconductor (BMS) after being functionalized with H atoms on both sides.[241]

3. Double transition metal MXenes [$(MM')_{n+1}X_nT_x$]

The MXenes of double transition metal carbides are also synthesized and predicted to be robust magnetic semiconductor or metal, making them desirable in spintronics.[242] Hu *et al.*[243] investigated the magnetic properties of ordered double-metal MXenes MM'C for M being Ti and M' being the other transition metal elements. They found that TiZrC and TiHfC are FM metals with T_C = 418 and 329 K, respectively, while TiCrC is an AFM metal. The magnetic moments of TiZrC and TiHfC mainly come from the Ti atoms, and the magnetic moments of Ti atoms in TiZrC (0.57 μ_B) and TiHrC (0.52 μ_B) are much less than the value of Ti atoms in Ti_2C (0.97 μ_B).[243] The magnetic properties of $Cr_2M'C_2T_2$ (M' = Ti, V; T = O, OH, F) systems have been investigated by first-principles calculations.[244] $Cr_2TiC_2F_2$ and $Cr_2TiC_2(OH)_2$ were predicted to be antiferromagnetic, while $Cr_2VC_2(OH)_2$, $Cr_2VC_2F_2$, and $Cr_2VC_2O_2$ were ferromagnets with Curie temperatures of 618, 77, and 695 K, respectively. Among $Hf_2MnC_2T_x$ and $Hf_2MnC_2T_x$ systems,[245] only $Hf_2MnC_2O_2$ and $Hf_2MnC_2O_2$ are ferromagnetic semiconductors, while the ground states of the rest of OH and F terminated ones are antiferromagnetic. More interestingly, the Curie temperatures of four reported MXenes, i.e., $Ti_2MnC_2O_2$, $Ti_2MnC_2(OH)_2$, $Hf_2MnC_2O_2$, and $Hf_2VC_2O_2$, are in the range from 495 to 1133 K, which are much higher than room temperature. For the experimentally realized $Mo_2TiC_2T_x$, F and OH terminations are shown to lead to antiferromagnetic semiconductors.[246] The magnetism of $Mo_2TiC_2T_x$ originates from the unpaired Mo 3*d* orbitals that locate in the outer layer. The magnetic properties of $Cr_2M_2C_3T_2$ (M = Ti, V, Nb, Ta; T = OH, O, F) were investigated using DFT calculations.[247] It was shown that ferromagnetic ordering is energetically more favorable for $Cr_2Ti_2C_3O_2$ and $Cr_2V_2C_3O_2$, while the magnetic ground states of the rest of $Cr_2M_2C_3T_2$ systems prefer AFM ordering. The Curie temperatures of FM $Cr_2Ti_2C_3O_2$ and $Cr_2V_2C_3O_2$ are 720 and 246 K, respectively. For the asymmetrically functionalized double MXene Cr_2TiC_2FCl, theoretical study by Sun *et al.* found that it behaves as bipolar antiferromagnetic semiconductors (BAFS) with opposite spin character in the conduction band minimum and valence band maximum.[248] The different chemical environments induce a mismatch of *d* states for the Cr atoms in the upper and lower surfaces, thereby resulting in the BAFS feature. Moreover, the mixed functionalized double MXenes remain as a BAFS. Based on the experimental synthesis, Sun *et al.*[249] focused on the group of Ti-centered double transition metal TiM_2X_2T (M = V, Cr, Mn; X = C, N; T = H, F, O, OH). After screening various combinations of metal elements and terminating groups, only $TiMn_2C_2F$ showed FM ordering, whereas AFM state is energetically more favorable in all other systems.

Motivated by the synthesis of in-plane ordered MAXs, i.e., $(M_{2/3}M_{1/3})_2AX$,[250] the magnetic properties of 319 kinds of $(M_{2/3}M'_{1/3})_2X$ MXene were investigated by high-throughput DFT calculations [Fig. 10(d)], from which 40 FM compounds and 26 AFM compounds were found.[251] Among these magnetic systems, there are five MXenes with out-of-plane MAE larger than 0.5 meV per f.u. Furthermore, the

predicted T_C of $(Zr_{2/3}Fe_{1/3})_2C$ and $(Hf_{2/3}Fe_{1/3})_2C$ are higher than room temperature.

Although the method to precisely control the surface functional group species and/or double transition metal MXene is yet to be discovered, one can see that the magnetism in a few MXenes, such as $Ti_2MnC_2T_2$[245] and Mn_2NTx,[252] is not sensitive to the nature of surface terminations. Using first-principles and Monte Carlo calculations, Frey *et al.*[252] have studied the effects of mixed termination and characterized a wide variety of magnetic and transport behavior in Janus M_2X. Janus Mn_2N systems were found to be robust ferromagnets regardless of surface termination structures and compositions. By analyzing the electron filling in transition metal cations and performing DFT calculations, Dong *et al.*[245] designed a series of 2D magnetic materials based on ordered double transition metal MXenes. They revealed that $Ti_2MnC_2T_x$ are ferromagnetic metals or semimetals, regardless of their surface termination of O, OH, or F. In short, the high Curie temperature and robust magnetism make these MXenes very attractive for experimental realization of 2D magnets.

4. MBene

MAB phases, as boron analog of MAX phases, are formed by stacked M–B blocks and interleaved A atomic planes.[253–256] Recently, boride analogues of MXene termed as MBene were predicted theoretically[215,257] and were soon confirmed in experiment by topochemical deintercalation of Al atoms from MAB structures ($M_2A_2B_2$ and M_2AB_2),[258–261] including 2D sheets of MoB, CrB, FeB, and TiB. Since the number of valence electrons of boron is one/two less than carbon/nitrogen, its electron deficiency and lower electronegativity would endow MBene with distinctly different magnetic performance from the conventional carbide or nitride based MXenes. For example, using DFT-based high-throughput search, Jiang *et al.*[215] identified 12 stable MBene nanosheets that are feasible to synthesize. Among them, 2D MnB MBene exhibits robust metallic ferromagnetism with 3.2 μ_B per Mn atom and a high Curie temperature of 345 K. After functionalization with F and OH groups, the ferromagnetic ground state of 2D MnB is well preserved. More excitingly, the Curie temperatures are even elevated to 405 K (with F groups) and 600 K (with OH groups), respectively, suggesting that careful choice of functional groups might be beneficial to the increase of T_C in MBene [Fig. 10(e)]. Similar to MnB MBene, the electronic and magnetic properties of Ti_2B monolayer were also investigated by DFT calculations. Its FM spin configuration corresponds to the magnetic ground state, and the predicted Curie temperature of is $T_C = 39$ K based on Heisenberg model.[262]

D. Other binary transition metal compounds

The itinerant and localized behavior of the *d* electrons in transition metals and the coupling between them are still the starting point of designing the 2D magnetic materials for spintronics using other binary transition metal compounds, such as carbides, nitrides, oxides, borides, phosphides, silicides, arsenides, and hydrides. The local environments of the transition metal ions, including symmetry, bonding types, and orbital hybridizations, are identified as the key factors to understand the details of crystal field splitting. Therefore, it is essential to establish a relationship between the local environment and the spin-polarized orbital filling of the central transition metal ion. Most reported binary transition metal compounds are listed in Table IV and categorized by their compositions as well as magnetic properties for discussions.

1. Transition metal carbides/nitrides

The magnetic properties of many transition metal carbides/nitrides have already been described as the 2D MXene family in Sec. III C. However, they are not limited to MXenes, which can be regarded as the transition metal rich compounds. In contrast, the 2D transition metal carbides/nitrides with fewer metal atoms, such as MN_2, MN, MC_2, and MC monolayers, show higher chemical stability. Compared to MXenes, these monolayers of transition metal carbides/nitrides have fewer exposed metal sites. As a result, the effect of surface modification might be avoided in them, which is in principle more favorable than MXenes for practical spintronic applications.

For the transition metal nitrides with stoichiometric ratio of 1:1, a monolayer structure obtained from (100) surface of rocksalt-structured CrN crystal was predicted to be a ferromagnet using PSO technique.[263] Analyses of its band structure and DOS revealed that this material is a half-metal, and the origin of ferromagnetism was ascribed to the *p-d* exchange interaction between Cr and N atoms. The corresponding Curie temperature was about 675 K. Hexagonal CrN,[264] VN,[265] and MnN[266] monolayers were also identified as intrinsic half-metallic ferromagnets. In their flat atomically thin hexagonal lattices, the coordinate number of the transition metal ions is three. Hence, the *d* orbital diagram is a typical example of crystalline orbitals of trigonal-type complexes in terms of crystal field theory, which is quite different from those of the octahedral O_h and C_{3v} crystal fields. In these transition metal mononitrides, the non-degenerate non-bonding d_{z2} orbital has highest energy and is localized on the top of the valence band. The next ones in energy are the doubly degenerate d_{xz} and d_{yz} orbitals, which overlap with N p_z states and form bonding π-dative orbitals localized above and below the sheet. The lowest-lying orbitals in energy are doubly degenerate d_{xy} and $d_{x2\text{-}y2}$ states, which hybridize with *s* orbitals of transition metals to form sd^2 hybridization. Bader population and orbital analyses revealed that the local magnetic moments on Cr, Mn, and V atom are 3, 4, and 2.1 μ_B, respectively. The Curie temperatures of 368 K for h-MnN monolayer and 768 K for h-VN monolayer were estimated from MC simulations.[265,266] Their results indicated that the easy axis for both 2D materials is in the in-plane direction, and the corresponding MAE values are 134 and 100 μeV per transition metal atom for h-MnN and h-VN, respectively. More interestingly, MnN monolayer can maintain FM half-metallicity and constant magnetic moment even under $\pm$10% strain, because 100% spin polarization of the electronic states near the Fermi level is fully preserved by the robust bandgap of the spin-down states.[266] The half metallic nature of h-VN and h-CrN will be retained even after contact with semiconducting 2D sheets of MoS_2 or $MoSe_2$, which can be used as the substrates for h-VN and h-CrN devices.[264,265] In addition, robust magnetic behavior was also observed in the buckled tetragonal t-VN monolayer, which has 99.9% spin polarization at the Fermi level and shows a rare p^2d^2 hybridization for V atoms.

Monolayer structures of transition metal carbides with 1:1 stoichiometry, including CoC, NiC, and CuC, were predicted by PSO structure search method and first-principles calculations. Among them, CoC monolayer is antiferromagnetic and NiC monolayer is ferromagnetic, while CuC monolayer is non-magnetic.[267] The local

TABLE IV. A list of 2D magnets in binary transition metal compounds with their compositions and key electronic and magnetic properties, including the magnetic ground state (GS), the values of Hubbard U, energy gap (E_g), magnetic moment on per transition metal (Ms), Curie temperature (T_C), and magnetic anisotropy energy per unit cell (MAE).

	Compositions	GS	U (eV)	E_g (eV)	Ms (μ_B)	T_C (K)	MAE (meV)	Ref.
Nitrides	CrN	FM	3	HM	3.19	675	–	263
	h-CrN	FM	3	HM	3	–	–	264
	h-MnN	FM	5.5	HM	4	368	−0.134	266
	h-VN	FM	–	HM	1.46	768	−0.1	265
	t-VN	FM	–	M	2.1	278	−0.021	265
	Mn_2N	FM	4	HM	3.6	913	–	270
Carbides	α-CoC	AFM	–	1.22	1.4	–	−0.545	267
	β-CoC	AFM	–	M	1.61	–	−0.216	267
	α-NiC	FM	–	M	0.43	–	−0.166	267
	β-NiC	FM	–	M	0.27	–	−0.107	267
	FeC_2	FM	5	HM	4	245	−0.98	268
	CrC_2	FM	4	HM	8.0	–	–	269
	VC_2	FM	4	M	2.21	–	–	269
	MnC_2	FM	4	M	6.81	–	–	269
	FeC_2	FM	4	1.62	8	–	–	269
	CoC_2	FM	4	SC	6.03	–	–	269
	NiC_2	FM	4	M	2.85	–	–	269
Borides	t-MnB	FM	3.32	M	2.65	406	0.218	271
	CoB_6	FM	3.5/6.0	D	1.377/1.382	–	–	78
Oxides	t-VO	AFM	–	SC	2.27	–	–	277
	t-CrO	AFM	–	SC	3.36	–	–	277
	t-MnO	AFM	–	SC	4.42	–	–	277
	Sq-TiO	AFM	–	M	1.22	–	–	277
	Sq-VO	AFM	–	SC	3.66	–	–	277
	Sq-MnO	AFM	–	SM	4.64	–	–	277
	h-V_2O_3	FM	–	HM	2.1	–	–	277
	h-Mn_2O_3	FiM	–	SC	4.55–2.69	–	–	277
	RuO_2	FM	1.5	–	1.60	38	−3.09	278
	OsO_2	FM	0.5	–	1.34	197	−42.67	278
	MnO_2	FM	3.9	3.41	3	140	–	273
	CrO_2	FM	3.5	M	2.75	219	–	277
	MnO_2	AFM	4	1.1	3.015	256	–	277
	TcO_2	FM	–	0.6	2.79	170	–	277
	FeO_2	AFM	4	M	1.823	108	–	277
	CoO_2	FM	4.5	M	0.743	60	–	277
	Fe_3O_4	AFM	4.2	2.4	3.7∼4.1	–	–	279
Hydrides	ScH_2	FM	1	M	0.59	339	0.3	283
	TiH_2	AFM	2.5	1.20	1.24	–	–	283
	VH_2	AFM	2	2.43	2.40	–	–	283
	CrH_2	AFM	2.5	1.57	3.52	–	–	283
	FeH_2	AFM	2.5	0.09	3.02	–	–	283
	CoH_2	FM	3	M	1.19	160	0.014	283
	NiH_2	AFM	4	1.90	1.17	–	–	283
Silicide	Fe_2Si	FM	3.5	HM	3.037	780	0.325	280
	$TiSi_2$	FM	–	M	0.563	–	–	281
	VSi_2	FM	–	M	2.148	–	–	281
	$CrSi_2$	FM	–	M	3.008	–	–	281

TABLE IV. (*Continued.*)

	Compositions	GS	U (eV)	E_g (eV)	Ms (μ_B)	T_C (K)	MAE (meV)	Ref.
	$MnSi_2$	AFM	–	M	2.512	–	–	281
	$FeSi_2$	AFM	–	M	1.508	–	–	281
	$NbSi_2$	FM	–	M	0.618	–	–	281
	$MoSi_2$	FM	–	M	0.207	–	–	281
	Ti_2Si	FM	1,2	M	0.685	–	–	282
Phosphide	MnP	FM	4	HM	4	495	0.166	75
	Fe_2P	AFM	–	M	1.6	23	–0.055	5
	Co_2P	FM	–	M	0.68	580	0.04	5
	Fe_3P	FM	2	M	2.55	420	0.356	76
Arsenides	MnAs	FM	4	HM	4	711	0.281	75
	FeAs-I	FM	4	M	3.07	645	0.645	73
	FeAs-II	FM	4	M	3.02	170	–	73
	FeAs-III	AFM	4	0.27	3.47	350	0.820	73

magnetic moments of α-CoC, β-CoC, α-NiC and β-NiC are 1.4, 1.61, 0.43, and 0.27 μ_B per metal atom, respectively. After considering magnetic anisotropy, the easy axis of α-CoC monolayer is [100] direction and the easy axis of β-CoC, α-NiC and β-NiC monolayers is [010] direction. Notably, the computed MAEs for antiferromagnetic CoC and ferromagnetic NiC are 107∼545 μeV per metal atom, which are at least one order of magnitude higher than those of Co (65 μeV per Co atom) and Ni (2.7 μeV per Ni atom) crystals.

Two-dimensional FeC_2[268] and CrC_2[269] sheets with 1:2 stoichiometry were predicted as half metals, and their spin polarization at the Fermi level is 100%. The C atoms in these 2D structures bind with each other to form C_2 dimers, which possess high electron affinity and gain electrons from Fe/Cr atoms. The significant amount of charge accumulation adjacent to C_2 dimers indicates strong interaction between the Fe/Cr atoms and the C_2 units. Therefore, Fe and Cr atoms are in high-spin states in FeC_2 and CrC_2 sheets, with magnetic moments of 4 and 3.83 μ_B per Fe/Cr atom, respectively. Based on MC simulation and mean-field theory, their Curie temperatures were estimated to be 245 and 965 K, respectively. N_2 dimers are also found in the penta-MnN_2 monolayer. The ferromagnetic state of penta-MnN_2 is energetically more favorable than the antiferromagnetic one, with predicted Curie temperature as high as 913 K.[270]

2. Transition metal borides

Combining DFT calculations and MC simulations, Abdullahi *et al.*[271] have presented a new phase of freestanding tetragonal Mn_2B_2 monolayer. The 2D tetra-Mn_2B_2 sheet showed metallic ferromagnetism with a magnetic moment of 2.65 μ_B per Mn atom and a Curie temperature of 406 K. Using an advanced crystal structure search method and extensive first-principles energetic and dynamic calculations, Tang *et al.*[78] have identified a planar CoB_6 monolayer exhibiting robust ferromagnetic ground state, which remains stable upon the adsorption of common environmental gases like O_2, CO_2, and H_2O. Electronic band structure calculations revealed remarkable features of Dirac cones with characteristic linear dispersions and high Fermi velocities. The atomically thin CoB_6 monolayer could be fabricated by either depositing Co atoms on the δ4 boron sheet or direct chemical growth based on precursors of planar $Co_4B_8^+$ cluster.

3. Transition metal oxides

In the on-going research of 2D materials, 2D metal oxides are tempting, owing to their natural abundance, suitable bandgap in a wide range, and high chemical inertness.[272] Originated from the half-filled 3*d* shell of Mn atom, the magnetic properties of 2D manganese oxide monolayer have been systematically investigated by first-principles calculations as representatives of the transition metal oxides family.[273,274] In experiment, 2D MnO_2 sheets were successfully synthesized by tetrabutylammonium intercalation and exfoliation.[275] It is an indirect semiconductor with a bandgap of 3.41 eV. Each unit cell of this 2D material possesses a magnetic moment of 3 μ_B, which is mainly contributed by the Mn atoms. In 2D MnO_2, Mn atoms prefer ferromagnetic coupling [Fig. 11(a)]. Furthermore, the Curie temperature is about 140 K, which can be further increased by strain.[273] Using first-principles calculations, Kan *et al.*[274] found that ultrathin films of the experimentally realized wurtzite MnO transform into a stable graphitic structure with ordered spin arrangement. Moreover, the AFM ordering of graphitic MnO monolayer can be switched into half-metallic ferromagnetism by moderate doping. They found that the Curie temperature is about 350 K when 0.25 hole/Mn is doped in single-layer MnO.

Aguilera-Granja and Ayuela[276] investigated the magnetic properties of monolayer metal oxides under MO_2 stoichiometry, including all 3*d*, 4*d*, and 5*d* transition metals. It is noteworthy that CrO_2 and FeO_2 layers are half-metals, while MnO_2 and TcO_2 layers with half-filled *d* orbitals in the transition metal elements behave as magnetic semiconductors. A simple model, depending on the hybridization between *d* orbitals of transition metals and 2*p* orbitals of oxygen, allows us to rationalize the magnetic behavior of the complete series of 2D metal oxides. In general, the Curie temperatures were estimated in the range of 170∼220 K for 3*d* oxides and below 100 K for 4*d* oxides, respectively.[276] Recently, Gog *et al.*[277] carried out a systematic DFT study (with HSE06 hybrid functional) on the atomically thin metal oxide

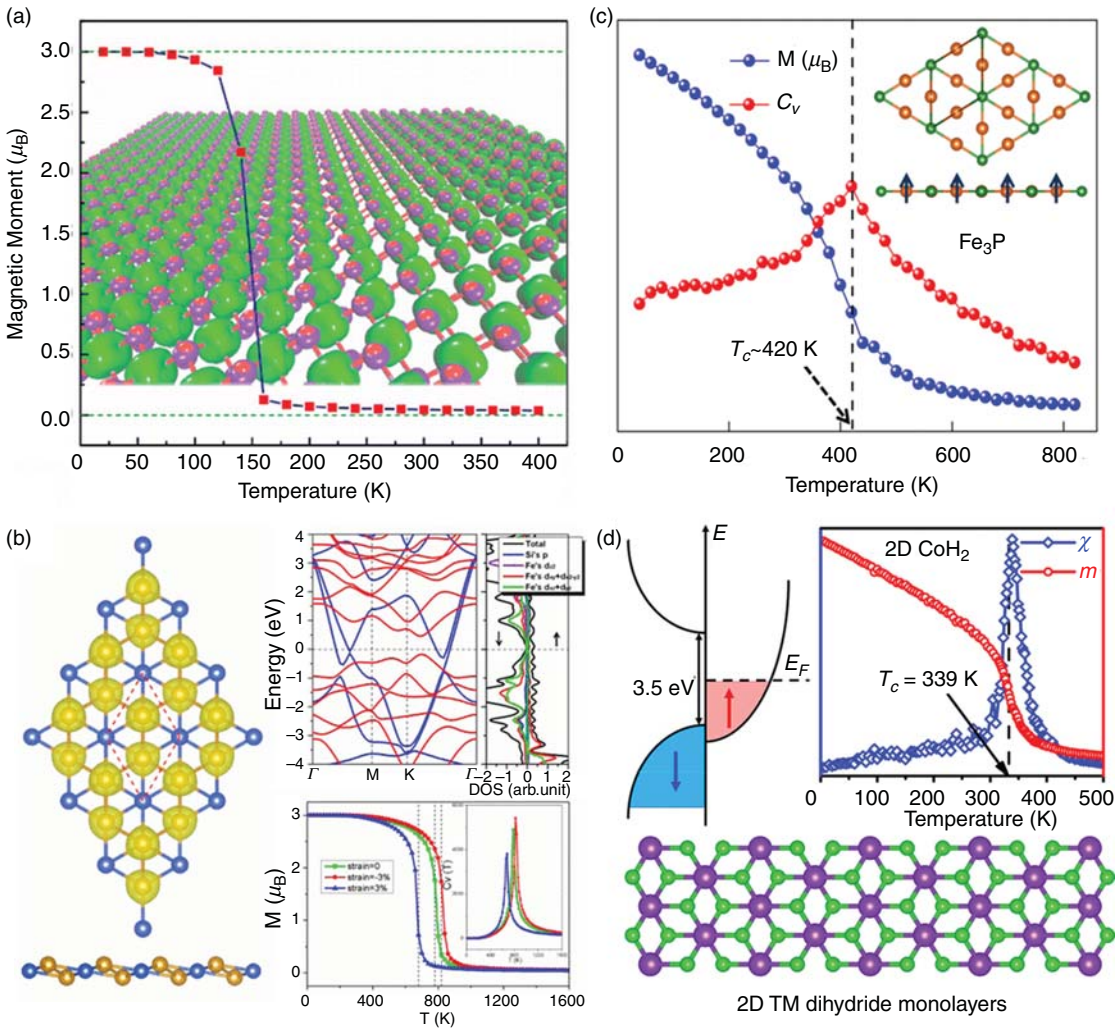

FIG. 11. (a) Total magnetic moment per unit cell as a function of temperature for 2D MnO_2 monolayer. (b) Spin charge density, band structures, total DOS, partial DOS, and simulated magnetic moment and specific heat as a function of temperature for 2D Fe_2Si monolayer. (c) Average magnetization per unit cell and specific heat (C_v) as a function of temperature for Fe_3P monolayer from MC simulations. (d) Schematic diagram of electronic band structure, and the magnetic susceptibility and magnetic moment as a function of temperature for CoH_2 monolayer from MC simulations. The atomic configurations of MnO_2, Fe_2Si, Fe_3P, and CoH_2 monolayers are also shown in insets. Panel (a) reproduced with permission from Kan *et al.*, J. Phys. Chem. Lett. **4**, 3382 (2013). Copyright 2013 American Chemical Society.[273] Panel (b) reproduced with permission from Sun *et al.*, Nano Lett. **17**, 2771 (2017). Copyright 2017 American Chemical Society.[280] Panel (c) reproduced with permission from Zheng *et al.*, J. Phys. Chem. Lett. **10**, 2733 (2019). Copyright 2019 American Chemical Society.[76] Panel (d) reproduced with permission from Wu *et al.*, J. Phys. Chem. Lett. **9**, 4260 (2018). Copyright 2018 American Chemical Society.[283]

films with compositions of MO, M_2O_3, and MO_2 for typical 3*d* transition metal elements (M = Sc, Ti, V, Cr, Mn). Of 20 2D transition metal oxides studied, a rich variety of magnetic properties were discovered for the thermally stable TMOs. Among them, the square MnO (Sq-MnO) was predicted to be a semimetal with antiferromagnetic ordering; h-V_2O_3, sq-ScO_2, and sq-CrO_2 were found to be ferromagnetic half-metals; and sq-MnO_2 was an antiferromagnetic half-metal. The magnetic moments are mainly originated from transition metal atoms, varying from 0.95 to 4.6 μ_B. 1T-RuO_2 and 1T-OsO_2 monolayers were also assigned as intrinsic 2D ferromagnets with large MAE. Their magnetic moments of 1.60 and 1.34 μ_B per transition metal atom and large MAE values come from Ru and Os atoms. In particular, the MAE of monolayer 1T-OsO_2 is as high as 42.67 meV per unit cell along [100] direction due to the strong SOC of Os atom, which is two orders of magnitude higher than the MAE of ferromagnetic monolayer materials composed of 3*d* transition metals (Table IV). According to the mean field theory, the Curie temperatures were 38 K for 1T-RuO_2 and 197 K for 1T-OsO_2 monolayer, respectively. By analyzing the density of states and *d* orbital resolved MAE of Os atom based on second-order perturbation theory, it is revealed that the large MAE of monolayer 1T-OsO_2 is mainly contributed by the matrix element differences between the opposite-spin d_{xy} and d_{x2-y2}

orbitals of Os atoms.[278] Olsson *et al.*[279] studied the magnetic order of a novel three-layered Fe_3O_4 film by means of Hubbard-corrected DFT calculations. The Fe_3O_4 film comprises a center layer with octahedrally coordinated Fe^{2+} ions sandwiched between two layers with tetrahedrally coordinated Fe^{3+} ions. The film exhibits an antiferromagnetic type I spin order.

4. Transition metal silicides

Two-dimensional Fe_2Si crystal has a slightly buckled triangular lattice composed of planar hexacoordinated Si and Fe atoms. DFT calculations with hybrid HSE06 functions indicated that 2D Fe_2Si in its ground state is a ferromagnetic half-metal with 100% spin-polarization ratio at the Fermi level. Its 2D lattice can be retained at very high temperature up to 1200 K [Fig. 11(b)]. MC simulations based on Ising model also predicted T_C as high as 780 K, which can be further modulated by biaxial strain. Moreover, the planar structure and strong in-plane Fe–Fe interaction endow Fe_2Si nanosheet sizable MAE (325 μeV per Fe atom), which is at least one to two orders of magnitude larger than those of Fe, Co, and Ni solids.[280]

Twenty 3*d* and 4*d* TM silicides with a fixed chemical formula of MSi_2 (M = Sc, Ti, V, Cr, Mn, Fe, Co, Ni, Cu, Zn, Y, Zr, Nb, Mo, Tc, Ru, Rh, Pd, Ag, Cd) have been investigated by first-principles calculations.[281] The transition metal silicides exhibit a variety of magnetic properties. Among them, $TiSi_2$, VSi_2, $CrSi_2$, $NbSi_2$, and $MoSi_2$ are ferromagnetic; $MnSi_2$ and $FeSi_2$ are antiferromagnetic; and the rest systems are nonmagnetic. The on-site moments of transition metal atom in $TiSi_2$, VSi_2, $CrSi_2$, $NbSi_2$, and $MoSi_2$ monolayers are 0.563, 2.148, 3.008, 0.618, and 0.207 μ_B, respectively, while the local spin moments of Mn and Fe atom in $MnSi_2$ and $FeSi_2$ are 2.512 and 1.508 μ_B, respectively.[281] Two-dimensional titanium silicide monolayers with different chemical compositions were globally searched by PSO simulations combined with DFT calculations. Among the explored 2D Ti-Si structures, Ti_2Si is ferromagnetic with a magnetic moment of 1.37 μ_B per unit cell.[282]

5. Transition metal phosphides/arsenides

Motivated by 2D $FeSi_2$ and FeC_2 as well as 3D Fe–P compounds, Zheng *et al.*[76] focused on the 2D materials with Fe-rich compositions of Fe_xP (x = 1∼3). With the aid of first-principles swarm structural search calculations, they have identified an unreported planar Fe_3P monolayer in Kagome lattice, showing several desirable properties for its application in spintronic devices, e.g., robust ferromagnetism with large MAE, and high thermal stability. As shown in Fig. 11(c), MC simulation yielded a Curie temperature of 420 K. In addition, five stable M_2P monolayers (M = Fe, Co, Ni, Ru, Pd) under P4/*mmm* symmetry group were predicted by high-throughput search and DFT calculations, which showed peculiar features of coexistence of in-plane M–P covalent bonds and M–M interlayer metallic bonds. Importantly, the distinct electronic configurations of transition metal atoms under a tetragonal crystal field lead to diverse magnetic properties in 2D M_2Ps. Among them, Co_2P is ferromagnetic with a Curie temperature of 580 K, while Fe_2P is antiferromagnetic with a Néel temperature of 23 K. Their long-range magnetic orderings originate from the interplay of M–P–M superexchange interactions and M–M direct exchange interactions.[5] Two experimentally feasible 2D intrinsic ferromagnetic materials, MnP and MnAs monolayers, were predicted by first-principles calculations,[75] which posses appreciable out-of-plane anisotropies with MAE of 166 and 281 μeV, respectively. These two monolayer sheets exhibit remarkable half-metallicity with high Curie temperatures of 495 K for MnP and 711 K for MnAs, respectively. Moreover, the excellent ferromagnetism and half-metallicity can be well preserved in few-layer MnP and MnAs. Based on DFT calculations combined with PSO algorithm, Jiao *et al.*[73] identified three new monolayer phases of iron arsenide with high stability. Specifically, monolayer FeAs-I and FeAs-III sheets crystallize in a tetragonal lattice with space group of P4/nmm, while 2D FeAs-II has a trigonal P-3*m*1 lattice. Among them, FeAs-I and FeAs-II are ferromagnetic metals, while FeAs-III is an antiferromagnetic semiconductor. FeAs-I and FeAs-III have Curie temperatures of 645 and 350 K, respectively, both of which are above room temperature. Importantly, their magnetic anisotropy energies of 645 and 820 μeV are comparable to the magnetic recording materials such as FeCo alloy (700∼800 μeV per atom).

6. Transition metal hydrides

Wu *et al.*[283] predicted a stable family of 2D transition metal dihydride MH_2 (M = Sc, Ti, V, Cr, Fe, Co, Ni) monolayers featuring pyramidal symmetry (C_{3v}). Among them, CoH_2 and ScH_2 monolayers are ferromagnetic metals, while the others are antiferromagnetic semiconductors. CoH_2 monolayer is a perfect half-metal with a wide spin gap of 3.48 eV and an above-room-temperature T_C of 339 K [Fig. 11(d)]. ScH_2 monolayer also possesses half-metallicity through hole doping. Notably, their half-metallicity can be well retained on some substrates such as Cu (111) surface, BN, MoS_2, and $MoSe_2$.

E. Ternary transition metal compounds

Ternary transition metal compounds of type M-X′-X″, where M is transition metal element, usually magnetic elements like Fe, Co, Ni, and X′/X″ is a nonmagnetic main group element from main groups IV, V, VI, or VII of the Periodic Table. These compounds exhibit a rich variety of compositions and diverse magnetic properties. Only recently, ternary transition chalcogenides and halides with common transition metal centered octahedral units have attracted attentions. Compared with the above discussed binary magnetic materials, ternary ones are composed of one type of metal cations and two kinds of non-metal elements. The fascinating magnetism still mainly stems from the cations. The metal atoms occupy different crystallographic sites and form distinct magnetic sublattices, while the addition of two kinds of non-metal elements provides sufficient flexibility to tune the structure and magnetic properties. For example, 2D $CrXTe_3$ systems (X = Si, Ge, Sn) have a layered structure with $CrTe_6$ octahedra forming a honeycomb lattice and are typically FM semiconductor. However, 2D $CrXTe_3$ for X = Sb and Ga as AFM semiconductors exhibit a pseudo-one-dimensional crystalline structure, in which $CrTe_6$ octahedra form an infinite, edge-sharing, and double rutile chain.[284] So far, the ongoing researches in identifying the 2D ternary vdW magnets include CrGe(Si, Sn)Te_3, FeGe(Si)Te_3, $MnBi_2Te_4$, MPS_3, transition oxyhalides, transition nitrohalides, and CrSI. In Secs. III E 1 through III E 5, we will review their important experimental and theoretical progress.

1. $CrXTe_3$ (X = Si, Ge, Sn)

The strong coupling between magnetic and lattice degrees of freedom was verified by Raman spectroscopy in ternary $CrGeTe_3$ and infrared spectroscopy in $CrSiTe_3$, respectively.[49,285] Actually, $CrGeTe_3$ is the first reported 2D ternary ferromagnetic material. As a representative of layered vdW materials, $Cr_2Ge_2Te_6$ has been mechanically exfoliated and the intrinsic long-range ferromagnetic ordering has persevered in bilayer $Cr_2Ge_2Te_6$, as revealed by scanning magneto-optic Kerr microscopy.[37] The optical image of the exfoliated $Cr_2Ge_2Te_6$ atomic layer is shown in Fig. 12(a). From Fig. 12(b), one can see that the long bilayer strip becomes clearly distinguishable at liquid helium temperature from the bare surrounding substrate. Figure 12(c) shows a monotonic decrease in Curie point with reducing thickness. The Curie temperature of bulk $Cr_2Ge_2Te_6$ is 68 K, and the bilayer value is about 30 K.[37] Subsequently, theoretical calculations have predicted that $Cr_2Ge_2Te_6$ is a semiconductor with a bandgap of 0.13 eV,[286] and 2D $Cr_2Ge_2Te_6$ possesses a magnetic moment of 2.4 μ_B per Cr atom with out-of-plane magnetic anisotropy.[99] Similar to its bulk counterpart, the magnetic behavior of $Cr_2Ge_2Te_6$ is well described by Heisenberg model, where spins can freely rotate and adopt any direction.[44] The mechanism of ferromagnetism in $Cr_2Ge_2Te_6$ structure is dominated by the superexchange interaction between half-filled Cr t_{2g} and empty e_g states via Te p orbitals.[286] The lengths of Cr–Cr bonds are too long to support strong antiferromagnetic coupling between direct Cr t_{2g} exchange interaction.[11]

Similar magnetic behavior also exists in ferromagnetic semiconductor $Cr_2Si_2Te_6$ due to the identical geometry, especially the same Te ligands. However, larger vdW interlayer gap and smaller in-plane Cr–Cr distance is presented in $Cr_2Si_2Te_6$ with regard to $Cr_2Ge_2Te_6$. In their bulk phase, the above two factors would weaken the T_C from 63 K for $Cr_2Ge_2Te_6$ to 32 K for $Cr_2Si_2Te_6$[287] and strength the magnetic anisotropy simultaneously. Neutron scattering measurements revealed that bulk $Cr_2Si_2Te_6$ is a strongly anisotropic 2D Ising-like ferromagnet.[109] The exfoliation of bulk $Cr_2Si_2Te_6$ to monolayer or few-layer 2D crystals and transfer onto Si/SiO_2 substrate have been achieved. Temperature-dependent resistivity measurements for the few-layer 2D $Cr_2Si_2Te_6$ FET devices observed a clear change in resistivity at 80∼120 K, which corresponds to the theoretically predicted T_C = 80 K.[62] The higher T_C in monolayer $Cr_2Si_2Te_6$ than $Cr_2Ge_2Te_6$ can be ascribed to the fact that intralayer Cr–Te–Cr superexchange interaction becomes dominant at the monolayer limit. Moreover, the ferromagnetic mechanism could be maintained when monolayer $Cr_2Si_2Te_6$ is described by the Heisenberg model.[288]

Using first-principles calculations with HSE06 functional, Zhuang *et al.*[289] predicted that single-layer $CrSnTe_3$ is also a ferromagnetic semiconductor. Moreover, the important magnetic parameters of $CrXTe_3$ (X = Si, Ge, Sn) have been comparatively analyzed within a unified framework. The estimated Curie temperature of $CrSnTe_3$ was 170 K, which is significantly higher than that of single-layer $CrSiTe_3$ (90 K) and $CrGeTe_3$ (130 K). Such enhancement is originated from the shorter Sn–Te bond length and stronger ionicity, which in turn increase the superexchange coupling between the magnetic Cr atoms. The corresponding exchange integral J parameters for $CrSnTe_3$, $CrSnTe_3$, and $CrSnTe_3$ are 3.92, 3.07, and 2.10 meV, respectively. Considerable magnitude of MAE was also obtained in these three $CrXTe_3$ systems. The calculated MAE values ranged from 69 to 419 μeV/f.u., whereas z axis is the easy direction for the magnetization in $CrXTe_3$ family.[289]

In 2017, an in-depth DFT survey with vdW-D2 correction on the magnetic phases of single-layer transition metal trichalcogenide ternary compounds (MAX_3) with a total of 54 compositions was performed, covering 3d transition metals (M = V, Cr, Mn, Fe, Co, Ni), main group IV elements (A = Si, Ge, Sn), and chalcogen elements (X = S, Se, Te).[290] Besides the reported FM $CrXTe_3$, their results indicated that a variety of magnetic ground states, including AFM phases in Néel, stripy, and zigzag configurations, as well as FM configurations, may exist depending on material composition. Among them, 2D $MnSiSe_3$ and $MnGeSe_3$ are highly anticipated, since their Curie temperatures from DFT-D2+U calculations are 345.4 and 310.1 K, respectively. Recently, You *et al.*[291] proposed three stable 2D ferromagnetic semiconductors $TcSiTe_3$, $TcGeSe_3$, and $TcGeTe_3$, with T_C of 538, 212, and 187 K, respectively, which were given by MC simulations. All of them have a spin moment of about 2 μ_B and an extraordinarily large orbital moment of about 0.5 μ_B per Tc atom. In addition, large MAE (26.5∼42.5 meV), high Kerr rotation angle (3.6°), and anomalous Hall conductivity have also been found. Replacing Si/Ge/Sn by Ga atom, $CrGaTe_3$ monolayer is an intrinsic ferromagnetic semiconductor with an indirect bandgap of 0.3 eV. Its Curie temperature estimated by Monte Carlo simulations was 71 K.[292]

2. MPX_3 (X = S, Se, Te)

Next, we discuss another series of ternary single-layer compounds MPX_3, which are structurally closely related to the above discussed transition metal trichalcogenide cousins MAX_3. The top and side view of 2D MPX_3 are shown in Fig. 12(d). In detail, each unit cell of MPS_3 is composed of two cations and one $[P_2S_6]^{4-}$ cluster. The M atoms are coordinated with six S atoms, while the P atoms are coordinated with three S atoms and one P atom to form a $[P_2S_6]^{4-}$ skeleton, which is arranged in a 2D honeycomb structure.[28] The main difference between MPX_3 and MAX_3 compounds is that the main group IV atom (A = Si, Ge, Sn) inside the $(A_2X_6)^{6-}$ bipyramids are replaced by the main group V element (P) inside the $(P_2X_6)^{4-}$ skeleton. The change from group IV element to group V element is responsible for the significant modifications in electronic structures and especially magnetic properties. Because of the surface S atoms, MPS_3 layers exhibit strong van der Waals character and can be easily exfoliated from the bulk phase. In 2015, Xiong *et al.*[293] first observed the mechanically fabricated 2D $FePSe_3$ and $MnPS_3$ sheets in the MPS_3 family, and finally they successfully obtained monolayer $FePS_3$. Soon after, bulk $NiPS_3$ and $MnPS_3$ materials were also mechanically exfoliated into 2D nanoflakes in the laboratory.[294,295] Therefore, it is natural to investigate their magnetic properties and those of the other stable MPS_3 systems at the monolayer limit. As a new catalogue of 2D vdW magnets, in the following we will discuss the details of magnetic properties of experimentally exfoliable $FePS_3$, $NiPS_3$, and $MnPS_3$, and recently predicted $CoPS_3$, $CrPS_3$, and $V_{0.9}PS_3$, and correlated the critical magnetic parameters with the number of layers.

Considering their $(P_2X_6)^{4-}$ skeleton, the metal cations in 2D MPS_3 have M^{2+} ionization states and are in their high-spin configurations. The Néel temperatures of 2D $FePS_3$, $NiPS_3$, and $MnPS_3$ were extracted from Raman spectroscopy, which is a common means to probe the spin properties. In principle, the appearance of two-magnon

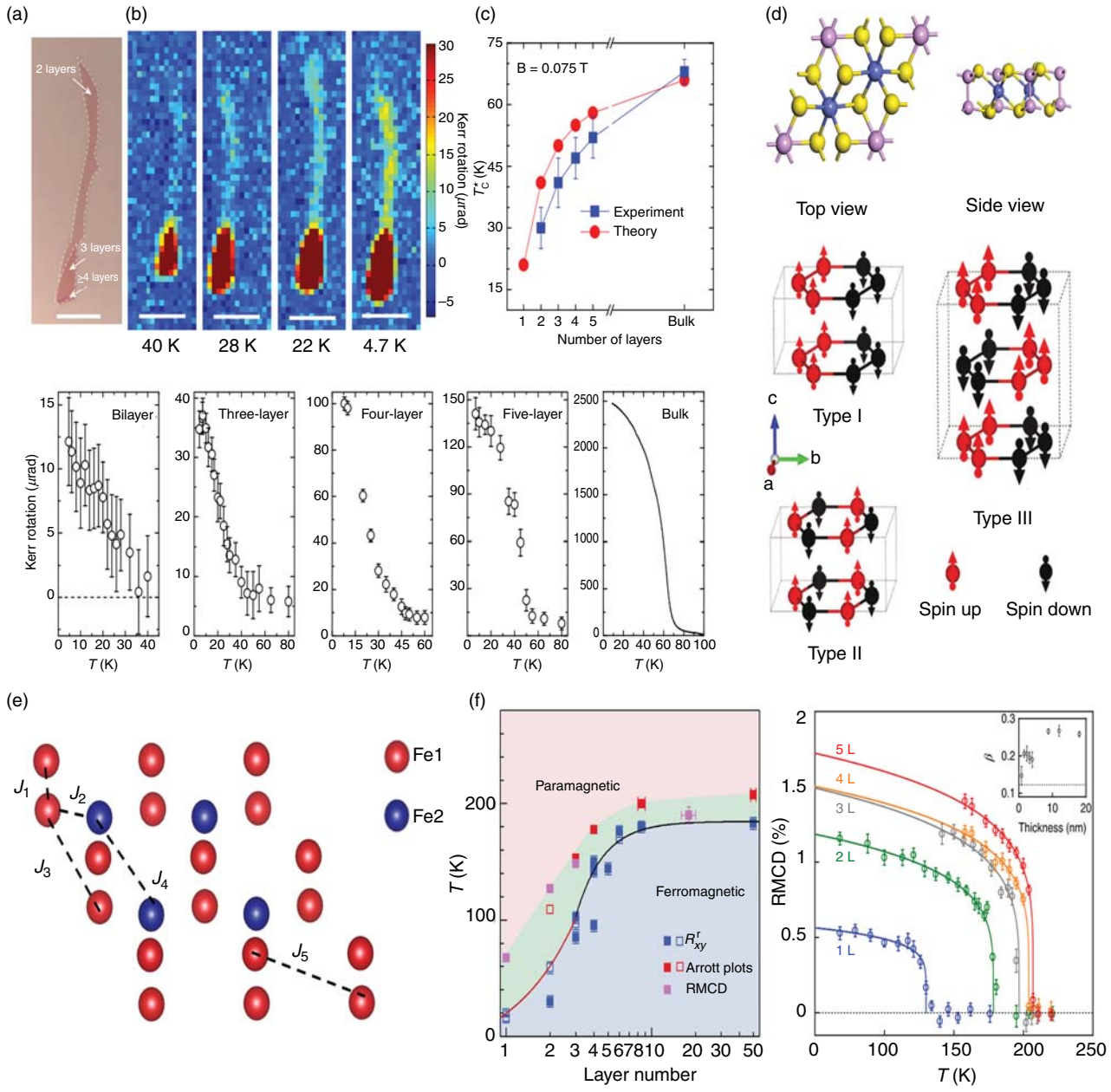

FIG. 12. (a) Optical image of exfoliated $Cr_2Ge_2Te_6$ atomic layer. (b) Kerr rotation signal under different temperatures. (c) Temperature-dependent Kerr rotation intensity of 2∼5 layer and bulk samples under a 0.075 T field. (d) The atomic models and schematic diagram of three magnetic structures of MPS_3. Type I, type II, and type III are for $NiPS_3$, $MnPS_3$, and $FePS_3$, respectively. (e) The schematic diagram of exchange coupling in Fe_3GeTe_2. (f) The measured T_C in Fe_3GeTe_2 with different thickness. The left one uses three measures with Remanent anomalous Hall resistance R_{xy}^r Arrott plots and RMCD, and the right one only chooses the RMCD measure. Panels (a)–(c) reproduced with permission from Gong *et al.*, Nature **546**, 265 (2017). Copyright 2017 Springer Nature.[37] Panel (d) reproduced with permission from Wang *et al.*, Adv. Funct. Mater. **28**, 1802151 (2018). Copyright 2018 John Wiley and Sons.[297] Panel (f) left reproduced with permission from Deng *et al.*, Nature **563**, 94 (2018). Copyright 2018 Springer Nature.[50] Panel (f) right reproduced with permission from Fei *et al.*, Nat. Mater. **17**, 778 (2018). Copyright 2018 Springer Nature.[41]

scattering and the change in Raman peak positions or intensities suggest ordered spin states.[48] All the three MPS_3 monolayers were predicted to be semiconductors with localized magnetic moments of 1∼4 μ_B and long-range antiferromagnetic ordering.[296] The electronic structures are greatly affected by metal and chalcogenide atoms, with bandgaps in range of 0.12 to 1.33 eV from PBE calculations.[107] The AFM ground state is governed by the competition between direct M–M exchange and indirect M–S–M superexchange interactions

within atomic layers, as well as interlayer exchange interactions.[112] Meanwhile, different metal atoms induce different distributions of magnetic moments and magnetic coupling—$FePS_3$ of Ising-type, $NiPS_3$ of XXZ type, and $MnPS_3$ of Heisenberg-type[297] [Fig. 12(d)].

Two-dimensional $FePS_3$ with a honeycomb lattice and that behaves as a large spin Mott insulator is an Ising-type antiferromagnetic material with Néel temperature of about 120 K.[298] Owing to the absence of long-range superexchange interaction between the Fe atoms from adjacent layers, multilayer $FePS_3$ systems do not show stronger magnetic exchange interaction. As a consequence, T_N decreases from 117 K in bulk to 104 K in monolayer $FePS_3$. Fortunately, the Ising-type magnetic ordering of $FePS_3$ is preserved down to the monolayer limit, which is demonstrated by the emergence of a series of new Raman modes pointing to antiferromagnetic ordering.[38] As 2D Ising magnets, the magnetic ordering is mainly dominated by the in-plane third nearest-neighboring Fe–Fe exchange interaction in 2D $FePS_3$, and the spins are aligned along the out-of-plane direction with MAE of 3.7 meV.[299] The intralayer spin moments are arranged ferromagnetically in each chain but coupled antiferromagnetically with their neighboring chains, and the neighboring planes are also coupled antiferromagnetically along the out-of-plane direction.[48]

The second member in the 2D MPS_3 family is 2D $MnPS_3$. Kim *et al.*[39] discovered a unique feature of Raman spectrum that correlates well with the stable antiferromagnetic ordering at the bilayer limit of $MnPS_3$. Its T_N could maintain at 78 K from bulk phase to five-layer system. The independence of number of layers stems from the weak interlayer coupling in $MnPS_3$. In the antiferromagnetic state of $MnPS_3$, each Mn atom is antiferromagnetically coupled with three nearest neighbors within the basal plane. The direction of spin moments is ∼8° along *c* axis, and there exists ferromagnetic coupling between the planes. By exploiting the spin-flop transition, Long *et al.* have shown that the magnetoresistance persists as thickness is reduced. The characteristic temperature and scale of magnetic field are nearly unchanged, albeit with a different dependence on magnetic field, indicating again the persistence of magnetism at the ultimate limit of individual monolayer.[300] Fascinatingly, $MnPS_3$ exhibits three spin-related critical transitions, including 2D single-ion anisotropy antiferromagnetic phase transition at 120 K, paramagnetic-antiferromagnetic transition at 80 K, and XY-like behavior at 55 K.[295] In addition, long-distance magnon transport was also detected in $MnPS_3$ crystal as antiferromagnet.[301] The antiferromagnetic transition at Néel temperature of around 78 K in few-layered $MnPS_3$ is completely suppressed by Mn vacancy, which leads to a lower magnetic transition temperature of 38 K.[302] Moreover, long-range magnon transport over several micrometers in the 2D antiferromagnet $MnPS_3$ has been observed experimentally.[301]

$NiPS_3$ is the third member of 2D MPS_3 family. In $NiPS_3$, eight *d* electrons from Ni atom occupy the split 3*d* shell under octahedral crystal field. The t_{2g} orbitals are fully occupied and two e_g orbitals are half filled. Combined with its honeycomb lattice, Gu *et al.*[303] suggested that 2D $NiPS_3$ is a Dirac material with strong electron-electron correlation. The unpaired electrons in the two e_g orbitals would "long-range" hop between two third nearest-neighboring Ni sites in the Ni honeycomb lattice via superexchange interaction. Similar to 2D $FePS_3$ and $MnPS_3$, both DFT calculations[296] and experimental measurements[40] suggested that the Ni honeycomb lattice forms zigzag antiferromagnetic insulating ground state, which is featured by AFM coupling between the double parallel ferromagnetic chains, while the planes are ferromagnetically coupled along the out-of-plane direction.[112] Unlike 2D $FePS_3$ and $MnPS_3$, on the one hand, the single-ion anisotropy of $NiPS_3$ would change from XY type to XXZ type as the number of layers decreases.[304] On the other hand, the antiferromagnetic ordering persists down to biayer $NiPS_3$, and its T_N is about 130 K. However, the antiferromagnetic ordering is drastically suppressed in the monolayer, indicating that intralayer exchange interactions are much stronger than the interlayer ones. Such variation could be understood by the strong spin fluctuations, which drastically suppress the bulk antiferromagnetic ordering.[304]

With the aid of DFT calculations, the metal element M in 2D MPX_3 family has been further extended to 3*d*/4*d*/5*d* transition metals and the non-metal X element extended to S, Se, and Te. Hence, a series of stable trichalcogenides were predicted. Due to weak interlayer coupling, parts of them are exfoliable 2D magnetic materials. For example, Chittari *et al.*[296] have systemically investigated the magnetic properties of 2D MPX_3 (M = V, Cr, Mn, Fe, Co, Ni, Cu, Zn; X = S, Se, Te). They concluded that the ground-state spin configuration depends on the combination of transition metal and chalcogen elements. Besides the reported Mn-, Fe-, and Ni-based 2D MPS_3 antiferromagnetic semiconductors, V-based compounds also exhibit semiconducting Néel antiferromagnetic states. Interestingly, isostructural Mott transition was observed in VPS_3.[305] When M changes from the strongly correlated 3*d* transition metals to the weakly correlated 4*d* and 5*d* elements, the ground state would transform from FM to PM. In the case of 4*d* $PdPS_3$, the lowest-energy state is still AFM,[306] while 2D $PtPS_3$ with 5*d* element is PM. Both Pt and Pd possess half-filled e_g orbitals; thus, they may also exhibit multiple Dirac cones at the same time. Moreover, replacing a smaller chalcogen atom (S) with a larger chalcogen atom (Se or Te) reduces the energy bandgap as well as the energy difference between FM and AFM states.[107,296,307]

3. Fe-Ge-Te ternary compounds

Previously mentioned 2D ternary compounds are ferromagnetic/antiferromagnetic semiconductors, while the series of Fe-Ge-Te (FGT) ternary compounds are ferromagnetic metals with significant uniaxial magnetocrystaline anisotropy. As a unique kind of itinerant ferromagnetic metals, the exchange mechanism in FGT can be described by Stoner model, whose exchange splitting is induced by Coulomb repulsion among itinerant electrons.[308] In addition, the itinerant ferromagnetism could be understood by mapping a classical Heisenberg model with RKKY exchange interaction.[309] Advantageously, the metallic nature enables the interplay of both spin and lattice degrees of freedom, which is the heart of various spintronic architectures.[310]

The most widely studied 2D FGT materials is Fe_3GeTe_2. Bulk Fe_3GeTe_2 crystal is a layered material with vdW gap of 2.95 Å. In a pioneer study in 2016, Zhuang *et al.* predicted that mechanical exfoliated single-layer Fe_3GeTe_2 exhibited strong out-plane magnetocrystalline anisotropy with MAE of 0.92 meV.[16] Very soon, this proposal was confirmed by Chu *et al.*, who successfully fabricated few-layered flakes of Fe_3GeTe_2 by cleaving Fe_3GeTe_2 crystal onto a gold film. The RMCD measurement probed the T_C values to be 180 and 130 K for bilayer and monolayer Fe_3GeTe_2, respectively. In addition, it was stated that monolayer Fe_3GeTe_2 with large out-of-plane anisotropy is

a truly 2D itinerant ferromagnet.[41] Subsequently, Zhang *et al.* used Al_2O_3-addisted exfoliation method instead of conventional mechanical exfoliation to protect the intralayer bonding. The Curie temperature of monolayer Fe_3GeTe_2 was determined to be 30 K by probing Remanent anomalous Hall resistance and 68 K by RMCD measurement, respectively. Moreover, a definite out-of-plane magnetocrystalline anisotropy energy of 2 meV was found, which is large enough to protect the magnetic ordering below a finite T_C.[50] This series of works opens a new era in the development of high-temperature 2D magnets.

Different from many other 2D magnets, Fe_3GeTe_2 exhibits two values of on-site spin moment because the Fe atoms occupy two different lattice sites, labeled as Fe_1 and Fe_2. The magnetic moment of Fe_1^{3+} is about 1.7 μ_B and that of Fe_2^{2+} is about 1 μ_B. The Stoner criterion states that formation of ferromagnetic ordering is dictated by density of states at the Fermi level. In turn, the half-filled *d* orbitals of Fe mainly affect the ferromagnetism in Fe_3GeTe_2. As shown in Fig. 12(e), the magnetic coupling parameters for interlayer Fe_1-Fe_1 coupling and Fe_1-Fe_2 coupling are 23.48 meV and 20.41 meV, respectively, which collaborate to determine the ferromagnetism in Fe_3GeTe_2. That is to say, the ferromagnetism in Fe_3GeTe_2 is dominated by the coupling between perpendicular Fe atoms. As it is known, the distance between adjacent Fe_3GeTe_2 layers also plays a crucial role in modulating the magnetic interactions. Wang *et al.* substantiated that the effective coupling becomes negligible when interlayer distance is increased by 1 Å in bilayer Fe_3GeTe_2.[311] Furthermore, Hwang *et al.* found that formation of oxide at the interface of Fe_3GeTe_2 induces antiferromagnetic coupling between pristine Fe_3GeTe_2 layer and oxidized Fe_3GeTe_2 layer in a bilayer system. The interlayer distance is too large to generate direct Fe-Fe coupling. Therefore, magnetic information between adjacent layers can only be mediated by the indirect interaction between oxygen *p* orbitals.[312]

As a kind of vdW ferromagnets, the effect of number of layers is clearly manifested in Fe_3GeTe_2. As shown in Fig. 12(f), T_C of Fe_3GeTe_2 closely depends on the thickness of flakes. As the number of layers decreases to 7, a dramatic drop of T_C would occur.[41,50] Experimental observation confirmed that T_C decreases monotonically with decreasing number of layers, while the strong perpendicular magnetic anisotropy is retained. The difference of the probed T_C might come from different environments of Fe_3GeTe_2 during experimental synthesis.[313,314] Han *et al.* deposited Fe_3GeTe_2 flakes onto three types of substrates—Al, Au, and SiO_2. The change of substrate from Al to Au could elevate the value of T_C significantly from 105 to 180 K for Fe_3GeTe_2 film of 10 nm thickness. Such big modulation of T_C by substrates could be attributed to lattice distortion and charge redistribution between the Fe_3GeTe_2 sample and the substrate.[313] Recently, Kim *et al.* successful synthesized and exfoliated Fe_4GeTe_2 flakes and obtained T_C of about 270 K for 7-layer Fe_4GeTe_2.[314]

Fe_5GeTe_2 has a similar structure with Fe_3GeTe_2, which is also made up of 2D slabs of Fe and Ge between layers of Te, but with two additional layers of Fe atoms. The magnetic state in Fe_5GeTe_2 is even more complicated than Fe_3GeTe_2 due to structural disorder and presence of short-range order associated with the occupation of split sites. May *et al.* exfoliated Fe_5GeTe_2 nanoflakes (12 nm/4 unit-cell layers) on SiO_2 substrates and determined T_C to be in range of 270 to 300 K. The magnetic moment of Fe_5GeTe_2 along the out-of-plane is 0.8∼2.6 μ_B per Fe atom on different Fe sites.[42] In contrast to Fe_3GeTe_2, however, bulk Fe_5GeTe_2 crystal does not exhibit a perpendicular magnetic anisotropy. Recently, Joe *et al.* predicted that both monolayer and bilayer Fe_5GeTe_2 systems remain metallic and ferromagnetic. The ferromagnetism originates from Fe atoms and the splitting of *d* orbitals occurs for both spin-up and spin-down states, presenting exchange splitting to satisfy Stoner's theory of ferromagnetism.[143] In addition, Zhang *et al.* reported that $Fe_{5-x}GeTe_2$ shows glassy cluster behavior below 110 K and revealed a transition from ferromagnet to ferrimagnet at 275 K. Meanwhile, they observed that the Fe-Ge-Te crystal with more Fe contents favors an in-plane easy magnetization at all temperatures up to T_C.[315]

Compared to 2D MPX_3 family, 2D MPX_4 sheets show different electron configuration formally with $M^{3+}[PX_4]^{3-}$. In the monolayer structure of MPS_4, six S atoms form a slightly distorted octahedron encapsulated with a transition atom (M) in the center. Meanwhile, the P atoms are in the center of tetrahedron consisting of four S atoms, suggesting a distinct magnetic ordering. Experimentally, single- and few-layered $CrPS_4$ sheets were mechanically isolated in 2016.[316] Further DFT calculations revealed that monolayer $CrPS_4$ is a ferromagnetic semiconductor, which is quite different from the antiferromagnetic ordering of its bulk form.[317] Later, Chen *et al.*[95] systematically discussed the magnetic ordering in monolayer MPS_4 and proposed that VPS_4, $MnPS_4$, and $NiPS_4$ prefer antiferromagnetic states while $CrPS_4$ and $FePS_4$ are ferromagnetic. The calculated T_C was 50 K for $CrPS_4$.[95] From their first-principles calculations, it was unveiled that V, Cr, Mn, Fe, and Ni in $TMPS_4$ monolayers carries local moment of 1.8, 2.9, 3.6, 0.9, and 0.5 μ_B, respectively. Indeed, Fe, Co, and Ni atoms in $TMPS_4$ are in the low-spin configuration because of the relatively strong field ligands, while V, Mn, and Cr atoms adopt the high-spin configurations. After replacing Cr (P) by Mn (As) atoms, the magnetic properties of single-layer $MnAsS_4$ have also been investigated.[318] The half-metallic spin gap for monolayer $MnAsS_4$ is about 1.46 eV, and it has a large spin splitting energy of about 0.49 eV in the conduction band. MC simulations predicted a rather high T_C of about 740 K.

4. $MnBi_2Te_4$ and $CoGa_2X_4$ (X = S, Se, or Te)

An emerging family of intrinsic magnets with tetrachalcogenides is also found on a 2D triangular lattice, i.e., $MnBi_2Te_4$ and $CoGa_2X_4$ (X = S, Se, Te). Based on DFT calculations, Li *et al.*[14] predicted a series of novel magnetic materials from $MnBi_2Te_4$ related ternary chalcogenides MB_2T_4, where M is transition metal or rare earth metal; B is Bi or Sb; and T is Te, Se, or S [Fig. 13(a)]. In these materials, the intralayer exchange coupling is ferromagnetic, giving rise to 2D ferromagnetism in the monolayer. By carefully controlling the film thickness and external magnetic fields, many interesting topological quantum states can be induced in $MnBi_2Te_4$ monolayer [Fig. 13(b)], including QAH insulators, axion insulators, and quantum spin Hall insulators. Intriguingly, magnetic and topological states are well combined in $MnBi_2Te_4$, where Mn atom introduces magnetism and Bi–Te layers could generate topological properties. The schematic mechanism is depicted in Fig. 13(c). The monolayer $MnBi_2Te_4$ is a topologically trivial FM insulator with a direct bandgap of 0.70 eV [Fig. 13(d)]. Moreover, the magnetic and topological transitions in $MnBi_2Te_4$ are thickness dependent.[319] The $MnBi_2Te_4$ systems with odd numbers of building blocks are uncompensated interlayer antiferromagnets, while those with even numbers of building blocks are compensated

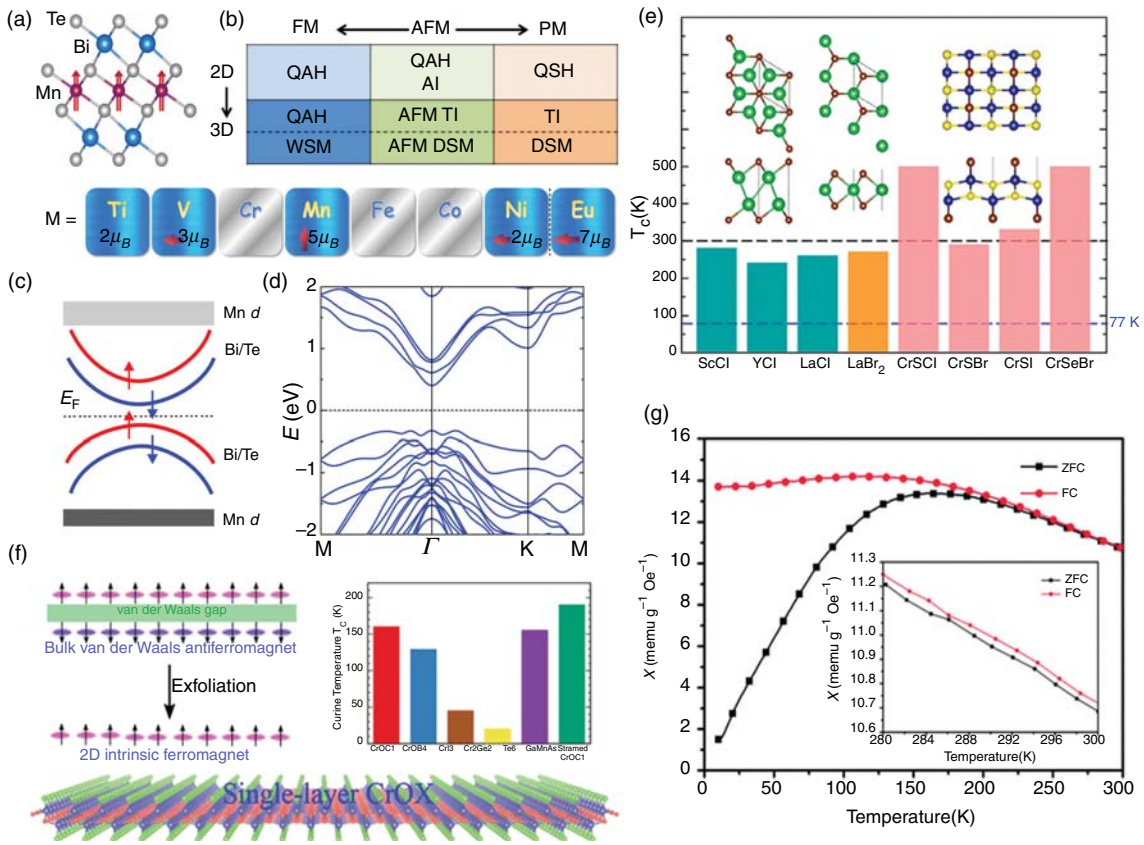

FIG. 13. (a) Monolayer $MnBi_2Te_4$ with FM configurations. (b) Various topological quantum states in MB_2T_4. (c) Schematic diagram of band magnetism and topology. (d) Band structure of monolayer $MnBi_2Te_4$. (e) Curie temperatures of eight MXY 2D ferromagnets, including ScCl, YCl, LaCl, $LaBr_2$, CrSCl, CrSBr, CrSI, and CrSeBr. (f) Exfoliation mechanism of 2D FM sheet from 3D vdW AFM crystal and the Curie temperatures of CrOCl, CrOBr, and strained CrOCl. (g) Temperature dependence of zero-field-cooled (ZFC) and field-cooled (FC) curves for magnetization of the as-synthesized δ-FeOOH ultrathin nanosheets. Inset: the magnified part of ZFC and FC curves in temperature range from 280 to 300 K. Panels (a)–(d) reproduced with permission from Li *et al.*, Sci. Adv. **5**, eaaw5685 (2019). Copyright 2019 American Association for the Advancement of Science.[14] Panel (e) reproduced with permission from Jiang *et al.*, ACS Appl. Mater. Inter. **10**, 39032 (2018). Copyright 2018 American Chemical Society.[65] Panel (f) reproduced with permission from Miao *et al.*, J. Am. Chem. Soc. **140**, 2417 (2018). Copyright 2018 American Chemical Society.[322] Panel (g) reproduced with permission from Chen *et al.*, Chem. Sci. **5**, 2251 (2014). Copyright 2014 Royal Society of Chemistry.[325]

interlayer antiferromagnets. Thickness dependent wide-band-gap quantum anomalous Hall and zero plateau quantum anomalous Hall states are observed. Li *et al.*[320] further analyzed its magnetic anisotropy and found that the magnetic anisotropy comes mainly from single ion anisotropy, which is caused by the SOC effect of Mn and Te atoms. The exchange interaction in the monolayer $MnBi_2Te_4$ is nearly isotropic, which has no contribution to the magnetic anisotropy. Thus, the Curie temperature was estimated to be about 20 K.

Two-dimensional half-metallic ferromagnets, $CoGa_2X_4$ (X = S, Se, Te), are also found to be stable against spin flipping at room temperature. Its robust HM ferromagnetism originates from the superexchange interaction of Co-X–Co bonds with bond angles close to 90°. The calculations of magnetic anisotropy with inclusion of SOC indicated that $CoGa_2X_4$ systems have easy plane magnetizations, which are expected to have Berezinsky-Kosterlitz-Thouless transitions following the classical 2D XY model.[96] Other 2D magnets in ternary sulfides with two nonmetal elements are also observed for single-layer pentagonal CoAsS[321] and CrP_2S_7.[66]

5. MXY-type compounds

A class of 2D magnetic materials, MXY (M = transition metal; X = O, S, Se, Te, N; Y = Cl, Br, I) will crystalize in an orthorhombic structure with *Pmmn* space group, which consists of M_2X_2 layers sandwiched by halogen atoms. The transition metal M atoms are in the center of distorted octahedron (D_{2h} symmetry) and bound with X and Y atoms.

In H phase, five *d* orbitals split into three groups, i.e., $d_{xy}/_{yz}$, $d_{x2\text{-}y2}/_{xy}$, and d_{z2} under trigonal prismatic ligand field. In T phase, the *d* orbitals can be divided into t_{2g} (d_{xy}, d_{yz}, d_{xz}) and e_g ($d_{x2\text{-}y2}$, d_{z2}) orbitals under octahedral ligand field. In D_{2h} phase of MX_2, the degenerated *d* orbitals further split owing to the reduction of symmetry. As observed in MoS_2 monolayer with D_{2h} symmetry, it induces two spin-polarized electrons occupying d_{xy} and d_{z2}, leaving d_{xz} state unoccupied. Obviously, moderate splitting between the occupied and the unoccupied *d* orbitals brings out a relatively small gap of 0.21 eV in D_{2h} symmetry instead of a severe splitting of ∼1.0 eV in semiconducting H

phase. As a result of such electronic structure, the magnetic moment per Mo atom reaches 2.0 μ_B at high-spin state ($S = 1$).

Chromium sulfide halides Cr-X-Y (X = S, Se, Te; Y = Cl, Br, I) with chemical composition from transition metal dichalcohalides to di-halides have been theoretically predicted. Similar to transition metal di-halides discussed in Sec. III A 2, monolayer Cr-X-Y systems are ferromagnetic semiconductors, having large spin polarization and high Curie temperature of 100∼500 K. Based on 1825 easily or potentially exfoliable compounds from high-throughput search of the crystalline materials database, 36 monolayer 2D ferromagnets have been identified.[67] Among them, a noticeable system is CrSBr monolayer. By carefully examining its magnetic behavior, Jiang *et al.*[65] demonstrated that 2D CrSBr is a semiconductor possessing a large magnetic moment of ∼3 μ_B per Cr atom and a high Curie temperature ($T_C = 290$ K). The robust ferromagnetism of the CrSBr monolayer has been ascribed to the halogen-mediated (Cr−Br−Cr) and chalcogen-mediated (Cr−S−Cr) superexchange interactions. Based on that mechanism, they further proposed an isoelectronic substitution strategy to tailor the magnetic coupling strength. Finally, CrSI, CrSCl, and CrSeBr were also predicted as stable FM semiconductors with appreciable Curie temperatures of 330, 500, and 500 K, respectively [see Fig. 13(e)].[65] Several other theoretical studies also found that CrTX (T = S, Se, Te; X = Cl, Br, I) monolayers are FM semiconductors.[26,70,131] Besides high Curie temperature (100∼500 K), large perpendicular magnetic anisotropy, wide range of bandgaps, high carrier mobilities, strong anisotropy of carrier effective mass, and large light absorption are also found in these materials, suggesting that this 2D family holds potential for high performance electronic and spintronic devices. From a material database containing around 560 monolayer compounds of MXY (M = metal; X = S, Se, Te; Y = F, Cl, Br, I), 46 potential magnetic semiconductors have been further identified from HSE06 calculations.[132] Among them, Curie temperatures of the newly reported TiTeI, VSI, VSeI, MoSI, WSeI, WTeI monolayers are 46, 1100, 913, 270, 76, 302, and 479 K, respectively.

Starting from 3D AFM transition metal oxyhalides, Miao *et al.*[322] proposed that the 2D CrOCl and CrOBr monolayers can be obtained by mechanical cleavage and further predicted that they are intrinsic ferromagnetic semiconductors with bandgaps of 2.38 and 1.59 eV as well as Curie temperatures of 160 and 129 K [Fig. 13(f)], respectively. Calculated with the same method, the T_C of CrOF sheet may even exceed those of CrOCl and CrOBr and reach up to ∼200 K.[323] The spins in both CrOCl and CrOBr monolayers align along the out-of-plane direction with considerably large MAE (0.03∼0.29 meV). These results have motivated some successive investigations on the magnetic properties of transition metal oxyhalides MOX (X = Cl, Br, I). All these FeOX (X = F, Cl, Br, I) monolayers are theoretically stable and could be exfoliated from their bulk phase.[133] These FeOX monolayers are revealed to be Mott insulators with bandgaps from 2.73 to 0.48 eV as element X changes from F to I. For all FeOX monolayers, the in-plane and inter-plane magnetic interactions between Fe atoms are dominated by AFM coupling. The Néel temperatures of FeOF and FeOI monolayers are 130 and 150 K, respectively. In addition, 2D VBrO, TiClO, VClO were predicted to be FM half-metals,[132] while 2D VOF was a FM semiconductor.[66]

Similar to transition halides, the ground state of 2D δ-FeOOH monolayer is AFM with an indirect bandgap of 2.4 eV, which is derived from bulk $Fe(OH)_2$ via oxidation.[324] The δ-FeOOH ultrathin films with thicknesses of 1.1∼1.3 nm have been experimentally synthesized via a topochemical transformation process. These films exhibit room-temperature ferromagnetism along with semiconducting behavior.[325] Besides the 2D ternary sulfide halides and oxyhalides, intrinsic magnets have also been observed in nitride halides, such as FeNF, MnNF, MnNCl, and MnNBr,[26,132] and the corresponding Curie temperatures are 398, 238, 261, and 492 K, respectively.

Since the 3D AMnBi family (A = K, Rb, Cs) with layered structure have strong AFM coupling between the Mn layers and weak interlayer coupling, AFM ordering is also anticipated at their 2D limit.[326] According to DFT calculations, AFM state is indeed favored for all of the 2D KMnBi, RbMnBi, and CsMnBi as the ground state. The strong Coulomb interaction arising from *d* orbitals of Mn atom results in their magnetic state. The easy magnetic axis is along the z direction with MAE values of 0.86∼1.1 meV. The Néel temperature is about 302–307 K, which is higher than that of the value of 2D $FePS_3$ (118 K). Moreover, the mobilities for both electron and hole carriers are in the order of 10^3 $cm^2/(V{\cdot}s)$, which is higher than 2D MoS_2 at room temperature.[327] Two-dimensional K_2CoS_2 is also an in-plane antiferromagnetic insulator,[328] and MC simulations predicted its transition temperature to be $T_N \approx 15$ K. Remarkably, bulk K_2CoS_2 also hosts an in-plane AFM state, and its magnetic ordering can persist even in ultrathin films down to monolayer limit.

F. 2D *f*-electron magnets

Up to now, most reported 2D magnets are based on d electrons. Generally speaking, d electrons are more localized and have stronger correlation effect than s and p electrons, which is the basic requirement of magnetic state. Compared to the d-electron based materials, *f* electrons are even more localized; thus, the direct overlap of *f* orbitals between neighboring rare earth atoms as well as the hybridization between *f* orbitals and *p* orbitals of neighbor anions, are mostly negligible. As a result, the direct exchange and superexchange interactions mediated by anions are usually very weak between rare earth magnetic anions, which is the most serious drawback for finding high-temperature *f* magnetism. However, the f-electron based 2D materials still have many advantages for future spintronic applications. Especially, f electrons usually have much stronger spin-orbit coupling than d electrons, which in turn leads to stronger magnetocrystalline anisotropy. Hence, it is still meaningful to design 2D *f*-electron magnets with high T_C. To this end, a few pioneer works have been reported.

In the 2D *f*-electron magnets, the most attractive element is gadolinium (Gd), which has half-filled and well-localized 4*f* subshell leading to ferromagnetic behavior with high saturation magnetization. Experimentally, Ormaza *et al.*[329] reported that single-layer $GdAg_2$ grown on Ag(111) is ferromagnetic with a Curie temperature of 85 K [Fig. 14(a)]. All the bands are spin-polarized owing to the presence of half-filled Gd 4*f* orbitals. The exchange interaction between Gd atoms is mediated by *s*, *p*–*d* Ag–Gd hybrid bands, similar as the effective *s*–*d* hybrid bands in pure Gd solid.[329,330] Twofold degenerate Weyl nodal lines in a 2D single-layer Gd-Ag compound were observed by combining angle-resolved photoemission spectroscopy measurements and theoretical calculations.[331] Lei *et al.*[332] demonstrated that $GdTe_3$ can be exfoliated to ultrathin flakes. The obtained monolayer $GdTe_3$ flake is an antiferromagnet, exhibiting a relatively high carrier mobility.

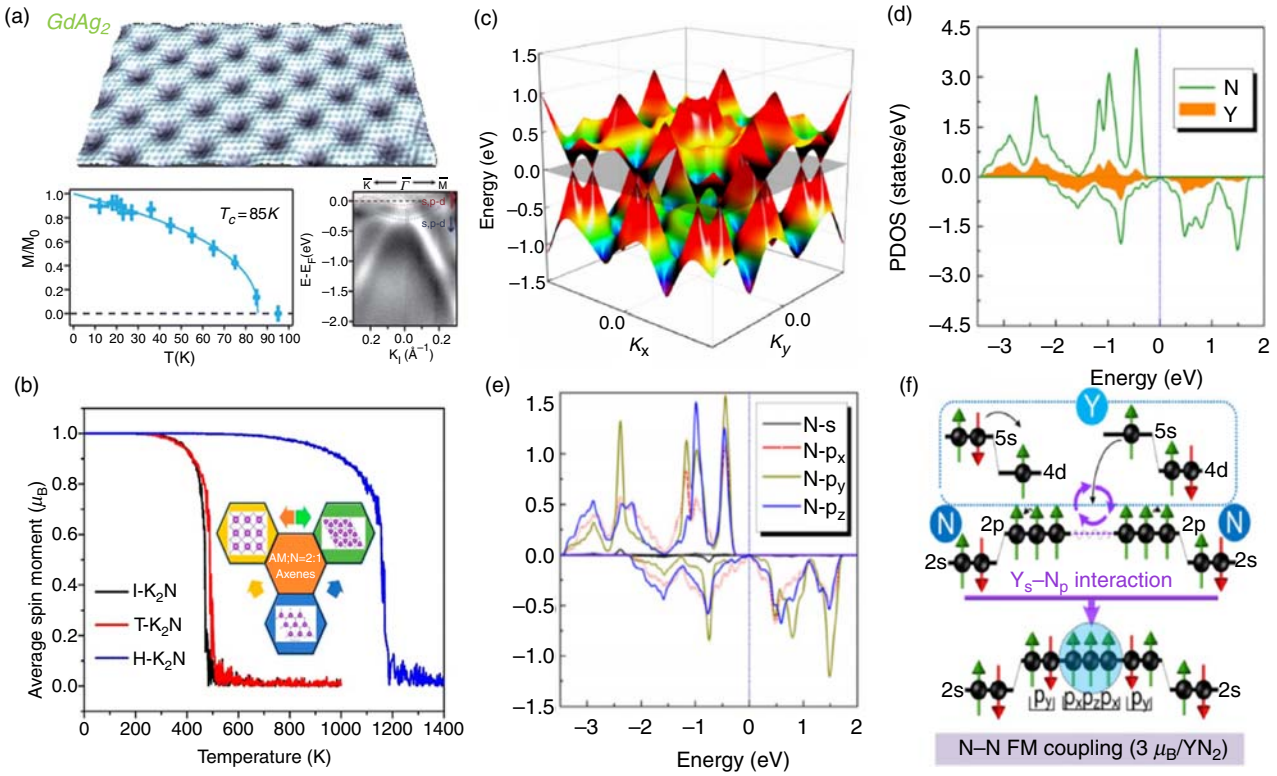

FIG. 14. (a) STM image, remanent magnetization at zero applied field, and angle-resolved photoemission of a $GdAg_2$ monolayer alloy. (b) Temperature-dependent spin moments of three different K_2N AXenes phases. (c) 3D band structure of the spin-down channel around the Fermi level. (d) PDOS of N and Y atoms for 1T-YN_2. (e) PDOS of *s* and *p* orbitals of N atom for 1T-YN_2. (f) Schematic diagram for the origin of magnetic moment of 1T-YN_2 monolayer. Panel (a) reproduced with permission from Ormaza *et al.*, Nano Lett. **16**, 4230 (2016). Copyright 2016 American Chemical Society.[329] Panel (b) reproduced with permission from Jiang *et al.*, J. Phys. Chem. Lett. **10**, 7753 (2019). Copyright 2019 American Chemical Society.[341] Panels (c)–(f) reproduced with permission from Liu *et al.*, Nano Res. **10**, 1972 (2017). Copyright 2017 Springer Nature.[6]

Rare earth metal functionalized silicene MSi_2 (M = Eu, Gd) were successfully synthesized by the reaction of M with Si(111) substrate using MBE technique. Strong magnetic response of transport was reported in $EuSi_2$ and $GdSi_2$ monolayers, suggesting indirect exchange interaction between localized *f*-shells of Eu/Gd and *p* orbitals of silicene. The extended p_z states of silicene can mediate the long-range magnetic interactions.[333] In addition, 4*f*-electron based $EuGe_2$ and $GdGe_2$[334] were also synthesized by direct reaction between these elements, with thickness from bulk down to monolayer. The common pattern is a transformation from 3D antiferromagnetism to 2D ferromagnetism, as revealed by magnetization and electron transport measurements.

Theoretically, high-temperature *f*-electron FM semiconductor has been found in GdI_2 monolayer.[129] The highly localized 4*f* electrons often lead to weak direct exchange and superexchange interactions. However, due to the coexistence of spin-polarized 5*d* orbitals and 4*f* orbitals in Gd^{2+} cation, the strong direct interaction between these two orbitals is found to determine the FM ground state of GdI_2 monolayer, whereas there still exists Gd 5*d*–I 5*p*–Gd 5*d* superexchange interaction. As a result, high T_C (241 K), large magnetization (8 μ_B/f.u.), and large magnetic anisotropy energy (0.553 meV/Gd) were observed in GdI_2 monolayer. According to a recent DFT study, Gd_2B_2 monolayer is a ferromagnetic metal, and its ferromagnetic state can sustain above room temperature as high as T_C = 550 K with a huge magnetic moment of $\mu = 7.30\ \mu_B$ per Gd atom.[335]

In addition to the 4*f* systems, Zhang *et al.*[336] firstly reported a potential 5*f*-electron 2D magnet, i.e., hexagonal UI_3 monolayer, using DFT calculations and MC simulations. Non-SOC calculations revealed that UI_3 monolayer is a Weyl semi-metal, while it becomes a semiconductor with a bandgap of 0.18 eV after inclusion of SOC effect. The projected density of states showed that the magnetism comes from *f* electrons of U atom. Noticeably, its exchange parameter and anisotropic energy are one order of magnitude larger than those of CrI_3 monolayer. Hence, the estimated Curie temperature was 110 K.[336]

G. 2D *p*-electron magnets

Among the 2D magnets discussed above, a common feature is that the high-spin states are guaranteed by the magnetic metal elements with partially filled 3*d* or 4*f* subshells. Apart from these conventional classes of 2D *d*/*f* ferromagnets, robust magnetic coupling has also been observed in many materials with partially occupied and localized/delocalized *p* orbitals, namely, *p*-electron magnets. Similar to *d* and *f* orbitals, the partially occupied *p* orbitals with certain localized character are mainly responsible for the magnetism. It is also explained

by the crystal symmetry protected flat bands model. Compared to the 2D *d*/*f*-electron magnets, *p* orbitals in the superexchange interaction are more delocalized, which is beneficial for the long-distance spin coupling. Thus, these 2D *p*-electron magnetic materials are likely to possess higher Fermi velocity and longer spin coherence length due to greater delocalization of *p* orbitals and smaller SOC strength, which are prominent advantages for high-speed and long-distance spin transport.

According to the origin of magnetism, 2D *p*-electron magnets can be divided into two categories—d^0 magnetism and d^n magnetism with paired spin-antiparallel *d* electron. Clearly, d^0 magnetism would be observed in many 2D materials without transition metal, rare earth, or actinide elements. First, these novel d^0 magnetism may originate from their hosting flat bands, which resulted in high density of states in the vicinity of the Fermi levels. Both theoretical and experimental studies proposed that zigzag graphene nanoribbons with localized edge states are room-temperature antiferromagnets.[337–339] The intrinsic magnetic ordering survives at room temperature in a novel B_5N_5 monolayer allotrope with decorated bounce lattice, which is also a 2D antiferromagnetic insulator. The antiferromagnetism arises from the nearly flat bands at the vicinity of the Fermi energy.[340]

Second, d^0 magnetism has been found in a few artificially designed 2D materials with nonstoichiometric compositions.[6,341] The periodic nonstoichiometric compound refers to the order compound with either cation deficient or electron deficient rather than the atomic defects, such as experimentally obtained 2D Na_2Cl and Na_3Cl[342] and theoretically predicted K_2N[341] and YN_2.[6] Such unconventional compounds may lead to long-range ordered unpaired *p* electrons in the magnetic lattice. By carefully considering the compositions and electronic configurations, a series of *p*-state intrinsic ferromagnetic A_2N compounds of alkali metal (A) and nitrogen (N), namely, AXenes, have been proposed.[341] Taking 2D K_2N as an example, all of the three predicted phases (H, T, and I) are half metals with high Curie temperature of 480∼1180 K [Fig. 14(b)]. As expected, the ferromagnetism in all three phases is mainly contributed by N atoms, with on-site moment of 0.81, 0.72, and 0.79 μ_B, respectively. Meanwhile, their high Curie temperatures arise from the coexistence of N–K–N superexchange and the carrier-mediated interaction mechanism. Very recently, Jin *et al.*[343] further found that K_2N monolayer with D_{3h} point group shows two nodal lines in its low-energy band structures, and these nodal lines are robust against weak SOC. Such feasible nonstoichiometric strategy has also attained long-range *p* electron magnetic ordering in 2D C_3Ca_2 and Na_2C with Honeycomb-Kagome lattice.[344,345] First-principles and tight-binding calculations revealed that both of them are intrinsic Dirac half-metals. Specifically, 2D C_3Ca_2 has a high-spin ferromagnetic configuration of 8 μ_B per unit cell with a Curie temperature of 30.7 K, which is mainly contributed by the 2*p* orbitals of carbon atoms. The mechanism of magnetism could be understood by the double exchange between carbon anions using Ca^{2+} cations as bridges. In a similar manner, ferromagnetism of 2D Na_2C is also mainly contributed by the unpaired 2*p* electrons of carbon with an estimated Curie temperature of 382 K. The origin of such 2*p* magnetism could be explained by the superexchange mechanism between C^{2-} anions with Na^+ cations as bridges. Indeed, the calculated Fermi velocities reach up to $\sim 10^5$ ms^{-1}, which are promising for high-speed spintronic devices.

Novel 2D *p*-electron magnets with paired *d* electrons that have antiparallel spin orientation have been reported in a few transition metal compounds, such as MoN_2, Y_2N, MoN_2, TcN_2, TaN_2, NbN_2, and $LaBr_2$. Using first-principles calculations, 1H-MoN_2 monolayer was theoretically proposed to be a 2D *p*-electron intrinsically FM material with a high Curie temperature of 420 K,[346] while it can be exfoliated experimentally.[347] Liu *et al.* found that 2D Y_2N with octahedral coordination is a novel *p*-state Dirac half metal,[6] as shown in Fig. 14(c). From the PDOS in Figs. 14(d) and 14(e), one can clearly see that N atoms instead of Y atoms contribute to the Dirac states. More interestingly, the half-metallic gap is 1.53 eV, the Fermi velocity is 3.74 $\times$ 10^5 m/s, and the Curie temperature estimated by mean-field approximation reaches over 332 K. Motivated by these studies, 2D *p*-electron intrinsic magnets have also been explored by first-principles computational search of thirty possible monolayer structures of transition metal dinitride. Among them, 1H-MoN_2 and 1H-TcN_2 are 2D *p*-state intrinsically ferromagnetic metals, while monolayer 1T-TaN_2 and 1T-NbN_2 are 2D *p*-state intrinsically ferromagnetic half-metals.[124,348] For all these materials, the robust FM ground state originates from the strong N–N direct exchange interaction.

Taking 1T-YN_2 monolayer as an example, we discuss the origin of paired *d* electrons and unpaired *p* electrons induced magnetism in Fig. 14(f).[6] The ground state electronic configurations of neutral Y and N atoms are $4d^15s^2$ and $3s^23p^3$, respectively. In YN_2 monolayer, one of the two 5*s* electrons in Y atom occupies 4*d* orbital of Y and the other one transfers to N-2*p* orbital, resulting in $4d^25s^0$ electronic configurations of Y^{2+} cation. Consequently, Y-4*d* orbitals are occupied by two spin-antiparallel electrons, exhibiting nearly zero magnetic moment. Meanwhile, 3*p* states of the two N atoms are occupied by a total of eleven 3*p* electrons via gaining one Y-5*s* electron. Following the eight-electron rule and assuming a nearly electron-free gas model, one can conclude that these eleven 3*p* electrons would exhibit an electronic shell configuration like: ↑↓ ↑↓ ↑↓ ↑↓ ↑ ↑ ↑. In other words, the three unpaired electrons would result in a magnetic moment of 3 μ_B per YN_2 formula unit, as obtained from spin-polarized DFT calculations.

H. 2D organic magnets

Apart from the rich family of 2D inorganic magnets, 2D organic magnetic materials have also attracted considerable attention due to their molecular diversity, flexibility in synthesis, easy processing, low cost, well-defined geometry, and potential applications in quantum Hall effect, magnetic storage, and spintronics. Research of the two fundamental physical concepts, i.e., exchange interaction and spin orbit coupling, represents the important branches of 2D organic magnets. Generally speaking, the magnetic properties of two conceptual classes of 2D organic materials have been discussed extensively in recent literature. One class of 2D organic materials is 2D metal organic frameworks (MOF), which is a kind of long-range network constructed by organic linkers and metal ion centers. The magnetism can be implemented by incorporating metal ions as the magnetic carriers. Another class of 2D organic magnets is covalent organic frameworks (COFs), which are formed by covalent bonding of the atoms of light elements (H, B, C, N and O). Without magnetic metal ions, the magnetism in 2D COF can be implemented by incorporating open-shell organic ligands. In addition, both ordered 2D MOF and COF conformations render the connection between magnetic moment carriers within an interacting distance.[101,349–352] The key electronic and magnetic properties of 2D MOF and COF are listed in Table V for discussion.

TABLE V. A list of 2D organic magnets with their compositions and representative electronic and magnetic properties, including the magnetic ground state (GS), the values of Hubbard U term, energy gap (E_g), magnetic moment on per transition metal (M_s), Curie temperature (T_C), and magnetic anisotropy energy per unit cell (MAE).

MOF	Compositions	GS	U (eV)	E_g (eV)	M_s (μ_B)	T_C (K)	MAE (meV)	Ref.
3*d*@Pc	Cr@Pc	AFM	3	0.36	4	–	–	101
	Cr@Pc-kag	AFM	–	0.94	4	–	0.67	362
	Mn@Pc	FM	3	HM	3	150	–	101
	Mn@Pc-kag	FM	–	0.09	3	125	1.18	362
	Fe@Pc	FM	–	Metal	1.95	–	–	357
	Fe@Pc	AFM	3	0.24	2	–	–	101
	Fe@Pc-kag	FM	–	0.32	2	–	–	362
	Co@Pc	AFM	–	Metal	1.01	–	–	363
	Co@Pc	AFM	3	0.10	1	–	–	101
	Co@Pc-kag	FM	–	1.09	1	–	–	362
	Ni@Pc	PM	–	0.7	0	–	–	365
	Ni@Pc	NM	3	0.34	0	–	–	101
	Ni@Pc-kag	NM	–	1.31	0	–	–	362
	Cu@Pc	PM	–	0.56	0.56	–	–	364
	Cu@Pc	PM[i]	–	1.5	–	–	–	358
	Cu@Pc	AFM[i]	–	–	–	–	–	359
	Cu@Pc	AFM	3	0.31	1	–	–	101
	Cu@Pc-kag	FM	–	1.34	1	–	–	362
	Zn@Pc	NM	3	0.30	0	–	–	101
	Zn@Pc-kag	NM	–	1.34	0	–	–	362
5*d*@Pc	W@Pc	AFM	–	–	2.4	–	19.9	360
	Re@Pc	FM	–	–	2.4	626	20.7	360
5d_2@Pc	Ta_2@Pc	AFM	–	–	1.6/0.2		26.9	360
	Os_2@Pc	FM	–	–	1.2/0	52	40.7	360
	Ir_2@Pc	FM	–	–	1.6/0.2	91	47.2	360
	Mo_2@Pc	AFM	–	0.93	0.88	–	–	366
NiM@OIPc	NiCr@OIPc	AFM	3	0.35	4	–	–	367
	NiMn@OIPc	FM	3	HM	3	170	0.74	367
	NiFe@OIPc	AFM	3	0.28	2	–	–	367
	NiCo@OIPc	AFM	3	0.35	1	–	–	367
	NiCu@OIPc	AFM	3	0.3	1	–	–	367
3*d*@Pp	V@Pp	FM	–	HM	2.54	197	–	79
	Cr@Pp	FM	3	Metal	3	187	–	80
	Mn@Pp	AFM	3	–	3.8	–	–	80
	Fe@Pp	AFM	3	–	2	–	–	80
	Co@Pp	AFM	3	–	1	–	–	80
	Ni@Pp	PM	3	–	0	–	–	80
	Cu@Pp	AFM	3	–	1.4	–	–	80
	Zn@Pp	PM	3	–	0	–	–	80
3*d*@Pp0	Cr@Pp0	AFM	3	0.36	4	–	–	368
	Mn@Pp0	FM	3	HM	3	320	–	368
	Fe@Pp0	AFM	3	0.19	2	–	–	368
	Co@Pp0	PM	3	0.4	1	–	–	368
	Cu@Pp0	AFM	3	Metal	1	–	–	368
3*d*@Pp45	Cr@Pp45	PM	–	1.51	4	–	–	368
	Mn@Pp45	PM	–	HM	3	–	–	368
	Fe@Pp45	PM	–	1.02	2	–	–	368

TABLE V. (*Continued.*)

MOF	Compositions	GS	U (eV)	E_g (eV)	M_s (μ_B)	T_C (K)	MAE (meV)	Ref.
	Co@Pp45	PM	–	1.04	1	–	–	368
	Cu@Pp45	PM	–	1.24	1	–	–	368
5*d*@Pp	W@Pp	AFM	–	–	2.7	–	24	369
	Re@Pp	FM	–	–	2.8	200	23.9	369
5*d*@M-Pp	W@M-Pp	AFM	–	–	2.7	–	26	369
	Re@M-Pp	FM	–	–	2.8	–	14.3	369
5*d*@H-Pp	W@H-Pp	AFM	–	HM	2.5	–	29.3	369
	Re@H-Pp	FM	–		2.5	–	51.8	369
5*d*@A-Pp	W@A-Pp	AFM	–	Metal	2.3	–	36.7	369
	Re@A-Pp	FM	–		2.5	–	60.8	369
M3@BHT-1	Ni@BHT-1	Expt.	–			–	–	356
	Cu@BHT-1	Expt.	–			–	–	370
	Co@BHT-1	Expt.	–			–	–	355
	Mn@BHT-1	FM	–	HM	3	–	–	372
	Fe@BHT-1	FM	–	HM	2	–	–	372
	Co@BHT-1	FM	–	HM	1	–	–	372
	Cr@BHT-1	AFM	–	SemiM	–	–	–	372
	Mn@BHT-1	FM	3	HM	3	212	–	371
	$Mn_3C_{12}N_{12}H_{12}$	FM	–	–	–	450	–	374
M3@BHT-1	Cu@BHT-2	FM	–	Metal		4	–	375
	Mg@BHT-2	NM	–	–	–	–	–	376
3*d*-Mg_2@BHT-2	Sc-Mg_2@BHT-2	PM	–	–	1	–	–	373
	Ti-Mg_2@BHT-2	PM	–	–	2	–	–	373
	V-Mg_2@BHT-2	FM	–	–	3	471	–	373
	Cr-Mg_2@BHT-2	PM	–	–	4	–	–	373
	Mn-Mg_2@BHT-2	PM	–	–	3	–	–	373
	Fe-Mg_2@BHT-2	PM	–	–	2	–	–	373
	Co-Mg_2@BHT-2	PM	–	–	1	–	–	373
5d_3(HITP)$_2$	Ta_3(HITP)$_2$	FM	–	∼0.6	1	–	–	377
	Re_3(HITP)$_2$	FM	–	∼0.4	1	–	–	377
	Ir_3(HITP)$_2$	FM	–	∼0.2	1	–	–	377
	Au_3(HITP)$_2$	FM	–	–	1	–	–	377
	$Ta_3(C_{18}H_{12}O_6)_2$	FM	–	0.024	3	–	–	377
		FM	2	0.011	3	–	–	377
	$Ir_3(C_{18}H_{12}O_6)_2$	FM	0	∼0.48	1	–	–	377
		FM	2	∼0.95	1	–	–	377
3*d*@DPP	Cr@DPP	FIM	–	1.46	3	316	0.24	7
	V@DPP	FIM	–	1.24	3	406	–	7
	Cr@DPP	FIM	–	1.57	3.52	540	–	125
3*d*@TCNQ	Cr@TCNQ	AFM	3	–	4	–	–	378
	Mn@TCNQ	AFM	3	–	3	–	–	378
	Fe@TCNQ	AFM	3	–	2	–	–	378
	Co@TCNQ	PM	3	–	1	–	–	378
naphthalene	Cr	FM	–	HM	3.38	–	–	82
	Mn	FM	–	Metal	3.99	–	–	82
	Fe	AFM	–	HM	2.64	–	–	82
	Co	AFM	–	HM	1.39	–	–	82
3*d*@CMP	Fe@CMP	FM	5	0.28	2	–	–	379

TABLE V. (*Continued.*)

MOF	Compositions	GS	U (eV)	E_g (eV)	M_s (μ_B)	T_C (K)	MAE (meV)	Ref.
3*d*@PTC	Fe@PTC	FM[i]	–	–	0.08	15	–	380
	Fe@PTC	FM	–	∼0.2	–	16	–	380
$M_2C_{18}H_{12}$	$Ni_2C_{18}H_{12}$	–	–	DHM	1	–	–	382
	$Co_2C_{18}H_{12}$	–	–	DHM	2	–	–	382
	$Mn_2C_{18}H_{12}$	FM	–	DHM	2	–	0.5	383
4*d*@IPOF	In-IPOF	FM	–	0.03	–	–	–	384
TM@PBP	Cr@PBP	Dimerized	3	0.73	4.36	–	–	385
	Mn@PBP	FM	3	0.12	4.33	105	–	385
	Fe@PBP	AFM	3	0.16	3.12	–	–	385
	Co@PBP	Dimerized	3	0.53	1.96	–	–	385
	Ni@PBP	Dimerized	3	0.73	0.96	–	–	385
3*d*@T4PT	Fe@T4PT	FM[i]	–	–	2	1.8	–	386
	$Ni_2C_{24}S_6H_{12}$	FM	3	DHM	1	630	–	387
M@TCB	Au@TCB	FM	–	HM	1	325	–	81
	Ag@TCB	FM	–	HM	1	200	–	81
	Cu@TCB	FM	–	HM	1	325	–	81
	Re@TCB	FM	–	0.06	3	630	19	388
TM@Ps	Ti@Ps	AFM	3	–	0.8	–	–	391
	V@Ps	FM	3	Metal	2.9	279	<1	391
	Cr@Ps	AFM	3	–	4.3	–	–	391
	Mn@Ps	FM	3	Metal	4.4	96	<1	391
	Co@Ps	AFM	3	–	2.1	–	–	391
$3d_2C_6S_{12}$	$Mn_2C_6S_{12}$	FM	4	DHM	4	1280	–	392
3*d*-TP-1	Cu-TP-1	AFM[i]		–	–	–	–	389
COF	DTPA	FM	–	HM	1	–	–	352
	GF	AFM	–	–	2	–	–	352
	B-dope DTPA	FM	–	–	1	–	–	352
	B-doped-GF	FM	–	HM	1	–	–	352
	g-C_4N_3	FM	–	HM	1	–	–	351
	C_3N	FM	–	0.39	0.4	<96	–	350

The rapid development of 2D organic magnets benefits from the synthesis of high-quality and highly stable 2D MOFs.[353–356] So far, the majority of magnetic frameworks in 2D MOFs contain paramagnetic metal centers, in particular, the open-shell 3*d* and 5*d* transition metals. These metal ions, which may exist in different oxidation states, allow variation of the two important parameters—spin quantum number and magnetic anisotropy. In addition, the diversity of organic molecule frameworks offers many opportunities to anchor the magnetic atoms, such as phthalocyanine (Pc), polyporphyrin (poly-Pp), benzenehexathiolate (BHT), and 5,5′-bis(4-pyridyl)(2,2′-bipirimidine) (PBP). These organic frameworks act as the medium to couple metal carriers. In addition, the organic ligands impose a coordination environment on the metal ions, namely, ligand field, which is important for determining the magnetic behavior. According to the symmetry of typical molecular architectures, the possible coordination numbers of central metal ions are 2, 3, 4, and 6.

Four is the most common coordination number for transition metal atoms in 2D organic magnets, especially Pc, Pp, and BHT frameworks. As an 18-electron conjugated system, Pc framework is a macrocyclic compound composed of an inner porphyrazine ring that connects four isoindole groups, giving rise to the characteristic cross-like shape. Pc framework has a cavity with a diameter of about 2.70 Å in the center of the large conjugated ring. Transition metal species embedded in the cavity can chelate with the Pc framework through coordination bonds and form metal phthalocyanine sheet (M@Pcs) with appreciable thermal stability. Both experimental and theoretical reports argued that a variety of M@Pc sheets are good conductors or semiconductors.[101,357–360] As listed in Table V, 3*d* and 5*d* transition metal substituted Pc frameworks have attracted much attention in the field of 2D magnetism.

Experimentally, Able *et al.* reported that 2D polymeric arrays of Fe@Pc can be obtained by co-evaporation of Fe and 1,2,4,5-tetracyanobenzene (TCNB) with 2:1 stoichiometry in ultrahigh vacuum condition onto Au(111), Ag(111) and even insulating NaCl substrates.[361] Cu@Pc film can be synthesized through the reaction of pyromellitic acid tetranitrile (PMTN) with copper in a CVD set-up.[358] As reported

by Honda *et al.*,[359] XRD analysis, TEM characterization, and magnetization measurements of 2D Cu@Pc sheets revealed the existence of antiferromagnetic exchange interactions between neighboring Cu^{2+} ions.

According to the linking way, there are two kinds of TM@Pc structures. As displayed in Figs. 15(a) and 15(b), they possess tetragonal symmetry with space group of P4/mmm (M@Pc) and six-fold symmetry within a Kagome lattice (M@Pc-kag), respectively. Among them, Cr@Pc and Mn@Pc have been proven to be stable antiferromagnetic semiconductors, while Cr@Pc-kag and Mn@Pc-kag are ferromagnetic half-metals. MC simulations within Ising model or Heisenberg model have revealed phase transition between FM and PM states at a critical temperature of 150 K and 125 K for Mn@Pc and Mn@Pc-kag, respectively.[101,362] However, Fe, Co and Cu-based systems exhibit different magnetic couplings under tetragonal and hexagonal lattices. The magnetic coupling in M@Pc-kag and M@Pc belongs to weak FM and weak AFM, respectively. In Mn@Pc and Cr@Pc, d_{xz} and d_{yz} orbitals of metal atoms hybridize strongly with p electrons of Pc in the proximity of Fermi level, thereby leading to robust long-range ferromagnetic ordering.[101,362] In contrast, the other 2D TM@Pc frameworks have larger bandgaps so that their magnetic couplings are relatively weaker.

During 2002 and 2006, Białek's group investigated the electronic structures of a series of M@Pcs (M = Fe, Co, Ni, and Cu) using the all-electron full-potential linearized augmented plane wave method.[357,363–365] They found that Fe@Pc and Co@Pc prefer long-range FM and AFM orderings with on-site magnetic moment of about 1.95 and 1.01 μ_B per Fe and Co atom, respectively. The result of Co@Pc is consistent with that of Zhou *et al.*[101] According to the spin-polarized density of state, Fe@Pc behaves as a half-metal and the other three systems possess moderate bandgaps in the range of 0.56 to 1.45 eV.

In addition, 5*d* TM single atoms and dimers adsorbed on the central hollow site of 2D Pc have been investigated using first-principles calculations.[360] The on-site magnetic moments of Re@Pc and W@Pc are approximately identical (c.a. 2.4 μ_B). The calculations of exchange energy indicated that the magnetic ground state of W@Pc system is antiferromagnetic. Attractively, Re@Pc exhibits stable FM state with a high Curie temperature of about 626 K and a

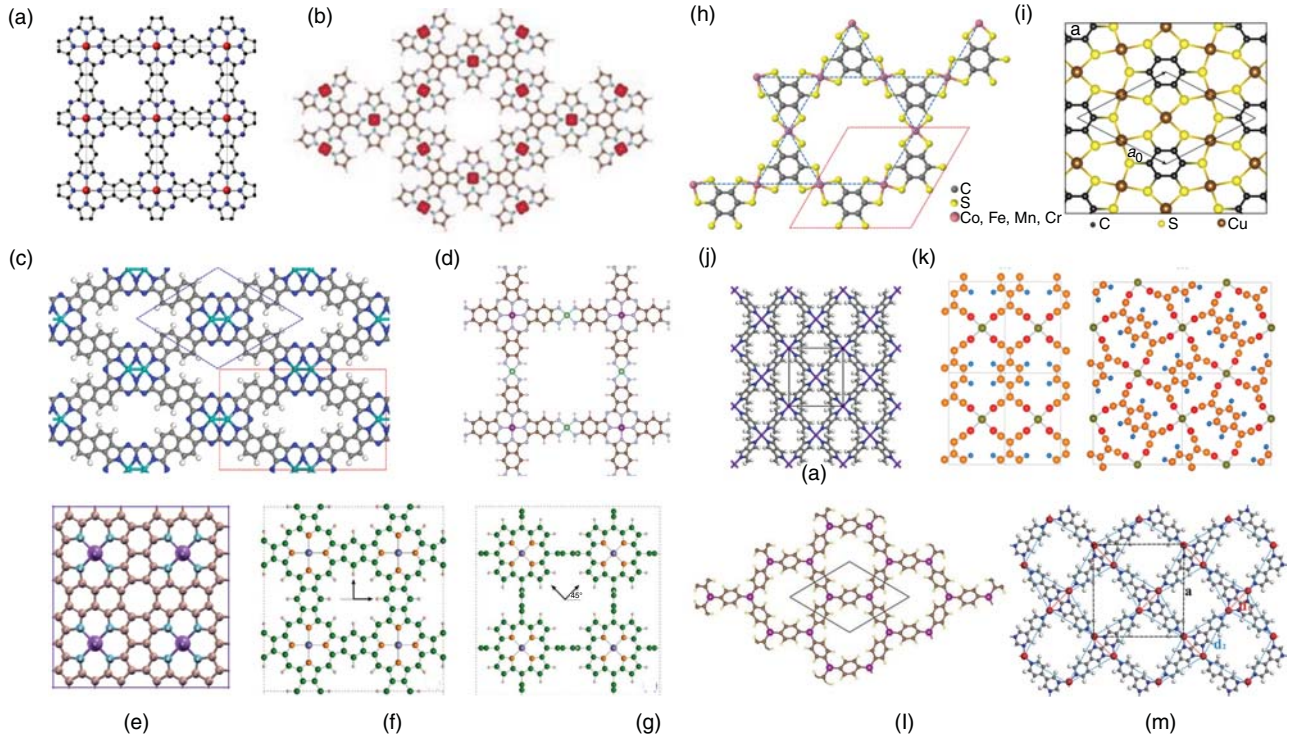

FIG. 15. Geometric structures of (a) M@Pc, (b) M@Pc-kag, (c) Mo_2@Pc, (d) NiM@OIPc, (e) M@Pp, (f) M@Pp0, (g) M@Pp45, (h) M@BHT-kag, (i) M@BHT, (j) Cr@DPP, (k) TM@TCNQ, and (l) Mn@T and TM@PBP. Panel (a) reproduced from Honda *et al.*, Appl. Phys. Lett. **110**, 133101 (2017), with the permission of AIP Publishing.[359] Panel (b) reproduced with permission from Chen *et al.*, Chinese J. Chem. Phys. **32**, 563 (2019). Copyright 2019 Chinese Physics Society.[362] Panel (c) reproduced with permission from Zhu *et al.*, J. Phys. Chem. A **118**, 304 (2014). Copyright 2014 American Chemical Society.[366] Panel (d) reproduced with permission from Li *et al.*, Chem. Sci. **8**, 2859 (2017). Licensed under a Creative Commons Attribution (CC-BY-3.0).[367] Panel (e) reproduced with permission from Singh *et al.*, J. Phys. Chem. C **119**, 25657 (2015). Copyright 2015 American Chemical Society.[79] Panels (f) and (g) reproduced with permission from Sun *et al.*, J. Mater. Chem. C **3**, 6901 (2015). Copyright 2015 Royal Society of Chemistry.[368] Panel (h) reproduced with permission from Chakravarty *et al.*, J. Phys. Chem. C **120**, 28307 (2016). Copyright 2016 American Chemical Society.[372] Panel (i) reproduced with permission from Zhang *et al.*, Nano Lett. **17**, 6166 (2017). Copyright 2017 American Chemical Society.[375] Panel (j) reproduced with permission from Li *et al.*, J. Phys. Chem. Lett. **10**, 2439 (2019). Copyright 2019 American Chemical Society.[7] Panel (k) reproduced with permission from Ma *et al.*, J. Phys. Chem. A **117**, 5171 (2013). Copyright 2013 American Chemical Society.[378] Panel (l) left reproduced with permission from Wang *et al.*, Rev. Lett. **110**, 196801 (2013). Copyright 2013 American Physical Society.[383] Panel (l) right reproduced with permission from Zhang *et al.*, Chem. Sci. **10**, 10381 (2019). Licensed under a Creative Commons Attribution (CC BY-NC 3.0).[385]

perpendicular MAE of about 20.7 meV. When a homonuclear dimer is adsorbed on Pc framework (denoted as TM_2@Pc), the MAE can be greatly enhanced,[360] i.e., 26.9, 40.7, and 47.2 meV for Ta_2@Pc, Os_2@Pc, and Re_2@Pc, respectively. Among those systems, Os_2@Pc and Ir_2@Pc are FM with T_C of 52 and 91 K, respectively. For 4*d* transition metals, Mo dimer embedded in Pc with another kind of atomic arrangement shown in Fig. 15(c) has been discussed by Sun's group.[366] In this 2D material, each Mo atom has a magnetic moment of about 0.88 μ_B, and the entire Mo_2@Pc system adopts AFM ground state. Using DFT calculations with the hybrid HSE06 functional, a direct gap of about 0.93 eV was obtained.

By replacing Pc with octaamino-substituted phthalocyanines (OIPc) and square planar Ni^{2+} ions, a new kind of square 2D MOFs with two different 4-coordinated transition metal centers in each unit cell has been predicted.[367] The OIPc organic molecule enables strong conjugation of π electrons, having a critical impact on the magnetic properties of the 2D lattices [Fig. 15(d)]. Among these charge neutral 2D MOFs candidates, NiMn@OIPc exhibits a half-metallic and ferromagnetic ground state. The large exchange energy of NiMn@OIPc results from the unique strong hybridization between d/π orbitals of Mn, Pc ring, and Ni-bisphenylenediimine nodes. This picture is consistent with the TM@Pc mentioned above. In addition, CrNi, FeNi, CoNi, and CuNi-based systems are all narrow-band-gap semiconductors (0.28∼0.35 eV) with weak AFM coupling.[367]

The porphyrin (Pp) ligand consisting of four pyrroles, is a planar, dianionic macrocycle with four nitrogen donors in a square planar arrangement with a hole size of around 2.0 Å in radius. Using Pp molecule as building block, a series of stable four-coordination 2D periodic metal porphyrin frameworks (M@Pp) have been proposed in recent years,[79,80] which are formed by embedding transition metal atoms in poly-Pp framework. Based on different bridged ligands, the Pp frameworks can be labeled as Pp, Pp0, and Pp45, which are shown in Figs. 15(e), 15(f), and 15(g), respectively. Benefiting from the abundant combinations of metal atoms, Pp frameworks, and bridged ligands, many 2D MOFs with diverse magnetic ground states can be designed.

When Fe and Cu atoms are embedded in Pp and Pp0 frameworks, AFM ground state is more favorable than FM ground state. For the other TM elements, magnetic coupling of ground state is sensitive to the organic frameworks and transition metals. As summarized in Table V, V@Pp, Cr@Pp, and Mn@Pp0 are FM; Mn@Pp and Co@Pp0 are AFM; while Ni@Pp, Zn@Pp, and Co@Pp0 are PM. In Cr@Pp[80] and V@Pp sheets,[79] robust FM ordering is obtained with considerable T_C of 187 and 197 K, respectively. Interestingly, half-metallicity can be achieved in these 2D systems as the Fermi level is lifted up via electron doping.[80] The magnetic coupling in Mn, Fe, Co, and Cu-based M@Pp systems are all AFM with on-site magnetic moment of 3.8, 2, 1 and 1.4 μ_B, respectively. For Ni@Pp and Zn@Pp nanosheets, the interactions between the local magnetic moments are almost negligible due to the large lattice constant, thereby exhibiting PM feature. Among the metal-embedded Pp0 frameworks, only Mn@Pp0 framework exhibits half-metallic nature as well as long-range FM coupling with room-temperature T_C of about 320 K, whereas 2D Cr@Pp0, Fe@Pp0, and Cu@Pp0 MOFs prefer weak antiferromagnetic coupling and Co@Pp0 exhibits PM behavior.[368] In Pp45 frameworks incorporated with 3*d* TM atoms, the inter-spin coupling is identified to be PM, mainly arising from their long spin coherence length. Meanwhile, different magnetic coupling states and large perpendicular magnetic anisotropy (PMA) in Pp45 frameworks are induced by various 5*d* TM atoms.[369]

Moreover, the magnetic moment and magnetic anisotropy can be modified by replacing the peripheral H atoms of Pp framework by methyl (-CH_3), hydroxyl (-OH), and amino (-NH_2) radicals, denoted as TM@M-Pp, TM@H-Pp, and TM@A-Pp, respectively. Among them, W@Pp based systems prefer AFM coupling, and the coupling strength is gradually strengthened with the electron donating capacity increasing, which is ascribed to the functional radicals. The on-site magnetic moment and PMA can be tailored in range of 2.3∼2.7 μ_B and 24∼36.7 meV, respectively.[369] In contrast, Re@Pp based systems prefer FM state with exchange energy over 180 meV, and the coupling strength changes slightly with functional radical. Amazingly, MAE of Re@Pp framework can be greatly enhanced from 23.9 to 60.8 meV when H atoms are replaced by NH_2 radicals. Furthermore, MC simulations yielded an estimated T_C of ∼200 K for Re@Pp, suggesting that its ferromagnetism can be retained at relatively high temperature.

A group of stable 2D tetra-coordination polymer complexes linked by conjugated benzenehexathiolate following two different Kagome frameworks (M_3@BHT-1 and M_3@BHT-2) were also experimentally prepared or theoretically designed, and parts of them showed magnetic behavior. In them, the metal ions (M = Mg, Zn, Ni, Cu) with sixfold symmetry were successfully synthesized by the coordination reaction between benzenehexathiol (BHT) and metal acetate [M-$(OAc)_2$], and the system with Co ions was calculated by first-principles method.[355,356,370] Since BHT is a polyphosphine ligand with three dithiolene donor groups ($C_6S_6^{6-}$), a series of M_3@BHT complexes were studied using first-principles calculations by considering all 3*d* transition metal elements. Indeed, three kinds of systems, such as $Mn_3C_{12}S_{12}$,[371] $M_3C_6S_6$ (M_3@BHT-1),[372] and $MMg_2C_{12}S_{12}$ (M-Mg_2@BHT-2),[373] have been reported to possess magnetic properties. Their structural models are depicted in Figs. 15(h) and 15(i). Among $Mn_3C_{12}S_{12}$ and M_3@BHT-1 systems with planar spin-frustrated Kagome lattice, Mn, Fe, and Co complexes have half-metallicity and FM ground state, whereas Cr@BHT-1 is stabilized in AFM ground state and behaves as a semimetal.[372] A similar study was reported by Liu and Sun in 2015,[374] and they predicted 2D $Mn_3C_{12}N_{12}H_{12}$ sheet to exhibit stronger FM coupling with T_C of 450 K. In 2D $Mn_3C_{12}N_{12}H_{12}$ sheet, the isoelectronic NH groups take the position of sulfur atoms, which result in smaller lattice constant and larger magnetic coupling strength. Furthermore, *d-p* hybridization not only makes the main contribution to the stable π-conjugated planar Kagome framework structure but also results in favorable FM magnetic coupling.

Based on DFT calculations, it was found that $Cu_3C_6H_6$ monolayer (Cu@BHT-2) is a FM metal with an altralow T_C of about 4 K,[375] while 2D $Mg_3C_6S_6$ is a nonmagnetic semiconductor.[376] The atomic model is shown in Fig. 15(i). When one of the Mg atoms in nonmagnetic $Mg_3C_6S_6$ is substituted by a 3*d* transition metal atom (i.e., Sc∼Co), intrinsically magnetic and semiconducting properties can be observed. Among these 2D systems, FM state is more stable than PM state for V-Mg_2@BHT-2 with rather high T_C of 471 K.[373] The π-*d* coupling between central metal atom and organic ligands effectively regulates the spin-polarized state of these systems and the coupling strength is greatly influenced by the magnetic moment of TM atoms and interatomic distance.

Apart from the above systems, magnetic MOFs have also been identified in other 2D materials with tetra-coordination, such as TM_3HITP_2 (HITP = 2, 3, 6, 7, 10, 11-hexaiminotriphenylene),[377] TM@DPP (DPP = diketopyrrolopyrrole),[125] TM@TCNQ (TCNQ =7,7,8,8-tetracyanoquinodimethane),[378] TM-naphthalene,[82] Fe@CMP,[379] and Fe@PTC (PTC = 1, 2, 3, 4, 5, 6, 7, 8, 9, 10, 11, 12-perthiolated coronene).[380] In 2014 and 2015, the experimentally synthesized $Ni_3(HITP)_2$ and $Cu_3(HITP)_2$ were reported to be semiconductors with high electrical conductivity.[353,381] Later, QAH effect in $TM_3(HIPT)_2$ was theoretically predicted by Dong *et al.*[377] In their study, $Ta_3(HITP)_2$, $Re_3(HITP)_2$, and $Ir_3(HITP)_2$ monolayers are ferromagnetic narrow-band-gap semiconductors with magnetic moment of 1 μ_B per TM atom. When all N atoms in $TM_3(HITP)_2$ are substituted by O atoms, the resulted $Ta_3(C_{18}H_{12}O_6)_2$ and $Ir_3(C_{18}H_{12}O_6)_2$ systems retain FM ground state. Meanwhile, QAH effect could be successfully realized at much higher temperature by chemical modification in $Ta_3(C_{18}H_{12}O_6)_2$. The magnetic moment of Ta ion is greatly enhanced to 3 μ_B as compared to that of $Ta_3(HITP)_2$ (1 μ_B).[377] The ground state of 2D V(Cr)-diketopyrrolopyrrole (DPP), as shown in Fig. 15(j), was theoretically predicted to be ferrimagnetic with an exchange energy more than 426 meV (328 meV).[7] The robust ferrimagnetic ordering originates from strong *d-p* direct exchange interactions between conjugated electron acceptors and electron providers.[125] TM-7,7,8,8-tetracyanoquinodimethane (TM@TCNQ), Cr@TCNQ, Mn@TCNQ, and Fe@TCNQ exhibit long-range AFM coupling [Fig. 15(k)], while Co@TCNQ is PM according to DFT calculations.[378] For a simple 2D MOF composed of substituted naphthalene moieties and transition metals, FM coupling can be achieved in Cr- and Mn-based systems with high on-site magnetic moment of about 4 μ_B. Except that Mn complex is metallic, Cr, Fe, and Co complexes are all half-metallic in nature. Furthermore, Fe and Cr complexes exhibit remarkable 100% spin-filtering efficiency. Therefore, TCNQ and TM-naphthalene could serve as ideal building blocks for the candidate materials of spintronic devices.[82] Another 2D ferromagnetic MOF, i.e., Fe@PTC [PTC = (1, 2, 3, 4, 5, 6, 7, 8, 9, 10, 11, 12)-perthiolated coronene] compound was synthesized from reaction of PTC with ammoniacal solutions of iron acetate [$Fe(OAc)_2$] and exhibited a high electrical conductivity of about 10 S/cm at 300 K through the measured I–V curves, which decreased upon cooling and suggested typical feature of semiconductor.[380]

Reducing the coordination number of transition metal centers from 4 to 3, there are still many 2D MOFs with intrinsic magnetism through rational design, such as M@triphenyl ($M_2C_{18}H_{12}$, M= Co, Ni and Mn),[382,383] indium-phenylene (In@IPOF),[384] TM@PBP [PBP = 5,5′-bis(4-pyridyl)(2,2′-bipirimidine],[385] bilayer Fe@T4PT [T4PT = 2,4,6-tris(4-pyridyl)-1,3,5-triazine],[386] and Ni-thiophene ($Ni_2C_{24}S_6H_{12}$).[387] Among these compounds, Fe@PBP framework has already been synthesized on Au(111) substrate by molecular self-assembly.[354] In@IPOF and M@T (M=Co, Ni, and Mn) share the same geometry, as shown in Fig. 15(l). Except for Fe@T4PT and TM@PBP, most of the above mentioned three-coordinated 2D MOFs possess amazing half-metallic Dirac point and are novel topologically nontrivial materials. Meanwhile, In@IPOF, Mn@T, Mn@PBP, Fe@T4PT, and $Ni_2C_{24}S_6H_{12}$ have been reported as 2D ferromagnets. Mn@PBP is the first ferromagnetic 2D MOF with the Shastry-Sutherland lattice [Fig. 15(m)], and its T_C was predicted to be about 105 K, while Fe@PBP and TM@PBP (TM = Cr, Co, Ni) were found to be AFM and magnetic-dimerized, respectively.[385]

Other 2D MOFs with even lower coordination of two have been theoretically designed. One kind of two-coordinated organometallic framework composed by (1,3,5)-benzenetricarbonitrile (TCB) molecules and noble metals (Au, Ag, and Cu) have been shown as FM half-metals with T_C as high as 325 K. Besides, TCB-Re exhibits intrinsically ferromagnetic ordering with a high T_C of 613 K predicted by MFT and a considerable MAE of 19 meV/atom.[388] In these organometallic frameworks, the strong electronegativity of C–N groups drives the charge transfer from metal atoms to the organic molecules, forming the local magnetic centers. These magnetic centers experience strong FM and AFM couplings through *d–p* covalent bonding.[81]

In addition, many researchers have also observed 2D magnetic MOFs with hexa-coordination. Experimentally, 2D Cu-TP-1 has been synthesized under solvothermal conditions from the Cu^{2+} and 2-tetrazole pyrimidine ($C_5H_5N_6$, H-TP). According to the field cooled (FC) and zero field cooled (ZFC) measurements, the system exhibited an antiferromagnetically coupled Cu–Cu interaction down to 8 K with a Weiss temperature around 108 K.[389] Another polynuclear Cu compound showed predominant ferromagnetic coupling even at 300 K.[390] Theoretically, Kan *et al.*[391] found that one kind of freestanding organometallic sheets (Ps) can be assembled by 3*d* TM atoms and benzene molecules. Among them, V@Ps and Mn@Ps are FM systems with T_C of 279 K and 96 K based on MFT, respectively, while Ti@Ps, Co@Ps, and Cr@Ps exhibit AFM ordering.[391] In these frameworks, their magnetic coupling can be explained by maximization of the virtual hopping between separated magnetic centers caused by the half-occupied d_{xz} and d_{yz} bands. In addition, another hexa-coordinate compound, i.e., $Mn_2C_6S_{12}$, has also been predicted. It is a honeycomb structure and possesses stable FM state at room temperature along with spin-polarized Dirac cone. Interestingly, the exchange interaction between Mn ions is achieved by the conduction electrons of C atoms acting as the intermediate.[392]

Due to large magnetic moments and remarkable magnetic anisotropy in the lanthanide ions, a series of 2D lanthanide-MOFs displayed strong magnetic interactions. Using hydrothermal method, a new 2D Dy^{3+} MOF was synthesized from 4-hydroxypyridine-2,6-dicarboxylic acid and showed intramolecular ferromagnetic interaction and two-step thermal magnetic relaxation.[393] Another dysprosium layered compound from reaction with 2-(3-pyridyl) pyrimidine-4-carboxylic acid also presented FM interactions between Dy^{3+} ions and slowed magnetic relaxation behavior.[394]

Another important member of 2D organic materials is COFs, which have been investigated widely as catalysts, energy storage and gas adsorption materials, and so on. Two-dimensional COFs are crystalline porous polymers formed by molecular building units and organic linkers via covalent bond without any transition metal.[395,396] Due to their transition metal free nature, it is hardly to found 2D magnets in COFs. However, some pioneer studies have proven that they can exhibit magnetic properties in the presence of some special atomic arrangements. In a theoretical study by Yang *et al.*,[352] single-layer organic porous sheets dimethylmethylene-bridged triphenylamine (DTPA) is a ferromagnetic half-metal with a bandgap in semiconducting channel of about 1 eV. In comparison with the boron-doped (FM) and pure graphene nanoflakes (GFs) (AFM), both of which possess similar molecular architecture with DTPA, the FM state can be explained by half-occupied π orbital and allowed virtual hopping for FM configurations. Graphitic carbon nitride ($g\text{-}C_4N_3$) as a novel material with FM ground state and intrinsic half-metallicity has

also been theoretically predicted by Du *et al.*[351] According the analysis of orbital-resolved DOS, the *p* orbitals of N atoms rather than C atoms make the main contributions to the half-metallicity and magnetism of g-C_4N_3. A 2D COF with D_{6h} symmetry, C_3N, was shown to have an intrinsic indirect bandgap of 0.39 eV under FM ground state from both experimental and theoretical studies.[350] No doubt, the above studies open a door for fundamental research and potential applications toward realistic metal-free spintronics.

IV. MODIFICATIONS

In the above discussions, we mainly focused on the database of 2D magnets and their dominant magnetic exchange interactions. For practical applications, we have to address the other issues, such as how to enhance the critical transition temperature (T_C or T_N) to room temperature in these existing 2D magnetic materials by post-treating with various manipulations. We have already shown that the magnetic ground state and exchange coupling strength are very sensitive to symmetry, charge distributions, Fermi level, valence states, orbital occupation, orbital hybridizations, energy level, hopping paths, and so on. According to these target parameters, many strategies have been proposed, including strain engineering, intercalation, external electronic/magnetic field, interfacial engineering, defect engineering, Janus structuring, and optical controlling. A schematic diagram of these modification mechanisms is displayed in Fig. 16.

A. Strain engineering

Strain engineering is a simple and efficient means for tailoring the magnetic properties. Experimentally, the strain effect on 2D magnets is inevitable during the synthesis processes. After exfoliation, 2D magnets (e.g., 2D CrI_3[28]) could be transferred on SiO_2 substrate and other 2D materials. In addition, there are also direct MBE/CVD growth of VSe_2, $MnSe_2$, and MnSe on Si(111)/SiO_2 substrates.[34,35] As a consequence, the lattice mismatch of substrate with 2D magnets would cause certain lattice strain. Even so, one should note that we mainly discussed 2D van der Waals materials in this review. Strain from the neighboring layers could be either non-uniform or quite small, despite the large lattice mismatch.

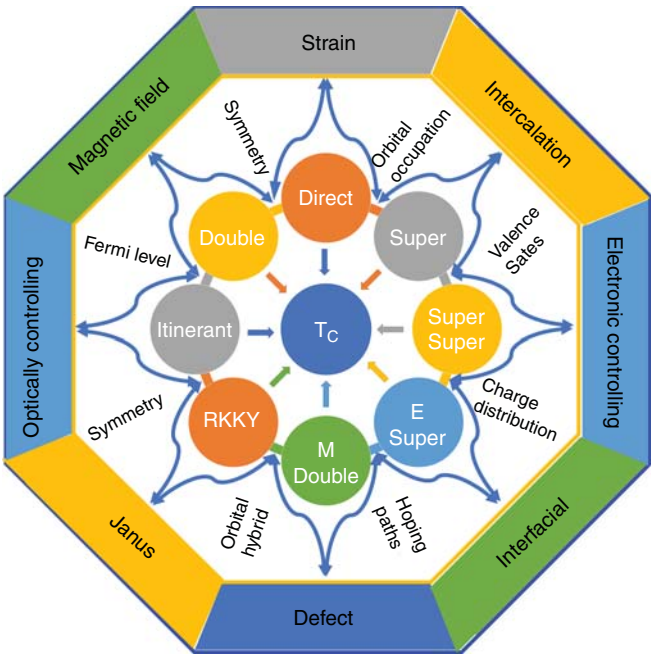

FIG. 16. The schematic diagram of the modification mechanisms of Curie temperature of 2D magnets. Many strategies have been included, such as strain engineering, intercalation, external electronic/magnetic field, interfacial engineering, defect engineering, Janus structuring, and optical controlling.

The effect of in-plane biaxial strain on the T_C of 2D magnetic materials has been thoroughly investigated, especially on the experimentally reported systems. From the structural point of view, biaxial tensile strain would immediately increase the bond lengths and widen the bond angle between the magnetic atoms, while compressive strain would reduce the bond length and narrow the bond angle. These two factors undoubtedly affect orbital hybridization and change the magnetic exchange parameters, which are described by the distance and angle dependent GKA rules.[126–128] Taking monolayer CrSi(Ge)Te_3 as an example, herein we further explain the strain effect. As shown in Fig. 17(a), the direct AFM interaction is short-ranged and decreases rapidly with the increase of Cr–Cr distance, while the superexchange FM interaction is comparatively long-ranged and decreases relatively slowly with the increase of Cr–Te–Cr distance. Under biaxial tensile strain, the Cr–Te–Cr angle gradually approaches to normative 90°, and the FM exchange interaction is strengthened.[397] These combined effects lead to increase of the energy difference between FM and AFM states. Moreover, the magnetic moment on Cr atoms increases monotonically with tensile strain.[398,399] Thus, the calculated T_C of $CrSiTe_3$ by MFA dramatically increases from 22.5 K in strain-free state to 290 K under 8% strain. Figure 17(b) displays T_C as a function of strain for $CrGeTe_3$. Under 3% and 5% tensile strains, the T_C can be enhanced to 326 and 421 K, respectively, in comparison to $T_C = 144$ K for strain-free state. Under a compressive strain of 1%, the T_C will decrease to 67 K.[398] The strain effect on the magnetic properties of VSe_2 was investigated by DFT calculations.[400] Figures 17(c) and 17(d) show the energy difference and individual magnetic moment in strained VSe_2, respectively. As the strain increases, the calculated magnetic moment of V atom increases from 0.77 to 1.18 μ_B. The T_C is monotonously enhanced from 290 to 812 K under a strain of 6%. Similar results and underlying mechanisms have also been found in monolayer CrI_3[401] and Fe_3GeTe_2[402] sheets.

The applied strain also yields a pronounced transition of magnetic ground state from AFM to FM under tensile strain or FM to AFM under compressive strain.[104,156,401,403–405] Depending on their ground states, the critical strains for phase transition in 2D $CrTe_3$, $RuCl_3$, and CrI_3 are 3%, 2%, and –5%, respectively. However, the tensile strain induced T_C enhancement and magnetic transition are not found in the ferromagnetic NiX_3 (X = I, Br, Cl) sheets. In these materials, compressive strain will enhance their T_C and induce a FM to AFM transition (8%). In fact, this is still consistent with GKA rules. In NiX_3 (X = I, Br, Cl), the intrinsic angle of Ni–X–Ni is about 95°, which deviates from 90°. The tensile strain would further enlarge the Ni–X–Ni angle, which weakens FM coupling and strengthens AFM coupling.[406]

In addition to the magnetic coupling parameters and T_C, MAE is another significant magnetic characteristic that can be successfully modulated by strain engineering. According to the second-order

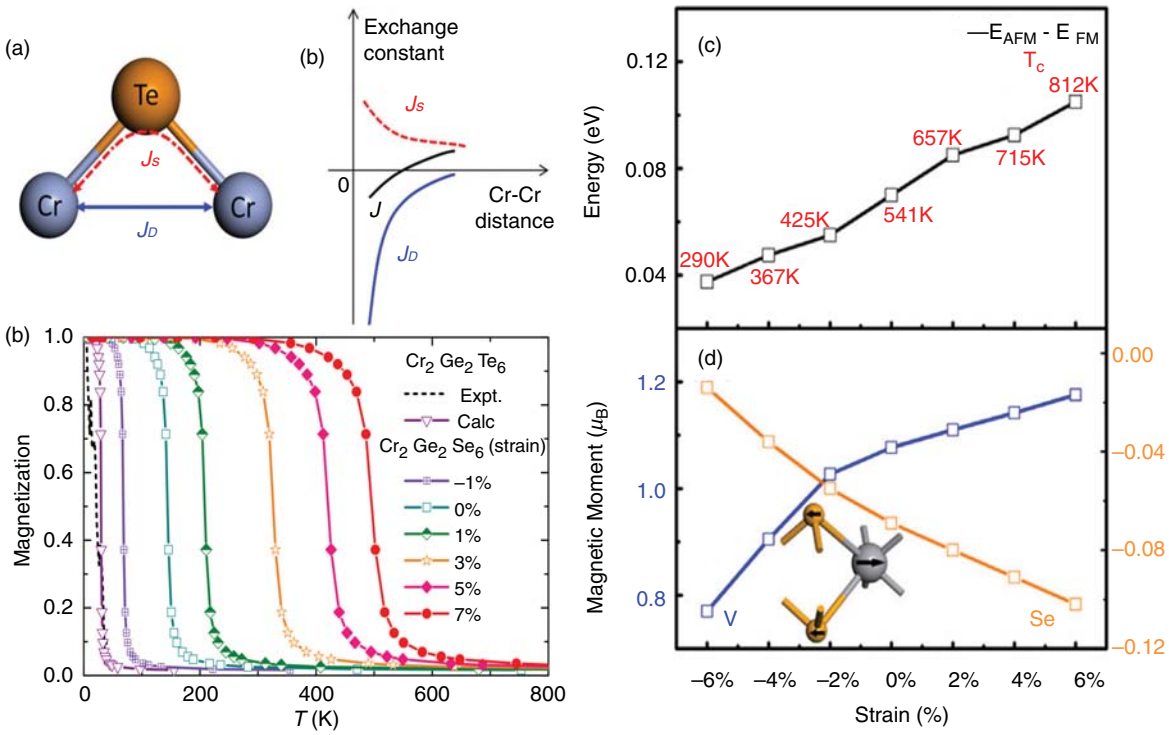

FIG. 17. (a) A schematic diagram of the nearest neighboring Cr–Cr direct AFM interaction and FM superexchange interaction mediated by the middle Te atom with Cr–Cr distance in monolayer CrSi(Ge)Te_3. (b) Normalized magnetization as a function temperature. (c) Energy difference between FM and AFM states for monolayer VSe_2 and the T_C as a function of strain. (d) The calculated magnetic moments of V and Se atoms in ferromagnetic VSe_2 monolayer as a function of strain. Panel (a) reproduced with permission from Chen *et al.*, Phys. Lett. A **379**, 60 (2015). Copyright 2015 Elsevier.[397] Panel (b) reproduced with permission from Dong *et al.*, Rev. Appl. **12**, 014020 (2019). Copyright 2019 American Physical Society.[398] Panels (c) and (d) reproduced with permission from Feng *et al.*, Surf. Sci. **458**, 191 (2018). Copyright 2018 Elsevier.[400]

perturbation theory, the value of MAE is very sensitive to strain, and no consistent mechanism has been found. For example, MAE increases with compressive strain in monolayer 1T-$FeCl_2$ because of the enhanced positive contribution to MAE from the SOC interaction between d_{x2-y2} (d_{xy}) and d_{yz} (d_{xz}) orbitals of Fe atom.[407] Han *et al.* reported that MAE of monolayer CrSI is mainly contributed by spin-polarized *p*-orbitals of nonmetal I atoms. The compressive strain enhances the MAE value to 0.52 meV/atom, which originates from the positive contribution of matrix element difference between spin-up p_x and p_y orbitals as well as spin-up p_y and p_z orbitals of I atoms.[408]

B. Intercalation

Owing to the existence of VDW gap and weak interlayer interaction, 2D materials are ideal host materials for various intercalant species, including small ions, atoms, and molecules. Chemical intercalation and electrochemical intercalation are two common methods to prepare intercalated systems.[409–416] For example, Zhao *et al.* showed that self-intercalation of native atoms into bilayer transition metal dichalcogenides during growth generates a class of ultrathin, covalently bonded materials.[417] To date, intercalation has been proven as a powerful approach to induce local spin and long-range magnetic ordering in the 2D non-magnetic materials.[417–422] In the 2D intrinsic magnets, intercalation can further modulate the electronic structure, reduce the interlayer coupling, and change the valence state of magnetic ions by doping electron/hole.

Wang *et al.*[423] successfully intercalated organic tetrabutyl ammonium (TBA) cations into $Cr_2Ge_2Te_6$ [Fig. 18(a)] and obtained a hybrid superlattice of (TBA)$Cr_2Ge_2Te_6$. Such electron doping leads to metallic behavior of (TBA)$Cr_2Ge_2Te_6$ at low temperature. Meanwhile, the Curie temperature has been significantly elevated to 208 K [Fig. 18(b)]. For comparison, pristine $Cr_2Ge_2Te_6$ is a FM semiconductor with T_C of 67 K only. The underlying exchange coupling mechanism is illustrated in Fig. 18(c). A weak superexchange mechanism is found in $Cr_2Ge_2Te_6$ semiconductor, while double exchange mechanism is dominated in FM metallic (TBA)$Cr_2Ge_2Te_6$. Weber *et al.* demonstrated that $Fe_{2.78}GeTe_2$ can be topotactically intercalated with sodium in the presence of benzophenone to yield $NaFe_{2.78}GeTe_2$.[424] The measured Curie temperatures of both $Fe_{2.78}GeTe_2$ and $NaFe_{2.78}GeTe_2$ from SQUID magnetometry were about 150 K. Even though the Curie temperature has not been appreciably changed, positive evidence of room-temperature magnetism resulted from the presence of $Fe_{2-x}Ge$ impurity was observed. Moreover, Qiu *et al.* have revealed sensitive dependence of Fe_3GeTe_2 T_C on its environmental change by Ga implantation. The T_C of bulk Fe_3GeTe_2 could increase up to 450 K by controlling the fluence of Ga irradiation, while the magnetic anisotropy could be inversed to in-plane direction.[425]

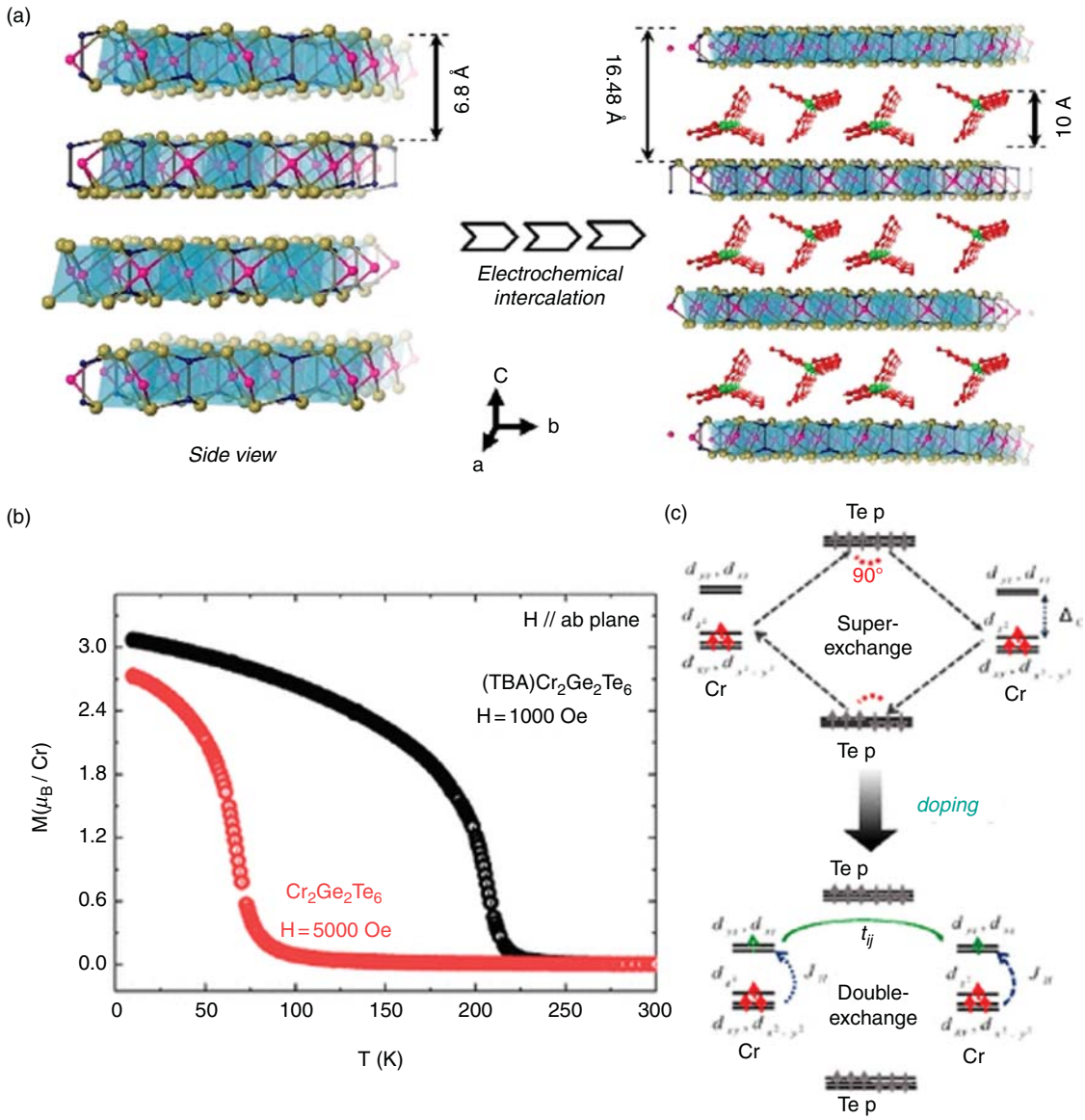

FIG. 18. (a) Side view plot of crystal structure of pristine $Cr_2Ge_2Te_6$ and (TBA)$Cr_2Ge_2Te_6$. Organic ion tetrabutyl ammonium is added into the van der Waals gap via electrochemical intercalated. (b) Temperature-dependent magnetic susceptibility of $Cr_2Ge_2Te_6$ and (TBA)$Cr_2Ge_2Te_6$. The Curie temperature is largely increased from 67 K in $Cr_2Ge_2Te_6$ to 208 K in intercalated (TBA)$Cr_2Ge_2Te_6$. (c) Schematic diagram of intercalation-induced magnetic exchange mechanism transition (from superexchange interaction to double exchange interaction). Reproduced with permission from Wang *et al.*, J. Am. Chem. Soc. **141**, 17166 (2019). Copyright 2019 American Chemical Society.[423]

In a recent theoretical study, Guo *et al.*[426] found that self-filling either Cr or I atoms into the vdW gap of stacked and twisted CrI_3 bilayer sheets can significantly strengthen the interlayer FM coupling. The exchange energy increases with the intercalated Cr concentration, reaching about 40 meV per formula compared to the values of pristine CrI_3 bilayer (2.95 meV/f.u. for the low-temperature stacked phase and −0.14 meV/f.u. for the high-temperature phase). Such strong ferromagnetism of self-intercalated CrI_3 bilayer results from the mid-gap states due to e_g-t_{2g} hybridization, which is related to the additional electron hoping paths through intercalated atoms, bridging I atoms, and intralayered Cr atoms. On the other hand, the intercalated and intralayer Cr atoms show different oxidation states. In turn, double exchange interaction among them would take over superexchange interaction to determine the magnetic behavior. Thus, much higher T_C with regard to that of pristine CrI_3 bilayer (low-temperature phase) is highly anticipated.

C. Electric control magnetism

As the essential tools for electric control of magnetism, the effects of electrostatic/ion liquid gating and electric field on the magnetic

properties of the recently emerged 2D magnets have been investigated. These studies offer exciting prospects of 2D magnets for processing and storing information in future spintronics. Due to the ultrathin nature of 2D magnets, electrostatic/ion liquid gating and electric field could largely modify the carrier concentration, electron population, orbital occupation, symmetry, and bandgap, which would further lead to the adjustment of magnetic ground state, exchange parameters, and magnetic anisotropy.

Jiang *et al.*[427] demonstrated control of the magnetic properties in both monolayer and bilayer CrI_3 by electrostatic doping. The doping effect on the magnetic properties of monolayer CrI_3 is illustrated in Fig. 19(a). From the saturation magnetization, coercive force, and Curie temperature, one can see strengthened/weakened magnetic ordering with hole/electron doping (-3×10^{13} to 3×10^{13}). The T_C of monolayer was finally modulated between 40 and 50 K. The doping effect on the magnetic properties of bilayer CrI_3 is shown in Fig. 19(b). The AFM phase shrinks continuously with increasing electron doping density. As electron doping concentration increases to 2.5×10^{13} cm^{-2}, the AFM ground state of bilayer CrI_3 would transform into FM. Under different gate voltages, the spin-flip field and interlayer exchange constant are extracted in Fig. 19(c).[427]

Two different gated bilayer CrI_3 devices have been built by Huang *et al.*,[428] and their magnetic behavior has been probed by MOKE microscopy. Under fixed magnetic fields, voltage-controlled switching between antiferromagnetic and ferromagnetic states was also found. Under zero magnetic fields, two distinct layered AFM states ("↑↓" and "↓↑") exist on gate voltage, which are related to two initialization processes. However, tunability of the net magnetization with gate voltage disappeared when the bilayer device was warmed to about 40 K, revealing that the bilayer T_N is unaffected within the range of applied gate voltage. Parallel to this study, dual-gate field-effect devices were also fabricated to investigate the electric field effect on the magnetic order of bilayer CrI_3. In the AFM bilayer CrI_3, the applied electric field creates an interlayer potential difference, which results in a large linear magnetoelectric effect. In addition, a reversible electrical switching of magnetic order has been observed near the AFM-FM spin-flip transition point.[429]

Similar to bilayer CrI_3, both gating and electronic field are able to modulate the magnetic properties of few-layer $Cr_2Ge_2Te_6$. Using ionic liquid and solid Si gates, the carrier density below 10^3 cm^{-2} was obtained in $Cr_2Ge_2Te_6$ FET transistors.[430] With such carrier density, $Cr_2Ge_2Te_6$ transistors show remarkable enhancement of saturation magnetization and reduction of saturation field. However, Micro-area Kerr measurements with different gate doping demonstrated bipolar tunable magnetization loops below the Curie temperature. The unchanged T_C may be attributed to a rebalance of the spin-polarized band structure while tuning its Fermi level. Using the electrical double layers transistors with a polymer gel based on ionic liquid, a higher electron-doped concentration ($\sim 10^{14}$ cm^{-2}) was achieved in few-layer $Cr_2Ge_2Te_6$.[431] Compared to the case of low carrier density, heavy electron doping not only enhances T_C to 200 K, but also turns the magnetic easy axis from out-of-plane to in-plane direction [Figs. 19(d)–19(e)]. First-principles calculations further clarified the origin of doping induced magnetic ordering. The large carrier density would render carrier-mediated indirect exchange mechanism as prevailing over the superexchange mechanism in $Cr_2Ge_2Te_6$. To understand the electric field effect, Xing *et al.* fabricated Hall-bar devices using the nanofabrication technique. The gate voltage dependence of channel resistances for 2D $Cr_2Ge_2Te_6$ devices has been investigated and a giant modulation of the channel resistance via electric field effect has been revealed.[99]

In contrast to these FM/AFM insulators, the itinerant magnetism possibly allows more effective tuning of T_C by ionic gating. As we have discussed above, the exchange mechanism of 2D Fe_3GeTe_2 is mediated through conduction electrons. Thus, the extreme ionic gating induced electron doping could drastically modulate DOS at the Fermi level. A trilayer Fe_3GeTe_2 ionic field-effect transistor was set up by covering solid electrolyte ($LiClO_4$) on both sides. The charge transfer between lithium ions and the Fe_3GeTe_2 film induces electron doping up to the order of 10^{14} cm^{-2} per layer. Such high doping level boosts T_C of Fe_3GeTe_2 to room temperature [Fig. 19(f)].[50] The gate-induced room-temperature FM ordering was also observed in a four-layer sample.

On the theoretical side, one can mimic the gating effect of 2D materials by adding carriers into the unit cell and calculate the electronic structures by neutralizing with a homogeneous charge background.[8] For example, *Wang* et al.[8] have explained the correlation between the Curie temperature and carrier concentration of CrI_3 monolayer. As discussed above, t_{2g} valence bands and e_g conduction bands of Cr atoms are separated by the insulating gap in CrI_3 monolayer. As seen in Fig. 19(g), electron doping shifts the Fermi level into conduction bands, while hole doping moves the Fermi level into valence bands. In both situations, the spin-up channel in CrI_3 monolayer becomes metallic, while the spin-down channel remains insulating. This phenomenon renders the transition of exchange coupling mechanism from weak superexchange semiconductor to itinerant FM half-metal, which strongly enhances the FM stability [Fig. 19(h)] as well as the Curie temperature. To be specific, the calculated T_C increases from 75 K for pure CrI_3 to 150 K (300 K) for half electron (hole) doped CrI_3.[8] In 2D AFM semiconductor $MnPSe_3$, doping concentrations of electron (hole) above 3×10^{13} (4×10^{13}) carriers/cm^2 would induce a transition from antiferromagnetic semiconductor to ferromagnetic half-metal. MC simulations suggested the Curie temperature of doped 2D $MnPSe_3$ crystal reaches up to 206 K [Fig. 19(i)].[307] In pristine monolayer VCl_3 and VI_3 sheets, the Curie temperatures are only 80 and 98 K, respectively. They can be also be enhanced up to room temperature by carrier doping.[161] The carrier density dependent total energy differences per MAX_3 formula unit (M = V, Cr, Mn, Fe, Co, Ni; A = Si, Ge, Sn; X = S, Se, Te) between the AFM and FM phases were obtained from DFT-D2 calculations.[290] In the case of FM semiconductors, the competition between antiferromagnetic and ferromagnetic ordering can be substantially altered for *n* doping in $VSiTe_3$, $VSnTe_3$, $MnSiSe_3$, and $FeSnTe_3$, and *p* doping for $NiSiSe_3$, $NiSTe_3$, and $MnSnTe_3$, respectively. Hence, the associate T_C can be also tailored. The investigated range of carrier density is $10^{13} \sim 10^{14}$ carriers/cm^2. Based on these experimental and theoretical results, we can infer that a higher electron/hole doped concentration injected into 2D magnetic semiconductors would modulate the magnetic exchange mechanism and enhance the T_C to room temperature.

Using first-principles quantum transport approach, Dolui *et al.*[432] predicted that injecting unpolarized charge current parallel to the interface of bilayer-CrI_3/monolayer-$TaSe_2$ vdW heterostructure would induce a spin-orbit torque. Such effect will convert the first CrI_3 layer from AFM to FM ordering in direct contact with $TaSe_2$ without requiring any external magnetic field. This reversible current-driven

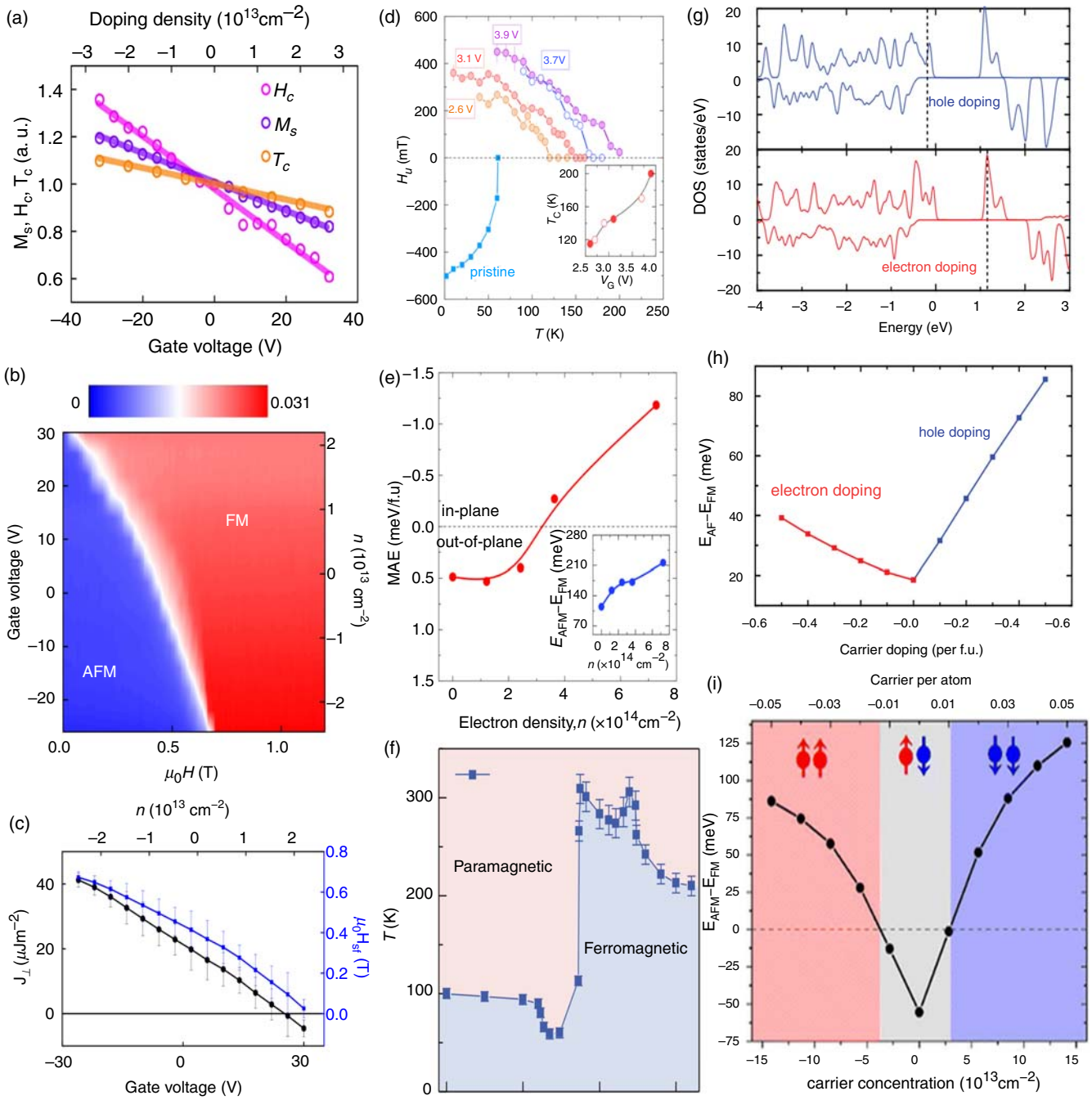

FIG. 19. (a) Coercive force, saturation magnetization, and Curie temperature as a function of gate voltage and gate induced doping density of bilayer CrI_3. (b) Doping density–magnetic field phase diagram of bilayer CrI_3 at 4 K. (c) Interlayer exchange constant and spin-flip transition field as a function of gate voltage and gate induced doping density for bilayer CrI_3. (d) Uniaxial magnetic anisotropy fields and T_C for different gate voltage of few-layer $Cr_2Ge_2Te_6$. (e) MAE of few-layer $Cr_2Ge_2Te_6$ as a function of electron density. (f) Phase diagram of trilayer Fe_3GeTe_2 sample varies with the gate voltage and temperature. (g) The DOS of 0.5 hole and 0.5 electron doped CrI_3 monolayer, and the dashed vertical lines refer to the shifting of Fermi level. (h) Relative energy of AFM and FM states under the variation of carrier concentration for CrI_3 monolayer. (i) Relative energy of AFM and FM states under the variation of carrier concentration for 2D $MnPSe_3$. Panels (a)–(c) reproduced with permission from Jiang *et al.*, Nat. Nanotechnol. **13**, 549 (2018). Copyright 2018 Springer Nature.[427] Panels (d) and (e) reproduced with permission from Verzhbitskiy *et al.*, Nat. Electron. **3**, 460 (2020). Copyright 2020 Springer Nature.[431] Panel (f) reproduced with permission from Deng *et al.*, Nature **563**, 94 (2018). Copyright 2018 Springer Nature.[50] Panels (g) and (h) reproduced with permission from Wang *et al.*, Europhys. Lett. **114**, 47001 (2016). Copyright 2016 IOP.[8] Panel (i) reproduced with permission from Li *et al.*, J. Am. Chem. Soc. **136**, 11065 (2014). Copyright 2014 American Chemical Society.[307]

nonequilibrium AFM-FM phase transition is due to the proximity effect, where evanescent wave functions from metallic $TaSe_2$ is injected to the first monolayer of CrI_3. During this process, the second monolayer of CrI_3 remains insulating.

D. Magnetic field

It is natural to utilize external magnetic field to control the magnetic properties of 2D magnets. As known, different types of magnetism are defined as how the system respond to the external magnetic fields. On the one hand, external magnetic field induced Zeeman spin splitting is used to control magnetic ordering. On the other hand, the applied magnetic field will enforce reorientation of the spin direction and thus determine their magnetic ground state. The Curie temperature may depend strongly on the applied magnetic field in terms of both strength and direction. If the external field is parallel to the direction of spontaneous magnetization, T_C typically increases with increasing external magnetic field. On the contrary, the magnetic ordering can be suppressed by applying an external magnetic field of opposite direction. For the perpendicular magnetic field direction, a complicated variation may arise because of the competition between the tendencies of both orderings.

For the recently reported 2D magnets, the effect of external magnetic field has been firstly investigated in atomic layers of $Cr_2Ge_2Te_6$. Gong *et al.*[37] found that bilayer $Cr_2Ge_2Te_6$ is a Heisenberg-type ferromagnet and the Curie temperature is about 40 K. The magnetic field control of the transition temperature of bilayer $Cr_2Ge_2Te_6$ is displayed in Fig. 20(a). Under a very small external magnetic field, magnetic anisotropy would be induced, and the corresponding T_C will increase rapidly. The picture of spin-wave excitation can explain the weak magnetic fields effect. For six-layer $Cr_2Ge_2Te_6$ under a magnetic field of 0.3 T, the calculated Curie temperature approaches the bulk value of 66 K. When ignoring the single ion anisotropy, the magnetic field helps increase the magnetic stiffness logarithmically in 2D materials, which is different from the exchange interactions in 3D materials. In bulk $Cr_2Ge_2Te_6$, the T_C enhancement originates from the effect of interlayer coupling.

Large external magnetic field can directly tune the magnetic coupling of 2D magnets. Liu *et al.*[433] systematically investigated the anisotropic behavior of $Fe_{3-x}GeTe_2$ in terms of anisotropic magnetization, magnetic entropy change, and critical behavior. Figure 20(b) presents the magnetization evolution between different magnetic field directions. The magnetization exhibits the minimum when H||ab, and it reaches the maximum when H||c, confirming that the easy axis of magnetization is along the c axis. The anisotropic magnetic entropy changes further give two types of magnetic couplings in $Fe_{3-x}GeTe_2$ for different magnetic field directions. Therefore, it was inferred that the magnetic correlation around T_C can be easily affected by magnetic field. Jiang *et al.*[434] suggested the spin direction of 2D CrI_3 can be switched from out-of-plane to in-plane by applying an in-plane external magnetic field to overcome the MAE barrier. The change of spin direction can significantly modify the electronic band structure, including Fermi surface, topological states, and bandgap [Fig. 20(c)]. Moreover, the impact of magnetic field is manifested by tunneling through the 2D magnets-based junctions. For example, Klein *et al.*[435] reported that metamagnetic transition results in magnetoresistance values of 95%, 300%, and 550% for bilayer, trilayer, and tetralayer CrI_3 barriers, respectively.

E. Interfacial engineering

The emerging 2D intrinsic vdW magnets offer an immediate playground to engineer them into various composites, which provide fruitful combinations for tailoring the physical properties and exploring the related applications on spintronics and quantum computing.[436] Choosing a 2D intrinsic magnet as one part of heterostructure,

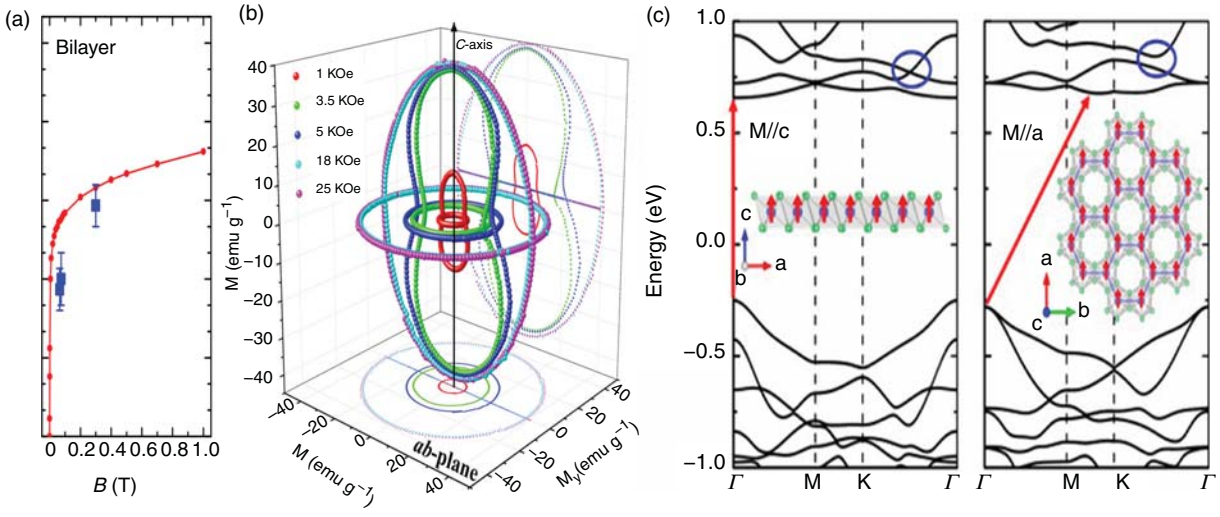

FIG. 20. (a) The magnetic field controlled T_C of bilayer $Cr_2Ge_2Te_6$. (b) The 3D plot of angle dependent magnetization under selected magnetic field. (c) The band structures with magnetic moment along in-plane a axis and out-of-plane c axis. Panel (a) reproduced with permission from Gong *et al.*, Nature **546**, 265 (2017). Copyright 2017 Springer Nature.[37] Panel (b) reproduced with permission from Liu *et al.*, Phys. Rev. B **100**, 104403 (2019). Copyright 2019 American Physical Society.[433] Panel (c) reproduced with permission from Klein *et al.*, Science **360**, 1218 (2018). Copyright 2018 American Association for the Advancement of Science.[435]

many different types of 2D materials can be stacked in the vertical direction as the other part. For example, one can integrate different 2D magnets together, stack the same kind of 2D magnets together, or combine 2D magnets with some other non-magnetic 2D materials. No doubt, the interlayer magnetic coupling in the resulting heterostructure is important, which is susceptible to the contacting materials in terms of vdW force/chemical bond, magnetic ordering, stacking modes, and the number of layers. Based on different combinations, many important mechanisms to modulate the magnetic properties have been proposed, including symmetry breaking, interlayer charge transfer, build-in electric field, overlap of electron wave functions, band alignment, orbital hybridization, dielectric screening, electron hopping paths, and SOC proximity.[90] These strategies for enhancing the T_C by tuning their interfacial interaction are broadly highlighted as interfacial engineering.

As we stated above, the magneto-optical Kerr effect firstly confirmed the existence of magnetism in atomically thin CrI_3 sheets.[28] Remarkably, 2D CrI_3 systems also exhibit magnetic response dependent on the number of layers. The magnetic ground states of monolayer, bilayer, and trilayer CrI_3 are FM, AFM, FM, respectively, while the magnetic ground state of 3D bulk CrI_3 crystal is FM. The AFM interlayer coupling in bilayer CrI_3 is mainly due to structural transition[437] and super-superexchange interaction.[23] The T_C of monolayer and trilayer CrI_3 is 45 and 61 K, respectively, meaning that the magnetic coupling is strengthened as the thickness of CrI_3 sheet increases. The dependences of T_C/T_N on the number of layers have also been found in the other experimentally fabricated 2D magnets, including Fe_3GeTe_2,[41,50] $CrGeTe_3$,[37] $FePS_3$,[48] and $MnBi_2Te_4$.[319] Unlike CrI_3, there is no thickness-induced flipping of magnetic ground state in multilayer Fe_3GeTe_2, $CrGeTe_3$, and $FePS_3$ systems. However, their increasing trend with the number of layers behaves differently, which are more pronounced in Fe_3GeTe_2 and $CrGeTe_3$. The T_C of four- or five-layer Fe_3GeTe_2 is 220 K, dropping to 180 K for bilayer, and finally to 130 K for monolayer.[41] For $CrGeTe_3$, the T_C of bilayer and bulk phase is 41 and 66 K, respectively. In contrast, the value of T_N in AFM $FePS_3$ is not sensitive to the number of layers, with a fixed value of 118 K.[48] In addition, the unique layer-dependent magnetism has also been found in $MnBi_2Te_4$.[319] The monolayer $MnBi_2Te_4$ is a topologically trivial ferromagnet, whereas the multilayer systems made up of odd and even numbers of layers are interlayer ferromagnets and antiferromagnets, respectively.

To further improve the Curie temperature, 2D heterostructures consisting of different magnetic materials are highly anticipated. At the interface of vdW heterostructures, more significant charge transfer and increasing external extra spin-exchange paths can be introduced to enhance the interlayer coupling strength.[438–440] For example, Fu *et al.*[439] proposed to induce out-of-plane surface magnetism in the AFM $MnBi_2Te_4$ films via magnetism proximity with magnetic CrI_3 substrate. A strong exchange bias of ∼40 meV originates from the long Cr-e_g orbital tails that hybridize strongly with Te-p orbitals. Taking monolayer CrI_3 on $MoTe_2$ as a prototype system, Chen *et al.*[440] revealed that CrI_3/$MoTe_2$ heterostructure is an intrinsic FM semiconductor with T_C of ∼60 K, which is 15 K higher than that of pure CrI_3. The value of T_C can be further enhanced to ∼85 K by applying an out-of-plane pressure of 4.2 GPa, which corresponds to the reduced interlayer distance of 1.2 Å. Such a doubling of T_C comes from the introduction of extra spin Cr–Te–Cr superexchange paths [Fig. 21(a)].

Motivated by these discussions, Liu *et al.*[441] recently investigated the magnetic coupling between selected bulk semiconducting substrates and bilayer CrI_3, such as CdSe (0001), ZnS (0001), ZnO (0001), Si (111), SnS, MoS_2, WSe_2, GaSe, h-BN, black phosphorus, and InSe. They found that the relatively strong covalent interaction, i.e., CdSe (0001), ZnS (0001), and ZnO (0001), would significantly enhance the interlayer exchange. Meanwhile, the stability of intralayer FM state has also been improved. Hence, AFM to FM transition was observed on bilayer CrI_3. DFT calculations further confirmed that such strong proximity effect originates from the prominent charge transfer from substrates. The interlayer coupling between semiconducting substrates and bilayer CrI_3 leads to charge doping from the semiconducting substrates to the band structures of CrI_3, which in turn enhances the occupation of e_g orbitals of Cr atom and significantly increases the t_{2g}-e_g hybridization. Consequently, the FM exchange coupling is strengthened.[441] On the experimental side, Xiu *et al.* also observed interfacial proximity effect at Fe_3GeTe_2/CrSb interface by performing elemental-specific XMCD measurements, which would enhance T_C of four-layer Fe_3GeTe_2 from 140 to 230 K. The inverse proximity effect drives the interfacial antiferromagnetic CrSb into ferromagnetic state, and the Fe-Te/Cr-Sb interface is strongly ferromagnetic coupled. Meanwhile, doping of spin-polarized electrons by the interfacial Cr layer gives rise to enhancement of T_C of the Fe_3GeTe_2 films.[442]

Within the framework of octahedral crystal field, a more direct electron-counting rule has been proposed to describe the interlayer magnetic coupling of magnetic bilayers.[443] The components include MX_2 (M=V, Cr, Mn; X = S, Se), MX_2 (M = Mn, Fe, Co, Ni; X = Cl, Br), MI_3 (M =V, Cr), and $CrGeTe_3$ monolayers. The exchange interaction in all these 2D magnetic monolayers has been well demonstrated by the superexchange mechanism. Based on the occupation number of d electrons, their electronic configurations can be denoted as type-I $t_{2g}^{x}e_g^{y}$ ($x + y < 5$) and type-II $t_{2g}^{x}e_g^{y}$ ($x + y \geq 5$). In other words, there is no empty low-energy d orbital in the type-II layer. Therefore, three types of bilayer heterostructures can be built by these two kinds of monolayer components, i.e., type I-I, II-II, and I-II. By considering the hopping pathways, one can figure out that the exchange interaction between the occupied and occupied orbitals (type II) belongs to AFM ordering. However, the hopping pathways through the occupied-to-occupied orbitals and the occupied-to-empty orbitals coexist; thus type I-I and I-II bilayer structures exhibit competing FM and AFM orderings. Moreover, FM coupling is usually more favorable for I-II bilayer because of the orbital orientation and large on-site U value. All these discussions are illustrated in Figs. 21(b)–21(d). This exchange mechanism can be also applied to explain most of the magnetic metallic bilayers well (VSe_2, CrS_2, $MnSe_2$, $FeCl_2$, and $FeBr_2$). Beyond this mechanism, the intralayer itinerant carriers should be introduced, which would bring about additional FM exchange effect.[443]

For the heterojunctions consisting of magnetic and non-magnetic monolayers, the non-magnetic part can experience strong magnetic exchange field (MEF), which is termed as magnetic proximity effect. This effect can break the time reversal symmetry either to introduce FM ordering into a topological insulator (TI)[444–448] or to lift the valley degeneracy of graphene and TMD.[449–456] When a TI is in contact with a ferromagnet, both time-reversal and inversion symmetries are broken at the interface. An energy gap is thus formed at the TI surface, and its electrons gain a net magnetic moment through

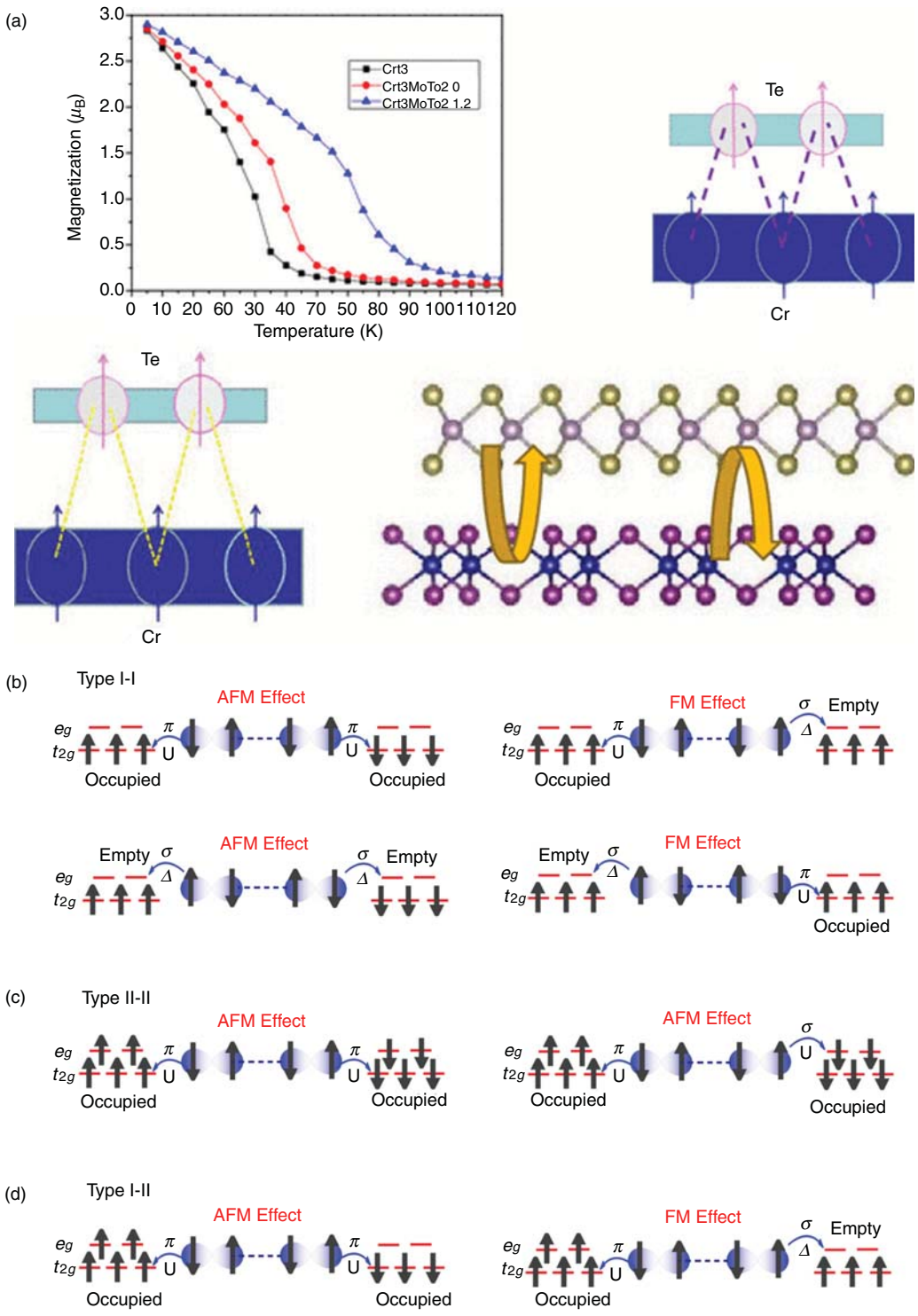

FIG. 21. (a) The Curie temperature and the additional superexchange interactions in compressed and uncompressed $CrI_3/MoTe_2$ heterostructure. (b)–(d) The exchange pathways for type I-I, type II-II, and type I-II bilayers, respectively. Δ and U represent the t_{2g}-e_g crystal field splitting and on-site Hubbard energy, respectively. π and σ represent the *d-p* atomic bonding type. Panel (a) reproduced with permission from Chen *et al.*, J. Phys. Chem. C **123**, 17987 (2019). Copyright 2019 American Chemical Society.[440] Panels (b)–(d) reproduced with permission from Xiao *et al.*, 2D Mater. **7**, 045010 (2020). Copyright 2020 IOP.[24]

short-range exchange interactions. For example, the integration of monolayer nonmagnetic WSe_2 and ultrathin FM semiconductor CrI_3 provides unprecedented control of spin and valley pseudospin in WSe_2, where a large MEF of nearly 13 T and rapid switching of the WSe_2 valley splitting and polarization via flipping of the CrI_3 magnetism are detected.[451] Moreover, the WSe_2 photoluminescence intensity strongly depends on the relative alignment between photoexcited spins in WSe_2 and CrI_3 magnetization, because of ultrafast spin-dependent charge hopping across the heterostructure interface. Zhang *et al.*[456] believe that the monolayer VSe_2 is on the verge of magnetic transition. Though interfacial hybridization with Co atomic overlayer, a magnetic moment of ~0.4 μ_B per V atom has been detected experimentally. Such magnetic interface is free from extrinsic contamination and could be useful for many spin-based effects.

For the heterojunctions consisting of magnetic and nonmagnetic monolayers, the magnetic part can also experience a magnetic phase transition. For example, heterostructures of α-$RuCl_3$ on graphene, WSe_2, and EuS have been recently synthesized.[457] Among them, the insulating α-$RuCl_3$ layer is thought to be in proximity to a quantum spin liquid. The heterostructure undergoes hole doping of the graphene, WSe_2, and EuS layers with low work function and electron doping of α-$RuCl_3$ layer,[457] respectively. This phenomenon mainly originates from charge transfer between the correlated insulating layer and itinerant layer.[458] In addition, magnetic tunnel junction is also very important to develop the spintronic device. The large magnetoresistance amounting was found in graphite-CrI_3-graphite and Fe_3GeTe_2-BN-Fe_3GeTe_2 multilayer structures.[154,435,459,460]

F. Defect engineering

Defects, such as vacancies, adatoms, and substitutional impurities, inevitably exist in 2D materials. The presence of these defects leads to significant impacts on the magnetic properties. For example, many experimental studies have revealed that room-temperature ferromagnetism can be introduced into nonmagnetic TMDs like MoS_2, $PtSe_2$, SnS_2, WS_2, $MoTe_2$, and WSe_2 via doping of 3*d*/4*d* transition metal atoms (i.e., Ti, V, Cr, Mn, Fe, Co, Ta, and Ni).[461–464] Therefore, various strategies of defect engineering can be developed for realization of the 2D intrinsic magnets with high Curie temperature. Rational design of defects is able to optimize their types, concentration, and spatial distribution. Hence, understanding the role of defects on magnetic exchange interaction as well as developing effective defect engineering schemes are of great significance for the future development of 2D spintronics.

Based on DFT calculations, Zhao *et al.*[465] investigated the electronic and magnetic properties of CrI_3 monolayer with surface I vacancies (denoted as IV-CrI_3). First, the incorporation of I vacancies would break the symmetry. The two Cr atoms located close to I vacancy (denoted as I-Cr atoms) are different from the other Cr atoms. The magnetic moment of the I-Cr atom increases from 3 to 3.5 μ_B due to about ~0.5 electrons gained from each I vacancy. Second, the introduction of I vacancies will reduce the bandgap. With vacancy concentration of 1.96×10^{-6} mol/m^2, the bandgap will decrease from 1.13 eV for pristine CrI_3 to 0.16 eV for IV-CrI_3. More importantly, incorporation of I vacancies is able to improve T_C. The T_C of defective IV-CrI_3 monolayers with vacancy concentrations of 0.65, 0.98, and 1.96×10^{-6} mol/m^2 are 38, 38, and 44 K, respectively, in comparison with T_C = 35 K for pristine CrI_3. To reveal the origin of such increments of Curie temperature, the exchange mechanisms of CrI_3 and IV-CrI_3 are schematically displayed in Figs. 22(a) and 22(b), respectively. The virtual hopping of two pathways, i.e., t_{2g} and e_g levels, and e_g and e_g levels, are affected by I vacancies. With I vacancy, the former hopping pathway enhances the FM superexchange interaction by shortening the separation of t_{2g} and e_g levels. The latter one also strengthens FM coupling around the I vacancy, which is dominated by double exchange interaction. As a result, the effective ferromagnetic exchange is enhanced.[465]

The effects of different defect types on the magnetic performance of CrI_3 monolayer have been discussed by Wang *et al.* based on defect theory and first-principles calculations.[466] In total, 20 types of defects have been constructed, including vacancy, interstitial, substitution, and bond-rotation defects. The calculated energy differences between FM and AFM states (ΔE) are summarized in Fig. 22(c). It was found that most point defects, such as V_{Cr}, V_I, V_{Cr2}-2, V_{Cr2}-4, and Cr_I, can increase the energy difference ΔE. Hence, the resulted T_C will be also enhanced, and the highest T_C reaches 210 K in CrI_3 system with Cr_I defect. In addition, the relationship between Cr–Cr distance and ΔE are discussed and shown in Fig. 22(d). One can see that AFM (FM) appears when Cr−Cr distance is less (larger) than 3.70 Å (4.04 Å). This means that point defects in 2D CrI_3 can trigger the FM-AFM transition by distorting their local configuration. Recently, similar results have also been discussed by Pizzochero *et al.*[467] The magnetic properties of CrI_3 monolayer embedded with transition metal atoms of most 3*d* and 4*d* elements have been evaluated using DFT calculations.[468] Among them, Ti implantation elevates the magnetic moment from 6.0 to 10 μ_B per unit cell and renders the CrI_3 monolayer transition from semiconducting to half-metallic. The estimated T_C of Ti-embedded CrI_3 monolayer reaches up to 282 K.

Since 2D materials have large surface-to-volume ratio, they are favorable for adsorption of other atoms or gas molecules. As a representative model, Guo *et al.*[469] found that ultrathin CrI_3 nanosheets can be tailored from FM insulator to FM half-metal by adsorption of Li atoms. The total magnetic moment and energy difference between FM and AFM phase (E_{AFM-FM}) of Li adsorbed CrI_3 sheets increase linearly with the increase of Li concentration. For 100% Li coverage, the E_{AFM-FM} can reach up to 125 meV, which is 50% higher than that of pure CrI_3 monolayer and suggests a much higher T_C. Bader charge analysis showed that each adsorbed Li atom donates about 0.83 electrons to the six surrounding I atoms. In Sec. IV C, we have already discussed that charge doping can significantly improve the magnetic stability.

Considering the exposed atmosphere, the magnetic properties of $Cr_2Ge_2Te_6$ monolayer adsorbed with various gas molecules (i.e., CO, CO_2, H_2O, N_2, NH_3, NO, NO_2, O_2, and SO_2) have been systematically investigated.[470] The former five molecules behave as donors, whereas the latter four molecules act as acceptors. All these gas molecules can effectively enhance the ferromagnetism and Curie temperature of $Cr_2Ge_2Te_6$ monolayer, which are ascribed to the considerable charge transfer as well as the alignment of the frontier molecular orbital. Among them, the T_C of NO and NO_2 adsorbed $Cr_2Ge_2Te_6$ systems are 213 and 205 K, respectively, which are substantially higher than 156 K of pristine $Cr_2Ge_2Te_6$.

Besides FM semiconductor, one should also note that the defects in itinerant FM metal may either suppress or retain the FM coupling. In 2D metal VSe_2, theoretical studies suggested that the weak

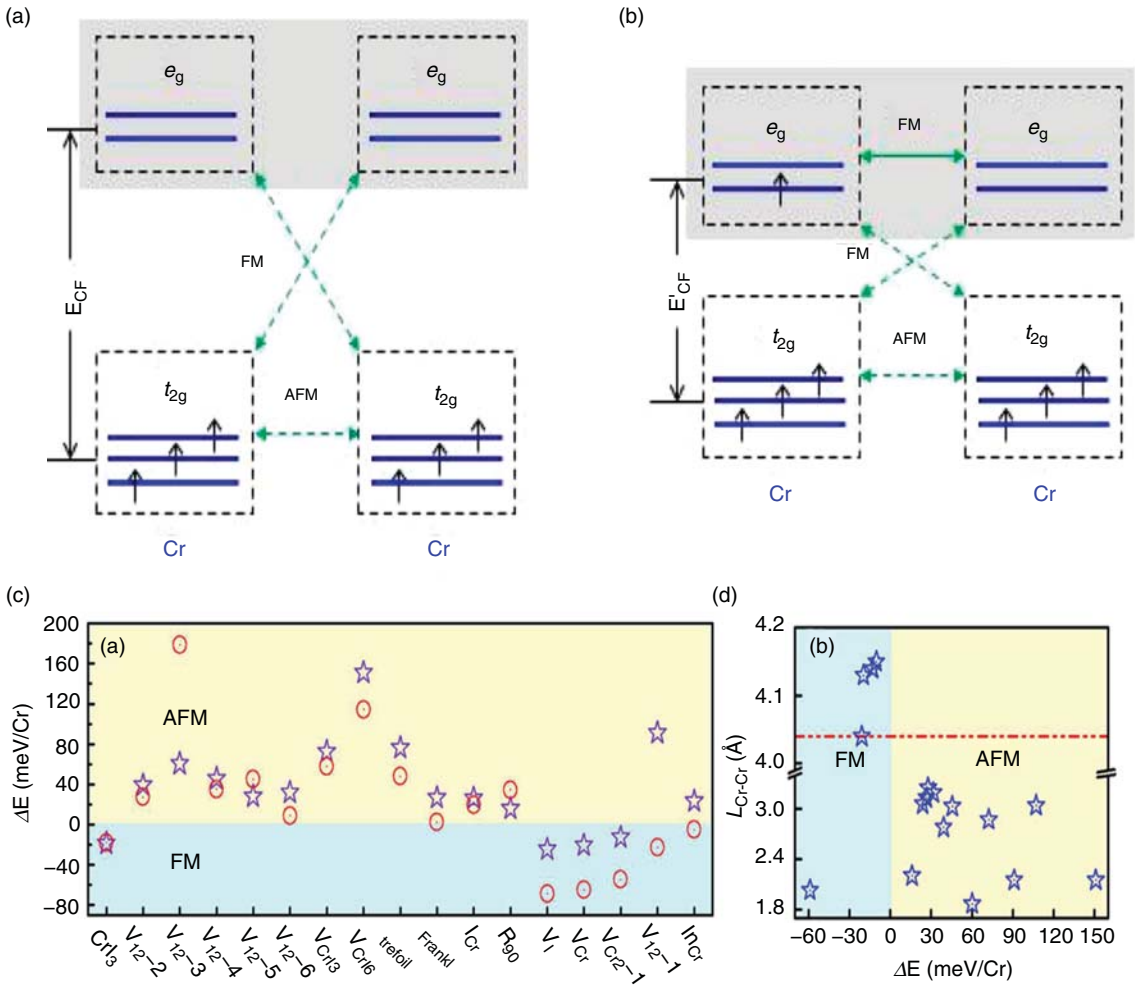

FIG. 22. (a) The magnetic exchange mechanism of pristine CrI_3. (b) The magnetic exchange mechanism of CrI_3 with I vacancy. (c) The energy difference of FM and AFM states (ΔE) from DFT calculations (blue stars) and Heisenberg model calculations (red circles). (d) Relationship between ΔE and the Cr–Cr bond length near the point defect. Panels (a) and (b) reproduced with permission from Zhao *et al.*, Nano Lett. **18**, 2943 (2018). Copyright 2018 American Chemical Society.[465] Panels (c) and (d) reproduced with permission from Wang *et al.*, Chem. Mater. **32**, 1545 (2020). Copyright 2020, American Chemical Society.[466]

localization effect introduced by some specific defects would lead to a FM-PM transformation.[471] Based on the magnetic data, the paramagnetism of 2D VSe_2 is possibly attributed to edge related defects, interstitial atoms or dislocations. Recent STM/XMCD/MFM experiments by Chua's group have also demonstrated this phenomenon.[192] They observed the formation of Se-deficient line epitaxially grown on MoS_2 via thermal annealing and these reconstructed VSe_2 monolayers displayed room temperature ferromagnetism. The corresponding DFT calculations have also indicated the enhancement of magnetization after reconstruction.

To confirm the intrinsic ferromagnetism, Chua *et al.* inferred that defect-free sample is the key in 2D VSe_2.[192] For 2D $MnSe_2$, the presence of high-density Se vacancies in single layer $MnSe_2$ can stay as a dynamically stable ferromagnetic 2D crystal.[144] Considering the total energies for two defective magnetic phases, the FM state still yields 15 meV more per formula than the AFM state.

G. Janus engineering

In the above contents, we have already discussed many feasible strategies to modify the magnetic properties of 2D materials, including intercalations, stacking the 2D van der Waals heterojunction, and applying an external electric field and strain. In fact, they all indicated the decisive role of symmetry breaking of atomic structures. Two-dimensional Janus materials, naturally possessing the out-of-plane mirror asymmetry, are expected to modify the magnetic exchange interaction. In experiments, such 2D Janus materials have been successfully fabricated. For example, Janus MoSSe monolayer materials have been prepared by selenizing MoS_2 monolayer or substituted sulfurization reaction for $MoSe_2$ monolayer.[472,473]

According to previous experiments, the transition metal trihalides CrI_3, VI_3, and TMD VSe_2 were reported to be FM materials. Starting from the structures of transition metal trihalides (MX_3) and TMD (MX_2), the corresponding Janus structures of MX_3 and MX_2

can be constructed by replacing all X atoms in one plane by another halide/chalcogenide Y atoms, labeled as $M_2X_3Y_3$ and MXY, respectively. The point group symmetry of both MX_3 and MX_2 monolayers is D_{3v}. Accordingly, the 3*d* orbitals of transition metal atom M would split into two-fold degenerate d_{z2} and d_{x2-y2} orbitals and three-fold degenerate d_{xz}, d_{yz}, and d_{xy} orbitals. Due to the breaking of mirror symmetry, the point group symmetry of Janus $M_2X_3Y_3$ and MXY reduces to C_{3v}. The different halide/chalcogenide atoms in the top and bottom layers would induce non-degenerated 3*d* states; that is to say, the five d_{xz}, d_{yz}, d_{xy}, d_{z2}, and d_{x2-y2} orbitals have distinct features. Based on different electronegativities of the halide/chalcogenide atoms in the top and bottom layers, the strength of FM coupling in $M_2X_3Y_3$ and MXY monolayers is mediated by X/Y atoms through a superexchange mechanism or a double exchange mechanism.[25,474] Therefore, high T_C could be obtained by Janus MX_3 and MX_2 monolayers.[474–477]

As a specific example, DFT calculations by He *et al.*[475] predicted that the Janus TMD monolayers have large spin polarization and high Curie temperature. The room-temperature Curie temperatures were found for 2D VSSe and VSeTe among Janus systems of MXY (M = V, Cr, Mn; X, Y = S, Se, Te; X ≠ Y). The V atoms and nearest-neighboring S/Se/Te atoms keep an AFM spin arrangement. Hence, double exchange interaction induced FM ordering is most favorable. Zhang *et al.*[476] have also found that VSSe monolayer is a highly stable room-temperature ferromagnet (T_C = 346∼1079 K) by particle-swarm search and DFT calculations.

Stimulated by the low T_C of CrI_3, the magnetic properties of 2D Janus $Cr_2I_3X_3$ (X = Br, Cl) monolayers have been studied by DFT calculations.[474] The exchange energies in CrI_3, $Cr_2I_3Br_3$, and $Cr_2I_3Cl_3$ were 42.7 meV, 25.7 meV, and 20.5 meV, respectively, indicating their FM ground states. Based on MFT theory and Heisenberg model, the T_C of CrI_3, $Cr_2I_3Br_3$, and $Cr_2I_3Cl_3$ were predicted to be 55, 33, and 26 K, respectively. Moaied *et al.* systemically explored the electronic and magnetic properties of CrX_3 (X = Cl, Br, I) and their Janus monolayers X_3-Cr_2-Y_3 (X, Y = Cl, Br, I, X; X ≠ Y). They found both electronic gap and Curie temperature are sensitive to the halide atoms. Unfortunately, the T_C of Janus systems is lower than that of CrI_3. Unlike in CrI_3, the Janus strategy shows a positive effect on T_C in VI_3.[477] From first-principles calculations, the Curie temperatures of VI_3-derived Janus monolayers, i.e., $V_2Cl_3I_3$, $V_2Br_3I_3$, and $V_2Cl_3Br_3$, were determined to be 240, 224, and 232 K, respectively, which is at least 170 K higher than the value of VI_3 (50 K). Such dramatic increment on the T_C of Janus VI_3 monolayers was ascribed to the reduced virtual exchange gap G_{ex} from one occupied t_{2g} state to empty e_g states, which mainly determines the strength of FM coupling. The corresponding G_{ex} values were 1.73, 2.156, 0.395, 0.397, and 0.445 for VI_3, CrI_3, $V_2Cl_3I_3$, $V_2Br_3I_3$, and $V_2Cl_3Br_3$, respectively. Thus, the superexchange interactions in $V_2Cl_3I_3$, $V_2Br_3I_3$, and $V_2Cl_3Br_3$ are enhanced relative to VI_3 and CrI_3, owing to the reduced virtual exchange gap, G_{ex}.

H. Optical controlling

Beyond the above modification strategies, optical controlling magnetic properties are also highly anticipated, since no contact is involved. To revolutionize the future technology of magnetic storage and spintronics, optical induced manipulation of spin has advantages of fast speed and low power dissipative.[478] Recent breakthrough in 2D magnets highlights the research of optically tuning of magnetism. Several pioneer works have already been carried out to investigate the interaction of light and magnetism.

Based on first-principles calculations, Tian *et al.*[479] studied the ground state of monolayer $RuCl_3$ under optical doping. They found that optical doping can cause a phase transition from spin-liquid phase to FM ordering with a moderate electron-hole (e-h) density. The optically tunable 2D magnetism in $RuCl_3$ and the calculated exchange coupling constants under different doping densities are schematically plotted in Figs. 23(a)–23(c). We can see both ferromagnetism and Curie temperature are significantly increased with increasing optical doping e-h pair density. As e-h pair reaches up to 3×10^{13} cm^{-2}, T_C is close to room temperature. Such enhancement originates from the itinerant electron mechanism, which is demonstrated by PDOS analysis. The Van Hove singularities in the PDOS appear right above and below the Fermi energy, which have the characteristics of localized Ru t_{2g} orbital.[479]

The optically manipulating magnetic order transition was also predicted in MXenes.[480] DFT calculations revealed that the initial ground states of $Cr_2VC_2F_2$, $Mo_2VC_2F_2$, $Mo_2VN_2F_2$, $Mo_3C_2F_2$, and $Mo_3N_2F_2$ are ferrimagnetic. The real time time-dependent DFT simulations on these MXenes showed that the FiM state will transform to FM state at the early stage of simulation. Figures 23(d)–23(h) display the spin dynamics of $Cr_2VC_2F_2$ MXene under a laser pulse. The local magnetic moments on both Cr and V atoms change dramatically. However, the total magnetic moment in the MXene is retained. At 5.8 fs, the spin direction of V atom is reversed from −0.4 to 0.9 μ_B, which results in a magnetic ordering transition from FiM to FM. The microscopic mechanism underpinning this ultrafast switching of magnetic ordering is governed by optically induced inter-site spin transfer effect. In addition, other critical magnetic parameters, such as MAE and magnetic exchange field, can be optically controlled in WSe_2/CrI_3 heterostructures and CrI_3 monolayer.[455,481]

V. CONCLUSION AND OUTLOOK

In this paper, we have comprehensively reviewed recent experimental and theoretical progress on the 2D intrinsic magnets. Their fundamental physical parameters, magnetic origin, and underlying mechanism of exchange interaction have been discussed. Despite the great achievements during the past decade, the research of 2D intrinsic magnets is still in its early stage and calls for continuous efforts. Going forward, there are four rapidly expanding fields in the foreseeable future. The first one is the discovery of "unknown" room-temperature 2D magnets. The second one is to deeply understand the spin coupling mechanism and provide some feasible ways to manipulate the spin. The third one is to further explore the complex spin-based effects, especially on systems with both magnetism and superconductivity, FM and ferroelectrics (FE), FM and ferroelastics (FA), magnetism and TI, and magnetism and thermoelectricity. Based on the newly found 2D intrinsic magnets, the fourth one is to integrate them into practical devices. We will further elaborate on these issues in this section.

From the theoretical point of view, many hypothetical 2D magnetic materials have been proposed. However, their structural stability, environmental stability at ambient air, and experimental feasibility for synthesis still need to be further confirmed.[31,92] Moreover, their magnetic ground states and Curie temperatures sometimes depend on the theoretical methodology, e.g., exchange-correlation functionals, the choice of U term and the details of Heisenberg model. Some are poor

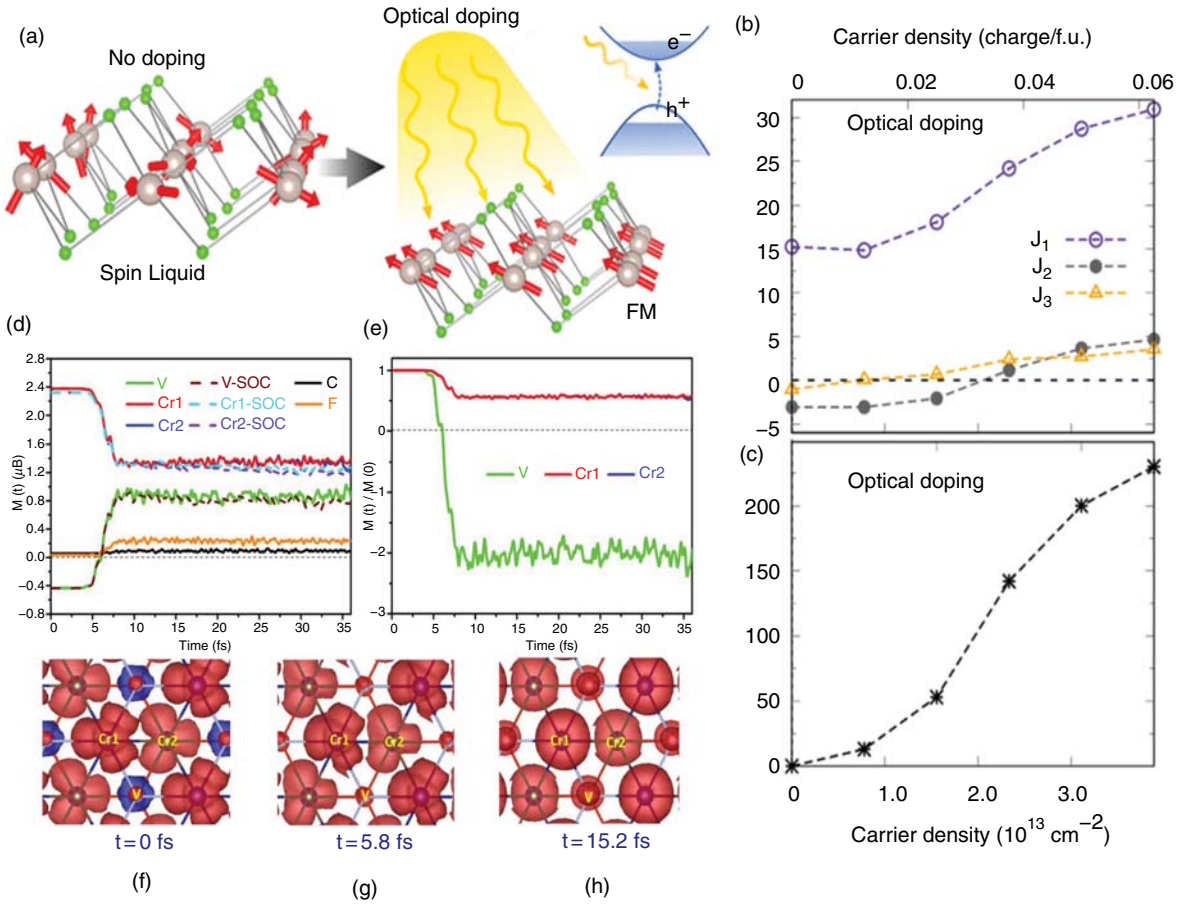

FIG. 23. (a) Schematic plot of the optically tunable magnetism in 2D $RuCl_3$. (b) The exchange coupling constants according to optical doping in $RuCl_3$. (c) Variation of T_C for $RuCl_3$ under optical e-h doping. (d) The time evolution of local magnetic moment in $Cr_2VC_2F_2$. (e) The relative magnetization dynamics for Cr_1, Cr_2, and V atom in $Cr_2VC_2F_2$. (f)–(h) The snapshots of magnetization density at different time. Panels (a)–(c) reproduced with permission from Tian *et al.*, Nano Lett. **19**, 7673 (2019). Copyright 2019 American Chemical Society.[479] Panels (d)–(h) reproduced with permission from He *et al.*, J. Phys. Chem. Lett. **11**, 6219 (2020). Copyright 2020 American Chemical Society.[480]

functionals and/or don't properly include correlation effect, which may give inaccurate results. In this regard, the electronic and magnetic properties of these 2D materials should be calculated with high-level accuracy. Meanwhile, these reliable results will provide a starting point for further data analysis and screening.[68,482] Then high-throughput computation and machine learning can greatly accelerate the discovery of 2D magnetic materials and help understand the magnetic exchange interaction as well as the origin of magnetic ordering thoroughly.[483]

On the experimental side, besides exfoliation of 2D magnets from the corresponding 3D layered materials, other approaches for directly growing high-quality 2D magnets should be developed. For example, MBE allows us to create novel 2D ultrathin films from those that are not inherently layered materials. This method has demonstrated its success in preparing 2D magnetic, CrI_3,[484] TMDs (VSe_2, $MnSe_2$, VTe_2, $CrTe_2$), and MnSn at high temperature.[34,35,192,485] By carefully controlling the temperature of CVD method, Kang *et al.*[209] have synthesized antiferromagnetic ultrathin 2D layered tetragonal FeTe nanoplates and ferromagnetic non-layered hexagonal FeTe nanoplates with thickness down to 2.8 and 3.6 nm on SiO_2/Si substrates, respectively. The observed T_N of the former phase is 71.8 K, while the T_C of the latter phase is 220 K. In addition, chemical vapor transport is also an efficient strategy for producing highly crystalline 2D magnets in industry, such as CrI_3 nanolayer.[486] Han *et al.*[487] further demonstrated the important role of iodine buffer layer and the role of CrI_2 clusters as building units, which pointed out the reason of achieving 2D CrI_3 sheets with nanolayer. In addition, syntheses of 2D magnetic films using techniques like electrochemical deposition, metal-organic chemical vapor deposition, pulsed laser deposition, sputtering, and thermal evaporation are in their infancy and need further investigation. All these methods provide valuable insights for the preparation of 2D magnets, which could certainly extend the experimental database of emerging 2D magnetic materials. Moreover, direct growth of 2D magnets on Si substrates is beneficial for compatibility with the mature Si technology.

With respect to the specific category of 2D intrinsic magnets, 2D binary transition halides have received the most attention so far. However, the dominated *d-p-d* superexchange interaction usually leads to very low T_C. Hence, the effective methods (such as electron

doping and phase controlling) to improve the T_C of these semiconductor need to be further explored. To date, few 2D TMD materials have been demonstrated as high-temperature FM metals. However, there are still some disagreements on their magnetic behavior. The effects of CDW and defects on the magnetic ground states need to be carefully examined. Both effects contribute to the ongoing controversial debates regarding the magnetic properties of 2D VSe_2.[192] Moreover, new FM semiconductor phases are still highly expected in the 2D TMD families. We surprisingly noticed that plenty of MXene phases are predicted to possess high T_C. However, their magnetic properties are sensitive to the functional groups terminated on the outer surface. Owing to the difficulty of attaining MXene sheets with ordered functional groups, it becomes a rather challenging task to prepare the robust magnetic MXenes in laboratory. Among ternary transition metal compounds M-X-Y, the relationship between magnetism and composition is an important topic. Among this big family of 2D materials, many promising systems stand out, such as $CrXTe_3$ (X = Si, Ge, Sn), MPX_3 (X = S, Se, Te), Fe-Ge-Te, $MnBi_2Te_4$, and MXY (X = O, S, Se, Te, N; Y = Cl, Br, I) compounds. Some of them have been successfully synthesized in laboratory and found to exhibit high T_C, novel layer-dependent AFM behavior, interesting topological quantum states, and high carrier mobility. Therefore, we expect to find more 2D analogues in this family. Moreover, the random combinations of M, X, and Y atoms in ternary transition metal compounds may further cause more complicated magnetic exchange interactions, which in turn would be beneficial to achieve high magnetic transition temperature.

The long-range *p*-electron and *f*-electron based 2D magnets were reported in a series nonstoichiometric compounds and Gd-based compounds, respectively. The competition between the localized and delocalized behavior of electrons may bring into new magnetic exchange interaction mechanism. Hence, relevant efforts toward high-temperature magnetism are promising. Moreover, a series of ultrathin films and non-vdW materials, which exhibit room temperature FM ordering, were also reported.[34,35,172,209,485,488] It is therefore anticipated that large amounts of 2D magnetic materials beyond vdW family will be unveiled soon. There is also plenty of room in the 2D organic magnets, as the combination of coordination chemistry and crystal engineering enables intentional design of organic molecule based 2D frameworks with good magnetic stability and highly tunable magnetic properties. So far, the general performance of 2D organic magnets is still modest compared to that of 2D inorganic magnets. Room-temperature FM semiconductors are expected by rational design of molecular assemblies and organic ligands.

Generally speaking, AFM ordering in 3D materials is more common than FM ordering. However, 2D antiferromagnetic materials are rarely reported in comparison with the widely investigated 2D ferromagnets. In fact, many unique properties make 2D AFM materials even superior to 2D ferromagnets for practical device implementations. 2D antiferromagnets may allow the continuous miniaturization of spintronic devices. They have the advantage of being insensitive to the parasitic external magnetic fields and high read/write memory, and are thus poise to become an integral part of the next-generation logical devices and memory.[489]

Recently, 2D magnets with complex spin configurations are also of great interest, which are most relevant to quantum Hall effect,[490,491] high-temperature superconductivity,[492] and data storage.[493] Therefore, their identification and interpretation are the important issues. For example, the concept of quantum spin liquid has been first proposed in 1973 as the ground state for a system of spin on a triangular lattice.[494] One intuitive description of the quantum spin liquid state is as a liquid of disordered spins. This state is not like the other disordered states, which will preserve its disorder to very low temperatures. Until now, no real 2D magnetic material with quantum spin liquid state has been identified. Based on previous investigations,[495] there have been many justifications to look for 2D quantum spin liquid: (1) frustration; (2) low spin; (3) the proximity to the Mott transition; (4) all the proposed spin liquid candidates follow the triangular, honeycomb, Kagome, hyperkagome, and square lattices.[496] Moreover, several theoretical spin models have been proposed to describe quantum spin liquid state, including Kitaev model, spin 1/2 antiferromagnetic Heisenberg model, triangle J_1-J_2 model, and so on. In addition, several semiempirical methods are also reported to screen out the 2D quantum spin liquid rapidly. For example, Liu *et al.* predicted the quantum phase transition occurs when the ratio between the second neighboring exchange interaction and the first neighboring interaction falls into the spin liquid range ($0.21 \sim 0.28$).[492]

Nowadays, many strategies have been proposed to modify the magnetic properties of 2D materials, including strain engineering, intercalation, electric controlling, magnetic field, interfacial engineering, defect engineering, Janus engineering, and optical tuning. However, these strategies have only been assessed for a few experimentally reported 2D magnets. For plenty of the newly discovered 2D magnets, their magnetic responses to strain, electronic doping, magnetic field, and other modification strategies have not been unveiled. In addition, these strategies mainly focus on optimization of the exchange interaction, while magnetic anisotropy is also crucial for suppressing fluctuations and destroying the long-range ordering, which should be taken into account simultaneously. For practical device applications, many approaches might be properly combined for the best performance of 2D magnets.

The coexistence of FM and ferroelectrics, FM and ferroelastics, namely, multiple ferroic phase, could lead to novel physics and new applications. For example, the FM-FE coupling, known as the magnetoelectric effect, is able to generate unique ability of tuning magnetism by applying electric field and vice versa, which are very promising for logic devices.[497,498] The strong FE and FA coupling will provide an extraordinary platform for the design of strain controllable spintronic devices. Among them, 2D FM has been well investigated, while 2D FE and FA are rarely found. So far, only a few candidates of 2D multiferroic materials have been proposed, including $VOCl_2$, $VOBr_2$, VOI_2, CrSX (X = Cl, Br, I), and $Hf_2VC_2F_2$.[19,499,500] Based on the finding of 2D FM materials, searching and designing 2D multiple ferroic materials are still underway. In this regard, 2D multiple ferroic materials hold promising opportunities in practical applications for subsequent investigations.[501]

It would be also important to know the interplay between magnetism and superconductivity, which is the main topic in the fields of high-temperature superconductivity and superconductor spintronics. Normally, these two states are mutually exclusive. However, their coexistence was observed in some specific layered cases, such as $LaAlO_2/SrTiO_3$ interfaces,[502,503] molecule-adsorbed $NbSe_2$,[504] cuprates, and Fe-based superconductors.[505–507] Several explanations of the appearance of magnetism in superconductivity have been proposed, including Fermi surface nesting, local moments interacting via

frustrated superexchange interactions, local moments interacting via longer range interactions primarily of itinerant nature, and orbital ordering. However, many of the details remain unknown, especially the investigation of long-range magnetic ordering present in 2D superconductors.[505]

Moreover, the combination between FM and TI will lead to QAH effect. So far, QAH effect has been experimentally confirmed in Cr-doped $(Bi,Sb)_2Te_3$,[508] layered materials of $MnBi_2Te_4$,[43] and twisted bilayer graphene.[509] However, the operational temperatures of them are low, which prohibit practical applications of the fascinating quantum transport phenomenon in QAH insulators. Therefore, one still needs to establish different physical scenarios to realize QAH insulators with high working temperature. Based on the known 2D magnet database, the reported high-temperature Dirac half metals without considering SOC should be carefully re-examined,[93,110,161,162,172,377,382,383,510–512] which are potential precursors of QAH insulator or Chern insulator. When SOC is considered, the ferromagnetic Dirac half metal[513] or Dirac spin gapless semimetal[514] will open a global gap at the Dirac points, giving rise to topological edge states with a nonzero integer Chern number.[383,510,511] Alternatively, one can directly design the QAH compounds, which combine the insulating heave elements with light 3*d* transition metal elements together. The former elements will help generate a large topological gap, while the latter elements would contribute to strong ferromagnetism. Such expectation has been fulfilled in $MnBi_2Te_4$ films, which have already been discussed in Sec. III E 4. Recently, several exciting works have been published,[14,43,515–517] which mainly focused on the thickness effect of $MnBi_2Te_4$ films on the interlayer magnetism and band topology.

Very recently, Duan, Xu, and co-workers[517] provided a powerful strategy to design 2D QAH insulators with high working temperature, and demonstrate its feasibility in the family of layered iron-based superconductor materials FeSe with Li decoration, i.e., LiFeSe. The electron injection from Li atoms to Fe atoms makes LiFeSe monolayer stably exist, and all Fe atoms are in the high-spin state with a magnetic moment of $\sim 3\ \mu_B$. Inherited from the robust magnetism of Fe monolayer, the estimated T_C of LiFeSe monolayer was about 1500 K. Moreover, there are four titled, anisotropic, and spin-polarized Dirac cones in LiFeSe monolayer, where QAH gap of 35 meV will be opened by inclusion SOC, which is larger than the thermal energy at room temperature. Intuitively, the idea of alkali metal injection can be extended to the other Fe/Co/Ni based 2D compounds.

To utilize the magnetic properties of 2D magnets, the correlations between charge and spin, as well as between phonon and spin are also crucial, because they play an important role in magnetic fluctuation, magnonic dissipation, and magnetic coupling.[49,518–520] Strong charge and spin couplings were found in a AFM $NiPS_3$ monolayer, i.e., a close relationship that exists between electronic structure and magnetic ordering.[519] The mechanism of spin and phonon coupling can be regarded as interplay between the exchange interaction and the lattice deformation.[49] Some pioneer experimental and theoretical investigations on spin and phonon coupling have been reported for $CrGe(Si)Te_3$.[518–521] Deep insights into the spin-phonon coupling in the other 2D magnets would be very worthwhile and may have impact on many relevant areas, such as spin filtering, spin Seebeck, and spin wave control.[518–521]

Based on manipulation of the spin states, many new concept devices based on 2D intrinsic magnets have been proposed, including ultralow power electronic devices, spin transistor, spin valve, spin filter, logic, and magnetic memory. For example, a tunnel field effect transistor with a large on-off ratio (400%) was realized in graphene/CrI_3/graphene junction.[427,522] Gong *et al.*[523] also demonstrated that vertical electrical field was an effective way to achieve half-metallicity in A-type antiferromagnetic bilayers on VSe_2 and realized the spin field effect transistor. Multiple spin filter magnetic tunnel junctions with a record of enhanced magnetoresistance (19 000%) were realized in four-layer CrI_3 junction structures.[154] Double spin filter was proposed in graphene/CrI_3/graphene junction. In this model, the CrI_3 tunnel barrier and the decoupled magnetic layers were used as the magnetic memory bit. Such decoupling provides electrical readout of the CrI_3 magnetization state without additional ferromagnetic sensor layers, enabling facile detection of spin-orbit torques on the layered magnetic insulators.[154] Based on the magnetic proximity exchange interaction at the interface, spin dependent optoelectronics and photonics have been observed in CrI_3/WSe_2 heterojunction.[451] The magnetization switching in 2D magnets by electric voltage was observed in Fe_3GeTe_2, which opens up new opportunities for potential voltage-controlled magnetoelectronics.[50] In addition, a new type of spin valve was theoretically designed in a CrI_3/bilayer graphene/CrI_3 heterojunction. Cardoso *et al.*[524] found that gap opening only exists at the Dirac point in the antiparallel configuration, whereas the graphene bilayer remains conducting in the parallel configuration. These exciting innovative devices are all related to magnetic heterostructures. Stacking more potential room-temperature 2D magnets as the building blocks and investigating their performances in spintronic and quantum devices are just beginning.

All these exciting progresses will shed light on the design and synthesis of room-temperature 2D magnets with intrinsic FM/AFM ordering. Compared to the bulk phases, the atomic thinness of the layers also leads to strong tunability via strain, intercalation, external fields (electronic, optical, and magnetic), interfacial interaction, defects, and functional groups, as discussed in Sec. IV. The successive research of 2D magnets with novel properties would not only provide more abundant platform to explore the fundamental physics but also move forward to develop efficient non-volatile memory, spin-based logic devices, spin-dependent optoelectronics, and so on. In this regard, we believe that the development of 2D magnets is still in its infancy but has already shown its huge potential.

AUTHORS' CONTRIBUTIONS

All authors have contributed equally to this manuscript. All authors have reviewed final version of this manuscript.

ACKNOWLEDGMENTS

This work was supported by the National Natural Science Foundation of China (Grant Nos. 11874097, 91961204, 12004065, 11964023) and the Fundamental Research Funds for the Central Universities of China (Grant No. DUT19LK12). We acknowledge the Xinghai Scholar project of Dalian University of Technology and the project of Dalian Youth Science and Technology Star (Grant No. 2017RQ012).

DATA AVAILABLITY

Data sharing is not applicable to this article as no new data were created or analyzed in this study.

REFERENCES

[1]M. N. Baibich, J. M. Broto, A. Fert, F. N. Van Dau, F. Petroff, P. Etienne, G. Creuzet, A. Friederich, and J. Chazelas, Phys. Rev. Lett. **61**(21), 2472 (1988).
[2]X. Li and J. Yang, Natl. Sci. Rev. **3**(3), 365 (2016).
[3]N. Mason and M. Stehno, Nat. Phys. **9**(2), 67 (2013).
[4]J. Stöhr and H. C. Siegmann, *Magnetism: From Fundamentals to Nanoscale Dynamics* (Springer, 2006).
[5]Q. Liu, J. Xing, Z. Jiang, X. Jiang, Y. Wang, and J. Zhao, Nanoscale **12**(12), 6776 (2020).
[6]Z. Liu, J. Liu, and J. Zhao, Nano Res. **10**(6), 1972 (2017).
[7]X. Li and J. Yang, J. Phys. Chem. Lett. **10**(10), 2439 (2019).
[8]H. Wang, F. Fan, S. Zhu, and H. Wu, Europhys. Lett. **114**(4), 47001 (2016).
[9]K. Yang, F. Fan, H. Wang, D. I. Khomskii, and H. Wu, Phys. Rev. B **101**(10), 100402 (2020).
[10]H. L. Zhuang and R. G. Hennig, Phys. Rev. B **93**(5), 054429 (2016).
[11]Y. Sun, R. C. Xiao, G. T. Lin, R. R. Zhang, L. S. Ling, Z. W. Ma, X. Luo, W. J. Lu, Y. P. Sun, and Z. G. Sheng, Appl. Phys. Lett. **112**(7), 072409 (2018).
[12]H. Kumar, N. C. Frey, L. Dong, B. Anasori, Y. Gogotsi, and V. B. Shenoy, ACS Nano **11**(8), 7648 (2017).
[13]J. He, P. Lyu, and P. Nachtigall, J. Mater. Chem. C **4**(47), 11143 (2016).
[14]J. Li, Y. Li, S. Du, Z. Wang, B.-L. Gu, S.-C. Zhang, K. He, W. Duan, and Y. Xu, Sci. Adv. **5**(6), eaaw5685 (2019).
[15]X. Zhang, B. Wang, Y. Guo, Y. Zhang, Y. Chen, and J. Wang, Nanoscale Horiz. **4**(4), 859 (2019).
[16]H. L. Zhuang, P. R. C. Kent, and R. G. Hennig, Phys. Rev. B **93**(13), 134407 (2016).
[17]Y. Ma, Y. Dai, M. Guo, C. Niu, Y. Zhu, and B. Huang, ACS Nano **6**(2), 1695 (2012).
[18]F. Li, K. Tu, and Z. Chen, J. Phys. Chem. C **118**(36), 21264 (2014).
[19]J.-J. Zhang, L. Lin, Y. Zhang, M. Wu, B. I. Yakobson, and S. Dong, J. Am. Chem. Soc. **140**(30), 9768 (2018).
[20]G. V. Pushkarev, V. G. Mazurenko, V. V. Mazurenko, and D. W. Boukhvalov, Phys. Chem. Chem. Phys. **21**(40), 22647 (2019).
[21]Y. Wen, Z. Liu, Y. Zhang, C. Xia, B. Zhai, X. Zhang, G. Zhai, C. Shen, P. He, R. Cheng, L. Yin, Y. Yao, M. Getaye Sendeku, Z. Wang, X. Ye, C. Liu, C. Jiang, C. Shan, Y. Long, and J. He, Nano Lett. **20**(5), 3130 (2020).
[22]D. Zhang, A. Rahman, W. Qin, X. Li, P. Cui, Z. Zhang, and Z. Zhang, Phys. Rev. B **101**(20), 205119 (2020).
[23]N. Sivadas, S. Okamoto, X. Xu, C. J. Fennie, and D. Xiao, Nano Lett. **18**(12), 7658 (2018).
[24]J. Xiao and B. Yan, 2D Mater. **7**(4), 045010 (2020).
[25]F. Zhang, Y.-C. Kong, R. Pang, L. Hu, P.-L. Gong, X.-Q. Shi, and Z.-K. Tang, New J. Phys. **21**(5), 053033 (2019).
[26]C. Wang, X. Zhou, L. Zhou, N.-H. Tong, Z.-Y. Lu, and W. Ji, Sci. Bull. **64**(5), 293 (2019).
[27]C. Wang, X. Zhou, L. Zhou, Y. Pan, Z.-Y. Lu, X. Wan, X. Wang, and W. Ji, Phys. Rev. B **102**(2), 020402 (2020).
[28]B. Huang, G. Clark, E. Navarro-Moratalla, D. R. Klein, R. Cheng, K. L. Seyler, D. Zhong, E. Schmidgall, M. A. McGuire, D. H. Cobden, W. Yao, D. Xiao, P. Jarillo-Herrero, and X. Xu, Nature **546**(7657), 270 (2017).
[29]S. Tian, J.-F. Zhang, C. Li, T. Ying, S. Li, X. Zhang, K. Liu, and H. Lei, J. Am. Chem. Soc. **141**(13), 5326 (2019).
[30]X. Cai, T. Song, N. P. Wilson, G. Clark, M. He, X. Zhang, T. Taniguchi, K. Watanabe, W. Yao, D. Xiao, M. A. McGuire, D. H. Cobden, and X. Xu, Nano Lett. **19**(6), 3993 (2019).
[31]Z. Zhang, J. Shang, C. Jiang, A. Rasmita, W. Gao, and T. Yu, Nano Lett. **19**(5), 3138 (2019).
[32]A. Banerjee, J. Yan, J. Knolle, C. A. Bridges, M. B. Stone, M. D. Lumsden, D. G. Mandrus, D. A. Tennant, R. Moessner, and S. E. Nagler, Science **356**(6342), 1055 (2017).
[33]B. Zhou, Y. Wang, G. B. Osterhoudt, P. Lampen-Kelley, D. Mandrus, R. He, K. S. Burch, and E. A. Henriksen, J. Phys. Chem. Solids **128**, 291 (2019).
[34]M. Bonilla, S. Kolekar, Y. Ma, H. C. Diaz, V. Kalappattil, R. Das, T. Eggers, H. R. Gutierrez, M.-H. Phan, and M. Batzill, Nature Nanotechnol. **13**(4), 289 (2018).
[35]J. Li, B. Zhao, P. Chen, R. Wu, B. Li, Q. Xia, G. Guo, J. Luo, K. Zang, Z. Zhang, H. Ma, G. Sun, X. Duan, and X. Duan, Adv. Mater. **30**(36), 1801043 (2018).
[36]D. J. O'Hara, T. Zhu, A. H. Trout, A. S. Ahmed, Y. K. Luo, C. H. Lee, M. R. Brenner, S. Rajan, J. A. Gupta, D. W. McComb, and R. K. Kawakami, Nano Lett. **18**(5), 3125 (2018).
[37]C. Gong, L. Li, Z. Li, H. Ji, A. Stern, Y. Xia, T. Cao, W. Bao, C. Wang, Y. Wang, Z. Q. Qiu, R. J. Cava, S. G. Louie, J. Xia, and X. Zhang, Nature **546**(7657), 265 (2017).
[38]X. Wang, K. Du, Y. Y. F. Liu, P. Hu, J. Zhang, Q. Zhang, M. H. S. Owen, X. Lu, C. K. Gan, P. Sengupta, C. Kloc, and Q. Xiong, 2D Mater. **3**(3), 031009 (2016).
[39]K. Kim, S. Y. Lim, J. Kim, J.-U. Lee, S. Lee, P. Kim, K. Park, S. Son, C.-H. Park, J.-G. Park, and H. Cheong, 2D Mater. **6**(4), 041001 (2019).
[40]G. Le Flem, R. Brec, G. Ouvard, A. Louisy, and P. Segransan, J. Phys. Chem. Solids **43**(5), 455 (1982).
[41]Z. Fei, B. Huang, P. Malinowski, W. Wang, T. Song, J. Sanchez, W. Yao, D. Xiao, X. Zhu, A. F. May, W. Wu, D. H. Cobden, J. H. Chu, and X. Xu, Nat. Mater. **17**(9), 778 (2018).
[42]A. F. May, D. Ovchinnikov, Q. Zheng, R. Hermann, S. Calder, B. Huang, Z. Fei, Y. Liu, X. Xu, and M. A. McGuire, ACS Nano **13**(4), 4436 (2019).
[43]Y. Deng, Y. Yu, M. Z. Shi, Z. Guo, Z. Xu, J. Wang, X. H. Chen, and Y. Zhang, Science **367**(6480), 895 (2020).
[44]N. D. Mermin and H. Wagner, Phys. Rev. Lett. **17**(22), 1133 (1966).
[45]K. S. Burch, D. Mandrus, and J.-G. Park, Nature **563**(7729), 47 (2018).
[46]W. Liu, Y. Xu, S. Hassan, J. Weaver, and G. van der Laan, in *Handbook of Spintronics*, edited by Y. Xu, D. D. Awschalom, and J. Nitta (Springer, Dordrecht, Netherlands, 2016), pp. 709–756.
[47]G. van der Laan, Phys. Rev. Lett. **82**(3), 640 (1999).
[48]J.-U. Lee, S. Lee, J. H. Ryoo, S. Kang, T. Y. Kim, P. Kim, C.-H. Park, J.-G. Park, and H. Cheong, Nano Lett. **16**(12), 7433 (2016).
[49]Y. Tian, M. J. Gray, H. Ji, R. J. Cava, and K. S. Burch, 2D Mater. **3**(2), 025035 (2016).
[50]Y. Deng, Y. Yu, Y. Song, J. Zhang, N. Z. Wang, Z. Sun, Y. Yi, Y. Z. Wu, S. Wu, J. Zhu, J. Wang, X. H. Chen, and Y. Zhang, Nature **563**(7729), 94 (2018).
[51]D. Hobbs, G. Kresse, and J. Hafner, Phys. Rev. B **62**(17), 11556 (2000).
[52]P. Mohn, *Magnetism in the Solid State: An Introduction* (Springer Science & Business Media, Berlin, 2006).
[53]W.-B. Zhang, Q. Qu, P. Zhu, and C.-H. Lam, J. Mater. Chem. C **3**(48), 12457 (2015).
[54]J. Liu, Q. Sun, Y. Kawazoe, and P. Jena, Phys. Chem. Chem. Phys. **18**(13), 8777 (2016).
[55]S. Sarikurt, Y. Kadioglu, F. Ersan, E. Vatansever, O. Ü. Aktürk, Y. Yüksel, Ü. Akıncı, and E. Aktürk, Phys. Chem. Chem. Phys. **20**(2), 997 (2018).
[56]C. Ataca, H. Şahin, and S. Ciraci, J. Phys. Chem. C **116**(16), 8983 (2012).
[57]W. Chen, J.-m. Zhang, Y.-z. Nie, Q.-l. Xia, and G.-h. Guo, J. Magn. Magn. Mater. **508**, 166878 (2020).
[58]H.-R. Fuh, C.-R. Chang, Y.-K. Wang, R. F. L. Evans, R. W. Chantrell, and H.-T. Jeng, Sci. Rep. **6**(1), 32625 (2016).
[59]H. Pan, J. Phys. Chem. C **118**(24), 13248 (2014).
[60]M. Kan, S. Adhikari, and Q. Sun, Phys. Chem. Chem. Phys. **16**(10), 4990 (2014).
[61]G. T. Lin, H. L. Zhuang, X. Luo, B. J. Liu, F. C. Chen, J. Yan, Y. Sun, J. Zhou, W. J. Lu, P. Tong, Z. G. Sheng, Z. Qu, W. H. Song, X. B. Zhu, and Y. P. Sun, Phys. Rev. B **95**(24), 245212 (2017).
[62]M.-W. Lin, H. L. Zhuang, J. Yan, T. Z. Ward, A. A. Puretzky, C. M. Rouleau, Z. Gai, L. Liang, V. Meunier, B. G. Sumpter, P. Ganesh, P. R. C. Kent, D. B. Geohegan, D. G. Mandrus, and K. Xiao, J. Mater. Chem. C **4**(2), 315 (2016).
[63]H.-S. Kim and H.-Y. Kee, Phys. Rev. B **93**(15), 155143 (2016).
[64]L. J. Sandilands, Y. Tian, K. W. Plumb, Y.-J. Kim, and K. S. Burch, Phys. Rev. Lett. **114**(14), 147201 (2015).
[65]Z. Jiang, P. Wang, J. Xing, X. Jiang, and J. Zhao, ACS Appl. Mater. Inter. **10**(45), 39032 (2018).
[66]H. Liu, J.-T. Sun, M. Liu, and S. Meng, J. Phys. Chem. Lett. **9**(23), 6709 (2018).
[67]N. Mounet, M. Gibertini, P. Schwaller, D. Campi, A. Merkys, A. Marrazzo, T. Sohier, I. E. Castelli, A. Cepellotti, G. Pizzi, and N. Marzari, Nat. Nanotechnol. **13**(3), 246 (2018).
[68]Y. Zhu, X. Kong, T. D. Rhone, and H. Guo, Phys. Rev. Mater. **2**(8), 081001 (2018).

[69]E. J. Telford, A. H. Dismukes, K. Lee, M. Cheng, A. W. A. K. Bartholomew, Y.-S. Chen, X. Xu, A. N. Pasupathy, X. Zhu, C. R. Dean, and X. Roy, arXiv:2005.06110 (2020).
[70]R. Han, Z. Jiang, and Y. Yan, J. Phys. Chem. C **124**(14), 7956 (2020).
[71]M. Abramchuk, S. Jaszewski, K. R. Metz, G. B. Osterhoudt, Y. Wang, K. S. Burch, and F. Tafti, Adv. Mater. **30**(25), 1801325 (2018).
[72]C. Huang, J. Feng, F. Wu, D. Ahmed, B. Huang, H. Xiang, K. Deng, and E. Kan, J. Am. Chem. Soc. **140**(36), 11519 (2018).
[73]Y. Jiao, W. Wu, F. Ma, Z.-M. Yu, Y. Lu, X.-L. Sheng, Y. Zhang, and S. A. Yang, Nanoscale **11**(35), 16508 (2019).
[74]H. Xiao, X. Wang, R. Wang, L. Xu, S. Liang, and C. Yang, Phys. Chem. Chem. Phys. **21**(22), 11731 (2019).
[75]B. Wang, Y. Zhang, L. Ma, Q. Wu, Y. Guo, X. Zhang, and J. Wang, Nanoscale **11**(10), 4204 (2019).
[76]S. Zheng, C. Huang, T. Yu, M. Xu, S. Zhang, H. Xu, Y. Liu, E. Kan, Y. Wang, and G. Yang, J. Phys. Chem. Lett. **10**(11), 2733 (2019).
[77]K. Zhao, X. Li, S. Wang, and Q. Wang, Phys. Chem. Chem. Phys. **21**(1), 246 (2019).
[78]X. Tang, W. Sun, Y. Gu, C. Lu, L. Kou, and C. Chen, Phys. Rev. B **99**(4), 045445 (2019).
[79]H. K. Singh, P. Kumar, and U. V. Waghmare, J. Phys. Chem. C **119**(45), 25657 (2015).
[80]J. Tan, W. Li, X. He, and M. Zhao, RSC Adv. **3**(19), 7016 (2013).
[81]H. Sun, B. Li, and J. Zhao, J. Phys.: Condens. Matter **28**(42), 425301 (2016).
[82]B. Mandal and P. Sarkar, Phys. Chem. Chem. Phys. **17**(26), 17437 (2015).
[83]X. Shi, Z. Huang, M. Huttula, T. Li, S. Li, X. Wang, Y. Luo, M. Zhang, and W. Cao, Crystals **8**(1), 24 (2018).
[84]D. L. Cortie, G. L. Causer, K. C. Rule, H. Fritzsche, W. Kreuzpaintner, and F. Klose, Adv. Funct. Mater. **30**(18), 1901414 (2020).
[85]N. Sethulakshmi, A. Mishra, P. M. Ajayan, Y. Kawazoe, A. K. Roy, A. K. Singh, and C. S. Tiwary, Mater. Today **27**, 107 (2019).
[86]D. L. Duong, S. J. Yun, and Y. H. Lee, ACS Nano **11**(12), 11803 (2017).
[87]P. Huang, P. Zhang, S. Xu, H. Wang, X. Zhang, and H. Zhang, Nanoscale **12**(4), 2309 (2020).
[88]K. F. Mak, J. Shan, and D. C. Ralph, Nat. Rev. Phys. **1**(11), 646 (2019).
[89]J. Hu, P. Wang, J. Zhao, and R. Wu, Adv. Phys.: X **3**(1), 1432415 (2018).
[90]W. Zhang, P. K. J. Wong, R. Zhu, and A. T. S. Wee, InfoMat **1**(4), 479 (2019).
[91]I. Choudhuri, P. Bhauriyal, and B. Pathak, Chem. Mater. **31**(20), 8260 (2019).
[92]X. Zhang and C. Gong, Science **363**(6428), 4450 (2019).
[93]T. Cai, X. Li, F. Wang, S. Ju, J. Feng, and C. D. Gong, Nano Lett. **15**(10), 6434 (2015).
[94]J. M. Coey, *Magnetism and Magnetic Materials* (Cambridge University Press, Cambridge, 2010).
[95]Q. Chen, Q. Ding, Y. Wang, Y. Xu, and J. Wang, J. Phys. Chem. C **124**(22), 12075 (2020).
[96]S. Zhang, R. Xu, W. Duan, and X. Zou, Adv. Funct. Mater. **29**(14), 1808380 (2019).
[97]Y. Yue, J. Magn. Magn. Mater. **434**, 164 (2017).
[98]M. A. U. Absor and F. Ishii, Phys. Rev. B **100**(11), 115104 (2019).
[99]W. Xing, Y. Chen, P. M. Odenthal, X. Zhang, W. Yuan, T. Su, Q. Song, T. Wang, J. Zhong, S. Jia, X. C. Xie, Y. Li, and W. Han, 2D Mater. **4**(2), 024009 (2017).
[100]V. V. Kulish and W. Huang, J. Mater. Chem. C**5**(34), 8734 (2017).
[101]J. Zhou and Q. Sun, J. Am. Chem. Soc. **133**(38), 15113 (2011).
[102]M. Mabrouk and R. Hayn, Phys. Rev. B **92**(18), 184424 (2015).
[103]X. Li, Z. Zhang, and H. Zhang, Nanoscale Adv. **2**(1), 495 (2020).
[104]L. Webster and J.-A. Yan, Phys. Rev. B **98**(14), 144411 (2018).
[105]E. Bruyer, D. Di Sante, P. Barone, A. Stroppa, M.-H. Whangbo, and S. Picozzi, Phys. Rev. B **94**(19), 195402 (2016).
[106]N. W. Ashcroft and N. D. Mermin, *Solid State Physics* (Holt, Rinehart and Winston, 1976).
[107]A. Hashemi, H.-P. Komsa, M. Puska, and A. V. Krasheninnikov, J. Phys. Chem. C **121**(48), 27207 (2017).
[108]G. Bhattacharyya, P. Garg, P. Bhauriyal, and B. Pathak, ACS Appl. Nano Mater. **2**(10), 6152 (2019).
[109]V. Carteaux, F. Moussa, and M. Spiesser, Europhys. Lett. **29**(3), 251 (1995).
[110]J. He, X. Li, P. Lyu, and P. Nachtigall, Nanoscale **9**(6), 2246 (2017).
[111]E. A. Kovaleva, I. Melchakova, N. S. Mikhaleva, F. N. Tomilin, S. G. Ovchinnikov, W. Baek, V. A. Pomogaev, P. Avramov, and A. A. Kuzubov, J. Phys. Chem. Solids **134**, 324 (2019).
[112]D. Lançon, R. A. Ewings, T. Guidi, F. Formisano, and A. R. Wildes, Phys. Rev. B **98**(13), 134414 (2018).
[113]I. Dzyaloshinsky, J. Phys. Chem. Solids **4**(4), 241 (1958).
[114]T. Moriya, Phys. Rev. Lett. **4**(5), 228 (1960).
[115]X. D. Wang, R. Q. Wu, D. S. Wang, and A. J. Freeman, Phys. Rev. B **54**(1), 61 (1996).
[116]D.-s. Wang, R. Wu, and A. J. Freeman, Phys. Rev. B **47**(22), 14932 (1993).
[117]M. Weinert, E. Wimmer, and A. J. Freeman, Phys. Rev. B **26**(8), 4571 (1982).
[118]A. Kitaev, Ann. Phys. **321**(1), 2 (2006).
[119]K. W. Plumb, J. P. Clancy, L. J. Sandilands, V. V. Shankar, Y. F. Hu, K. S. Burch, H.-Y. Kee, and Y.-J. Kim, Phys. Rev. B **90**(4), 041112 (2014).
[120]J. Chaloupka, G. Jackeli, and G. Khaliullin, Phys. Rev. Lett. **110**(9), 097204 (2013).
[121]S. Baierl, M. Hohenleutner, T. Kampfrath, A. K. Zvezdin, A. V. Kimel, R. Huber, and R. V. Mikhaylovskiy, Nat. Photon. **10**(11), 715 (2016).
[122]A. J. Freeman and R. E. Watson, Phys. Rev. **124**(5), 1439 (1961).
[123]Q. Pei, X.-C. Wang, J.-J. Zou, and W.-B. Mi, Front. Phys. **13**(4), 137105 (2018).
[124]J. Liu, Z. Liu, T. Song, and X. Cui, J. Mater. Chem. C **5**(3), 727 (2017).
[125]X. Li and J. Yang, J. Am. Chem. Soc. **141**(1), 109 (2019).
[126]J. B. Goodenough, Phys. Rev. **100**(2), 564 (1955).
[127]J. Kanamori, J. Appl. Phys. **31**(5), S14 (1960).
[128]P. W. Anderson, Phys. Rev. **115**(1), 2 (1959).
[129]B. Wang, X. Zhang, Y. Zhang, S. Yuan, Y. Guo, S. Dong, and J. Wang, Mater. Horiz. **7**, 1623 (2020).
[130]P. G. De Gennes, Phys. Rev. **118**(1), 141 (1960).
[131]Y. Guo, Y. Zhang, S. Yuan, B. Wang, and J. Wang, Nanoscale **10**(37), 18036 (2018).
[132]J. Pan, J. Yu, Y.-F. Zhang, S. Du, A. Janotti, C.-X. Liu, and Q. Yan, npj Computat. Mater. **6**, 152 (2020).
[133]S. Wang, J. Wang, and M. Khazaei, Phys. Chem. Chem. Phys. **22**(20), 11731 (2020).
[134]P. Jiang, C. Wang, D. Chen, Z. Zhong, Z. Yuan, Z.-Y. Lu, and W. Ji, Phys. Rev. B **99**(14), 144401 (2019).
[135]C. Wang, X. Zhou, Y. Pan, J. Qiao, X. Kong, C.-C. Kaun, and W. Ji, Phys. Rev. B **97**(24), 245409 (2018).
[136]C. Si, J. Zhou, and Z. Sun, ACS Appl. Mater. Inter. **7**(31), 17510 (2015).
[137]T. Cao, Z. Li, and S. G. Louie, Phys. Rev. Lett. **114**(23), 236602 (2015).
[138]S.-H. Zhang and B.-G. Liu, J. Mater. Chem. C **6**(25), 6792 (2018).
[139]S. Gong, W. Wan, S. Guan, B. Tai, C. Liu, B. Fu, S. A. Yang, and Y. Yao, J. Mater. Chem. C **5**(33), 8424 (2017).
[140]H. Xiang, B. Xu, Y. Xia, J. Yin, and Z. Liu, Sci. Rep. **6**(1), 39218 (2016).
[141]Y. Nie, M. Rahman, P. Liu, A. Sidike, Q. Xia, and G.-h. Guo, Phys. Rev. B **96**(7), 075401 (2017).
[142]H. Y. Lv, W. J. Lu, X. Luo, X. B. Zhu, and Y. P. Sun, Phys. Rev. B **99**(13), 134416 (2019).
[143]M. Joe, U. Yang, and C. Lee, Nano Mater. Sci. **1**(4), 299 (2019).
[144]I. Eren, F. Iyikanat, and H. Sahin, Phys. Chem. Chem. Phys. **21**(30), 16718 (2019).
[145]P. K. J. Wong, W. Zhang, F. Bussolotti, X. Yin, T. S. Herng, L. Zhang, Y. L. Huang, G. Vinai, S. Krishnamurthi, D. W. Bukhvalov, Y. J. Zheng, R. Chua, A. T. N'Diaye, S. A. Morton, C.-Y. Yang, K.-H. O. Yang, P. Torelli, W. Chen, K. E. J. Goh, J. Ding, M.-T. Lin, G. Brocks, M. P. de Jong, A. H. C. Neto, and A. T. S. Wee, Adv. Mater. **31**(23), 1901185 (2019).
[146]E. Vatansever, S. Sarikurt, and R. F. L. Evans, Mater. Res. Express **5**(4), 046108 (2018).
[147]X. Sun, W. Li, X. Wang, Q. Sui, T. Zhang, Z. Wang, L. Liu, D. L. Li, S. Feng, S. Zhong, H. Wang, V. Bouchiat, M. N. Regueiro, N. Rougemaille, J. Coraux, Z. Wang, B. Dong, X. Wu, T. Yang, G. Yu, B. Wang, Z. V. Han, X. Han, and Z. Zhang, Nano Res. **13**, 3358 (2020).
[148]L. Onsager, Phys. Rev. **65**(3–4), 117 (1944).
[149]A. M. McGuire, Crystals **7**(5), 121 (2017).
[150]J. F. Dillon, Jr. and C. E. Olson, J. Appl. Phys. **36**(3), 1259 (1965).
[151]J. L. Lado and J. Fernández-Rossier, 2D Mater. **4**(3), 035002 (2017).

[152]J. Cenker, B. Huang, N. Suri, P. Thijssen, A. Miller, T. Song, T. Taniguchi, K. Watanabe, M. McGuire, X. Di, and X. Xu, arXiv:2001.07025 (2020).
[153]Z. Wang, I. Gutierrez-Lezama, N. Ubrig, M. Kroner, M. Gibertini, T. Taniguchi, K. Watanabe, A. Imamoglu, E. Giannini, and A. F. Morpurgo, Nat. Commun. **9**(1), 2516 (2018).
[154]T. Song, X. Cai, M. W.-Y. Tu, X. Zhang, B. Huang, N. P. Wilson, K. L. Seyler, L. Zhu, T. Taniguchi, K. Watanabe, M. A. McGuire, D. H. Cobden, D. Xiao, W. Yao, and X. Xu, Science **360**(6394), 1214 (2018).
[155]M. Moaied, J. Lee, and J. Hong, Phys. Chem. Chem. Phys. **20**(33), 21755 (2018).
[156]F. Iyikanat, M. Yagmurcukardes, R. T. Senger, and H. Sahin, J. Mater. Chem. C **6**(8), 2019 (2018).
[157]W. Jin, H. H. Kim, Z. Ye, S. Li, P. Rezaie, F. Diaz, S. Siddiq, E. Wauer, B. Yang, C. Li, S. Tian, K. Sun, H. Lei, A. W. Tsen, L. Zhao, and R. He, Nat. Commun. **9**(1), 5122 (2018).
[158]T. Kong, K. Stolze, E. I. Timmons, J. Tao, D. Ni, S. Guo, Z. Yang, R. Prozorov, and R. J. Cava, Adv. Mater. **31**(17), 1808074 (2019).
[159]J. Yan, X. Luo, F. C. Chen, J. J. Gao, Z. Z. Jiang, G. C. Zhao, Y. Sun, H. Y. Lv, S. J. Tian, Q. W. Yin, H. C. Lei, W. J. Lu, P. Tong, W. H. Song, X. B. Zhu, and Y. P. Sun, Phys. Rev. B **100**(9), 094402 (2019).
[160]M. An, Y. Zhang, J. Chen, H.-M. Zhang, Y. Guo, and S. Dong, J. Phys. Chem. C **123**(50), 30545 (2019).
[161]J. He, S. Ma, P. Lyu, and P. Nachtigall, J. Mater. Chem. C **4**(13), 2518 (2016).
[162]J. Sun, X. Zhong, W. Cui, J. Shi, J. Hao, M. Xu, and Y. Li, Phys. Chem. Chem. Phys. **22**(4), 2429 (2020).
[163]Q. Sun and N. Kioussis, Phys. Rev. B **97**(9), 094408 (2018).
[164]S. Tomar, B. Ghosh, S. Mardanya, P. Rastogi, B. S. Bhadoria, Y. S. Chauhan, A. Agarwal, and S. Bhowmick, J. Magn. Magn. Mater. **489**, 165384 (2019).
[165]Y. Zhou, H. Lu, X. Zu, and F. Gao, Sci. Rep. **6**(1), 19407 (2016).
[166]W.-x. Zhang, Y. Li, H. Jin, and Y.-c. She, Phys. Chem. Chem. Phys. **21**(32), 17740 (2019).
[167]M. A. McGuire, J. Yan, P. Lampen-Kelley, A. F. May, V. R. Cooper, L. Lindsay, A. Puretzky, L. Liang, S. Kc, E. Cakmak, S. Calder, and B. C. Sales, Phys. Rev. Mater. **1**(6), 064001 (2017).
[168]D. Weber, L. M. Schoop, V. Duppel, J. M. Lippmann, J. Nuss, and B. V. Lotsch, Nano Lett. **16**(6), 3578 (2016).
[169]C. Huang, J. Zhou, H. Wu, K. Deng, P. Jena, and E. Kan, Phys. Rev. B **95**(4), 045113 (2017).
[170]Q. Sun and N. Kioussis, Nanoscale **11**(13), 6101 (2019).
[171]F. Ersan, E. Vatansever, S. Sarikurt, Y. Yüksel, Y. Kadioglu, H. D. Ozaydin, O. Ü. Aktürk, Ü. Akıncı, and E. Aktürk, J. Magn. Magn. Mater. **476**, 111 (2019).
[172]J.-Y. You, C. Chen, Z. Zhang, X.-L. Sheng, S. A. Yang, and G. Su, Phys. Rev. B **100**(6), 064408 (2019).
[173]X.-L. Sheng and B. K. Nikolić, Phys. Rev. B **95**(20), 201402 (2017).
[174]A. S. Botana and M. R. Norman, Phys. Rev. Mater. **3**(4), 044001 (2019).
[175]X. Zhou, B. Brzostowski, A. Durajski, M. Liu, J. Xiang, T. Jiang, Z. Wang, S. Chen, P. Li, Z. Zhong, A. Drzewiński, M. Jarosik, R. Szczęśniak, T. Lai, D. Guo, and D. Zhong, J. Phys. Chem. C **124**(17), 9416 (2020).
[176]E. Torun, H. Sahin, S. K. Singh, and F. M. Peeters, Appl. Phys. Lett. **106**(19), 192404 (2015).
[177]E. Torun, H. Sahin, C. Bacaksiz, R. T. Senger, and F. M. Peeters, Phys. Rev. B **92**(10), 104407 (2015).
[178]M. Ashton, D. Gluhovic, S. B. Sinnott, J. Guo, D. A. Stewart, and R. G. Hennig, Nano Lett. **17**(9), 5251 (2017).
[179]J. Zhou, Y. P. Feng, and L. Shen, arXiv:1904.04952 (2019).
[180]B. Wang, Q. Wu, Y. Zhang, Y. Guo, X. Zhang, Q. Zhou, S. Dong, and J. Wang, Nanoscale Horiz. **3**(5), 551 (2018).
[181]J. Jiang, Q. Liang, R. Meng, Q. Yang, C. Tan, X. Sun, and X. Chen, Nanoscale **9**(9), 2992 (2017).
[182]B. J. Kim, B. J. Jeong, S. Oh, S. Chae, K. H. Choi, S. S. Nanda, T. Nasir, S. H. Lee, K.-W. Kim, H. K. Lim, L. Chi, I. J. Choi, M.-K. Hong, D. K. Yi, H. K. Yu, J.-H. Lee, and J.-Y. Choi, Phys. Status Solidi R **13**(3), 1800448 (2019).
[183]D. Puotinen and R. E. Newnham, Acta Crystallogr. **14**(6), 691 (1961).
[184]Z. Sun, H. Lv, Z. Zhuo, A. Jalil, W. Zhang, X. Wu, and J. Yang, J. Mater. Chem. C **6**(5), 1248 (2018).
[185]Y. Sun, Z. Zhuo, and X. Wu, J. Mater. Chem. C **6**(42), 11401 (2018).
[186]W. Yu, J. Li, T. S. Herng, Z. Wang, X. Zhao, X. Chi, W. Fu, I. Abdelwahab, J. Zhou, J. Dan, Z. Chen, Z. Chen, Z. Li, J. Lu, S. J. Pennycook, Y. P. Feng, J. Ding, and K. P. Loh, Adv. Mater. **31**(40), e1903779 (2019).
[187]G. Duvjir, B. K. Choi, I. Jang, S. Ulstrup, S. Kang, T. Thi Ly, S. Kim, Y. H. Choi, C. Jozwiak, A. Bostwick, E. Rotenberg, J.-G. Park, R. Sankar, K.-S. Kim, J. Kim, and Y. J. Chang, Nano Lett. **18**(9), 5432 (2018).
[188]P. Chen, W. W. Pai, Y. H. Chan, V. Madhavan, M. Y. Chou, S. K. Mo, A. V. Fedorov, and T. C. Chiang, Phys. Rev. Lett. **121**(19), 196402 (2018).
[189]J. Feng, D. Biswas, A. Rajan, M. D. Watson, F. Mazzola, O. J. Clark, K. Underwood, I. Marković, M. McLaren, A. Hunter, D. M. Burn, L. B. Duffy, S. Barua, G. Balakrishnan, F. Bertran, P. Le Fèvre, T. K. Kim, G. van der Laan, T. Hesjedal, P. Wahl, and P. D. C. King, Nano Lett. **18**(7), 4493 (2018).
[190]P. M. Coelho, K. Nguyen Cong, M. Bonilla, S. Kolekar, M.-H. Phan, J. Avila, M. C. Asensio, I. I. Oleynik, and M. Batzill, J. Phys. Chem. C **123**(22), 14089 (2019).
[191]A. O. Fumega, M. Gobbi, P. Dreher, W. Wan, C. González-Orellana, M. Peña-Díaz, C. Rogero, J. Herrero-Martín, P. Gargiani, M. Ilyn, M. M. Ugeda, V. Pardo, and S. Blanco-Canosa, J. Phys. Chem. C **123**(45), 27802 (2019).
[192]R. Chua, J. Yang, X. He, X. Yu, W. Yu, F. Bussolotti, P. K. J. Wong, K. P. Loh, M. B. H. Breese, K. E. J. Goh, Y. L. Huang, and A. T. S. Wee, Adv. Mater. **32**(24), 2000693 (2020).
[193]M. Nakano, Y. Wang, S. Yoshida, H. Matsuoka, Y. Majima, K. Ikeda, Y. Hirata, Y. Takeda, H. Wadati, Y. Kohama, Y. Ohigashi, M. Sakano, K. Ishizaka, and Y. Iwasa, Nano Lett. **19**(12), 8806 (2019).
[194]J. Zhang, B. Yang, H. Zheng, X. Han, and Y. Yan, Phys. Chem. Chem. Phys. **19**(35), 24341 (2017).
[195]H. Guo, N. Lu, L. Wang, X. Wu, and X. C. Zeng, J. Phys. Chem. C **118**(13), 7242 (2014).
[196]P. K. J. Wong, W. Zhang, J. Zhou, F. Bussolotti, X. Yin, L. Zhang, A. T. N'Diaye, S. A. Morton, W. Chen, J. Goh, M. P. de Jong, Y. P. Feng, and A. T. S. Wee, ACS Nano **13**(11), 12894 (2019).
[197]Y. Wang, J. Ren, J. Li, Y. Wang, H. Peng, P. Yu, W. Duan, and S. Zhou, Phys. Rev. B **100**(24), 241404 (2019).
[198]X. Ma, T. Dai, S. Dang, S. Kang, X. Chen, W. Zhou, G. Wang, H. Li, P. Hu, Z. He, Y. Sun, D. Li, F. Yu, X. Zhou, H. Chen, X. Chen, S. Wu, and S. Li, ACS Appl. Mater. Inter. **11**(11), 10729 (2019).
[199]K. Sugawara, Y. Nakata, K. Fujii, K. Nakayama, S. Souma, T. Takahashi, and T. Sato, Phys. Rev. B **99**(24), 241404 (2019).
[200]S. Divilov, W. Wan, P. Dreher, M. M. Ugeda, and F. Ynduráin, arXiv:005.06210 (2020).
[201]L. Pan, H. Wen, L. Huang, L. Chen, H.-X. Deng, J.-B. Xia, and Z. Wei, Chin. Phys. B **28**(10), 107504 (2019).
[202]R. Z. Zhang, Y. Y. Zhang, and S. X. Du, Chin. Phys. B **29**(7), 077504 (2020).
[203]J. Chu, Y. Zhang, Y. Wen, R. Qiao, C. Wu, P. He, L. Yin, R. Cheng, F. Wang, Z. Wang, J. Xiong, Y. Li, and J. He, Nano Lett. **19**(3), 2154 (2019).
[204]P. Lv, G. Tang, C. Yang, J. Deng, Y. Liu, X. Wang, X. Wang, and J. Hong, 2D Mater. **5**(4), 045026 (2018).
[205]J.-Y. Chen, X.-X. Li, W.-Z. Zhou, J.-L. Yang, F.-P. Ouyang, and X. Xiong, Adv. Electron. Mater. **6**(1), 2070001 (2020).
[206]L. Zhang, C.-w. Zhang, S.-F. Zhang, W.-x. Ji, P. Li, and P.-j. Wang, Nanoscale **11**(12), 5666 (2019).
[207]Y. Zhang, J. Pang, M. Zhang, X. Gu, and L. Huang, Sci. Rep. **7**(1), 15993 (2017).
[208]Y. Zhang, J. Chu, L. Yin, T. A. Shifa, Z. Cheng, R. Cheng, F. Wang, Y. Wen, X. Zhan, Z. Wang, and J. He, Adv. Mater. **31**(19), 1900056 (2019).
[209]L. Kang, C. Ye, X. Zhao, X. Zhou, J. Hu, Q. Li, D. Liu, C. M. Das, J. Yang, D. Hu, J. Chen, X. Cao, Y. Zhang, M. Xu, J. Di, D. Tian, P. Song, G. Kutty, Q. Zeng, Q. Fu, Y. Deng, J. Zhou, A. Ariando, F. Miao, G. Hong, Y. Huang, S. J. Pennycook, K.-T. Yong, W. Ji, X. R. Wang, and Z. Liu, Nat. Commun. **11**(1), 3729 (2020).
[210]Q.-Q. Yuan, Z. Guo, Z.-Q. Shi, H. Zhao, Z.-Y. Jia, Q. Wang, J. Sun, D. Wu, and S.-C. Li, Chin. Phys. Lett. **37**(7), 077502 (2020).
[211]M. Khazaei, A. Ranjbar, M. Arai, T. Sasaki, and S. Yunoki, J. Mater. Chem. C **5**(10), 2488 (2017).
[212]N. C. Frey, C. C. Price, A. Bandyopadhyay, H. Kumar, and V. B. Shenoy, *Predicted Magnetic Properties of MXenes* (Springer, Cham, 2019).

[213]B. Anasori, M. R. Lukatskaya, and Y. Gogotsi, Nat. Rev. Mater. **2**(2), 16098 (2017).
[214]M. Naguib, V. N. Mochalin, M. W. Barsoum, and Y. Gogotsi, Adv. Mater. **26**(7), 992 (2014).
[215]Z. Jiang, P. Wang, X. Jiang, and J. Zhao, Nanoscale Horiz. **3**(3), 335 (2018).
[216]D. Khomskii, *Transition Metal Compounds* (Cambridge University Press, Cambridge, 2014).
[217]Y. Xie and P. R. C. Kent, Phys. Rev. B **87**(23), 235441 (2013).
[218]N. J. Lane, M. W. Barsoum, and J. M. Rondinelli, EPL-Europhys. Lett. **101**(5), 57004 (2013).
[219]J. Li, Y. Du, C. Huo, S. Wang, and C. Cui, Ceram. Int. **41**(2), 2631 (2015).
[220]L. Hu, X. Wu, and J. Yang, Nanoscale **8**(26), 12939 (2016).
[221]C. Xu, L. Wang, Z. Liu, L. Chen, J. Guo, N. Kang, X.-L. Ma, H.-M. Cheng, and W. Ren, Nat. Mater. **14**(11), 1135 (2015).
[222]S. Zhao, W. Kang, and J. Xue, Appl. Phys. Lett. **104**(13), 133106 (2014).
[223]G. Gao, G. Ding, J. Li, K. Yao, M. Wu, and M. Qian, Nanoscale **8**(16), 8986 (2016).
[224]B. Akgenc, A. Mogulkoc, and E. Durgun, J. Appl. Phys. **127**(8), 084302 (2020).
[225]B. Akgenc, Solid State Commun. **303–304**, 113739 (2019).
[226]G. Wang, J. Phys. Chem. C **120**(33), 18850 (2016).
[227]G. Wang and Y. Liao, Appl. Surf. Sci. **426**, 804 (2017).
[228]F. Wu, K. Luo, C. Huang, W. Wu, P. Meng, Y. Liu, and E. Kan, Solid State Commun. **222**, 9 (2015).
[229]Y. Zhang and F. Li, J. Magn. Magn. Mater. **433**, 222 (2017).
[230]X. Xiao, P. Urbankowski, K. Hantanasirisakul, Y. Yang, S. Sasaki, L. Yang, C. Chen, H. Wang, L. Miao, S. H. Tolbert, S. J. L. Billinge, H. D. Abruña, S. J. May, and Y. Gogotsi, Adv. Funct. Mater. **29**(17), 1809001 (2019).
[231]M. A. Hope, A. C. Forse, K. J. Griffith, M. R. Lukatskaya, M. Ghidiu, Y. Gogotsi, and C. P. Grey, Phys. Chem. Chem. Phys. **18**(7), 5099 (2016).
[232]P. Srivastava, A. Mishra, H. Mizuseki, K.-R. Lee, and A. K. Singh, ACS Appl. Mater. Inter. **8**(36), 24256 (2016).
[233]Y. Yoon, T. A. Le, A. P. Tiwari, I. Kim, M. W. Barsoum, and H. Lee, Nanoscale **10**(47), 22429 (2018).
[234]X.-H. Zha, J.-C. Ren, L. Feng, X. Bai, K. Luo, Y. Zhang, J. He, Q. Huang, J. S. Francisco, and S. Du, Nanoscale **10**(18), 8763 (2018).
[235]S.-s. Li, S.-j. Hu, W.-x. Ji, P. Li, K. Zhang, C.-w. Zhang, and S.-s. Yan, Appl. Phys. Lett. **111**(20), 202405 (2017).
[236]P. Urbankowski, B. Anasori, T. Makaryan, D. Er, S. Kota, P. L. Walsh, M. Zhao, V. B. Shenoy, M. W. Barsoum, and Y. Gogotsi, Nanoscale **8**(22), 11385 (2016).
[237]X. Zhang, T. He, W. Meng, L. Jin, Y. Li, X. Dai, and G. Liu, J. Phys. Chem. C **123**(26), 16388 (2019).
[238]N. C. Frey, H. Kumar, B. Anasori, Y. Gogotsi, and V. B. Shenoy, ACS Nano **12**(6), 6319 (2018).
[239]J. He, P. Lyu, L. Z. Sun, Á. Morales García, and P. Nachtigall, J. Mater. Chem. C **4**(27), 6500 (2016).
[240]J. Hu, B. Xu, C. Ouyang, S. A. Yang, and Y. Yao, J. Phys. Chem. C **118**(42), 24274 (2014).
[241]X. Ma and W. Mi, J. Phys. Chem. C **124**(5), 3095 (2020).
[242]B. Anasori, Y. Xie, M. Beidaghi, J. Lu, B. C. Hosler, L. Hultman, P. R. C. Kent, Y. Gogotsi, and M. W. Barsoum, ACS Nano **9**(10), 9507 (2015).
[243]Y. Hu, X. L. Fan, W. J. Guo, Y. R. An, Z. F. Luo, and J. Kong, J. Magn. Magn. Mater. **486**, 165280 (2019).
[244]J. Yang, X. Zhou, X. Luo, S. Zhang, and L. Chen, Appl. Phys. Lett. **109**(20), 203109 (2016).
[245]L. Dong, H. Kumar, B. Anasori, Y. Gogotsi, and V. B. Shenoy, J. Phys. Chem. Lett. **8**(2), 422 (2017).
[246]B. Anasori, C. Shi, E. J. Moon, Y. Xie, C. A. Voigt, P. R. C. Kent, S. J. May, S. J. L. Billinge, M. W. Barsoum, and Y. Gogotsi, Nanoscale Horiz. **1**(3), 227 (2016).
[247]J. Yang, X. Luo, X. Zhou, S. Zhang, J. Liu, Y. Xie, L. Lv, and L. Chen, Comput. Mater. Sci. **139**, 313 (2017).
[248]J. He, G. Ding, C. Zhong, S. Li, D. Li, and G. Zhang, Nanoscale **11**(1), 356 (2019).
[249]W. Sun, Y. Xie, and P. R. C. Kent, Nanoscale **10**(25), 11962 (2018).
[250]Q. Tao, J. Lu, M. Dahlqvist, A. Mockute, S. Calder, A. Petruhins, R. Meshkian, O. Rivin, D. Potashnikov, E. a. N. Caspi, H. Shaked, A. Hoser, C. Opagiste, R.-M. Galera, R. Salikhov, U. Wiedwald, C. Ritter, A. R. Wildes, B. Johansson, L. Hultman, M. Farle, M. W. Barsoum, and J. Rosen, Chem. Mater. **31**(7), 2476 (2019).
[251]Q. Gao and H. Zhang, Nanoscale **12**(10), 5995 (2020).
[252]N. C. Frey, A. Bandyopadhyay, H. Kumar, B. Anasori, Y. Gogotsi, and V. B. Shenoy, ACS Nano **13**(3), 2831 (2019).
[253]W. Jeitschko, Monatshefte für Chemie und verwandte Teile anderer Wissenschaften **97**(5), 1472 (1966).
[254]W. Jeitschko, Acta Crystallograph. Sec. B **25**(1), 163 (1969).
[255]M. Ade and H. Hillebrecht, Inorg. Chem. **54**(13), 6122 (2015).
[256]Y. Liu, Z. Jiang, X. Jiang, and J. Zhao, RSC Adv. **10**(43), 25836 (2020).
[257]Z. Guo, J. Zhou, and Z. Sun, J. Mater. Chem. A **5**(45), 23530 (2017).
[258]L. T. Alameda, P. Moradifar, Z. P. Metzger, N. Alem, and R. E. Schaak, J. Am. Chem. Soc. **140**(28), 8833 (2018).
[259]H. Zhang, F.-Z. Dai, H. Xiang, X. Wang, Z. Zhang, and Y. Zhou, J. Mater. Sci. Technol. **35**(8), 1593 (2019).
[260]L. T. Alameda, R. W. Lord, J. A. Barr, P. Moradifar, Z. P. Metzger, B. C. Steimle, C. F. Holder, N. Alem, S. B. Sinnott, and R. E. Schaak, J. Am. Chem. Soc. **141**(27), 10852 (2019).
[261]J. Wang, T.-N. Ye, Y. Gong, J. Wu, N. Miao, T. Tada, and H. Hosono, Nat. Commun. **10**(1), 2284 (2019).
[262]I. Ozdemir, Y. Kadioglu, O. Ü. Aktürk, Y. Yuksel, Ü. Akıncı, and E. Aktürk, J. Phys.: Condens. Matter **31**(50), 505401 (2019).
[263]S. Zhang, Y. Li, T. Zhao, and Q. Wang, Sci. Rep. **4**(1), 5241 (2014).
[264]A. V. Kuklin, A. A. Kuzubov, E. A. Kovaleva, N. S. Mikhaleva, F. N. Tomilin, H. Lee, and P. V. Avramov, Nanoscale **9**(2), 621 (2017).
[265]A. V. Kuklin, S. A. Shostak, and A. A. Kuzubov, J. Phys. Chem. Lett. **9**(6), 1422 (2018).
[266]Z. Xu and H. Zhu, J. Phys. Chem. C **122**(26), 14918 (2018).
[267]C. Zhu, H. Lv, X. Qu, M. Zhang, J. Wang, S. Wen, Q. Li, Y. Geng, Z. Su, X. Wu, Y. Li, and Y. Ma, J. Mater. Chem. C **7**(21), 6406 (2019).
[268]T. Zhao, J. Zhou, Q. Wang, Y. Kawazoe, and P. Jena, ACS Appl. Mater. Inter. **8**(39), 26207 (2016).
[269]B. Zhou, X. Wang, and W. Mi, J. Mater. Chem. C **6**(15), 4290 (2018).
[270]K. Zhao and Q. Wang, Appl. Surf. Sci. **505**, 144620 (2020).
[271]Y. Z. Abdullahi, Z. D. Vatansever, E. Aktürk, Ü. Akıncı, and O. Ü. Aktürk, Phys. Chem. Chem. Phys. **22**, 10893 (2020).
[272]Y. Guo, L. Ma, K. Mao, M. Ju, Y. Bai, J. Zhao, and X. C. Zeng, Nanoscale Horiz. **4**(3), 592 (2019).
[273]M. Kan, J. Zhou, Q. Sun, Y. Kawazoe, and P. Jena, J. Phys. Chem. Lett. **4**(20), 3382 (2013).
[274]E. Kan, M. Li, S. Hu, C. Xiao, H. Xiang, and K. Deng, J. Phys. Chem. Lett. **4**(7), 1120 (2013).
[275]Y. Omomo, T. Sasaki, Wang, and M. Watanabe, J. Am. Chem. Soc. **125**(12), 3568 (2003).
[276]F. Aguilera-Granja and A. Ayuela, J. Phys. Chem. C **124**(4), 2634 (2020).
[277]H. van Gog, W.-F. Li, C. Fang, R. S. Koster, M. Dijkstra, and M. van Huis, npj 2D Mater. Appl. **3**(1), 18 (2019).
[278]Y. Wang, F. Li, H. Zheng, X. Han, and Y. Yan, Phys. Chem. Chem. Phys. **20**(44), 28162 (2018).
[279]P. A. T. Olsson, L. R. Merte, and H. Grönbeck, Phys. Rev. B **101**(15), 155426 (2020).
[280]Y. Sun, Z. Zhuo, X. Wu, and J. Yang, Nano Lett. **17**(5), 2771 (2017).
[281]N. Han, H. Liu, and J. Zhao, J. Supercond. Nov. Magn. **28**(6), 1755 (2015).
[282]Q. Wu, J.-J. Zhang, P. Hao, Z. Ji, S. Dong, C. Ling, Q. Chen, and J. Wang, J. Phys. Chem. Lett. **7**(19), 3723 (2016).
[283]Q. Wu, Y. Zhang, Q. Zhou, J. Wang, and X. C. Zeng, J. Phys. Chem. Lett. **9**(15), 4260 (2018).
[284]T. Kong, K. Stolze, D. Ni, S. K. Kushwaha, and R. J. Cava, Phys. Rev. Mater. **2**(1), 014410 (2018).
[285]L. D. Casto, A. J. Clune, M. O. Yokosuk, J. L. Musfeldt, T. J. Williams, H. L. Zhuang, M. W. Lin, K. Xiao, R. G. Hennig, B. C. Sales, J. Q. Yan, and D. Mandrus, APL Mater. **3**(4), 041515 (2015).
[286]Y. Fang, S. Wu, Z.-Z. Zhu, and G.-Y. Guo, Phys. Rev. B **98**(12), 125416 (2018).

[287]Y. Liu and C. Petrovic, Phys. Rev. Mater. **3**(1), 014001 (2019).
[288]M. S. Baranava, D. C. Hvazdouski, V. A. Skachkova, V. R. Stempitsky, and A. L. Danilyuk, Mater. Today: Proc. **20**, 342 (2020).
[289]H. L. Zhuang, Y. Xie, P. R. C. Kent, and P. Ganesh, Phys. Rev. B **92**(3), 035407 (2015).
[290]B. L. Chittari, D. Lee, N. Banerjee, A. H. MacDonald, E. Hwang, and J. Jung, Phys. Rev. B **101**(8), 085415 (2020).
[291]J.-Y. You, Z. Zhang, X.-J. Dong, B. Gu, and G. Su, Phys. Rev. Res. **2**(1), 013002 (2020).
[292]M. Yu, X. Liu, and W. Guo, Phys. Chem. Chem. Phys. **20**(9), 6374 (2018).
[293]K.-z. Du, X.-z. Wang, Y. Liu, P. Hu, M. I. B. Utama, C. K. Gan, Q. Xiong, and C. Kloc, ACS Nano **10**(2), 1738 (2015).
[294]C. T. Kuo, M. Neumann, K. Balamurugan, H. J. Park, S. Kang, H. W. Shiu, J. H. Kang, B. H. Hong, M. Han, T. W. Noh, and J. G. Park, Sci. Rep. **6**, 20904 (2016).
[295]Y.-J. Sun, Q.-H. Tan, X.-L. Liu, Y.-F. Gao, and J. Zhang, J. Phys. Chem. Lett. **10**(11), 3087 (2019).
[296]B. L. Chittari, Y. Park, D. Lee, M. Han, A. H. MacDonald, E. Hwang, and J. Jung, Phys. Rev. B **94**(18), 184428 (2016).
[297]F. Wang, T. A. Shifa, P. Yu, P. He, Y. Liu, F. Wang, Z. Wang, X. Zhan, X. Lou, F. Xia, and J. He, Adv. Funct. Mater. **28**(37), 1802151 (2018).
[298]P. A. Joy and S. Vasudevan, Phys. Rev. B **46**(9), 5425 (1992).
[299]A. R. Wildes, K. C. Rule, R. I. Bewley, M. Enderle, and T. J. Hicks, J. Phys.: Condens. Matter **24**(41), 416004 (2012).
[300]G. Long, H. Henck, M. Gibertini, D. Dumcenco, Z. Wang, T. Taniguchi, K. Watanabe, E. Giannini, and A. F. Morpurgo, Nano Lett. **20**(4), 2452 (2020).
[301]W. Xing, L. Qiu, X. Wang, Y. Yao, Y. Ma, R. Cai, S. Jia, X. C. Xie, and W. Han, Phys. Rev. X **9**(1), 011026 (2019).
[302]W. Bai, Z. Hu, C. Xiao, J. Guo, Z. Li, Y. Zou, X. Liu, J. Zhao, W. Tong, W. Yan, Z. Qu, B. Ye, and Y. Xie, J. Am. Chem. Soc. **142**, 10849 (2020).
[303]Y. Gu, Q. Zhang, C. Le, Y. Li, T. Xiang, and J. Hu, Phys. Rev. B **100**(16), 165405 (2019).
[304]K. Kim, S. Y. Lim, J.-U. Lee, S. Lee, T. Y. Kim, K. Park, G. S. Jeon, C.-H. Park, J.-G. Park, and H. Cheong, Nat. Commun. **10**(1), 345 (2019).
[305]M. J. Coak, S. Son, D. Daisenberger, H. Hamidov, C. R. S. Haines, P. L. Alireza, A. R. Wildes, C. Liu, S. S. Saxena, and J.-G. Park, npj Quantum Mater. **4**(1), 38 (2019).
[306]Y. Sugita, T. Miyake, and Y. Motome, Phys. Rev. B **97**(3), 035125 (2018).
[307]X. Li, X. Wu, and J. Yang, J. Am. Chem. Soc. **136**(31), 11065 (2014).
[308]E. C. Stoner, Proc. R. Soc. London, Ser. A **165**, 372 (1938).
[309]R. Prange and V. Korenman, Phys. Rev. B **19**(9), 4691 (1979).
[310]S. Bhatti, R. Sbiaa, A. Hirohata, H. Ohno, S. Fukami, and S. N. Piramanayagam, Mater. Today **20**(9), 530 (2017).
[311]C. Hu, D. Zhang, F. Yan, Y. Li, Q. Lv, W. Zhu, Z. Wei, K. Chang, and K. Wang, Sci. Bull. **65**(13), 1072 (2020).
[312]D. Kim, S. Park, J. Lee, J. Yoon, S. Joo, T. Kim, K. J. Min, S. Y. Park, C. Kim, K. W. Moon, C. Lee, J. Hong, and C. Hwang, Nanotechnology **30**(24), 245701 (2019).
[313]L. Zhang, L. Song, H. Dai, J.-H. Yuan, M. Wang, X. Huang, L. Qiao, H. Cheng, X. Wang, W. Ren, X. Miao, L. Ye, K.-H. Xue, and J.-B. Han, Appl. Phys. Lett. **116**(4), 042402 (2020).
[314]J. Seo, D. Y. Kim, E. S. An, K. Kim, G.-Y. Kim, S.-Y. Hwang, D. W. Kim, B. G. Jang, H. Kim, G. Eom, S. Y. Seo, R. Stania, M. Muntwiler, J. Lee, K. Watanabe, T. Taniguchi, Y. J. Jo, J. Lee, B. I. Min, M. H. Jo, H. W. Yeom, S.-Y. Choi, J. H. Shim, and J. S. Kim, Sci. Adv. **6**(3), eaay8912 (2020).
[315]H. Zhang, R. Chen, K. Zhai, X. Chen, L. Caretta, X. Huang, R. V. Chopdekar, J. Cao, J. Sun, J. Yao, R. Birgeneau, and R. Ramesh, Phys. Rev. B **102**(6), 064417 (2020).
[316]J. Lee, T. Y. Ko, J. H. Kim, H. Bark, B. Kang, S.-G. Jung, T. Park, Z. Lee, S. Ryu, and C. Lee, ACS Nano **11**(11), 10935 (2017).
[317]H. L. Zhuang and J. Zhou, Phys. Rev. B **94**(19), 195307 (2016).
[318]T. Hu, W. Wan, Y. Ge, and Y. Liu, J. Phys.: Condens. Matter **32**, 385803 (2020).
[319]M. M. Otrokov, I. P. Rusinov, M. Blanco-Rey, M. Hoffmann, A. Y. Vyazovskaya, S. V. Eremeev, A. Ernst, P. M. Echenique, A. Arnau, and E. V. Chulkov, Phys. Rev. Lett. **122**(10), 107202 (2019).
[320]Y. Li, Z. Jiang, J. Li, S. Xu, and W. Duan, Phys. Rev. B **100**(13), 134438 (2019).
[321]L. Liu and H. L. Zhuang, APL Mater. **7**(1), 011101 (2019).
[322]N. Miao, B. Xu, L. Zhu, J. Zhou, and Z. Sun, J. Am. Chem. Soc. **140**(7), 2417 (2018).
[323]T. Xiao, G. Wang, and Y. Liao, Chem. Phys. **513**, 182 (2018).
[324]I. Khan, A. Hashmi, M. U. Farooq, and J. Hong, ACS Appl. Mater. Inter. **9**(40), 35368 (2017).
[325]P. Chen, K. Xu, X. Li, Y. Guo, D. Zhou, J. Zhao, X. Wu, C. Wu, and Y. Xie, Chem. Sci. **5**(6), 2251 (2014).
[326]Z. Zhu, C. Liao, S. Li, X. Zhang, W. Wu, Z.-M. Yu, R. Yu, W. Zhang, and S. A. Yang, arXiv preprint arXiv:2003.10671 (2020).
[327]X. Li, T. Gao, and Y. Wu, Sci. China Inform. Sci. **59**(6), 061405 (2016).
[328]A. B. Sarkar, B. Ghosh, B. Singh, S. Bhowmick, H. Lin, A. Bansil, and A. Agarwal, arXiv preprint arXiv:2005.12868 (2020).
[329]M. Ormaza, L. Fernández, M. Ilyn, A. Magaña, B. Xu, M. J. Verstraete, M. Gastaldo, M. A. Valbuena, P. Gargiani, A. Mugarza, A. Ayuela, L. Vitali, M. Blanco-Rey, F. Schiller, and J. E. Ortega, Nano Lett. **16**(7), 4230 (2016).
[330]A. Correa, B. Xu, M. J. Verstraete, and L. Vitali, Nanoscale **8**(45), 19148 (2016).
[331]B. Feng, R.-W. Zhang, Y. Feng, B. Fu, S. Wu, K. Miyamoto, S. He, L. Chen, K. Wu, K. Shimada, T. Okuda, and Y. Yao, Phys. Rev. Lett. **123**(11), 116401 (2019).
[332]S. Lei, J. Lin, Y. Jia, M. Gray, A. Topp, G. Farahi, S. Klemenz, T. Gao, F. Rodolakis, J. L. McChesney, C. R. Ast, A. Yazdani, K. S. Burch, S. Wu, N. P. Ong, and L. M. Schoop, Sci. Adv. **6**(6), eaay6407 (2020).
[333]O. E. Parfenov, A. M. Tokmachev, D. V. Averyanov, I. A. Karateev, I. S. Sokolov, A. N. Taldenkov, and V. G. Storchak, Mater. Today **29**, 20 (2019).
[334]A. M. Tokmachev, D. V. Averyanov, A. N. Taldenkov, O. E. Parfenov, I. A. Karateev, I. S. Sokolov, and V. G. Storchak, Mater. Horiz. **6**(7), 1488 (2019).
[335]T. Gorkan, E. Vatansever, U. Akıncı, G. Gökoglu, E. Aktürk, and S. Ciraci, J. Phys. Chem. C **124**, 12816 (2020).
[336]S. Li, Z. Wang, M. Zhou, F. Zheng, X. Shao, and P. Zhang, J. Phys. D: Appl. Phys. **53**(18), 185301 (2020).
[337]Y.-W. Son, M. L. Cohen, and S. G. Louie, Nature **444**(7117), 347 (2006).
[338]G. Z. Magda, X. Jin, I. Hagymási, P. Vancsó, Z. Osváth, P. Nemes-Incze, C. Hwang, L. P. Biró, and L. Tapasztó, Nature **514**(7524), 608 (2014).
[339]M. Slota, A. Keerthi, W. K. Myers, E. Tretyakov, M. Baumgarten, A. Ardavan, H. Sadeghi, C. J. Lambert, A. Narita, and K. Müllen, Nature **557**(7707), 691 (2018).
[340]D. Zhang, Q. Xiong, and K. Chang, Nanoscale Adv. **2**, 4421 (2020).
[341]X. Jiang, Q. Liu, J. Xing, and J. Zhao, J. Phys. Chem. Lett. **10**(24), 7753 (2019).
[342]G. Shi, L. Chen, Y. Yang, D. Li, Z. Qian, S. Liang, L. Yan, L. H. Li, M. Wu, and H. Fang, Nat. Chem. **10**(7), 776 (2018).
[343]L. Jin, X. Zhang, Y. Liu, X. Dai, X. Shen, L. Wang, and G. Liu, Phys. Rev. B **102**, 125118 (2020).
[344]W.-x. Ji, B.-m. Zhang, S.-f. Zhang, C.-w. Zhang, M. Ding, P. Li, and P.-j. Wang, J. Mater. Chem. C **5**(33), 8504 (2017).
[345]W.-X. Ji, B.-M. Zhang, S.-F. Zhang, C.-W. Zhang, M. Ding, P.-J. Wang, and R. Zhang, Nanoscale **10**(28), 13645 (2018).
[346]F. Wu, C. Huang, H. Wu, C. Lee, K. Deng, E. Kan, and P. Jena, Nano Lett. **15**(12), 8277 (2015).
[347]S. Wang, H. Ge, S. Sun, J. Zhang, F. Liu, X. Wen, X. Yu, L. Wang, Y. Zhang, H. Xu, J. C. Neuefeind, Z. Qin, C. Chen, C. Jin, Y. Li, D. He, and Y. Zhao, J. Am. Chem. Soc. **137**(14), 4815 (2015).
[348]R. Li, B. Yang, F. Li, Y. Wang, X. Du, and Y. Yan, J. Phys.: Condens. Matter **31**(33), 335801 (2019).
[349]M. Kurmoo, Chem. Soc. Rev. **38**(5), 1353 (2009).
[350]S. Yang, W. Li, C. Ye, G. Wang, H. Tian, C. Zhu, P. He, G. Ding, X. Xie, and Y. Liu, Adv. Mater. **29**(16), 1605625 (2017).
[351]A. Du, S. Sanvito, and S. C. Smith, Phys. Rev. Lett. **108**(19), 197207 (2012).
[352]E. Kan, W. Hu, C. Xiao, R. Lu, K. Deng, J. Yang, and H. Su, J. Am. Chem. Soc. **134**(13), 5718 (2012).
[353]D. Sheberla, L. Sun, M. A. Blood-Forsythe, S. l. Er, C. R. Wade, C. K. Brozek, A. n. Aspuru-Guzik, and M. Dincă, J. Am. Chem. Soc. **136**(25), 8859 (2014).
[354]D. Grumelli, B. Wurster, S. Stepanow, and K. Kern, Nat. Commun. **4**(1), 2904 (2013).

[355]A. J. Clough, J. W. Yoo, M. H. Mecklenburg, and S. C. Marinescu, J. Am. Chem. Soc. **137**(1), 118 (2015).
[356]T. Kambe, R. Sakamoto, K. Hoshiko, K. Takada, M. Miyachi, J. H. Ryu, S. Sasaki, J. Kim, K. Nakazato, and M. Takata, J. Am. Chem. Soc. **135**(7), 2462 (2013).
[357]B. Białek, I. G. Kim, and J. I. Lee, Surf. Sci. **526**(3), 367 (2003).
[358]D. M. Sedlovets, M. V. Shuvalov, Y. V. Vishnevskiy, V. T. Volkov, I. I. Khodos, O. V. Trofimov, and V. I. Korepanov, Mater. Res. Bull. **48**(10), 3955 (2013).
[359]Z. Honda, Y. Sakaguchi, M. Tashiro, M. Hagiwara, T. Kida, M. Sakai, T. Fukuda, and N. Kamata, Appl. Phys. Lett. **110**(13), 133101 (2017).
[360]P. Wang, X. Jiang, J. Hu, X. Huang, and J. Zhao, J. Mater. Chem. C **4**(11), 2147 (2016).
[361]M. Abel, S. Clair, O. Ourdjini, M. Mossoyan, and L. Porte, J. Am. Chem. Soc. **133**(5), 1203 (2011).
[362]H. Chen, H. Shan, A. Zhao, and B. Li, Chinese J. Chem. Phys. **32**(5), 563 (2019).
[363]B. Białek, I. G. Kim, and J. I. Lee, Thin Solid Films **513**(1–2), 110 (2006).
[364]B. Białek, I. G. Kim, and J. I. Lee, Thin Solid Films **436**(1), 107 (2003).
[365]B. Białek, I. G. Kim, and J. I. Lee, Synth. Met. **129**(2), 151 (2002).
[366]G. Zhu, M. Kan, Q. Sun, and P. Jena, J. Phys. Chem. A **118**(1), 304 (2014).
[367]W. Li, L. Sun, J. Qi, P. Jarillo-Herrero, M. Dincă, and J. Li, Chem. Sci. **8**(4), 2859 (2017).
[368]Q. Sun, Y. Dai, Y. Ma, X. Li, W. Wei, and B. Huang, J. Mater. Chem. C **3**(26), 6901 (2015).
[369]P. Wang, X. Jiang, J. Hu, and J. Zhao, Adv. Sci. **4**(10), 1700019 (2017).
[370]X. Huang, P. Sheng, Z. Tu, F. Zhang, J. Wang, H. Geng, Y. Zou, C.-a. Di, Y. Yi, and Y. Sun, Nat. Commun. **6**(1), 1 (2015).
[371]M. Zhao, A. Wang, and X. Zhang, Nanoscale **5**(21), 10404 (2013).
[372]C. Chakravarty, B. Mandal, and P. Sarkar, J. Phys. Chem. C **120**(49), 28307 (2016).
[373]L. Tang, Q. Li, C. Zhang, F. Ning, W. Zhou, L. Tang, and K. Chen, J. Magn. Magn. Mater. **488**, 165354 (2019).
[374]J. Liu and Q. Sun, Chemphyschem **16**(3), 614 (2015).
[375]X. Zhang, Y. Zhou, B. Cui, M. Zhao, and F. Liu, Nano Lett. **17**(10), 6166 (2017).
[376]L. Tang, L. Tang, D. Wang, H. Deng, and K. Chen, J. Phys.: Condens. Matter **30**(46), 465301 (2018).
[377]L. Dong, Y. Kim, D. Er, A. M. Rappe, and V. B. Shenoy, Phys. Rev. Lett. **116**(9), 096601 (2016).
[378]Y. Ma, Y. Dai, W. Wei, L. Yu, and B. Huang, J. Phys. Chem. A **117**(24), 5171 (2013).
[379]A. Pimachev, R. D. Nielsen, A. Karanovich, and Y. Dahnovsky, Phys. Chem. Chem. Phys. **21**(46), 25820 (2019).
[380]R. Dong, Z. Zhang, D. C. Tranca, S. Zhou, M. Wang, P. Adler, Z. Liao, F. Liu, Y. Sun, W. Shi, Z. Zhang, E. Zschech, S. C. B. Mannsfeld, C. Felser, and X. Feng, Nat. Commun. **9**(1), 2637 (2018).
[381]M. G. Campbell, D. Sheberla, S. F. Liu, T. M. Swager, and M. Dincă, Angew. Chem. Int. Ed. **54**(14), 4349 (2015).
[382]Y. Ma, Y. Dai, X. Li, Q. Sun, and B. Huang, Carbon **73**, 382 (2014).
[383]Z. Wang, Z. Liu, and F. Liu, Phys. Rev. Lett. **110**(19), 196801 (2013).
[384]Z. Liu, Z. Wang, J. Mei, Y. Wu, and F. Liu, Phys. Rev. Lett. **110**(10), 106804 (2013).
[385]L.-C. Zhang, L. Zhang, G. Qin, Q.-R. Zheng, M. Hu, Q.-B. Yan, and G. Su, Chem. Sci. **10**(44), 10381 (2019).
[386]T. Umbach, M. Bernien, C. F. Hermanns, A. Krüger, V. Sessi, I. Fernandez-Torrente, P. Stoll, J. I. Pascual, K. Franke, and W. Kuch, Phys. Rev. Lett. **109**(26), 267207 (2012).
[387]L. Wei, X. Zhang, and M. Zhao, Phys. Chem. Chem. Phys. **18**(11), 8059 (2016).
[388]J. Xing, P. Wang, Z. Jiang, X. Jiang, Y. Wang, and J. Zhao, APL Mater. **8**(7), 071105 (2020).
[389]P. Pachfule, R. Das, P. Poddar, and R. Banerjee, Cryst. Growth Des. **10**(6), 2475 (2010).
[390]X. Zhu, J. Zhao, B. Li, Y. Song, Y. Zhang, and Y. Zhang, Inorg. Chem. **49**(3), 1266 (2010).
[391]E. Kan, X. Wu, C. Lee, J. H. Shim, R. Lu, C. Xiao, and K. Deng, Nanoscale **4**(17), 5304 (2012).
[392]A. Wang, X. Zhang, Y. Feng, and M. Zhao, J. Phys. Chem. Lett. **8**(16), 3770 (2017).
[393]C. Liu, J. Xiong, D. Zhang, B. Wang, and D. Zhu, RSC Adv. **5**(127), 104854 (2015).
[394]D. Yin, Q. Chen, Y. Meng, H. Sun, Y. Zhang, and S. Gao, Chem. Sci. **6**(5), 3095 (2015).
[395]X. Li, P. Yadav, and K. P. Loh, Chem. Soc. Rev. **49**(14), 4835 (2020).
[396]S. B. Alahakoon, S. D. Diwakara, C. M. Thompson, and R. A. Smaldone, Chem. Soc. Rev. **49**(5), 1344 (2020).
[397]X. Chen, J. Qi, and D. Shi, Phys. Lett. A **379**(1–2), 60 (2015).
[398]X.-J. Dong, J.-Y. You, B. Gu, and G. Su, Phys. Rev. Appl. **12**(1), 014020 (2019).
[399]K. Wang, T. Hu, F. Jia, G. Zhao, Y. Liu, I. V. Solovyev, A. P. Pyatakov, A. K. Zvezdin, and W. Ren, Appl. Phys. Lett. **114**(9), 092405 (2019).
[400]S. Feng and W. Mi, Appl. Surf. Sci. **458**, 191 (2018).
[401]Z. Wu, J. Yu, and S. Yuan, Phys. Chem. Chem. Phys. **21**(15), 7750 (2019).
[402]X. Hu, Y. Zhao, X. Shen, A. V. Krasheninnikov, Z. Chen, and L. Sun, ACS Appl. Mater. Inter. **12**(23), 26367 (2020).
[403]Z.-W. Lu, S.-B. Qiu, W.-Q. Xie, X.-B. Yang, and Y.-J. Zhao, J. Appl. Phys. **127**(3), 033903 (2020).
[404]Z. Guan, N. Luo, S. Ni, and S. Hu, Mater. Adv. **1**(2), 244 (2020).
[405]E. Vatansever, S. Sarikurt, F. Ersan, Y. Kadioglu, O. Ü. Aktürk, Y. Yüksel, C. Ataca, E. Aktürk, and Ü. Akıncı, J. Appl. Phys. **125**(8), 083903 (2019).
[406]Z. Li, B. Zhou, and C. Luan, RSC Adv. **9**(61), 35614 (2019).
[407]H. Zheng, J. Zheng, C. Wang, H. Han, and Y. Yan, J. Magn. Magn. Mater. **444**, 184 (2017).
[408]R. Han and Y. Yan, Phys. Chem. Chem. Phys. **21**(37), 20892 (2019).
[409]S. C. Ganguli, H. Singh, I. Roy, V. Bagwe, D. Bala, A. Thamizhavel, and P. Raychaudhuri, Phys. Rev. B **93**(14), 144503 (2016).
[410]T. H. Bointon, I. Khrapach, R. Yakimova, A. V. Shytov, M. F. Craciun, and S. Russo, Nano Lett. **14**(4), 1751 (2014).
[411]J. Seel and J. Dahn, J. Electrochem. Soc. **147**(3), 892 (2000).
[412]D. Voiry, H. Yamaguchi, J. Li, R. Silva, D. C. Alves, T. Fujita, M. Chen, T. Asefa, V. B. Shenoy, and G. Eda, Nat. Mater. **12**(9), 850 (2013).
[413]K. J. Koski, C. D. Wessells, B. W. Reed, J. J. Cha, D. Kong, and Y. Cui, J. Am. Chem. Soc. **134**(33), 13773 (2012).
[414]H. Yuan, H. Wang, and Y. Cui, Acc. Chem. Res. **48**(1), 81 (2015).
[415]J. P. Motter, K. J. Koski, and Y. Cui, Chem. Mater. **26**(7), 2313 (2014).
[416]N. I. Kovtyukhova, Y. Wang, R. Lv, M. Terrones, V. H. Crespi, and T. E. Mallouk, J. Am. Chem. Soc. **135**(22), 8372 (2013).
[417]X. Zhao, P. Song, C. Wang, A. C. Riis-Jensen, W. Fu, Y. Deng, D. Wan, L. Kang, S. Ning, and J. Dan, Nature **581**(7807), 171 (2020).
[418]E. Morosan, H. Zandbergen, L. Li, M. Lee, J. Checkelsky, M. Heinrich, T. Siegrist, N. P. Ong, and R. Cava, Phys. Rev. B **75**(10), 104401 (2007).
[419]W. J. Hardy, C.-W. Chen, A. Marcinkova, H. Ji, J. Sinova, D. Natelson, and E. Morosan, Phys. Rev. B **91**(5), 054426 (2015).
[420]C. Zhang, Y. Yuan, M. Wang, P. Li, J. Zhang, Y. Wen, S. Zhou, and X.-X. Zhang, Phys. Rev. Mater. **3**(11), 114403 (2019).
[421]V. Pleshchev and N. Selezneva, Phys. Solid State **61**(3), 339 (2019).
[422]X. Zhang, Y. Sun, L. Ma, X. Zhao, and X. Yao, Nanotechnology **29**(30), 305706 (2018).
[423]N. Wang, H. Tang, M. Shi, H. Zhang, W. Zhuo, D. Liu, F. Meng, L. Ma, J. Ying, and L. Zou, J. Am. Chem. Soc. **141**(43), 17166 (2019).
[424]D. Weber, A. H. Trout, D. W. McComb, and J. E. Goldberger, Nano Lett. **19**(8), 5031 (2019).
[425]M. Yang, Q. Li, R. V. Chopdekar, C. Stan, S. Cabrini, J. W. Choi, S. Wang, T. Wang, N. Gao, A. Scholl, N. Tamura, C. Hwang, F. Wang, and Z. Qiu, Adv. Quantum Technolog. **3**(4), 2000017 (2020).
[426]Y. Guo, N. Liu, Y. Zhao, X. Jiang, Si Zhou, and J. Zhao, Chin. Phys. Lett. **37**(10), 107506 (2020).
[427]S. Jiang, L. Li, Z. Wang, K. F. Mak, and J. Shan, Nat. Nanotechnol. **13**(7), 549 (2018).
[428]B. Huang, G. Clark, D. R. Klein, D. MacNeill, E. Navarro-Moratalla, K. L. Seyler, N. Wilson, M. A. McGuire, D. H. Cobden, D. Xiao, W. Yao, P. Jarillo-Herrero, and X. Xu, Nat. Nanotechnol. **13**(7), 544 (2018).

[429]S. Jiang, J. Shan, and K. F. Mak, Nat. Mater. **17**(5), 406 (2018).
[430]Z. Wang, T. Zhang, M. Ding, B. Dong, Y. Li, M. Chen, X. Li, J. Huang, H. Wang, X. Zhao, Y. Li, D. Li, C. Jia, L. Sun, H. Guo, Y. Ye, D. Sun, Y. Chen, T. Yang, J. Zhang, S. Ono, Z. Han, and Z. Zhang, Nat. Nanotechnol. **13**(7), 554 (2018).
[431]I. A. Verzhbitskiy, H. Kurebayashi, H. Cheng, J. Zhou, S. Khan, Y. P. Feng, and G. Eda, Nat. Electron. **3**(8), 460 (2020).
[432]K. Dolui, M. D. Petrovic, K. Zollner, P. Plechac, J. Fabian, and B. K. Nikolic, Nano Lett. **20**(4), 2288 (2020).
[433]W. Liu, Y. Wang, J. Fan, L. Pi, M. Ge, L. Zhang, and Y. Zhang, Phys. Rev. B **100**(10), 104403 (2019).
[434]P. Jiang, L. Li, Z. Liao, Y. X. Zhao, and Z. Zhong, Nano Lett. **18**(6), 3844 (2018).
[435]D. R. Klein, D. MacNeill, J. L. Lado, D. Soriano, E. Navarro-Moratalla, K. Watanabe, T. Taniguchi, S. Manni, P. Canfield, J. Fernández-Rossier, and P. Jarillo-Herrero, Science **360**(6394), 1218 (2018).
[436]M. Gibertini, M. Koperski, A. F. Morpurgo, and K. S. Novoselov, Nat. Nanotechnol. **14**(5), 408 (2019).
[437]L. Thiel, Z. Wang, M. A. Tschudin, D. Rohner, I. Gutiérrez-Lezama, N. Ubrig, M. Gibertini, E. Giannini, A. F. Morpurgo, and P. Maletinsky, Science **364**(6444), 973 (2019).
[438]K. Zollner, P. E. Faria, and J. Fabian, Phys. Rev. B **101**(8), 085112 (2020).
[439]H. X. Fu, C. X. Liu, and B. H. Yan, Sci. Adv. **6**(10), eaaz0948 (2020).
[440]S. B. Chen, C. X. Huang, H. S. Sun, J. F. Ding, P. Jena, and E. J. Kan, J. Phys. Chem. C **123**(29), 17987 (2019).
[441]N. Liu, S. Zhou, and J. Zhao, Phys. Rev. Mater. **4**(9), 094003 (2020).
[442]F. Xiu, H. Wu, Y. Xu, J. Zou, X. Kou, S. A. Morton, A. T. N'Diaye, A. T. S. Wee, P. K. J. Wong, L. Ai, C. Huang, H. Gao, Y. Yang, J. Sun, W. Zhang, Z. Liao, X. Zhang, Z. Li, E. Zhang, W. Liu, K. Yang, and S. Liu, Natl. Sci. Rev. **7**(4), 745 (2020).
[443]J. Xiao and B. Yan, arXiv:2003.09942 (2020).
[444]F. Katmis, V. Lauter, F. S. Nogueira, B. A. Assaf, M. E. Jamer, P. Wei, B. Satpati, J. W. Freeland, I. Eremin, D. Heiman, P. Jarillo-Herrero, and J. S. Moodera, Nature **533**(7604), 513 (2016).
[445]C. Y. Yang, Y. H. Lee, K. H. O. Yang, K. C. Chiu, C. Tang, Y. W. Liu, Y. F. Zhao, C. Z. Chang, F. H. Chang, H. J. Lin, J. Shi, and M. T. Lin, Appl. Phys. Lett. **114**(8), 082403 (2019).
[446]C. Lee, F. Katmis, P. Jarillo-Herrero, J. S. Moodera, and N. Gedik, Nat. Commun. **7**(1), 12014 (2016).
[447]Y. S. Hou, J. Kim, and R. Q. Wu, Sci. Adv. **5**(5), eaaw1874 (2019).
[448]Q. L. He, X. F. Kou, A. J. Grutter, G. Yin, L. Pan, X. Y. Che, Y. X. Liu, T. X. Nie, B. Zhang, S. M. Disseler, B. J. Kirby, W. Ratcliff, Q. M. Shao, K. Murata, X. D. Zhu, G. Q. Yu, Y. B. Fan, M. Montazeri, X. D. Han, J. A. Borchers, and K. L. Wang, Nat. Mater. **16**(1), 94 (2017).
[449]Y. F. Wu, H. D. Song, L. Zhang, X. Yang, Z. H. Ren, D. M. Liu, H. C. Wu, J. S. Wu, J. G. Li, Z. Z. Jia, B. M. Yan, X. S. Wu, C. G. Duan, G. R. Han, Z. M. Liao, and D. P. Yu, Phys. Rev. B **95**(19), 195426 (2017).
[450]C. Zhao, T. Norden, P. Y. Zhang, P. Q. Zhao, Y. C. Cheng, F. Sun, J. P. Parry, P. Taheri, J. Q. Wang, Y. H. Yang, T. Scrace, K. F. Kang, S. Yang, G. X. Miao, R. Sabirianov, G. Kioseoglou, W. Huang, A. Petrou, and H. Zeng, Nat. Nanotechnol. **12**(8), 757 (2017).
[451]D. Zhong, K. L. Seyler, X. Y. Linpeng, R. Cheng, N. Sivadas, B. Huang, E. Schmidgall, T. Taniguchi, K. Watanabe, M. A. McGuire, W. Yao, D. Xiao, K. M. C. Fu, and X. D. Xu, Sci. Adv. **3**(5), e1603113 (2017).
[452]J. F. Xie, L. Jia, H. G. Shi, D. Z. Yang, and M. S. Si, Jpn. J. Appl. Phys. **58**(1), 010906 (2019).
[453]Z. Y. Zhang, X. J. Ni, H. Q. Huang, L. Hu, and F. Liu, Phys. Rev. B **99**(11), 115441 (2019).
[454]K. Zollner, P. E. Faria, and J. Fabian, Phys. Rev. B **100**(8), 085128 (2019).
[455]K. L. Seyler, D. Zhong, B. Huang, X. Linpeng, N. P. Wilson, T. Taniguchi, K. Watanabe, W. Yao, D. Xiao, M. A. McGuire, K.-M. C. Fu, and X. Xu, Nano Lett. **18**(6), 3823 (2018).
[456]W. Zhang, L. Zhang, P. K. J. Wong, J. Yuan, G. Vinai, P. Torelli, G. van der Laan, Y. P. Feng, and A. T. S. Wee, ACS Nano **13**(8), 8997 (2019).
[457]Y. Wang, J. Balgley, E. Gerber, M. Gray, N. Kumar, X. Lu, J.-Q. Yan, A. Fereidouni, R. Basnet, S. J. Yun, D. Suri, H. Kitadai, T. Taniguchi, K. Watanabe, X. Ling, J. Moodera, Y. H. Lee, H. O. H. Churchill, J. Hu, L. Yang, E.-A. Kim, D. G. Mandrus, E. A. Henriksen, and K. S. Burch, Nano Lett. **20**(12), 8446 (2020).
[458]S. Biswas, Y. Li, S. M. Winter, J. Knolle, and R. Valentí, Phys. Rev. Lett. **123**(23), 237201 (2019).
[459]H. H. Kim, B. Yang, T. Patel, F. Sfigakis, C. Li, S. Tian, H. Lei, and A. W. Tsen, Nano Lett. **18**(8), 4885 (2018).
[460]Z. Wang, D. Sapkota, T. Taniguchi, K. Watanabe, D. Mandrus, and A. F. Morpurgo, Nano Lett. **18**(7), 4303 (2018).
[461]A. Avsar, A. Ciarrocchi, M. Pizzochero, D. Unuchek, O. V. Yazyev, and A. Kis, Nat. Nanotechnol. **14**(7), 674 (2019).
[462]B. Li, T. Xing, M. Zhong, L. Huang, N. Lei, J. Zhang, J. Li, and Z. Wei, Nat. Commun. **8**(1), 1958 (2017).
[463]P. M. Coelho, H.-P. Komsa, K. Lasek, V. Kalappattil, J. Karthikeyan, M.-H. Phan, A. V. Krasheninnikov, and M. Batzill, Adv. Electron. Mater. **5**(5), 1900044 (2019).
[464]L. Yang, H. Wu, W. Zhang, X. Lou, Z. Xie, X. Yu, Y. Liu, and H. Chang, Adv. Electron. Mater. **5**(10), 1900552 (2019).
[465]Y. Zhao, L. Lin, Q. Zhou, Y. Li, S. Yuan, Q. Chen, S. Dong, and J. Wang, Nano Lett. **18**(5), 2943 (2018).
[466]R. Wang, Y. Su, G. Yang, J. Zhang, and S. Zhang, Chem. Mater. **32**(4), 1545 (2020).
[467]M. Pizzochero, J. Phys. D: Appl. Phys. **53**(24), 244003 (2020).
[468]A.-M. Hu, X.-H. Zhang, H.-J. Luo, and W.-Z. Xiao, Mater. Today Commun. **25**, 101438 (2020).
[469]Y. Guo, S. Yuan, B. Wang, L. Shi, and J. Wang, J. Mater. Chem. C **6**(21), 5716 (2018).
[470]J. He, G. Ding, C. Zhong, S. Li, D. Li, and G. Zhang, J. Mater. Chem. C **7**(17), 5084 (2019).
[471]Q. Cao, F. F. Yun, L. Sang, F. Xiang, G. Liu, and X. Wang, Nanotechnology **28**(47), 475703 (2017).
[472]A.-Y. Lu, H. Zhu, J. Xiao, C.-P. Chuu, Y. Han, M.-H. Chiu, C.-C. Cheng, C.-W. Yang, K.-H. Wei, Y. Yang, Y. Wang, D. Sokaras, D. Nordlund, P. Yang, D. A. Muller, M.-Y. Chou, X. Zhang, and L.-J. Li, Nat. Nanotechnol. **12**(8), 744 (2017).
[473]J. Zhang, S. Jia, I. Kholmanov, L. Dong, D. Er, W. Chen, H. Guo, Z. Jin, V. B. Shenoy, L. Shi, and J. Lou, ACS Nano **11**(8), 8192 (2017).
[474]F. Zhang, W. Mi, and X. Wang, Adv. Electron. Mater. **6**(1), 1900778 (2020).
[475]J. He and S. Li, Comput. Mater. Sci. **152**, 151 (2018).
[476]C. Zhang, Y. Nie, S. Sanvito, and A. Du, Nano Lett. **19**(2), 1366 (2019).
[477]Y. Ren, Q. Li, W. Wan, Y. Liu, and Y. Ge, Phys. Rev. B **101**(13), 134421 (2020).
[478]J. K. Dewhurst, P. Elliott, S. Shallcross, E. K. U. Gross, and S. Sharma, Nano Lett. **18**(3), 1842 (2018).
[479]Y. Tian, W. Gao, E. A. Henriksen, J. R. Chelikowsky, and L. Yang, Nano Lett. **19**(11), 7673 (2019).
[480]J. He and T. Frauenheim, J. Phys. Chem. Lett. **11**(15), 6219 (2020).
[481]J. Kim, K.-W. Kim, B. Kim, C.-J. Kang, D. Shin, S.-H. Lee, B.-C. Min, and N. Park, Nano Lett. **20**(2), 929 (2020).
[482]J. Zhou, L. Shen, M. D. Costa, K. A. Persson, S. P. Ong, P. Huck, Y. Lu, X. Ma, Y. Chen, H. Tang, and Y. P. Feng, Sci. Data **6**(1), 86 (2019).
[483]J. Nelson and S. Sanvito, Phys. Rev. Mater. **3**(10), 104405 (2019).
[484]P. Li, C. Wang, J. Zhang, S. Chen, D. Guo, W. Ji, and D. Zhong, Sci. Bull. **65**(13), 1064 (2020).
[485]K. Lasek, P. M. Coelho, K. Zberecki, Y. Xin, S. K. Kolekar, J. Li, and M. Batzill, ACS Nano **14**(7), 8473 (2020).
[486]M. Grönke, B. Buschbeck, P. Schmidt, M. Valldor, S. Oswald, Q. Hao, A. Lubk, D. Wolf, U. Steiner, B. Büchner, and S. Hampel, Adv. Mater. Inter. **6**(24), 1901410 (2019).
[487]N. Han, D. Yang, C. Zhang, X. Zhang, J. Shao, Y. Cheng, and W. Huang, J. Phys. Chem. Lett. **11**(21), 9453 (2020).
[488]A. P. Balan, S. Radhakrishnan, C. F. Woellner, S. K. Sinha, L. Deng, C. L. Reyes, B. M. Rao, M. Paulose, R. Neupane, A. Apte, V. Kochat, R. Vajtai, A. R. Harutyunyan, C. W. Chu, G. Costin, D. S. Galvao, A. A. Martí, P. A. van Aken, O. K. Varghese, C. S. Tiwary, A. Malie Madom Ramaswamy Iyer, and P. M. Ajayan, Nat. Nanotechnol. **13**(7), 602 (2018).
[489]C. Ó. Coileáin and H. C. Wu, Spin **7**(3), 1740014 (2017).

[490]M. Lee, W. Kang, Y. Onose, Y. Tokura, and N. P. Ong, Phys. Rev. Lett. **102**(18), 186601 (2009).
[491]A. Neubauer, C. Pfleiderer, B. Binz, A. Rosch, R. Ritz, P. G. Niklowitz, and P. Böni, Phys. Rev. Lett. **102**(18), 186602 (2009).
[492]P. Liu, X. Luo, Y. Cheng, X.-W. Wang, W. Wang, H. Liu, K. Cho, W.-H. Wang, and F. Lu, J. Phys.: Condens. Matter **30**(32), 325801 (2018).
[493]D. Foster, C. Kind, P. J. Ackerman, J.-S. B. Tai, M. R. Dennis, and I. I. Smalyukh, Nat. Phys. **15**(7), 655 (2019).
[494]P. W. Anderson, Mater. Res. Bull. **8**(2), 153 (1973).
[495]L. Savary and L. Balents, Rep. Prog. Phys. **80**(1), 016502 (2017).
[496]L. Balents, Nature **464**(7286), 199 (2010).
[497]Y. Lu, R. Fei, X. Lu, L. Zhu, L. Wang, and L. Yang, ACS Appl. Mater. Interfaces **12**(5), 6243 (2020).
[498]C. Huang, Y. Du, H. Wu, H. Xiang, K. Deng, and E. Kan, Phys. Rev. Lett. **120**(14), 147601 (2018).
[499]H. Tan, M. Li, H. Liu, Z. Liu, Y. Li, and W. Duan, Phys. Rev. B **99**(19), 195434 (2019).
[500]B. Xu, S. Li, K. Jiang, J. Yin, Z. Liu, Y. Cheng, and W. Zhong, Appl. Phys. Lett. **116**(5), 052403 (2020).
[501]X. Tang and L. Kou, J. Phys. Chem. Lett. **10**(21), 6634 (2019).
[502]J. A. Bert, B. Kalisky, C. Bell, M. Kim, Y. Hikita, H. Y. Hwang, and K. A. Moler, Nat. Phys. **7**(10), 767 (2011).
[503]L. Li, C. Richter, J. Mannhart, and R. C. Ashoori, Nat. Phys. **7**(10), 762 (2011).
[504]X. Zhu, Y. Guo, H. Cheng, J. Dai, X. An, J. Zhao, K. Tian, S. Wei, X. C. Zeng, C. Wu, and Y. Xie, Nat. Commun. **7**(1), 11210 (2016).
[505]M. D. Lumsden and A. D. Christianson, J. Phys.: Condens. Matter **22**(20), 203203 (2010).
[506]A. A. Kordyuk, Low Temp. Phys. **38**(9), 888 (2012).
[507]C. V. Topping, F. K. K. Kirschner, S. J. Blundell, P. J. Baker, D. N. Woodruff, F. Schild, H. Sun, and S. J. Clarke, Phys. Rev. B **95**(13), 134419 (2017).
[508]C.-Z. Chang, J. Zhang, X. Feng, J. Shen, Z. Zhang, M. Guo, K. Li, Y. Ou, P. Wei, L.-L. Wang, Z.-Q. Ji, Y. Feng, S. Ji, X. Chen, J. Jia, X. Dai, Z. Fang, S.-C. Zhang, K. He, Y. Wang, L. Lu, X.-C. Ma, and Q.-K. Xue, Science **340**(6129), 167 (2013).
[509]M. Serlin, C. L. Tschirhart, H. Polshyn, Y. Zhang, J. Zhu, K. Watanabe, T. Taniguchi, L. Balents, and A. F. Young, Science **367**(6480), 900 (2020).
[510]Y. Li, D. West, H. Huang, J. Li, S. B. Zhang, and W. Duan, Phys. Rev. B **92**(20), 201403 (2015).
[511]X. Zhang, A. Wang, and M. Zhao, Carbon **84**, 1 (2015).
[512]X. Kong, L. Li, O. Leenaerts, W. Wang, X.-J. Liu, and F. M. Peeters, Nanoscale **10**(17), 8153 (2018).
[513]H. Ishizuka and Y. Motome, Phys. Rev. Lett. **109**(23), 237207 (2012).
[514]Z. Yue, Z. Li, L. Sang, and X. Wang, Small **16**(31), 1905155 (2020).
[515]C. Liu, Y. Wang, H. Li, Y. Wu, Y. Li, J. Li, K. He, Y. Xu, J. Zhang, and Y. Wang, Nat. Mater. **19**(5), 522 (2020).
[516]J. Ge, Y. Liu, J. Li, H. Li, T. Luo, Y. Wu, Y. Xu, and J. Wang, Natl. Sci. Rev. **7**(8), 1280 (2020).
[517]Z. Li, J. Li, K. He, X. Wan, W. Duan, and Y. Xu, Phys. Rev. B **102**(8), 081107 (2020).
[518]A. Milosavljević, A. Šolajić, J. Pešić, Y. Liu, C. Petrovic, N. Lazarević, and Z. V. Popović, Phys. Rev. B **98**(10), 104306 (2018).
[519]S. Y. Kim, T. Y. Kim, L. J. Sandilands, S. Sinn, M.-C. Lee, J. Son, S. Lee, K.-Y. Choi, W. Kim, B.-G. Park, C. Jeon, H.-D. Kim, C.-H. Park, J.-G. Park, S. J. Moon, and T. W. Noh, Phys. Rev. Lett. **120**(13), 136402 (2018).
[520]S. Petit, F. Moussa, M. Hennion, S. Pailhès, L. Pinsard-Gaudart, and A. Ivanov, Phys. Rev. Lett. **99**(26), 266604 (2007).
[521]B. H. Zhang, Y. S. Hou, Z. Wang, and R. Q. Wu, arXiv:1909.12968 (2019).
[522]J. J. Heath, M. Costa, M. Buongiorno-Nardelli, and M. A. Kuroda, Phys. Rev. B **101**(19), 195439 (2020).
[523]S. J. Gong, C. Gong, Y. Y. Sun, W. Y. Tong, C. G. Duan, J. H. Chu, and X. Zhang, Proc. Natl. Acad. Sci. **115**(34), 8511 (2018).
[524]C. Cardoso, D. Soriano, N. A. García-Martínez, and J. Fernández-Rossier, Phys. Rev. Lett. **121**(6), 067701 (2018).
[525]M. Khazaei, M. Arai, T. Sasaki, C.-Y. Chung, N. S. Venkataramanan, M. Estili, Y. Sakka, and Y. Kawazoe, Adv. Funct. Mater. **23**(17), 2185 (2013).